Dissertation zur Erlangung des Doktorgrades

der Fakultät für Chemie und Pharmazie

der Ludwig-Maximilians-Universität München

# Synthesis and Functionalization of Mesoporous Silica Materials for Applications as Host-Guest-Systems

M. Sc. Alexandra Schmidt

aus

München, Deutschland

2014

**Erklärung**

Diese Dissertation wurde im Sinne von § 7 der Promotionsordnung vom 28. November 2011 von Herrn Prof. Dr. Thomas Bein betreut.


**Eidesstattliche Versicherung**

Diese Dissertation wurde eigenständig und ohne unerlaubte Hilfe bearbeitet.



      München, 11.09.2014








Dissertation eingereicht am    11.09.2014

1. Gutachter: Prof. Dr. Thomas Bein

2. Gutachter: Prof. Dr. Christoph Bräuchle

Mündliche Prüfung am        09.10.2014

# Abstract

Mesoporous silica materials have attracted much interest in the past decades due to their potential in numerous fields including adsorption, sensing, catalysis and biomedical applications. Especially mesoporous silica nanoparticles (MSNs) have been widely studied as delivery vehicles and bioimaging devices on the nanoscale allowing for successful cell internalization due to their small sizes. These silica-based nanoparticles feature a well-defined and controllable porosity, high surface areas and the possibility to introduce a large variety of functionalities for controlled host-guest interactions, fluorescent labeling and cell-surface recognition. Different methods for the facile introduction of organo-moieties to the silica surface have been established in the past years, including post-synthesis grafting, delayed co-condensation approaches and functionalization with metal-organic reagents. The porous structure of the nano-carriers allows for the shielded transport of fragile and expensive cargos such as chemotherapeutics. A major challenge in modern nano-medicine is the development and engineering of nanostructures for the efficient encapsulation of drug molecules avoiding premature release before the target site is reached; temporally- and spatially-controlled release properties of the nano-carriers are highly favored. Furthermore, the adsorption of different therapeutics at high concentrations, the targeted delivery into tumor or inflammatory tissues and the controllable release at the target site are key prerequisites in the field of advanced drug delivery and will be addressed in this work. Various gatekeepers for successful pore sealing have been developed in the past years, ranging from inorganic nanoparticles and polymeric shells to enzyme caps and highly biocompatible supported lipid bilayers. To enable a stimuli-responsive release of the cargo molecules, redox- or light-driven opening pathways have been widely studied. Additionally, endosomal entrapment after successful internalization into the targeted cell, a major bottleneck in delivery of membrane impermeable drugs, has to be overcome. Different opening strategies have been developed recently, ranging from photosensitizers for light-induced disruption of the endosomal membrane to *proton-sponge-effect*-driven release mechanisms, based on the internal acidification of the endosome. Yet, the development of multifunctional stimuli-responsive release on-demand systems combining all prerequisites for successful drug delivery systems is still a major goal of current research.

In addition to the above-mentioned issues, MSNs with ultra-large pores (LP_MSNs, exhibiting pore sizes up to 20 nm) and distinct small particle sizes have become a main focus of

MSN-based research as they should allow the incorporation of high molecular weight cargos and thus the successful delivery of oligonucleotides to cancer cells and *in vivo* systems. Tailor-made oligonucleotides together with polyplexes and liposomes as carrier vehicles are already widely used in gene-therapy for effective gene-silencing. Despite the existence of such nano-vehicles, encapsulation of the siRNA in the mesoporous framework of LP_MSNs is highly desirable since unspecific RNA degradation could be overcome as the pores are not accessible for RNA-cleaving enzymes (RNAses). An important prerequisite of such nanocarriers for successful adsorption and delivery of oligonucleotides is the possibility to modify the silica surface with functional groups enabling control of host-guest interactions with the cargo molecules. Additionally, fine-tuning of the outer shell of the LP_MSNs should allow for efficient capping of the mesopores, preventing premature release of the cargo molecules. Yet, to the best of our knowledge, the reported nano-agents with large pores (over 5 nm) lack the possibility for *in situ* organo-functionalization of the drug delivery vehicle and typically require an additional grafting process.

The further development and improvement of structurally stable mesoporous silica nanoparticles with different pore sizes, exhibiting distinct recognition and trigger functions for successful cellular uptake are part of recent research and will be addressed in detail in this work.

In a first project in collaboration with the group of Prof. J. Rädler (LMU München, Department of Physics), we designed a fluorimetric reporter system based on supported lipid bilayer coated mesoporous silica nanoparticles (SLB@MSN) to obtain time distributions of endosomal escape events, which enables us to evaluate the efficiency of drug and gene delivery vectors. The developed system is equipped with a blue-light sensitive on-board photosensitizer (protoporphyrin IX, PpIX) on the outer surface enabling endosomal escape upon singlet oxygen generation and subsequent membrane rupture. The core of the silica nanoparticles is modified with a redox-labile dye/quencher system, allowing an estimation of the number of particles per endosome as well as the timescales at which endosomal lysis takes place. Furthermore, the varying uptake behavior of our lipid-coated drug delivery system in different cell-lines (Renca LacZ, 3T3 and HuH7) was successfully investigated in this study.

Multifunctional mesoporous silica nanoparticles (MSNs) exhibit excellent cellular internalization behavior via endocytosis due to their small size (diameter of 80 nm) but it has to be noted that endosomal entrapment is the major bottleneck of drug delivery nano-carriers and hinders efficient cargo release. Therefore, in collaboration with the group of Prof. Bräuchle

we developed a release on-demand system based on highly biocompatible SLB-capped MSNs and a light-responsive external stimulus. A novel core-shell MSN-system with pore diameter of 5 nm (a 25% higher value compared to common MSNs) was developed and post-synthetically modified with a covalently bound red-light sensitive photosensitizer (AlPcS$_{2a}$) excitable near the therapeutic window. Two differently sized targeting ligands (folate and epidermal growth factor) were successfully incorporated into the SLB via diffusion. Fluorescence live-cell imaging allowed us to evaluate the functionality of the targeting ligands on two different cell lines (KB and HuH7). The successful release of different fluorescent model drugs (calcein and a rhodamine derivative) upon singlet oxygen generation and subsequent membrane rupture was monitored with *in vial* and *in vitro* methods. We have developed a highly efficient custom-made release on-demand nano-carrier system for efficient cell targeting and cargo release, which provides high potential for *in vivo* applications.

A second approach for successful targeted drug delivery and stimuli-responsive release was based on the covalent attachment of a pH-responsive polymer to the outer surface of our MSNs. The use of the bi-functional, pH-sensitive polymer poly-(2-vinylpyridine) [PVP] permits the sequential attachment of polyethylene glycol (PEG), enhancing the dispersibility of the nano-carriers and the subsequent modification with a photosensitizer (AlPcS$_{2a}$) and targeting ligands (folate). The long-term stability of the multifunctional drug delivery vehicles in cell media was studied at different pH values, yielding important information on the behavior of the nano-carrier in biological fluids. The efficient targeting ability of the drug delivery system was proven by competition experiments with free folic acid *in vitro* and fluorescence live-cell imaging in co-operation with the group of Prof. Bräuchle. Endosomal acidification was used as internal trigger for the subsequent release of cargo molecules from the mesopores: membrane permeable cargos (colchicine and DAPI) could be delivered without applying an external stimulus to the system, whereas a photosensitizer was employed to release non-membrane permeable cargos (fluorescein) from the endosome. Thus, a modular toolbox based on a pH-responsive system with long term stability suitable for *in vitro* and *in vivo* applications was designed.

A major interest of the present work was the development of organo-modified mesoporous silica nanoparticles with ultra-large pores and defined small particle sizes (LP_MSNs) allowing for the adsorption of high molecular weight cargos (e.g. enzymes and oligonucleotides). In chapter 8, we demonstrate the successful optimization of the pore diameter and the molecular functionalization of the mesopores in order to permit the facile diffusion and attachment of

guest molecules into the host. An increase in pore diameter to values of 7 – 15 nm was achieved with high molecular weight surfactants (Pluronic F127) and novel fluorinated co-surfactants (FC-4), special low temperature synthesis protocols and the employment of organic micellar expanders. For the first time the successful synthesis of organo-functionalized LP_MSNs (LP_MSN-SH, LP_MSN-NH$_2$/Ph and LP_MSN-N$_3$) via a co-condensation approach is reported, making these nanoparticles highly promising candidates for various biomedical applications.

Enzyme immobilization for catalytic processes is a key application of mesoporous silica materials, as the pores can protect the fragile cargo from external influences such as degradation. The covalent attachment of active, functional biomolecules at the large internal surface of the newly developed organo-functionalized LP_MSNs (pore diameter of 13 nm) was investigated. For this purpose, a facile synthesis of azide-modified LP_MSNs based on a co-condensation approach was successfully developed, which permits a mild and bioorthogonal click chemistry reaction within the porous network. Two acetylene-functionalized enzymes of different sizes (cytochrome C and trypsin) were immobilized in the pores of LP_MSN-N$_3$ and their catalytic activity was investigated with fluorogenic reactions. It was demonstrated that both enzymes provide an extraordinary increase in activity in their immobilized state compared to previous studies and free enzymes; a 2.9 times higher activity was observed for LP_MSN-CytC compared to the free enzyme.

In addition to the immobilization of biocatalysts, mesoporous silica nanoparticles with ultra-large pores (LP_MSNs) are promising candidates for the *in vivo* delivery of oligonucleotides, as the porous network meets the molecular dimensions of the bioactive molecules. We designed a stimuli-responsive nano-carrier system based on LP_MSNs with amino-functionality modified with a red-light sensitive phthalocyanine photosensitizer (AlPcS$_{2a}$). In a joint project with Prof. Bräuchle and coworkers, the successful cellular uptake behavior of supported lipid bilayer capped LP_MSNs was studied with fluorescence live-cell imaging. This system provides an on-demand release mechanism based on photoactivation and subsequent singlet oxygen production. The successful membrane rupture was proven by *in vial* and *in vitro* cargo release experiments with model drugs of different sizes (calcein, propidium iodide, fluorescently-labeled dextran 10 kD).

Another aim of this work was the organo-functionalization of MCM-41 with aromatic systems, introduced into the mesoporous framework via metal-organic reagents. ^{13}C MAS ssNMR

studies revealed that the choice of the lithiation agent is of key importance; the lithiation of 4-bromo arenes with *tert*-butyllithium is highly favorable compared to the lithiation with n-butyllithium since no unwanted side-reactions can occur. With this newly generated approach it was possible to introduce multiple aromatic compounds into the mesopores of MCM-41 without destruction of the mesoporous framework. Since all introduced organo-functionalities are suitable for post-synthesis modification with functionalities such as catalysts, this approach offers a versatile toolbox for the highly efficient post-synthesis modification of mesoporous materials.

In summary, we have established different multifunctional mesoporous silica nanoparticle systems that allow successful release of different cargo molecules via external (photoactivation) and internal (pH-responsive polymer) stimuli after targeted cellular internalization. It could be shown in different projects that due to their unique properties, mesoporous silica nanoparticles are highly promising candidates for advanced biomedical applications. Furthermore, different MSNs with ultra-large pores (7 – 15 nm average pore size) and organo-functionalization were developed during this work and successfully employed for enzyme immobilization and *in vitro* release experiments. The future aim is to combine the different approaches to achieve targeted delivery of chemotherapeutics and oligonucleotides for effective gene-silencing in tumors *in vivo,* thus achieving the ultimate spatio-temporal control of the nanoparticle agents.

# Table of contents

# 1 Introduction

## 1.1 Mesoporous silica materials

To date a large variety of differently shaped mesoporous silica materials is known, ranging from films[1, 2] to micrometer-sized particles[3, 4], rod-like silica structures[5, 6] and nanometer-sized mesoporous silica nanoparticles (MSNs)[7-9]. The most widely studied family of nanostructured mesoporous materials, the M41S-family and its relatives, was discovered in the early 1990s by researchers from Mobil Research and Development Corporation and others.[10-12] These mesoporous silica materials were synthesized via silica condensation under basic conditions employing organic surfactants including cetyltrimethylammonium bromide/chloride (CTAB/CTAC) as templates.[13] Depending on the surfactant concentration, the formed material exhibits three main subgroups, namely MCM-41 (Mobile Composition of Matter), MCM-48 and MCM-50 together with a variety of less ordered phases.[11, 12] MCM-41 forms hexagonally packed micelle structures whereas MCM-48 features a cubic and MCM-50 a lamellar arrangement of the mesopores (Figure 1.1).[11, 12, 14, 15]
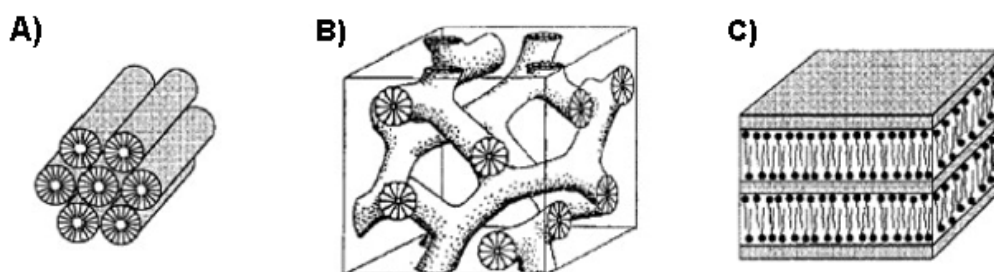


**Figure 1.1:** M41S structure types. **A)** hexagonal, **B)** cubic bi-continuous and, **C)** lamellar.[14]

Further research in the following years led to a rapid development in the area of ordered mesoporous silica materials due to their unique properties, which provide a variety of nanotechnological applications in the fields of separation, catalysis, adsorption, and sensing.[16-20] Another well-established representative of mesoporous silica materials is the Santa Barbara Amorphous 15 (SBA-15), exhibiting a 2D hexagonal mesostructure.[3, 4] SBA-15 has been extensively studied for various applications, ranging from enzyme immobilization[21-23], catalysis[24-27] to single molecule studies with oligonucleotides[28, 29] due to its well-ordered pore

structures with uniform, tuneable mesopores (9 – 30 nm) and large specific surface areas. Kruk and co-workers showed that a substitution of the micellar expander 1,3,5-trimethylbenzene (TMB) by 1,3,5-triisopropylbenzene (TiPB) leads to an increase in pore size of SBA-15 particles.[30, 31] The application of SBA-15 materials in drug delivery, however, is limited due to their typically large particle sizes in the micrometer-range, which hinders efficient cell uptake.[32] Spherical and rod-like SBA-15 in the sub-micrometer range have been synthesized, yet particle sizes below 200 nm could not be obtained with these methods to date.[22, 23]

### 1.1.1 Mesoporous silica nanoparticles (2 – 5 nm pores)

The application field of conventional mesoporous materials (SBA-15 and MCM-41) in drug delivery, a main focus of today's mesoporous silica research, is limited due to their large particle diameters ($\geq$ 500 nm). Different studies have evaluated the size-dependent cellular uptake of nano-carriers via endocytosis.[32, 33] Thus, considerable effort has been extended towards the design of novel silica materials exhibiting small and controllable particle sizes, suitable for endocytosis. Since the first report of MCM-41 type mesoporous silica nanoparticles (MSNs) with defined small sizes as drug delivery system in 2000, interest in these nanomaterials has dramatically increased.[34] Brinker and co-workers developed an aerosol-based synthesis procedure for the formation of MSNs with different pore geometries, depending on the employed structure directing agent (CTAB, Brij-58 and Pluronic P123; Figure 1.2).[7] The method relies on an evaporation induced self-assembly (EISA) process of the silica precursor in the aerosol droplets.
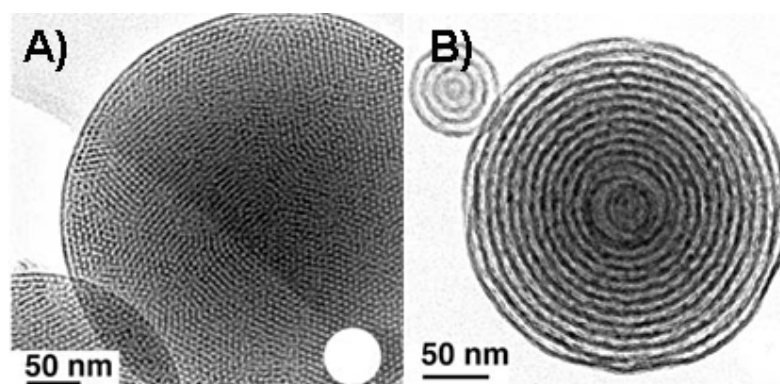


**Figure 1.2: A)** Template-free particles with cubic mesostructure (Brij-58 as surfactant), and **B)** calcined particles with a vesicular mesophase (Pluronic P123 as surfactant).[7]

The research groups of Grün[35], Cai[36], Mann[37], and Ostafin[38] developed MSNs of sub-micrometer sizes based on a modified Stöber[39] procedure by adding different cationic surfactants to the reaction mixture. These approaches paved the way for the success of mesoporous silica nanoparticles, because the synthesis is straightforward compared to the aerosol method, which requires special equipment. Since then, considerable effort has been extended regarding the synthesis of MSNs with a focus on mesostructural diversity, compositional flexibility and morphological control.[9, 40-45] Lin and co-workers have synthesized thiol-functionalized MSNs with a mean diameter of 200 nm and pore sizes of 2.9 nm and showed successful capping of the mesopores with CdS nanoparticles to prevent cargo leakage (Figure 1.3A).[8] A standard synthesis approach for the generation of MCM-41-like silica nanoparticles follows a condensation procedure of the silica precursors (TEOS and organotrialkoxy silanes) at highly basic conditions (pH 12.5) and is widely used for the development of multifunctional nanoparticles.[46-49] Another strategy for highly homogeneous MSNs meeting the prerequisites for drug delivery applications was developed in our group.[9] Instead of sodium hydroxide, triethanolamine is used as base and complexing ligand for the silica precursor. This CTAC-mediated pathway allows for the facile synthesis of uniform MSNs with 4 nm pores (worm-like pore structure, suggesting a seed-growth mechanism) and spherically shaped particles with sizes of about 80 nm (Figure 1.3B).[9, 40, 50] Recently, this synthesis approach was refined by adding the micellar expander TiPB. This modification of the synthesis approach led to an pore size enlargement of 25% (5 nm) compared to the previously described MSNs.[41] Additionally, small amounts of ammonium fluoride were added to the reaction mixture resulting in perfectly spherically shaped nanoparticles that seem to exhibit a radial growth mechanism (Figure 1.3C). The multifunctional MSNs developed by Bein and co-workers were already successfully examined as promising drug delivery vehicles in cells, exhibiting stimuli-responsive release properties..[41, 51, 52] Gai *et al.* were able to synthesize MSNs with fibrous morphology by a urea assisted synthesis. These nanoparticles have been shown to efficiently adsorb the anti-cancer therapeutic doxorubicin (Dox).[53] The particle size of MSNs could be easily varied by a change of the TEOS:CTAB-ratio.
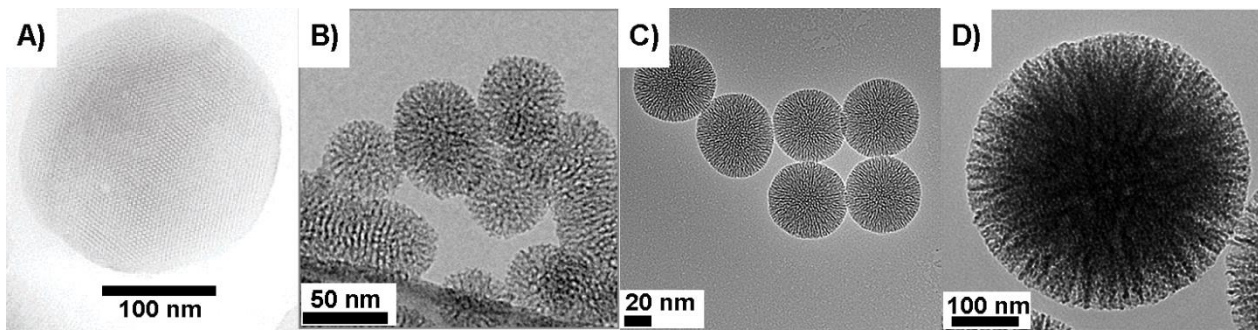
**Figure 1.3:** TEM micrographs of different, template-free mesoporous silica nanoparticles. **A)** Organo-modified MCM-41-like silica nano-spheres,[8] **B)** core-shell MSNs with 4 nm pore size exhibiting a worm-like mesoporous framework,[40] **C)** core-shell MSNs with 5 nm pores,[41] and **D)** MSNs with fibrous morphology.[53]

In addition to the above-mentioned systems, other types such as the Singapore Institute of Bioengineering and Nanotechnology (IBN)[42, 54] and FDU-n (Fudan University) series[55] show great potential in various biomedical applications. In general, multifunctional MSNs have been widely studied as promising nano-carriers for anti-cancer drugs such as doxorubicin[56, 57] or paclitaxel[58, 59] both *in vitro* as well as *in vivo*.[60, 61]

### 1.1.2 Functionalization of mesoporous silica materials

The selective functionalization of mesoporous silica materials is of key importance to allow the attachment of shielding polymers (poly(ethylene glycol), PEG), targeting ligands and stimuli-responsive trigger systems, among others. These requirements for successful drug delivery vehicles will be explored in the following chapters. Different functionalization methods to modify mesoporous silica materials are known: post-synthesis grafting with organo-silanes, co-condensation methods, synthesis of periodic mesoporous organosilicas (PMO) and modification with metal-organic reagents.[62-67] Post-synthetic grafting with organo-silanes is the most common method to introduce organo-moieties to the silica surface. However, the grafting procedure shows several disadvantages. For instance, no distinct control over the location of the functionalization is possible and is not always evenly distributed over the pore walls and external particle surface. Furthermore, the amount of introduced functionality can vary from one reaction to another, which requires a detailed analysis and calculation of the grafted material prior to subsequent reactions.

Another promising approach is the so-called co-condensation method, which enables a direct incorporation of organo-silanes into the mesoporous framework during the synthesis procedure. It has to be noted that certain organo-silanes, especially with amino-functionality (e.g., 3-aminopropyl triethoxysilane (APTES)), are able to disrupt the mesostructure formation due to a change of the pH value during the synthesis. In particular, Lebold *et al.* showed that amino-functionalized SBA-15 can only be synthesized by a co-condensation approach when a distinct amount of stabilizing phenyl-silane is added to the synthesis.[68] Similar results were obtained for large pore mesoporous silica nanoparticles (cf. chapter 7). Another elegant way to establish organo-functionalities is their introduction via a site-selective delayed co-condensation approach, which allows for a facile synthesis of core-shell functionalized MSNs (Figure 1.4).[40] The onion-like structure provides a selective successive decoration of the nanoparticle interior with fluorescent dyes or the fine-tuning of host-guest interactions. Moreover, the outer surface can be selectively modified with biocompatible polyethylene glycol (PEG) linkers or stimuli-responsive gatekeepers without affecting the core of the MSNs, and thus the pores remain accessible for the efficient uptake and release of cargo molecules.[51, 69]
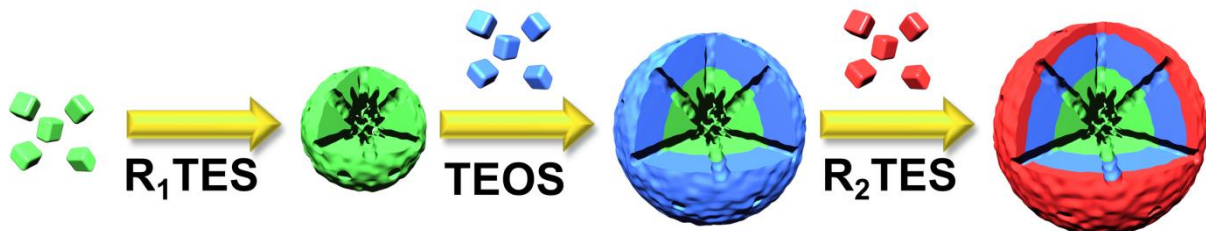


**Figure 1.4:** Facile synthesis of core-shell MSNs via a delayed co-condensation approach. In a first step the silica core with organo-functionalization is synthesized ($R_1$TES, green), followed by a thin pure silica layer (blue) that shields the core from the differently modified shell of the MSN ($R_2$TES, red).

Several studies of our group in the past years have already shown the great potential of the delayed co-condensation approach for the synthesis of advanced drug delivery nano-carriers.[70-74] It can be concluded that surface modification with organic-moieties permits the introduction of a large variety of functionalities to control host-guest interactions, diffusion and release, fluorescent labeling, and cell-surface recognition, amongst others. This will be addressed in the following chapters.

### 1.1.3   Large-pore mesoporous silica nanoparticles

Although a wide application of MSNs as versatile vehicles for advanced drug delivery purposes was observed in the past twenty years,[13, 51, 75-78] limits arise when large cargos should be immobilized. The relatively small pore sizes of conventional MSNs limit their application as host system for macromolecules such as enzymes and cell-active oligonucleotides. Great efforts have been made to optimize the pore diameter with regard to the adsorption of large biomolecules. Furthermore, an optimization of the molecular functionalization of the mesopores will provide a facile diffusion and attachment of guest molecules into the host material.[28, 29] In particular, the adsorption of small interfering RNA (siRNA) into large pore MSNs (LP_MSNs) is of great current interest. Artificially generated siRNA is a promising therapeutic in gene therapy since it can be specifically designed to knock down messenger RNA (mRNA). Subsequently, it inhibits the translation of a target protein that is known to cause a certain disease.[79-81] Hom *et al.* attached siRNA to the external surface of PEI-modified mesoporous silica nanoparticles and observed an effective gene silencing of enhanced green fluorescent protein (EGFP).[81] It is highly desirable to incorporate the fragile and expensive molecules within the mesoporous channels of the drug delivery vehicles to prevent premature degradation and leakage before the targeted compartment is reached. Proof that the oligonucleotides are actually adsorbed in the mesopores of the LP_MSNs and not only complexed at the outer surface remains vague in both above-mentioned reports. A well-established representative of mesoporous silica materials with large pores is the μm-sized SBA-15, which was introduced by Stucky and co-workers in 1998, exhibiting a high hydrothermal stability and large, tuneable pore sizes (4.9 – 30 nm).[3, 4] However, it has to be noted that in addition to large pore sizes, a distinctly small particle size (within a size range of 50 – 300 nm) of the nano-carrier is of key importance for cell experiments and *in vivo* applications.[13] Recently, several strategies for the synthesis of LP_MSNs with a particle diameter of 70 – 300 nm and very large pores (up to 17 nm) using a novel fluorocarbon surfactant (FC-4) and triblock copolymers (Pluronic F127, P123 and P65) have been published by different groups.[42, 54] Han *et al.* studied the impact of different non-ionic triblock copolymers (Pluronic P65, P123 and F127) and FC-4 (cf. Table 1.1). FC-4 which acts as co-surfactant was found to limit the particle growth at moderate temperatures.[42] Different Singapore Institute of Bioengineering and Nanotechnology (IBN) mesoporous silica materials were synthesized with this approach, exhibiting distinctive pore sizes depending on the employed surfactant and

reaction temperatures. 3D cubic, 2D hexagonal as well as foam-like and disordered pore structures with varying pore sizes were synthesized (Table 1.1).

**Table 1.1:** LP_MSNs obtained with a fluorocarbon-mediated synthesis.[42]

| Sample | Mesostructure | Template | BET surface area [m²/g] | Pore volume [cm³/g] | Pore size[b] [nm] |
|--------|---------------|----------|-------------------------|---------------------|-------------------|
| **IBN-1** | 3D cubic (*Im3m*) | F127 | 779 | 0.73 | 5.8 |
| **IBN-2** | 3D cubic (*Fm3m*) | F127 + TMB | 804 | 0.65 | 9.5 |
| **IBN-3** | Mesocellular foam | P65 + TMB | 821 | 0.72 | 19.5 |
| **IBN-4** | 2D hexagonal (*p6m*) | P123 | 709 | 0.88 | 6.4 |
| **IBN-5** | disordered | F108 | 575 | 0.54 | 5.2 |

The use of FC-4 during the syntheses proved to be necessary as very large and irregular mesoporous particles were obtained without the co-surfactant. Additionally, the reported syntheses were carried out under mildly acidic conditions and moderate reaction temperatures (25 – 30 °C). Higher acidity and temperatures are known to promote a rapid and uncontrolled hydrolysis of the silica precursors, hindering the formation of well-defined nanoparticles.[42] Gao *et al*. developed a facile strategy for the generation of LP_MSNs based on the work of Ying and co-workers.[54] A dual surfactant system consisting of the triblock copolymer Pluronic F127 together with FC-4 and TMB as micellar expander was studied in detail at different low temperatures (5 – 10 °C). Different studies report that low synthesis temperatures favor the diffusion of the micellar expander into the hydrophobic core of the micelles during the particle formation and therefore help to enlarge the pore size.[42, 54, 55, 82] Additionally, the post-synthesis hydrothermal treatment was varied by Gao *et al.* in comparison to the original publication.[54] Spherical, unfunctionalized LP_MSNs with ultra-large pores were obtained with this modified procedure (Figure 1.5C).
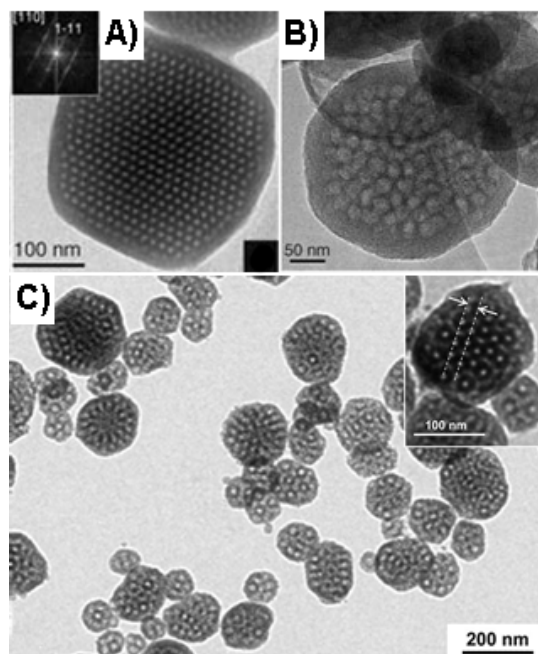
**Figure 1.5:** Transmission electron micrographs of LP_MSNs generated with a fluorocarbon-assisted synthesis. **A)** HRTEM image of 3D cubic LP_MSNs taken along the [111] direction (inset: corresponding FT patterns),[42] **B)** HRTEM image of calcined LP_MSNs (mesocellular foam) synthesized with Pluronic P65 and TMB,[42] and **C)** LP_MSNs obtained at a synthesis temperature of 15 °C with a hydrothermal treatment at 135 °C. The inset shows the view from the [110] direction and the local arrangement.[54]

Besides the fluorocarbon surfactant mediated syntheses, several other possibilities for the generation of LP_MSNs are known: Shi and co-workers developed core-shell structured mesoporous silica spheres (Figure 1.6A and B) via an amphiphilic block copolymer (polystyrene-*b*-poly (acrylic acid), PS-*b*-PAA) route in combination with CTAB as template. Several different core-shell nanoparticles were generated by this procedure.[83] Ryoo and co-workers obtained mesoporous silica nanoparticles with an average pore diameter of 23 nm via a post-synthesis pore expansion procedure with TMB under static conditions (Figure 1.6C).[43]
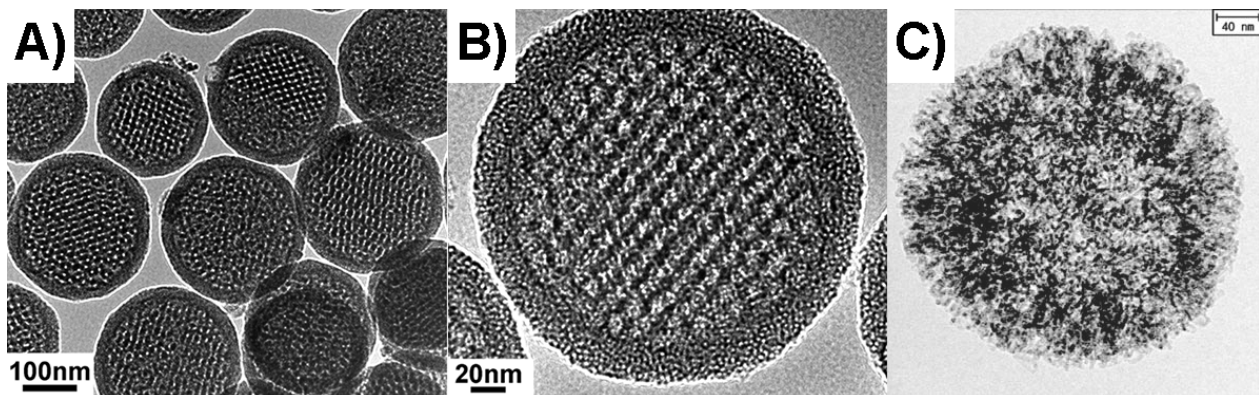
**Figure 1.6: A)** and **B)** TEM images of core-shell structured dual-mesoporous silica spheres (DMSS-PS100) synthesized with an amphiphilic block copolymer (polystyrene-*b*-poly (acrylic acid), PS-*b*-PAA) and cetyltrimethyl ammonium bromide (CTAB) acting as co-templates.[83] **C)** MSN23 after hydrothermal treatment.[43]

Importantly, the above-mentioned LP_MSNs synthesis protocols lack the possibility of a direct incorporation of organo-functionalities into the silica framework and employ post-synthesis grafting for surface modification. However, a controlled distribution of the functionality is a key prerequisite for the attachment of external triggers such as targeting ligands and/or stimuli-responsive capping mechanisms. Different strategies for an efficient delivery of modified LP_MSNs to cells have been reported previously, but it has to be noted that all approaches were based on post-synthesis grafting methods.[43, 54] Gao *et al.* modified the silica surface with amino-moieties for efficient plasmid DNA (pDNA) adsorption.[54] In contrast, Hartono *et al.* described the post-synthesis attachment of poly-L-lysine (PLL) to the outer surface of LP_MSNs for efficient siRNA delivery to osteosarcoma cancer cells.[84] However, cationic polymers such as PLL are widely used for the generation of polyplexes for efficient gene delivery due to their interaction with the negative backbone of the oligonucleotides and no evidence of a direct incorporation of the siRNA in the mesopores is given. Another class of promising large pore mesoporous silica materials which was recently discovered and extensively studied for various applications are so-called hollow spheres and rattle-type (yolk-shell) materials.[13, 85, 86] These MSNs exhibit low densities, high specific surface areas and loading capacities that make them promising candidates for various biomedical applications.[13] Different synthesis routes are available for the generation of hollow spheres, namely (1) a soft-templating approach, (2) a selective etching strategy and (3) a self-templating method. We refrain from discussing possibilities (2) and (3) in this chapter. Yeh *et al.* reported in 2006 a facile synthesis of hollow sphere mesoporous silica materials with a ternary surfactant system

consisting of Pluronic P123, CTAB and sodium dodecyl sulfate (SDS)[87], an approach which was later modified by Lu *et al.*.[88] Mou and co-workers generated hollow spheres with a water-in-oil (w/o) microemulsion technique, employing cyclohexane, Triton X-100 and water.[89] Aminopropyl trimethoxysilane (APTMES) combined with TEOS was used as silica source in this approach (Figure 1.7A and B). The APTMES amount is crucial to control the particle size of the hollow spheres. Lu *et al.* synthesized yolk-shell MSNs of tuneable wall thickness by employing Pluronic F127 together with FC-4 and a distinct amount of ammonium nitrate.[88, 90] The core of the yolk-shell MSNs was composed of $Fe_3O_4$ nanoparticles, allowing their application in catalysis. Besides the soft-templating approaches, numerous yolk-shell MSNs were obtained by etching methods, enabling the facile synthesis of large amounts (up to 10 g) in a convenient one-pot synthesis (Figure 1.7 C and D).[13, 91-94] Additionally, the particle size can be effectively tuned from sub-100 nm nanoparticles to micrometer-sized rattle-spheres.[13] It can be concluded that nowadays several different methods are available for a precise formation of hollow sphere silica nanoparticles and yolk-shell nano-rattles.
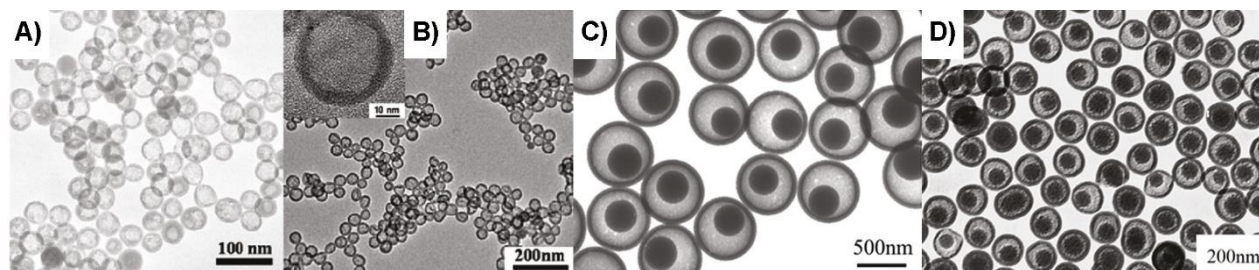


**Figure 1.7: A)** and **B)** TEM micrographs of hollow sphere silica nanoparticles[89], and **C)** and **D)** of yolk-shell nano-rattles.[94]

Many of the above-mentioned materials are promising candidates for advanced drug delivery with flexible and tuneable nano-carriers. This topic will be addressed in the following chapters.

## 1.2 Targeted drug delivery for cancer treatment with nano-carriers

### 1.2.1 Nano-material based cancer therapy

Cancer is one of the most devastating diseases worldwide with more than 14 million new cases per year, with an increasing tendency.[95] Modern cancer treatments utilize surgical intervention, radiation and chemotherapeutic drugs (such as doxorubicin, paclitaxel and cis-platin) that cause severe side-effects.[96] Doxorubicin (DOX) is the most commonly used anti-cancer therapeutic causing an efficient induction of apoptosis in cancer cells but also showing a high cardiotoxicity.[13] The fluorescence of this drug allows for the direct observation with fluorescence microscopy.[97] In the context of reducing the side-effects and the required amount of drug, nanomaterials have attracted an increasing interest in cancer treatment due to their securely and shielded delivery of the therapeutics to the desired targeting sites without affecting healthy tissues.[96, 98-102] Potential nano-carriers should fulfill several prerequisites for successful applications in drug delivery, namely (1) a high loading capacity with regard to the drug, (2) a site-specific delivery mechanism (targeting) exclusively to cancer cells, (3) no premature release before the target site is reached, (4) high level of cellular internalization, (5) a stimuli-responsive release mechanism that enables a selective drug release at the target site, and (6) a composition of biocompatible /biodegradable/bioexcretable materials.[101] The most widely studied nano-vehicle systems are based on 'soft', organic carriers due to their high biocompatibility and possibility for functionalization, most commonly the decoration with polyethylene glycol (PEG). The most prominent representatives are liposomes that complex the cytostatic agents and form so-called active lipoplexes. The liposomal drug complexes Doxil (for doxorubicin) and Daunoxome (for daunorubicine) were the first to find their use in the clinic and are successfully used in cancer treatment, limiting the side-effects of the free drugs.[101, 103] To date, a total of six drugs with liposomal carrier systems have been approved for cancer treatments[100] and about additional 20 liposomal drugs are in clinical trials.[99, 102] However, it has to be noted that liposomal systems show several disadvantages ranging from instability under physiological conditions and the lack of temporal control over the drug release rate, showing sustained release.[104] Additionally, Doxil shows side-effects, namely skin toxicity, which is not present upon administration of the free drug.[105] Another class of organic carriers that has been widely studied in the past years are so called polyplexes consisting of polymers that enable complexation of the drugs.[98, 106-108] The most prominent application of such polyplexes is the successful delivery of oligonucleotides, mainly small interfering RNA

(siRNA) and single-stranded oligonucleotides for artificially induced gene silencing (gene knock-down).[109] For instance, 21-23 base pair (bp) long double-stranded siRNA[110, 111] is delivered to the cytosol where the antisense strand is integrated into the RNA-induced silencing complex (RISC).[107] This complex binds and cleaves the complementary messenger RNA (mRNA) with high precision, leading to a knock-down of the expressed gene. The most widely used polymers for gene delivery are cationic polymers that bind nucleic acids via electrostatic interactions with the negatively charged backbone of the oligonucleotides. The cationic polymers used for this purpose include linear or branched poly(ethyleneimine) (PEI), poly(amidoamine) (PAMAM) dendrimers and poly-L-lysine (PLL).[112-115] The major drawback of these nano-carriers is a possible premature unpacking of the polyplexes by serum proteins and extracellular matrix components before the target site is reached.[116] PEI-siRNA-polyplexes were found to dissociate in full human serum immediately after their administration.[117, 118] To solve this so-called 'polyplex-dilemma' (of polyplexes being too labile in extracellular medium and too stable for intracellular dissociation)[107] attention is likely to be focused on bio-responsive polymers that respond to internal stimuli.[119-121] By 2014, two therapeutic drugs based on nucleic acids, namely Vitravene (Fomivirsen) and Kynamro (Mipomersen)[122], have been approved by the FDA, and several other antisense therapeutics have reached advanced stages of clinical trials.[123, 124] Despite the above-mentioned achievements in nano-medicine, novel drug delivery systems are of key importance, allowing to overcome certain disadvantages (low drug loading, high costs, low synthesis yields) and facilitating cost-effective alternatives.[13] Inorganic nano-carriers such as mesoporous silica nanoparticles provide a multiplicity of advantages for drug delivery applications including selective size and shape control, tuneable pore sizes, and large pore volume and surface area for high loading capacities. Additionally, they are more robust than many organic supports and comparably cheap.[34, 101] Selective post-synthesis functionalization of the silica surface permits the circumvention of undesired biological interactions (e.g., cargo degradation prior to reaching the target), and facilitates bioavailability and effective cellular uptake.[41, 69, 77, 125, 126] The ultimate goal of modern nano-medicine is to enable efficient and patient-friendly treatments by a reduction of the systemic drug concentration and dosing frequency and  by offering easier administration and improved safety.[127]

### 1.2.2 Mesoporous silica nanoparticles as drug delivery vehicles[i]

Mesoporous silica nanoparticles (MSNs) with sizes up to 500 nm have attracted much interest for their potential as drug delivery vehicles to control various cell functions by the stimuli-responsive delivery of bioactive cargos.[13, 78, 128-133] For further reading on this topic, see full review article of Argyo *et al.*.[133] The first application of MSNs as potential drug delivery systems was reported by Vallet-Regí and co-workers in 2000.[34] Ibuprofen was successfully adsorbed into the mesopores of MCM-41 type MSNs, yielding high loading capacities and subsequent drug release. Ever since, an exponential increase in MSN-based drug delivery research could be observed, as the MSNs feature well-defined and controllable porosity at the nanometer scale.[13] Furthermore, the host-guest interactions can be selectively modified for increased cargo adsorption, which results in higher yields of drug loading. Efficient uptake of the MSNs via endocytosis into different types of cells was observed.[76, 134, 135] However, Mou and co-workers reported a size-dependent endosomal uptake in HeLa cells, favoring a size-range of 50 – 120 nm.[33] Particles with a size of 190 nm already showed significant cytotoxicity at concentrations higher than 25 mg/mL. An ideal drug delivery vehicle based on MSNs may be composed of a multifunctional silica core to be able to specifically control the interaction with diverse active cargo components. The cargo molecules (e.g. fluorescent dyes or pharmaceutically active drugs) are adsorbed in the mesopores of the nanoparticle, yielding a sufficient shielding from external degradation in biological fluids.[69, 136] Efficient pore closure, and consequently a prevention of premature release, is achieved via stimuli-responsive bulky gatekeepers (e.g. gold nanoparticles, polymers, rotaxanes, enzymes, oligonucleotides) that efficiently block the pore entrances. These gatekeepers can respond to external or internal cellular stimuli for a specifically controlled cargo release.[137-142] To enable high cellular uptake of the multifunctional MSNs, targeting ligands can be covalently attached to the outer surface of the particles via a flexible PEG-linker that additionally shields the particle from external influences. It is known that many receptors are overexpressed on the extracellular surface of cancer cells and can be specifically targeted with corresponding ligands. The mechanism follows a key-lock principle and is highly selective towards receptor-mediated endocytosis. The most commonly used receptor target is the folic acid receptor (FAR) and the epidermal growth

---

[i]) This part of the introduction was inspired by the perspective article of C. Argyo *et al.*, *Chem. Mater.* **2013**, *26*, 435–451.

factor (EGF). Since endosomal escape is a major bottle-neck for successful drug delivery, a trigger that helps the nano-carrier to escape its entrapment and to release its cargo into the cytosol is highly desirable. Different approaches based on internal (acidification of the endosome, membrane fusion) as well as external triggers (light-induced membrane rupture) are reported in the literature (Figure 1.8).[133]
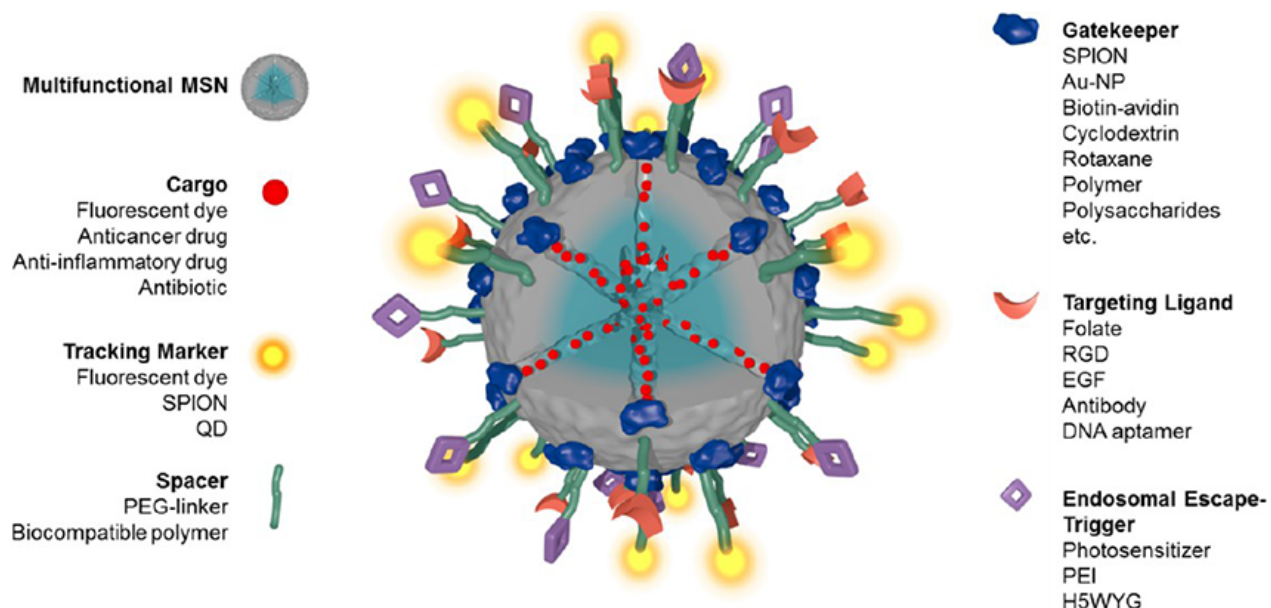


**Figure 1.8:** Schematic illustration of a multifunctional mesoporous silica nanoparticle (MSN) based on the core-shell MSNs developed by Bein and co-workers,[40] exhibiting the key features for stimuli-responsive drug release from the endosomal compartment of a targeted cancer cell. Ideally, the vehicle consists of a fluorescent tracking marker, a stimuli-responsive gatekeeper, a targeting ligand on the outer surface enabling receptor-mediated endocytosis and an endosomal escape trigger. (SPION: superparamagnetic iron oxide nanoparticle, QD: quantum dot, PEG: poly(ethylene glycol), Au-NP: gold nanoparticle, RGD: Arg-Gly-Asp amino acid sequence, EGF: epidermal growth factor, PEI: poly(ethylene imine), H5WYG: endosomolytic peptide).[133]

Various model drugs and pharmaceutically active cargos such as ibuprofen[34], doxorubicin[48, 53, 56, 143], cis-platin[144-146] and paclitaxel[58] have been successfully delivered by MSNs until today. In addition to their application as promising nano-carriers for the treatment of chronic inflammation diseases and cancer, the MSNs have also been widely studied in the field of bone tissue engineering[147] and treatment of diabetes.[148]

### 1.2.3 Cellular uptake in cancer cells and receptor-targeting

A major limitation of common cytostatic drugs used for chemotherapy is the insufficient target selectivity that can lead to nonspecific toxicity and severe side-effects as well as a reduction of therapeutic efficacy, requiring higher applied drug doses. This "vicious circle" in anticancer treatment can be overcome by specially designed drug delivery vehicles for targeted cell internalization. Cellular uptake of nanoparticles within a distinct size range (< 200 nm) usually occurs via endocytosis where the nano-carriers are engulfed by the cell membrane and delivered to the intracellular matrix in membrane bound vesicles.[134, 135, 149, 150] Mou and co-workers investigated the influence of the particle size on the cellular internalization by HeLa cells.[33] It was shown that the cellular uptake is highly size-dependent in the order 50 nm > 30 nm > 110 nm > 280 nm > 170 nm. Shi and co-workers examined the *in vivo* biodistribution and urinary excretion of spherical MSNs of different sizes (80, 120, 200, and 360 nm) by intravenous administration of the nano-carrier.[151] Smaller sizes of the PEGylated MSNs proved to have a slower biodegradability and correspondingly lower degradation products in the urine.

Site-specific targeting can be classified into two different types, namely passive and active targeting. Passive targeting is based on the so-called enhanced permeability and retention (EPR) effect which is commonly observed in solid tumors; the tumor tissues grow extraordinary quickly in comparison to healthy cells, leading to leaky microvasculatures and impaired lymphatic function. Thus, nanoparticles in the suitable size-range present in the tumor-surrounding blood vessels tend to accumulate in the tumor tissue.[152] In contrast, active targeting is based on a ligand-receptor interaction following a lock-key-principle which requires the modification of the drug delivery vehicles with a targeting ligand (TL), enabling increased cell uptake.[153] In general, receptors are membrane-bound proteins of different sizes being commonly overexpressed on the extracellular membrane of various cancer cell types. The main challenge of targeted drug delivery with nano-vehicles is to selectively design stable, non-immunogenic carriers that are able to achieve a high targeting specificity but avoid non-specific binding to the cell membranes. TLs range from small molecules (folic acid) to different macromolecules (e.g. epidermal growth factor), which all enable an efficient uptake of the drug delivery vehicles via a receptor-mediated endocytosis. An overview of the major receptors together with their overexpression in cancer cell types is given in Table 1.2.[152] FA is one of the most frequently used targeting ligands in current research as the folate receptor is highly up-regulated in many human cancers.[154-157] Additionally, folate is highly stable, non-toxic, comparably cheap and easily modified to meet the requirements of successful

attachment onto the nano-carrier. A broad variety of FA modified lipids and PEG-chains is actually commercially available, which enables the facile modification of the vehicles. Lee *et al.* showed that a flexible PEG-spacer between FA and the lipid is mandatory to successfully target liposomes[158], a strategy that was recently employed by our group to deliver supported lipid bilayer capped MSNs (SLB@MSN) to cancer cells.[41] Mamaeva *et al.* demonstrated active targeting by covalent conjugation of folate to MSNs and the successful delivery of γ-secretase inhibitors (GSIs) down-regulating the notch signaling pathway.[159] Two other widely studied receptors for the targeting of nano-carriers are the epidermal growth factor receptor (EGFR)[160-162] and the integrin receptor.[163-165] Additionally, nano-sized drug delivery vehicles modified with so called dual-receptor targeting have gained high attention in recent years since these systems enable the addressing of two different cells which are related to a certain disease process with a single nano-carrier. Xu *et al.* designed a branched copolymer with cyclicRGDfK and transferrin on the outer surface for successful delivery of paclitaxel.[166] These systems are highly attractive for the treatment of glioma as the blood brain barrier restricts the diffusion of larger molecules such as common chemotherapeutics and nano-carriers.[167, 168] Recently, aptamers have attracted great attention as receptor targeting ligands for cancer cells.[169] The custom-made aptamers consist of single-stranded deoxyribonucleic acid (DNA) or ribonucleic acid (RNA) oligonucleotides selectively designed for the interaction with a target receptor.[170] For instance, the human transferrin receptor CD71 (TfR), which is overexpressed in a number of cancer cell lines and the blood brain barrier, can be targeted by DNA aptamers.[171] Wilner and co-workers synthesized specific aptamers that are stabilized against serum via a modified selection protocol to target stable nucleic acid lipid particles (SNALPs). A minimized aptamer (c2.min) was reported to be specific for the human receptor, allowing a successful internalization into various cancer cell lines.[171]

**Table 1.2:** Summary of overexpressed cell membrane receptors on cancer cells widely used for selective drug delivery using receptor–ligand pairs in preclinical models of cancer.[152]

| Major Receptor Type | Specific receptor | Overexpression in cancer cell types |
|---|---|---|
| **G protein coupled receptors (GPCRs)** | *Bombesin receptor (BnR)* | Lung, prostate, breast, pancreatic, head/neck, colon, uterine, ovarian, renal cell, glioblastomas, neuroblastomas, gastrointestinal carcinoids, intestinal carcinoids, and bronchial carcinoids. |
| | *Somatostatin receptors (SSTRs)* | Small cell lung, neuroendocrine tumor, prostate cancer, breast cancer, colorectal carcinoma, gastric cancer, hepatocellular carcinoma. |
| | *Endothelin receptors (ETRs)* | Melanoma tissues |
| **Integrins** | *αvβ3 is of particular interest in selective drug targeting* | Activated endothelial cells and tumor cells (such as U87MG glioblastoma cells), ovarian cancer cells |
| **Folate receptors (FRs)** | *FRα, FRβ and FRγ; FRα, a cell surface glycosyl phosphatidylinositol-anchored glycoprotein most commonly studied* | Most tissues including breast cancer cells. |
| **Transferrin receptors (TfRs)** | *TfR1 & TfR2* | Breast, ovary, and brain cancers such as glioma and glioblastomas |
| **Epidermal growth factor receptor (EGFR)** | *EGFR (or ErbB1, HER1) ErbB2 (HER2, in rodents) ErbB3 (HER3) ErbB4 (HER4)* | Lung, breast, bladder, and ovarian cancers. |
| **Fibroblast growth factors (FGFRs)** | *So called 'acid box'* | Breast, prostate, bladder, and gastric cancer |
| **Sigma receptors (SRs)** | *S1R and S2R* | Non-small cell lung carcinoma, prostate cancer, melanoma, and breast cancer |
| **Others** | *Follicle stimulating hormone receptors (FSHRs)* | Ovarian surface epithelium |
| | *Biotin receptors (BRs)* | Leukemia |
| | *C-type lectin receptors (CLRs)* | Hepatocytes, dendritic cells, macrophages |
| | *Asialoglycoprotein receptor (ASGPR)* | |
| | *NRP-1* | Human vascular cells |

It has to be noted that although the main research interest lies on active targeting in recent years, passive targeting of nano-carriers via the EPR effect is already successfully being employed for several systems (e.g. Doxil) in the clinic.[152]

### 1.2.4 Endosomal escape

Drug delivery vehicles based on nanomaterials show good cellular internalization via the endocytosis pathway, but endosomal entrapment is a major challenge for successful drug delivery, especially for membrane-impermeable cargos and those exhibiting a low solubility. The typical fate of nanoparticles internalized by endocytosis includes intracellular trafficking of early endosomes to late endosomes or endolysosomes. A drastic acidification of the vesicle occurs by proton pumps (ATPases) and results in a change of internal pH-value (from 7.4 to 5.5).[172] In addition to the decrease in pH, the transition leads to an increase of the enzymatic concentration (including e. g. proteases, reductases) within the compartment which can be harmful to many therapeutic molecules and can finally lead to the degradation of the drugs.[173] Therefore, major efforts have been made to develop mechanisms that allow the nano-carriers to escape the endosome. Endosomal escape is of high importance and several possibilities to overcome this have been studied in the past years. To date, various different methods are known for a successful endosomal membrane rupture and subsequent cargo release, based on external (light irradiation, ultrasonic radiation, change in temperature) and internal (change of the pH-value within the endosome) stimuli. The most intensively studied endosomal escape pathway relies on pH-buffering effects (so called 'proton sponge')[174, 175] and on the photochemical activation of photosensitizers that generate singlet oxygen leading to a disintegration of the endosomal membrane.[41, 51, 176] Brinker and co-workers developed a multifunctional drug delivery system based on MSNs with a supported lipid bilayer for cargo encapsulation, which is equipped with an endosomolytic peptide (H5WYG) on the outer surface of the nano-carrier (Figure 1.9).[75] The peptide sequence derives from the active subunit of the glycoprotein hemagglutinin of the influenza virus A and undergoes a conformational change upon protonation, facilitating endosomal escape. In addition, the attached targeting ligand (SP94) enables efficient receptor-mediated uptake of the "protocells" into cells via endocytosis. Due to neutral pH-values in early endosomes, the endosomolytic peptide remains inactive but

undergoes a conformational change during the subsequent endosomal acidification into its active state, leading to membrane rupture. Thus, the cargo molecules such as 5-fluoruracil, siRNA and cis-platin were released into the cytosol and found to accumulate on their target site (Figure 1.9-4). It has to be noted that, although these H5WYG-peptides are commonly used together with nano-vehicles, experimental evidence and proof for the exact mechanism is not yet available.[177-179]
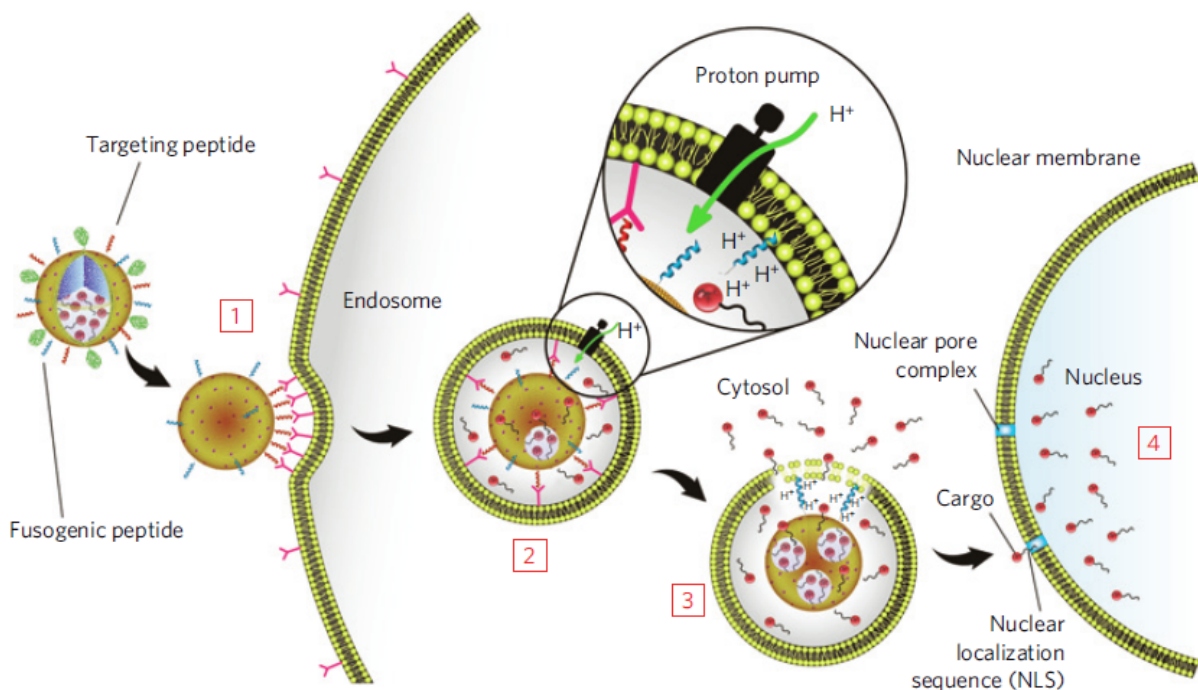


**Figure 1.9:** Scheme of efficient internalization of multifunctional, lipid-coated "protocells" (MSNs) and subsequent drug release upon endosomal acidification. **1)** DOPC-coated protocells with a targeting peptide (SP94) and a fusogenic peptide on the outer surface are internalized via receptor-mediated endocytosis, **2)** uptake of the protocell is followed by subsequent acidification of the cellular compartment, **3)** upon acidification a conformational change of the fusogenic peptide takes place (blue) leading to endosomal membrane rupture and subsequent cargo release into the cytosol, and **4)** cargo modified with a nuclear localization sequence (NLS) accumulates in the nucleus.[75]

Another widely studied endosomal escape mechanism based on the internal stimulus of compartment acidification is the so called 'proton sponge effect'. This mechanism is based on an intrinsic osmotic swelling caused by the buffering capacity of specially designed nano-vehicles which finally leads to endosomal membrane rupture.[172] Several cationic, amino-modified lipids and polymers such as PEI and PAMAM dendrimer structures were examined as potential proton sponges as they exhibit a substantial buffering capacity below the

physiological pH.[175, 180, 181] PAMAM dendrimers have been originally introduced by Tomalia *et al.*[182] in 1985 and have already gained high attention for various applications.[183] Lin and co-workers developed a gene-transfection drug delivery system based on MSNs with covalently attached PAMAM dendrimer (second generation, G2)[184], whereas Nel and co-workers used non-covalently attached PEI on the surface of MSNs for the successful delivery of DNA and siRNA to cells.[59]

An alternative mechanism for endosomal escape relies on external stimuli such as light-activation of photosensitizers (PS), which leads to subsequent membrane rupture by singlet oxygen.[76, 176] In comparison to internal triggers, the endosomal escape events can be precisely controlled with such systems, facilitating a spatial and temporal controlled cargo release. In contrast to photodynamic therapy (PDT), the photosensitizer (PS) does not act as actual "drug" in these systems, but as tool for endosomal escape of the nano-carriers by the generation of reactive oxygen species (ROS) upon photoactivation. Recently, different approaches with on-board photosensitizers excitable with visible light have been developed by our group, providing control of the endosomal escape events and thus, the release of the drug into the cytosol of cancer cells. The utilization of photosensitizers is not only a reliable method for the disintegration of the supported lipid bilayer which encloses the MSNs, but also a powerful tool to overcome nanoparticle and cargo entrapment by the endosomal membrane.[51] Schlossbauer *et al.* developed an on-board system with a blue light excitable photosensitizer based on protoporphyrin IX for a successful chromobody delivery[51], which was investigated in more detail by Dobay *et al.*.[74] Due to the low penetration depth of short wavelength light in tissues, a recent study by Bräuchle and co-workers employs a phthalocyanine-based photosensitizer where successful targeting of MSNs and subsequent endosomal escape was shown (cf. chapter 4).[41] Importantly, the activation of the PS with red light instead of blue light reduces the phototoxicity and significantly increases the depth of tissue penetration[185] which will be crucial when activation *in vivo* is required as shown by Kataoka and co-workers.[186] Novel approaches to overcome endosomal entrapment by light responsive opening mechanisms are based on two-photon excitation or near infrared photosensitizers.[187-190]

### 1.2.5 Controlled, stimuli-responsive cargo release

The precise spatial and temporal control of nano-vehicles allowing an on-demand cargo release in cell compartments can be described as the holy grail of advanced drug delivery research, since premature cargo release is highly undesirable. A broad variety of different triggered-release capping systems were presented in the past years, based on external stimuli such as light[51, 191, 192], heat[71, 193-195] or magnetic fields,[57] or triggered by intracellular events including a change in pH[196-198], redox reactions[8, 199] or the presence of enzymes.[200]

*Exogenous stimuli-responsive systems.* The most widely studied stimuli-responsive capping systems are based on external triggers that allow control and activation of the internalized nano-carriers on demand and without invasive methods. Light-triggered release has attracted great interest since the development of photo-responsive azobenzene ligands by Brinker and co-workers in 2003 that enable the switching of molecular valves by *cis-trans* isomerization.[192] Matsukata and co-workers developed a UV-light responsive capping system for MCM-41 based on the 2+2 photodimerization of coumarin at distinct wavelengths.[191] The photodimerziation-cleavage cycle of thymine was successfully employed by He *et al.* for the gating of MSNs.[201] Zhao and co-workers developed a photothermal-responsive system based on rotaxane-modified MSNs (Figure 1.10 A).[202] The movement of the α-cyclodextrin ring (green) can be controlled by *cis-trans* isomerization of azobenzene linkers, which allows for efficient cargo loading (at 365 nm) and subsequent curcumin release upon irradiation with visible light. Another possibility for light-triggered release is the employment of singlet oxygen responsive lipids (e.g. DOPC) to generate a supported lipid bilayer (SLB) around photosensitizer-functionalized MSNs.[41, 51, 76] The highly biocompatible SLB enables successful uptake into different cells, and efficient cargo encapsulation in the mesoporous framework of MSNs. The photo-induced release mechanism is based on a two-step cascaded membrane rupture by singlet oxygen; the SLB around the MSN is disintegrated in a first step, followed by subsequent rupture of the endosomal membrane, and consequently cargo release into the cytosol can be achieved. Therefore, light-responsive mechanisms relying on two photon excitation and photosensitizers excitable in the NIR-range are promising possibilities for tumor treatment in deeper tissues.[203-205] Another possibility for a non-invasive and stimuli-responsive, controlled drug delivery approach for cancer therapy is the design of nano-carriers sensitive to applied magnetic fields. Several multifunctional core-shell nanosystems based on a superparamagnetic iron oxide core ($Fe_3O_4$) and a silica or polymer shell have been designed recently[206, 207] and tested both *in vitro* and *in vivo* for targeted cell uptake and cargo release upon magnetization.[208, 209] Lee and

co-workers used polymer-coated zinc-doped iron oxide nanoparticles for the successful *in vivo* delivery of doxorubicin.[210] Zink and co-workers developed an iron oxide/MSN core-shell system which was modified with a pseudorotaxane on the outer surface of the nano-carrier, serving as efficient capping system (Figure 1.10 B).[57] The dye-loaded MSNs were successfully internalized in cancer cells with no premature release observable prior to the application of the external magnet field. In addition to the previously described studies, magnetically guided nano-carriers based on cationic polymers, iron oxide nanoparticles and oligonucleotides are also used for the successful delivery of nucleic acids to cancer cells. The so-called magnetofection has led to an increased effectiveness of siRNA directed against breast[211] and prostate cancers.[212] Moreover, in addition to the triggered drug release, with these particles it is possible to perform magnetic resonance imaging (MRI), which facilitates the combination of diagnostics with therapy in a single nano-carrier system (so called theranostic approach).[213] Current research is based on an enhancement of the magnetic strength of the iron oxide core by doping with $Mn^{2+}$ and $Zn^{2+}$ ions.[214, 215] Among the opening mechanisms based on exogenous stimuli, thermo-responsiveness is the most widely studied approach in nano-medicine, and thermoresponsive liposomes (TSLs) with encapsulated doxorubicin (ThermoDox) reacting to mild hypothermia have already reached phase III of clinical trials for unresectable hepatocellular carcinoma.[173] Nevertheless, due to the known disadvantages of liposomal carriers, the development of novel drug delivery vehicles reacting to heat is a major topic of current research. Al-Ahmady *et al.* developed an alternative approach for thermosensitive liposomes by incorporating a thermoresponsive peptide, a so-called leucine-zipper into the liposomes.[216] Upon an increase in temperature (43 °C) the peptide undergoes a conformational change leading to membrane rupture and subsequent cargo release. A completely different approach for thermosensitive pore opening was developed by Bein and co-workers.[71] Multifunctional MSNs were modified with a thermo-labile DNA-valve system (Figure 1.10C-1). This release on-demand system employs double-stranded DNA of different length and biotin-avidin coupling for effective pore closure. Depending on the length of the DNA-linker, different opening temperatures of the gates were observed, enabling a fine-tuning of the stimuli-responsive release system.

A different strategy is based on thermoresponsive polymers, with poly(*N*-isopropyl acrylamide) (PNIPAM) the most commonly used among them.[173] A temperature-sensitive inorganic-organic hybrid system was developed by You and co-workers; MSNs were coated with

PNIPAM to achieve efficient pore closure and successful encapsulation of fluorescein (Figure 1.10C-2) at 38 °C.[217] The model drug is released upon a decrease to ambient temperature. It has to be noted that an opposite closure-opening mechanism (closure at ambient temperature, release at mild hypothermia conditions) would be highly favorable for a successful application of silica-polymer systems in drug delivery applications and is part of current research.

*Endogenous stimuli-responsive systems.* In comparison to the aforementioned triggered-release mechanisms based on exogenous stimuli that require external triggers for successful drug release, internal stimuli based on enzyme activity, cell compartment acidification and redox-sensitive triggers have also gained much interest in recent years. Specific enzymes (e.g. proteases, phospholipases and glycosidases) were found to be overexpressed under the pathologic conditions of inflammation and cancer and can therefore be exploited as potential biological target. Especially so-called matrix metalloproteinases (MMPs), zinc-dependent endopeptides, are overexpressed during advanced stages of several cancers, as the MMP-mediated matrix degradation increases the metastatic potential of tumor cells whereas healthy cells show almost no expression of MMPs.[218] Zhu *et al.* described the use of short peptide sequences that are exclusively cleavable by MMP-2.[219] They were used as linkers between PEG and TAT-functionalized liposomes with encapsulated siRNA (Figure 1.10D), masking the bioactive compounds. After successful cleavage in the tumor, the active ligands are exposed showing increased intracellular penetration and thus, high amounts of gene silencing *in vivo* (70%). A similar approach was applied by Singh *et al.* to obtain bioresponsive MSNs for successful in vivo application.[220] A different strategy for bioresponsive MSNs is based on pore closure/opening with enzymes. Schlossbauer *et al.* developed a protease-responsive capping system based on biotin-avidin interaction and showed successful cargo release in the presence of the protease trypsin.[70] In addition to the previously described methods of enzyme-responsive release systems, an exploitation of the increased enzyme concentration in lysosomes has become a major focus of research.[221, 222] Another intrinsic stimulus is based on the reductive milieu of certain cell compartments: the concentrations of glutathione vary between extracellular (~2–10 μM) and intracellular compartments (~2–10 mM) and can therefore be used for selective cleavage of redox-labile bonds, most commonly disulfide bridges.[173] Lin and co-workers attached organo-modified quantum dots via a disulfide bridge to the outer surface of MSNs and achieved successful capping of the mesopores with this method, showing no premature release of the adsorbed cargo. Upon the addition of dithiothreitol the disulfide bridge was cleaved and a successful release of ATP and vancomycin

was observed (Figure 1.9E - schematic).[8] Additionally, redox-sensitive systems have been studied for dendrimer-drug conjugates[223], liposomes with conjugates[224], MSNs with snap-top caps[140] and reducible cationic polymers together with nucleic acids.[225, 226] It has to be mentioned that the strength of the reductive milieu varies strongly within different cell lines and endosomal entrapment might be a bottle-neck for redox-driven release in some cases.[76]

Cargo release can also be triggered by an intrinsic change of the pH value within cellular compartments. As described above, an acidification of the endosomal compartments takes place when the endosomes change from early to late endosomes (pH 7.4 to 5.5). Additionally, it is known that cancer tissues exhibit a slightly lower pH (6.5–7.2) than healthy tissues, which has led to an increase in research interest on pH-responsive systems.[173] A promising approach that takes advantage of this internal trigger involves pH-responsive linkers based on acetals. Schlossbauer *et al.* attached the bee venom melittin with a pH-responsive acetal-linker to SBA-15 mesoporous silica and showed successful release upon acidification whereas no release was observed for a non-cleavable linker (Figure 1.10F-1).[198] Another commonly used strategy is the design of pH-responsive ligands for the attachment of gatekeepers for efficient pore capping of MSNs. Especially, cyclodextrin rings have been widely studied as capping systems for MSNs, preventing premature release of the cargo molecules under physiological conditions. Zink and co-workers have developed several pH-responsive MSN systems based on cyclodextrin rings and rotaxanes that allow triggered release of encapsulated cargo molecules.[56, 227] Zhu *et al.* have developed an entirely different strategy for intrinsic, pH-triggered cargo release.[143] Zinc oxide nanoparticles, matching the pore size of the mesoporous material were covalently attached to the outer surface after adsorption of doxorubicin, preventing premature release of the chemotherapeutic before the nano-lids were dissolved upon internal acidification (Figure 1.10F-2).
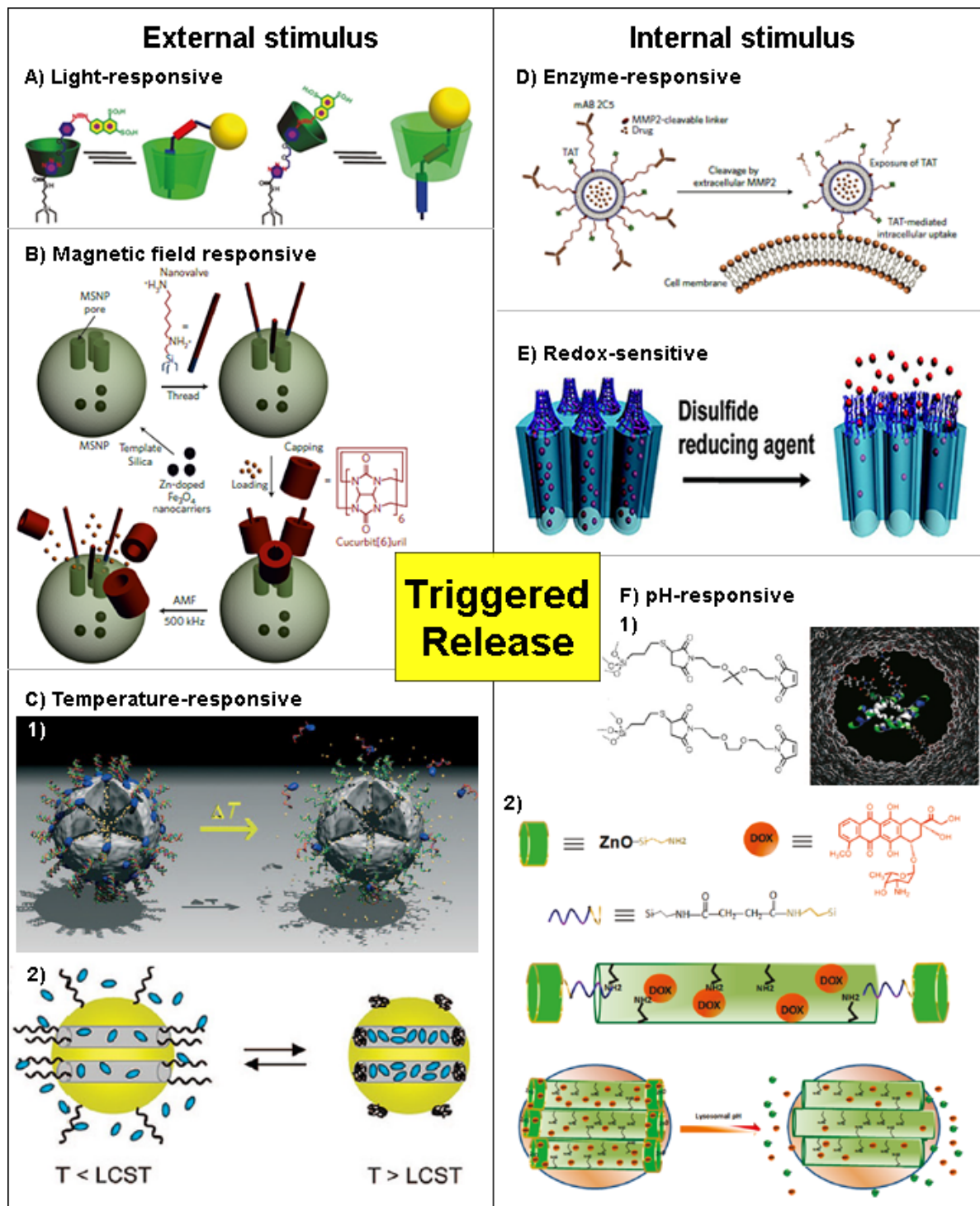
**Figure 1.10:** Exogenous and endogenous stimuli-responsive release mechanisms. **A)** Light-responsive cargo release based on *cis-trans* isomerization of the organic linker.[202] **B)** Cargo release based on an external magnetic field.[57] **C-1)** Temperature-responsive DNA-valve.[71] **C-2)** Pore closure and opening with PNIPAM.[217] **D)** Enzyme-responsive liposome system based on matrix metalloproteases.[219] **E)** Redox-labile disulfide capping system.[133] **F-1)** Delivery of melittin from SBA-15 by cleaving of a pH-responsive acetal-linker.[198] **F-2)** Pore-capping with pH-responsive ZnO nano-lids.[143]

Until now, only drug delivery vehicles reacting to exogenous stimuli are successfully being tested in clinical trials, namely thermosensitive liposomes (ThermoDox, Phase I – III, depending on the target cancer) and magneto-responsive nano-carriers (iron-oxide magnetite, Phase I for prostate and pancreatic carcinoma).[173] The major challenge with endogenous triggers is the probability of variation from one patient to another and between different cancer types.

## 1.3  Enzyme immobilization in mesoporous silica hosts

Enzymes exhibit outstanding properties as catalysts in terms of environmental safety, high efficiency, high chemo-, regio- and stereo selectivity, and they enable shorter synthetic routes compared to conventional catalysts.[228] Especially the enantioselective conversion of organic molecules is of great importance and a main focus of current research, especially in the production of pharmaceuticals.[229] Despite all the above advantages, the industrial use of enzymes is limited by difficulties in recovery of the biocatalyst, as well as by low operational stability.[230] The main goals of the immobilization of enzymes onto various solid supports are an enhancement of stability and the simplification of enzyme recovery. Therefore, many immobilization techniques on various solid support materials such as organo silica[231-235], metal oxides[236], metals[237], carbons[238] and polymers[239] have been investigated in the past years. Among the inorganic host systems, organo-functionalized nanostructured mesoporous silica materials have attracted great attention since they offer outstanding properties for the encapsulation of various catalytically active biomolecules.[21, 229, 240, 241] The broad variety of available mesoporous silica materials enables the adjustment and fine-tuning of the pore- and particle size, matching the requirements of the enzyme. Additionally, structural arrangements and surface properties for optimized loading capacities can be modified matching the targeted biocatalyst.[242] It is of high importance that the physiochemical properties of the protein and the support are matching, and this has to be taken into account upon selection of the solid support. Especially the hydrodynamic radius of the enzymes has to be considered; Diaz and co-workers showed that horse-radish peroxidase with a mean diameter of 4.6 nm cannot be immobilized into the comparably small pores of MCM-41 (average 2.8 nm).[243] Yiu *et al*. investigated the immobilization of trypsin in different mesoporous materials, namely MCM-41, MCM-48 and SBA-15; it was shown that the amount of adsorbed enzyme was directly correlated to the pore

size of the support material.[244] Studies on standard silica materials (e.g. SBA-15) revealed that enzyme confinement within different supports can increase its stability and reduce denaturation by protein unfolding, one major drawback in the industrial application of biocatalysis.[232] However, it was reported by Takahashi *et al.* for horse-radish peroxidase that an enhanced enzyme activity in organic solvents and an increased hydrothermal stability requires similar diameters of the porous network and the guest molecules.[245, 246] These results were supported by several other studies of different research groups.[247-249] Besides the optimal choice of the support material, a sufficient immobilization technique must be employed. The most prominent techniques are (1) physical adsorption via van der Waals forces, hydrophobic interactions and hydrogen bonding, (2) covalent attachment of the biocatalyst, and (3) cross-linking of enzymes in the mesoporous framework of the support material.[228] It has to be noted that each immobilization route has certain advantages as well as disadvantages (e.g. leakage, conformational change of the enzyme).[228] However, in this work, we will mainly focus on the covalent attachment of enzymes within the mesopores of silica supports. Hartmann and co-workers and Lee *et al*. and have reviewed different methods of covalent enzyme immobilization onto mesoporous silica supports.[228, 250] The most prominent approach for covalent immobilization is the linkage via an amino-moiety on the silica surface, which facilitates the attachment of the enzyme via a glutaraldehyde linker (Figure 1.11A). This approach significantly improves the stability and reduces leakage, leading to increased reusability of the material. Several different enzymes have been immobilized with this approach, namely glucose oxidase[251], lipase[252] and invertase.[253] Additionally, glutaric anhydride (Figure 1.11B) and succinimido-3-maleimidopropionate are commonly used as linkers. Mou and co-workers covalently immobilized cytochrome C (CytC) with the above mentioned linkers onto the solid support and studied the catalytic activity of the obtained hybrid materials.[254] It was revealed that the orientation of the enzyme, and therefore the catalytic activity, is controlled by the specific binding of CytC. Another study investigating the influence of different attachment mechanisms was carried out by Jung and co-workers. Chloroperoxidase and glucose oxidase were immobilized on amine- and epoxy-modified SBA-15 supports, revealing that the epoxy-pathway diminishes the activity of chloroperoxidase, whereas glucooxidase was not affected; no change of activity could be observed for the amino-functionalized supports.[255] The immobilization of biocatalysts via a click chemistry approach has gained much interest in recent years as the reaction is highly efficient and shows extraordinary bioorthogonality (Figure 1.11D).[21, 256] This approach was successfully employed

by Bein and co-workers to immobilize trypsin into the pores of SBA-15[21] and by Fried *et al.* to covalently attach glycopyranose.[257]
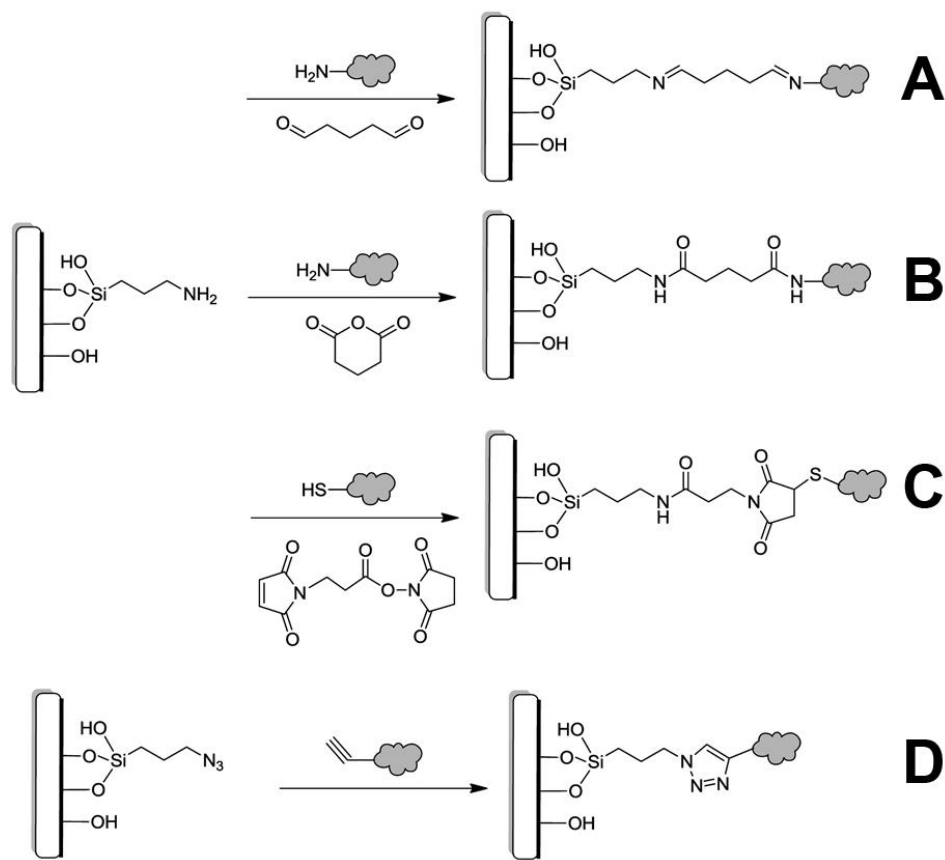


**Figure 1.11:** Different routes for the immobilization of enzymes on mesoporous silica by covalent attachment. **A)** Enzyme immobilization via a glutaraldehyde linker, **B)** enzyme immobilization using glutar anhydride, **C)** enzyme immobilization using succinimido-3-maleimidopropionate, and **D)** enzyme immobilization via an azide-alkyne cycloaddition.[228]

Biocatalysis is the most prominent field of applications for immobilized enzymes, yet it can be noted that several additional applications have been studied recently, e.g. drug delivery and immunosensing. Chen and co-workers showed the successful delivery of superoxide dismutase, an antioxidant enzyme that detoxifies intracellular reactive oxygen species, to HeLa cells, employing mesoporous silica nanoparticles as inorganic carrier vehicle.[258]

## 1.4 References

1. Zürner, A.; Kirstein, J.; Döblinger, M.; Bräuchle, C.; Bein, T. *Nature* **2007**, *450*, 705-708.

2. Ruehle, B.; Davies, M.; Lebold, T.; Bräuchle, C.; Bein, T. *ACS Nano* **2012**, *6*, 1948-1960.

3. Zhao, D.; Feng, J.; Huo, Q.; Melosh, N.; Fredrickson, G. H.; Chmelka, B. F.; Stucky, G. D. *Science* **1998**, *279*, 548-552.

4. Zhao, D.; Huo, Q.; Feng, J.; Chmelka, B. F.; Stucky, G. D. *J. Am. Chem. Soc.* **1998**, *120*, 6024-6036.

5. Che, S.; Liu, Z.; Ohsuna, T.; Sakamoto, K.; Terasaki, O.; Tatsumi, T. *Nature* **2004**, *429*, 281-284.

6. Shen, S.; Chow, P. S.; Kim, S.; Zhu, K.; Tan, R. B. *J. Colloid. Interface Sci.* **2008**, *321*, 365-372.

7. Lu, Y.; Fan, H.; Stump, A.; Ward, T. L.; Rieker, T.; Brinker, C. J. *Nature* **1999**, *398*, 223-226.

8. Lai, C.-Y.; Trewyn, B. G.; Jeftinija, D. M.; Jeftinija, K.; Xu, S.; Jeftinija, S.; Lin, V. S. Y. *J. Am. Chem. Soc.* **2003**, *125*, 4451-4459.

9. Möller, K.; Kobler, J.; Bein, T. *Adv. Funct. Mater.* **2007**, *17*, 605-612.

10. Beck, J. S.; Vartuli, J. C.; Roth, W. J.; Leonowicz, M. E.; Kresge, C. T.; Schmitt, K. D.; Chu, C. T. W.; Olson, D. H.; Sheppard, E. W. *J. Am. Chem. Soc.* **1992**, *114*, 10834-10843.

11. Kresge, C. T.; Leonowicz, M. E.; Roth, W. J.; Vartuli, J. C.; Beck, J. S. *Nature* **1992**, *359*, 710-712.

12. Inagaki, S.; Fukushima, Y.; Kuroda, K. *J. Chem. Soc., Chem. Commun.* **1993**, 680-682.

13. Tang, F.; Li, L.; Chen, D. *Adv. Mater.* **2012**, *24*, 1504-1534.

14. Raman, N. K.; Anderson, M. T.; Brinker, C. J. *Chem. Mater.* **1996**, *8*, 1682-1701.

15. Zhao, X. S.; Lu, G. Q.; Millar, G. J. *Ind. Eng. Chem. Res.* **1996**, *35*, 2075-2090.

16. Corma, A. *Chem. Rev.* **1997**, *97*, 2373-2420.

17. Kumar, D.; Schumacher, K.; du Fresne von Hohenesche, C.; Grün, M.; Unger, K. K. *Colloids Surf., A* **2001**, *187–188*, 109-116.

18. Das, P.; Silva, A.; Carvalho, A.; Pires, J.; Freire, C. *J. Mater. Sci.* **2009**, *44*, 2865-2875.

19. Balcar, H.; Shinde, T.; Žilková, N.; Bastl, Z. *Beilstein J. Org. Chem.* **2011**, *7*, 22-28.

20. Descalzo, A. B.; Rurack, K.; Weisshoff, H.; Martinez-Manez, R.; Marcos, M. D.; Amoros, P.; Hoffmann, K.; Soto, J. *J. Am. Chem. Soc.* **2005**, *127*, 184-200.

21. Schlossbauer, A.; Schaffert, D.; Kecht, J.; Wagner, E.; Bein, T. *J. Am. Chem. Soc.* **2008**, *130*, 12558-12559.

22. Hildebrandt, P.; Heimburg, T.; Marsh, D.; Powell, G. L. *Biochemistry* **1990**, *29*, 1661-1668.

23. Gustafsson, H.; Thorn, C.; Holmberg, K. *Colloids Surf., B.* **2011**, *87*, 464-471.

24. Kala Raj, N. K.; Deshpande, S. S.; Ingle, R.; Raja, T.; Manikandan, P. *Catal. Lett.* **2004**, *98*, 217-224.

25. Hess, C. *ChemPhysChem* **2009**, *10*, 319-326.

26. Demel, J.; Lamac, M.; Cejka, J.; Stepnicka, P. *ChemSusChem* **2009**, *2*, 442-451.

27. Liu, G.; Yao, M.; Zhang, F.; Gao, Y.; Li, H. *Chem. Commun.* **2008**, 347-349.

28. Lebold, T.; Schlossbauer, A.; Schneider, K.; Schermelleh, L.; Leonhardt, H.; Bein, T.; Bräuchle, C. *Adv. Funct. Mater.* **2012**, *22*, 106-112.

29. Feil, F.; Cauda, V.; Bein, T.; Bräuchle, C. *Nano Lett.* **2012**, *12*, 1354-1361.

30. Cao, L.; Man, T.; Kruk, M. *Chem. Mater.* **2009**, *21*, 1144-1153.

31. Cao, L.; Kruk, M. *Colloids Surf., A* **2010**, *357*, 91-96.

32. Chithrani, B. D.; Ghazani, A. A.; Chan, W. C. W. *Nano Lett.* **2006**, *6*, 662-668.

33. Lu, F.; Wu, S.-H.; Hung, Y.; Mou, C.-Y. *Small* **2009**, *5*, 1408-1413.

34. Vallet-Regi, M.; Rámila, A.; del Real, R. P.; Pérez-Pariente, J. *Chem. Mater.* **2000**, *13*, 308-311.

35. Grün, M.; Lauer, I.; Unger, K. K. *Adv. Mater.* **1997**, *9*, 254-257.

36. Cai, Q.; Luo, Z.-S.; Pang, W.-Q.; Fan, Y.-W.; Chen, X.-H.; Cui, F.-Z. *Chem. Mater.* **2001**, *13*, 258-263.

37. Fowler, C. E.; Khushalani, D.; Lebeau, B.; Mann, S. *Adv. Mater.* **2001**, *13*, 649-652.

38. Nooney, R. I.; Thirunavukkarasu, D.; Chen, Y.; Josephs, R.; Ostafin, A. E. *Chem. Mater.* **2002**, *14*, 4721-4728.

39. Stöber, W.; Fink, A.; Bohn, E. *J. Colloid. Interf. Sci.* **1968**, *26*, 62-69.

40. Cauda, V.; Schlossbauer, A.; Kecht, J.; Zürner, A.; Bein, T. *J. Am. Chem. Soc.* **2009**, *131*, 11361-11370.

41. Mackowiak, S. A.; Schmidt, A.; Weiss, V.; Argyo, C.; von Schirnding, C.; Bein, T.; Bräuchle, C. *Nano Lett.* **2013**, *13*, 2576-2583.

42.     Han, Y.; Ying, J. Y. *Angew. Chem. Int. Ed.* **2005**, *44*, 288-292.

43.     Na, H.-K.; Kim, M.-H.; Park, K.; Ryoo, S.-R.; Lee, K. E.; Jeon, H.; Ryoo, R.; Hyeon, C.; Min, D.-H. *Small* **2012**, *8*, 1752-1761.

44.     Suzuki, K.; Ikari, K.; Imai, H. *J. Am. Chem. Soc.* **2003**, *126*, 462-463.

45.     Ikari, K.; Suzuki, K.; Imai, H. *Langmuir* **2006**, *22*, 802-806.

46.     Huh, S.; Wiench, J. W.; Yoo, J.-C.; Pruski, M.; Lin, V. S. Y. *Chem. Mater.* **2003**, *15*, 4247-4256.

47.     Popat, A.; Liu, J.; Lu, G. Q.; Qiao, S. Z. *J. Mater. Chem.* **2012**, *22*, 11173-11178.

48.     Lin, Y. S.; Abadeer, N.; Hurley, K. R.; Haynes, C. L. *J. Am. Chem. Soc.* **2011**, *133*, 20444-20457.

49.     Ma, K.; Werner-Zwanziger, U.; Zwanziger, J.; Wiesner, U. *Chem. Mater.* **2013**, *25*, 677-691.

50.     Kecht, J.; Schlossbauer, A.; Bein, T. *Chem. Mater.* **2008**, *20*, 7207-7214.

51.     Schlossbauer, A.; Sauer, A. M.; Cauda, V.; Schmidt, A.; Engelke, H.; Rothbauer, U.; Zolghadr, K.; Leonhardt, H.; Bräuchle, C.; Bein, T. *Adv. Healthcare Mater.* **2012**, *1*, 316-320.

52.     Argyo, C.; Cauda, V.; Engelke, H.; Rädler, J.; Bein, G.; Bein, T. *Chem. Eur. J.* **2012**, *18*, 428-432.

53.     Gai, S.; Yang, P.; Ma, P. a.; Wang, L.; Li, C.; Zhang, M.; Jun, L. *Dalton Trans.* **2012**, *41*, 4511-4516.

54.     Gao, F.; Botella, P.; Corma, A.; Blesa, J.; Dong, L. *J. Phys. Chem. B.* **2009**, *113*, 1796-1804.

55.     Fan, J.; Yu, C.; Lei, J.; Zhang, Q.; Li, T.; Tu, B.; Zhou, W.; Zhao, D. *J. Am. Chem. Soc.* **2005**, *127*, 10794-10795.

56.     Meng, H.; Xue, M.; Xia, T.; Zhao, Y.-L.; Tamanoi, F.; Stoddart, J. F.; Zink, J. I.; Nel, A. E. *J. Am. Chem. Soc.* **2010**, *132*, 12690-12697.

57.     Thomas, C. R.; Ferris, D. P.; Lee, J. H.; Choi, E.; Cho, M. H.; Kim, E. S.; Stoddart, J. F.; Shin, J. S.; Cheon, J.; Zink, J. I. *J. Am. Chem. Soc.* **2010**, *132*, 10623-10625.

58.     Lu, J.; Liong, M.; Sherman, S.; Xia, T.; Kovochich, M.; Nel, A. E.; Zink, J. I.; Tamanoi, F. *Nanobiotechnology* **2007**, *3*, 89-95.

59.     Xia, T.; Kovochich, M.; Liong, M.; Meng, H.; Kabehie, S.; George, S.; Zink, J. I.; Nel, A. E. *ACS Nano* **2009**, *3*, 3273-3286.

60.     Shen, J.; Kim, H. C.; Su, H.; Wang, F.; Wolfram, J.; Kirui, D.; Mai, J.; Mu, C.; Ji, L. N.; Mao, Z. W.; Shen, H. *Theranostics* **2014**, *4*, 487-97.

61.    Wittig, R.; Rosenholm, J. M.; von Haartman, E.; Hemming, J.; Genze, F.; Bergman, L.; Simmet, T.; Linden, M.; Sahlgren, C. *Nanomedicine* **2014**, *7*, 971-987.

62.    Hoffmann, F.; Cornelius, M.; Morell, J.; Fröba, M. *Angew. Chem. Int. Ed.* **2006**, *45*, 3216-3251.

63.    Yamamoto, K.; Tatsumi, T. *Chem. Lett.* **2000**, *29*, 624-625.

64.    Lim, J. E.; Shim, C. B.; Kim, J. M.; Lee, B. Y.; Yie, J. E. *Angew. Chem. Int. Ed.* **2004**, *43*, 3839-3842.

65.    Angloher, S.; Bein, T. *J. Mater. Chem.* **2006**, *16*, 3629-3634.

66.    Angloher, S.; Kecht, J.; Bein, T. *Chem. Mater.* **2007**, *19*, 3568-3574.

67.    Angloher, S.; Kecht, J.; Bein, T. *Microporous Mesoporous Mater.* **2008**, *115*, 629-633.

68.    Lebold, T., *Doctoral Thesis, Mesoporous silica nanostructures: A versatile platform in Drug Delivery and Material Science*. Ludwig-Maximilians-University Munich: Munich,  Germany, 2010.

69.    Cauda, V.; Argyo, C.; Bein, T. *J. Mater. Chem.* **2010**, *20*, 8693-8699.

70.    Schlossbauer, A.; Kecht, J.; Bein, T. *Angew. Chem. Int. Ed.* **2009**, *48*, 3092-3095.

71.    Schlossbauer, A.; Warncke, S.; Gramlich, P. M.; Kecht, J.; Manetto, A.; Carell, T.; Bein, T. *Angew. Chem. Int. Ed.* **2010**, *49*, 4734-4737.

72.    Cauda, V.; Engelke, H.; Sauer, A.; Arcizet, D.; Bräuchle, C.; Rädler, J.; Bein, T. *Nano Lett.* **2010**, *10*, 2484-2492.

73.    Cauda, V.; Argyo, C.; Schlossbauer, A.; Bein, T. *J. Mater. Chem.* **2010**, *20*, 4305-4311.

74.    Dobay, M. P.; Schmidt, A.; Mendoza, E.; Bein, T.; Rädler, J. O. *Nano Lett.* **2013**, *13*, 1047-1052.

75.    Ashley, C. E.; Carnes, E. C.; Phillips, G. K.; Padilla, D.; Durfee, P. N.; Brown, P. A.; Hanna, T. N.; Liu, J.; Phillips, B.; Carter, M. B.; Carroll, N. J.; Jiang, X.; Dunphy, D. R.; Willman, C. L.; Petsev, D. N.; Evans, D. G.; Parikh, A. N.; Chackerian, B.; Wharton, W.; Peabody, D. S.; Brinker, C. J. *Nat. Mater.* **2011**, *10*, 389-97.

76.    Sauer, A. M.; Schlossbauer, A.; Ruthardt, N.; Cauda, V.; Bein, T.; Bräuchle, C. *Nano Lett.* **2010**, *10*, 3684-3691.

77.    Rosenholm, J. M.; Meinander, A.; Peuhu, E.; Niemi, R.; Eriksson, J. E.; Sahlgren, C.; Linden, M. *ACS Nano* **2009**, *3*, 197-206.

78.    Vivero-Escoto, J. L.; Slowing, I. I.; Trewyn, B. G.; Lin, V. S. Y. *Small* **2010**, *6*, 1952-1967.

79. Shim, M. S.; Kwon, Y. J. *Biomacromolecules* **2008**, *9*, 444-455.

80. Tietze, N.; Pelisek, J.; Philipp, A.; Roedl, W.; Merdan, T.; Tarcha, P.; Ogris, M.; Wagner, E. *Oligonucleotides* **2008**, *18*, 161-74.

81. Hom, C.; Lu, J.; Liong, M.; Luo, H.; Li, Z.; Zink, J. I.; Tamanoi, F. *Small* **2010**, *6*, 1185-1190.

82. Fan, J.; Yu, C.; Gao, F.; Lei, J.; Tian, B.; Wang, L.; Luo, Q.; Tu, B.; Zhou, W.; Zhao, D. *Angew. Chem. Int. Ed.* **2003**, *42*, 3146-3150.

83. Niu, D.; Ma, Z.; Li, Y.; Shi, J. *J. Am. Chem. Soc.* **2010**, *132*, 15144-15147.

84. Hartono, S. B.; Gu, W.; Kleitz, F.; Liu, J.; He, L.; Middelberg, A. P. J.; Yu, C.; Lu, G. Q.; Qiao, S. Z. *ACS Nano* **2012**, *6*, 2104-2117.

85. Lou, X. W.; Archer, L. A.; Yang, Z. *Adv. Mater.* **2008**, *20*, 3987-4019.

86. Liu, J.; Qiao, S. Z.; Chen, J. S.; Lou, X. W.; Xing, X.; Lu, G. Q. *Chem. Commun.* **2011**, *47*, 12578-12591.

87. Yeh, Y.-Q.; Chen, B.-C.; Lin, H.-P.; Tang, C.-Y. *Langmuir* **2005**, *22*, 6-9.

88. Liu, J.; Yang, H. Q.; Kleitz, F.; Chen, Z. G.; Yang, T.; Strounina, E.; Lu, G. Q.; Qiao, S. Z. *Adv. Funct. Mater.* **2012**, *22*, 591-599.

89. Lin, Y.-S.; Wu, S.-H.; Tseng, C.-T.; Hung, Y.; Chang, C.; Mou, C.-Y. *Chem. Commun.* **2009**, 3542-3544.

90. Liu, J.; Qiao, S. Z.; Budi Hartono, S.; Lu, G. Q. *Angew. Chem. Int. Ed.* **2010**, *49*, 4981-4985.

91. Loy, D. A.; Shea, K. J. *Chem. Rev.* **1995**, *95*, 1431-1442.

92. Yang, Y.; Liu, J.; Li, X.; Liu, X.; Yang, Q. *Chem. Mater.* **2011**, *23*, 3676-3684.

93. Roca, M.; Haes, A. J. *J. Am. Chem. Soc.* **2008**, *130*, 14273-14279.

94. Li, L.; Tang, F.; Liu, H.; Liu, T.; Hao, N.; Chen, D.; Teng, X.; He, J. *ACS nano* **2010**, *4*, 6874-6882.

95. Stewart, B. W.; Wild, C. P., *World Cancer Report* World Health Organization Press: Geneva, 2014.

96. Peer, D.; Karp, J. M.; Hong, S.; Farokhzad, O. C.; Margalit, R.; Langer, R. *Nat. Nanotechnol.* **2007**, *2*, 751-760.

97. Changenet-Barret, P.; Gustavsson, T.; Markovitsi, D.; Manet, I.; Monti, S. *Phys. Chem. Chem. Phys.* **2013**, *15*, 2937-2944.

98. Schaffert, D.; Wagner, E. *Gene Ther.* **2008**, *15*, 1131-1138.

99. Chang, H. I.; Yeh, M. K. *Int. J. Nanomedicine* **2012**, *7*, 49-60.

100. Venditto, V. J.; Szoka Jr, F. C. *Adv. Drug Deliv. Rev.* **2013**, *65*, 80-88.

101. Mai, W. X.; Meng, H. *Integr. Biol.* **2013**, *5*, 19-28.

102. Fan, Y.; Zhang, Q. *Asian Journal of Pharmaceutical Sciences* **2013**, *8*, 81-87.

103. Ang, C. Y.; Tan, S. Y.; Zhao, Y. *Org. Biomol. Chem.* **2014**, *12*, 4776-4806.

104. Davis, M. E.; Chen, Z. G.; Shin, D. M. *Nat. Rev. Drug Discov.* **2008**, *7*, 771-782.

105. Uziely, B.; Jeffers, S.; Isacson, R.; Kutsch, K.; Wei-Tsao, D.; Yehoshua, Z.; Libson, E.; Muggia, F. M.; Gabizon, A. *J. Clin. Oncol.* **1995**, *13*, 1777-1785.

106. Yu, H.; Wagner, E. *Curr. Opin. Mol. Ther.* **2009**, *11*, 165-178.

107. Edinger, D.; Wagner, E. *Wiley Interdiscip. Rev. Nanomed. Nanobiotechnol.* **2011**, *3*, 33-46.

108. Miyata, K.; Nishiyama, N.; Kataoka, K. *Chem. Soc. Rev.* **2012**, *41*, 2562-2574.

109. Krützfeldt, J.; Rajewsky, N.; Braich, R.; Rajeev, K. G.; Tuschl, T.; Manoharan, M.; Stoffel, M. *Nature* **2005**, *438*, 685-689.

110. Elbashir, S. M.; Harborth, J.; Lendeckel, W.; Yalcin, A.; Weber, K.; Tuschl, T. *Nature* **2001**, *411*, 494-498.

111. Fire, A.; Xu, S.; Montgomery, M. K.; Kostas, S. A.; Driver, S. E.; Mello, C. C. *Nature* **1998**, *391*, 806-181.

112. Kukowska-Latallo, J. F.; Bielinska, A. U.; Johnson, J.; Spindler, R.; Tomalia, D. A.; Baker, J. R., Jr. *Proc. Nat. Acad. Sci. U. S. A.* **1996**, *93*, 4897-4902.

113. Tang, M. X.; Szoka, F. C. *Gene Ther.* **1997**, *4*, 823-832.

114. Esbjoerner, E. K.; Oglecka, K.; Lincoln, P.; Graeslund, A.; Norden, B. *Biochemistry* **2007**, *46*, 13490-13504.

115. Zhou, J.; Wu, J.; Hafdi, N.; Behr, J. P.; Erbacher, P.; Peng, L. *Chem. Commun.* **2006**, 2362-2364.

116. Burke, R. S.; Pun, S. H. *Bioconjug. Chem.* **2008**, *19*, 693-704.

117. Buyens, K.; Lucas, B.; Raemdonck, K.; Braeckmans, K.; Vercammen, J.; Hendrix, J.; Engelborghs, Y.; De Smedt, S. C.; Sanders, N. N. *J. Control. Release* **2008**, *126*, 67-76.

118. Buyens, K.; Meyer, M.; Wagner, E.; Demeester, J.; De Smedt, S. C.; Sanders, N. N. *J. Control. Release* **2010**, *141*, 38-41.

119. Rozema, D. B.; Ekena, K.; Lewis, D. L.; Loomis, A. G.; Wolff, J. A. *Bioconjug. Chem.* **2003**, *14*, 51-57.

120. Rozema, D. B.; Lewis, D. L.; Wakefield, D. H.; Wong, S. C.; Klein, J. J.; Roesch, P. L.; Bertin, S. L.; Reppen, T. W.; Chu, Q.; Blokhin, A. V.; Hagstrom, J. E.; Wolff, J. A. *Proc. Nat. Acad. Sci. U. S. A.* **2007**, *104*, 12982-12987.

121. Meyer, M.; Dohmen, C.; Philipp, A.; Kiener, D.; Maiwald, G.; Scheu, C.; Ogris, M.; Wagner, E. *Mol. Pharm.* **2009**, *6*, 752-762.

122. Rader, D. J.; Kastelein, J. J. *Circulation* **2014**, *129*, 1022-1032.

123. Behlke, M. A. *Oligonucleotides* **2008**, *18*, 305-319.

124. Castanotto, D.; Rossi, J. J. *Nature* **2009**, *457*, 426-433.

125. Vallet-Regí, M.; Balas, F.; Arcos, D. *Angew. Chem. Int. Ed.* **2007**, *46*, 7548-7558.

126. Yang, P.; Gai, S.; Lin, J. *Chem. Soc. Rev.* **2012**, *41*, 3679-3698.

127. Mamaeva, V.; Sahlgren, C.; Linden, M. *Adv. Drug Deliv. Rev.* **2013**, *65*, 689-702.

128. Wu, S.-H.; Hung, Y.; Mou, C.-Y. *Chem. Commun.* **2011**, *47*, 9972-9985.

129. Lee, J. E.; Lee, N.; Kim, T.; Kim, J.; Hyeon, T. *Acc. Chem. Res.* **2011**, *44*, 893-902.

130. Ambrogio, M. W.; Thomas, C. R.; Zhao, Y.-L.; Zink, J. I.; Stoddart, J. F. *Acc. Chem. Res.* **2011**, *44*, 903-913.

131. Rosenholm, J. M.; Sahlgren, C.; Linden, M. *Nanoscale* **2010**, *2*, 1870-1883.

132. Slowing, I. I.; Vivero-Escoto, J. L.; Wu, C.-W.; Lin, V. S. Y. *Adv. Drug Deliv. Rev.* **2008**, *60*, 1278-1288.

133. Argyo, C.; Weiss, V.; Bräuchle, C.; Bein, T. *Chem. Mater.* **2013**, *26*, 435-451.

134. Tao, Z.; Toms, B. B.; Goodisman, J.; Asefa, T. *Chem. Res. Toxicol.* **2009**, *22*, 1869-1880.

135. Zhu, J.; Tang, J.; Zhao, L.; Zhou, X.; Wang, Y.; Yu, C. *Small* **2010**, *6*, 276-282.

136. Lin, Y. S.; Abadeer, N.; Haynes, C. L. *Chem. Commun.* **2011**, *47*, 532-534.

137. Giri, S.; Trewyn, B. G.; Stellmaker, M. P.; Lin, V. S. *Angew. Chem. Int. Ed.* **2005**, *44*, 5038-5044.

138. Chen, L.; Wen, Y.; Su, B.; Di, J.; Song, Y.; Jiang, L. *J. Mater. Chem.* **2011**, *21*, 13811-13816.

139. Gan, Q.; Lu, X.; Yuan, Y.; Qian, J.; Zhou, H.; Lu, X.; Shi, J.; Liu, C. *Biomaterials* **2011**, *32*, 1932-1942.

140. Ambrogio, M. W.; Pecorelli, T. A.; Patel, K.; Khashab, N. M.; Trabolsi, A.; Khatib, H. A.; Botros, Y. Y.; Zink, J. I.; Stoddart, J. F. *Org. Lett.* **2010**, *12*, 3304-3307.

141. Mendez, J.; Monteagudo, A.; Griebenow, K. *Bioconjug. Chem.* **2012**, *23*, 698-704.

142. Yang, X.; Liu, X.; Liu, Z.; Pu, F.; Ren, J.; Qu, X. *Adv. Mater.* **2012**, *24*, 2890-5.

143.  Muhammad, F.; Guo, M.; Qi, W.; Sun, F.; Wang, A.; Guo, Y.; Zhu, G. *J. Am. Chem. Soc.* **2011**, *133*, 8778-8781.

144.  Lin, C. H.; Cheng, S. H.; Liao, W. N.; Wei, P. R.; Sung, P. J.; Weng, C. F.; Lee, C. H. *Int. J. Pharm.* **2012**, *429*, 138-147.

145.  Gu, J.; Liu, J.; Li, Y.; Zhao, W.; Shi, J. *Langmuir* **2013**, *29*, 403-410.

146.  Gu, J.; Su, S.; Li, Y.; He, Q.; Zhong, J.; Shi, J. *J. Phys. Chem. Lett.* **2010**, *1*, 3446-3450.

147.  Zhu, M.; Wang, H.; Liu, J.; He, H.; Hua, X.; He, Q.; Zhang, L.; Ye, X.; Shi, J. *Biomaterials* **2011**, *32*, 1986-1995.

148.  Zhao, Y.; Trewyn, B. G.; Slowing, I. I.; Lin, V.-S. *J. Am. Chem. Soc.* **2009**, *131*, 8398-8400.

149.  Liu, J.; Stace-Naughton, A.; Brinker, C. J. *Chem. Commun.* **2009**, 5100-5102.

150.  Meng, H.; Yang, S.; Li, Z.; Xia, T.; Chen, J.; Ji, Z.; Zhang, H.; Wang, X.; Lin, S.; Huang, C.; Zhou, Z. H.; Zink, J. I.; Nel, A. E. *ACS Nano* **2011**, *5*, 4434-4447.

151.  He, Q.; Zhang, Z.; Gao, F.; Li, Y.; Shi, J. *Small* **2011**, *7*, 271-280.

152.  Akhtar, M. J.; Ahamed, M.; Alhadlaq, H. A.; Alrokayan, S. A.; Kumar, S. *Clin. Chim. Acta* **2014**, *436*, 78-92.

153.  Iyer, A. K.; Khaled, G.; Fang, J.; Maeda, H. *Drug Discov. Today* **2006**, *11*, 812-818.

154.  Sudimack, J.; Lee, R. J. *Adv. Drug Deliv. Rev.* **2000**, *41*, 147-162.

155.  Lu, Y.; Low, P. S. *Adv. Drug Deliv. Rev.* **2002**, *54*, 675-693.

156.  Low, P. S.; Kularatne, S. A. *Curr. Opin. Chem. Biol.* **2009**, *13*, 256-262.

157.  Zeng, Q.; Wen, H.; Wen, Q.; Chen, X.; Wang, Y.; Xuan, W.; Liang, J.; Wan, S. *Biomaterials* **2013**, *34*, 4632-4642.

158.  Lee, R. J.; Low, P. S. *BBA. Biomembranes* **1995**, *1233*, 134-144.

159.  Mamaeva, V.; Rosenholm, J. M.; Bate-Eya, L. T.; Bergman, L.; Peuhu, E.; Duchanoy, A.; Fortelius, L. E.; Landor, S.; Toivola, D. M.; Linden, M.; Sahlgren, C. *Mol. Ther.* **2011**, *19*, 1538-1546.

160.  Gao, Y.; Chen, L.; Gu, W.; Xi, Y.; Lin, L.; Li, Y. *Mol. Pharm.* **2008**, *5*, 1044-1054.

161.  Zeng, F.; Lee, H.; Allen, C. *Bioconjug. Chem.* **2006**, *17*, 399-409.

162.  Scaltriti, M.; Baselga, J. *Clin. Cancer Res.* **2006**, *12*, 5268-5272.

163.  Cai, W.; Niu, G.; Chen, X. *Curr. Pharm. Des.* **2008**, *14*, 2943-2973.

164.  Danhier, F.; Breton, A. L.; Préat, V. *Mol. Pharm.* **2012**, *9*, 2961-2973.

165.  Desgrosellier, J. S.; Cheresh, D. A. *Nat. Rev. Cancer* **2010**, *10*, 9-22.

166.	Xu, Q.; Liu, Y.; Su, S.; Li, W.; Chen, C.; Wu, Y. *Biomaterials* **2012**, *33*, 1627-1639.

167.	Li, Y.; He, H.; Jia, X.; Lu, W.-L.; Lou, J.; Wei, Y. *Biomaterials* **2012**, *33*, 3899-3908.

168.	Du, J.; Lu, W.-L.; Ying, X.; Liu, Y.; Du, P.; Tian, W.; Men, Y.; Guo, J.; Zhang, Y.; Li, R.-J.; Zhou, J.; Lou, J.-N.; Wang, J.-C.; Zhang, X.; Zhang, Q. *Mol. Pharm.* **2009**, *6*, 905-917.

169.	Zhou, J.; Rossi, J. J. *Mol. Ther. Nucleic Acids* **2014**, *3*, e169.

170.	Zhu, C.-L.; Song, X.-Y.; Zhou, W.-H.; Yang, H.-H.; Wen, Y.-H.; Wang, X.-R. *J. Mater. Chem.* **2009**, *19*, 7765-7770.

171.	Wilner, S. E.; Wengerter, B.; Maier, K.; de Lourdes Borba Magalhaes, M.; Del Amo, D. S.; Pai, S.; Opazo, F.; Rizzoli, S. O.; Yan, A.; Levy, M. *Mol. Ther. Nucleic Acids* **2012**, *1*, e21.

172.	Gruenberg, J.; Maxfield, F. R. *Curr. Opin. Cell Biol.* **1995**, *7*, 552-563.

173.	Mura, S.; Nicolas, J.; Couvreur, P. *Nat. Mater.* **2013**, *12*, 991-1003.

174.	Behr, J.-P. *CHIMIA International Journal for Chemistry* **1997**, *51*, 34-36.

175.	Akinc, A.; Thomas, M.; Klibanov, A. M.; Langer, R. *J. Gene Med.* **2005**, *7*, 657-663.

176.	Febvay, S. b.; Marini, D. M.; Belcher, A. M.; Clapham, D. E. *Nano letters* **2010**, *10*, 2211-2219.

177.	Lee, E. S.; Shin, H. J.; Na, K.; Bae, Y. H. *J. Control. Release* **2003**, *90*, 363-374.

178.	Yamada, Y.; Shinohara, Y.; Kakudo, T.; Chaki, S.; Futaki, S.; Kamiya, H.; Harashima, H. *Int. J. Pharm.* **2005**, *303*, 1-7.

179.	Kakudo, T.; Chaki, S.; Futaki, S.; Nakase, I.; Akaji, K.; Kawakami, T.; Maruyama, K.; Kamiya, H.; Harashima, H. *Biochemistry* **2004**, *43*, 5618-5628.

180.	Esfand, R.; Tomalia, D. A. *Drug Discov. Today.* **2001**, *6*, 427-436.

181.	Suh, J.; Paik, H. J.; Hwang, B. K. *Bioorg. Chem.* **1994**, *22*, 318-327.

182.	Tomalia, D. A.; Baker, H.; Dewald, J.; Hall, M.; Kallos, G.; Martin, S.; Roeck, J.; Ryder, J.; Smith, P. *Polym. J.* **1985**, *17*, 117-132.

183.	Menjoge, A. R.; Kannan, R. M.; Tomalia, D. A. *Drug Discov. Today* **2010**, *15*, 171-185.

184.	Radu, D. R.; Lai, C.-Y.; Jeftinija, K.; Rowe, E. W.; Jeftinija, S.; Lin, V. S. Y. *J. Am. Chem. Soc.* **2004**, *126*, 13216-13217.

185.	Anderson, R. R.; Parrish, J. A. *J Investig Dermatol* **1981**, *77*, 13-19.

186.	Nishiyama, N.; Iriyama, A.; Jang, W.-D.; Miyata, K.; Itaka, K.; Inoue, Y.; Takahashi, H.; Yanagi, Y.; Tamaki, Y.; Koyama, H.; Kataoka, K. *Nat. Mater.* **2005**, *4*, 934-941.

187. Croissant, J.; Maynadier, M.; Gallud, A.; Peindy N'dongo, H.; Nyalosaso, J. L.; Derrien, G.; Charnay, C.; Durand, J. O.; Raehm, L.; Serein-Spirau, F.; Cheminet, N.; Jarrosson, T.; Mongin, O.; Blanchard-Desce, M.; Gary-Bobo, M.; Garcia, M.; Lu, J.; Tamanoi, F.; Tarn, D.; Guardado-Alvarez, T. M.; Zink, J. I. *Angew. Chem. Int. Ed.* **2013**, *52*, 13813-13817.

188. Fowley, C.; Nomikou, N.; McHale, A. P.; McCaughan, B.; Callan, J. F. *Chem. Commun.* **2013**, *49*, 8934-8936.

189. Luo, T.; Wilson, B. C.; Lu, Q. B. *J. Photochem. Photobiol. B* **2014**, *132*, 102-110.

190. Wang, X.; Liu, K.; Yang, G.; Cheng, L.; He, L.; Liu, Y.; Li, Y.; Guo, L.; Liu, Z. *Nanoscale* **2014**.

191. Mal, N. K.; Fujiwara, M.; Tanaka, Y.; Taguchi, T.; Matsukata, M. *Chem. Mater.* **2003**, *15*, 3385-3394.

192. Liu, N.; Chen, Z.; Dunphy, D. R.; Jiang, Y.-B.; Assink, R. A.; Brinker, C. J. *Angw. Chem. Int. Ed.* **2003**, *42*, 1731-1734.

193. Barhoumi, A.; Wang, W.; Zurakowski, D.; Langer, R. S.; Kohane, D. S. *Nano Lett.* **2014**.

194. Lopez-Noriega, A.; Ruiz-Hernandez, E.; Quinlan, E.; Storm, G.; Hennink, W. E.; O'Brien, F. J. *J. Control. Release* **2014**, *187*, 158-166.

195. Chen, K. J.; Chaung, E. Y.; Wey, S. P.; Lin, K. J.; Cheng, F.; Lin, C. C.; Liu, H. L.; Tseng, H. W.; Liu, C. P.; Wei, M. C.; Liu, C. M.; Sung, H. W. *ACS Nano* **2014**, *8*, 5105-5115.

196. Lee, C. H.; Cheng, S. H.; Huang, I. P.; Souris, J. S.; Yang, C. S.; Mou, C. Y.; Lo, L. W. *Angew. Chem. Int. Ed.* **2010**, *49*, 8214-8219.

197. Ma, Y.; Zhou, L.; Zheng, H.; Xing, L.; Li, C.; Cui, J.; Che, S. *J. Mater. Chem.* **2011**, *21*, 483-9486.

198. Schlossbauer, A.; Dohmen, C.; Schaffert, D.; Wagner, E.; Bein, T. *Angew. Chem. Int. Ed.* **2011**, *50*, 6828-6830.

199. Wang, C.; Li, Z.; Cao, D.; Zhao, Y. L.; Gaines, J. W.; Bozdemir, O. A.; Ambrogio, M. W.; Frasconi, M.; Botros, Y. Y.; Zink, J. I.; Stoddart, J. F. *Angew. Chem. Int. Ed.* **2012**, *51*, 5460-5465.

200. Coll, C.; Mondragon, L.; Martinez-Manez, R.; Sancenon, F.; Marcos, M. D.; Soto, J.; Amoros, P.; Perez-Paya, E. *Angew. Chem. Int. Ed.* **2011**, *50*, 2138-2140.

201. He, D.; He, X.; Wang, K.; Cao, J.; Zhao, Y. *Langmuir* **2012**, *28*, 4003-4008.

202. Yan, H.; Teh, C.; Sreejith, S.; Zhu, L.; Kwok, A.; Fang, W.; Ma, X.; Nguyen, K. T.; Korzh, V.; Zhao, Y. *Angew. Chem. Int. Ed.* **2012**, *6*, 8373-8377.

203. Zhao, Z. X.; Huang, Y. Z.; Shi, S. G.; Tang, S. H.; Li, D. H.; Chen, X. L. *Nanotechnology* **2014**, *25*.

204. Guardado-Alvarez, T. M.; Sudha Devi, L.; Russell, M. M.; Schwartz, B. J.; Zink, J. I. *J. Am. Chem. Soc.* **2013**, *135*, 14000-14003.

205. Yang, J.; Lee, J.; Kang, J.; Oh, S. J.; Ko, H.-J.; Son, J.-H.; Lee, K.; Suh, J.-S.; Huh, Y.-M.; Haam, S. *Adv. Mater.* **2009**, *21*, 4339-4342.

206. Zhang, L.; Wang, T.; Yang, L.; Liu, C.; Wang, C.; Liu, H.; Wang, Y. A.; Su, Z. *Chem. Eur. J.* **2012**, *18*, 12512-12521.

207. Hua, M. Y.; Liu, H. L.; Yang, H. W.; Chen, P. Y.; Tsai, R. Y.; Huang, C. Y.; Tseng, I. C.; Lyu, L. A.; Ma, C. C.; Tang, H. J.; Yen, T. C.; Wei, K. C. *Biomaterials* **2011**, *32*, 516-527.

208. Liong, M.; Lu, J.; Kovochich, M.; Xia, T.; Ruehm, S. G.; Nel, A. E.; Tamanoi, F.; Zink, J. I. *ACS Nano* **2008**, *2*, 889-896.

209. Kim, J.; Kim, H. S.; Lee, N.; Kim, T.; Kim, H.; Yu, T.; Song, I. C.; Moon, W. K.; Hyeon, T. *Angew. Chem. Int. Ed.* **2008**, *47*, 8438-8441.

210. Lee, J. H.; Chen, K. J.; Noh, S. H.; Garcia, M. A.; Wang, H.; Lin, W. Y.; Jeong, H.; Kong, B. J.; Stout, D. B.; Cheon, J.; Tseng, H. R. *Angew. Chem. Int. Ed.* **2013**, *52*, 4384-4388.

211. Prijic, S.; Prosen, L.; Cemazar, M.; Scancar, J.; Romih, R.; Lavrencak, J.; Bregar, V. B.; Coer, A.; Krzan, M.; Znidarsic, A.; Sersa, G. *Biomaterials* **2012**, *33*, 4379-4391.

212. Park, J. W.; Bae, K. H.; Kim, C.; Park, T. G. *Biomacromolecules* **2011**, *12*, 457-465.

213. Yu, M. K.; Jeong, Y. Y.; Park, J.; Park, S.; Kim, J. W.; Min, J. J.; Kim, K.; Jon, S. *Angew. Chem. Int. Ed.* **2008**, *47*, 5362-5365.

214. Jang, J. T.; Nah, H.; Lee, J. H.; Moon, S. H.; Kim, M. G.; Cheon, J. *Angew. Chem. Int. Ed.* **2009**, *48*, 1234-1248.

215. Lee, J. H.; Huh, Y. M.; Jun, Y. W.; Seo, J. W.; Jang, J. T.; Song, H. T.; Kim, S.; Cho, E. J.; Yoon, H. G.; Suh, J. S.; Cheon, J. *Nat. Med.* **2007**, *13*, 95-99.

216. Al-Ahmady, Z. S.; Al-Jamal, W. T.; Bossche, J. V.; Bui, T. T.; Drake, A. F.; Mason, A. J.; Kostarelos, K. *ACS Nano* **2012**, *6*, 9335-9346.

217. You, Y.-Z.; Kalebaila, K. K.; Brock, S. L.; Oupický, D. *Chem. Mater.* **2008**, *20*, 3354-3359.

218. Schveigert, D.; Cicenas, S.; Bruzas, S.; Samalavicius, N. E.; Gudleviciene, Z.; Didziapetriene, J. *Adv. Med. Sci.* **2013**, *58*, 73-82.

219. Zhu, L.; Kate, P.; Torchilin, V. P. *ACS Nano* **2012**, *6*, 3491-3498.

220. Singh, N.; Karambelkar, A.; Gu, L.; Lin, K.; Miller, J. S.; Chen, C. S.; Sailor, M. J.; Bhatia, S. N. *J. Am. Chem. Soc.* **2011**, *133*, 19582-19585.

221. Bernardos, A.; Mondragon, L.; Aznar, E.; Marcos, M. D.; Martinez-Manez, R.; Sancenon, F.; Soto, J.; Barat, J. M.; Perez-Paya, E.; Guillem, C.; Amoros, P. *ACS Nano* **2010**, *4*, 6353-6368.

222. Lee, J. S.; Groothuis, T.; Cusan, C.; Mink, D.; Feijen, J. *Biomaterials* **2011**, *32*, 9144-9153.

223. Kurtoglu, Y. E.; Navath, R. S.; Wang, B.; Kannan, S.; Romero, R.; Kannan, R. M. *Biomaterials* **2009**, *30*, 2112-2121.

224. Ong, W.; Yang, Y.; Cruciano, A. C.; McCarley, R. L. *J. Am. Chem. Soc.* **2008**, *130*, 14739-14744.

225. Kim, S. H.; Jeong, J. H.; Kim, T. I.; Kim, S. W.; Bull, D. A. *Mol. Pharm.* **2009**, *6*, 718-726.

226. Stevenson, M.; Ramos-Perez, V.; Singh, S.; Soliman, M.; Preece, J. A.; Briggs, S. S.; Read, M. L.; Seymour, L. W. *J. Control. Release* **2008**, *130*, 46-56.

227. Zhao, Y. L.; Li, Z.; Kabehie, S.; Botros, Y. Y.; Stoddart, J. F.; Zink, J. I. *J. Am. Chem. Soc.* **2010**, *132*, 13016-13025.

228. Zhou, Z.; Hartmann, M. *Chem. Soc. Rev.* **2013**, *42*, 3894-3912.

229. Hartmann, M.; Jung, D. *J. Mater. Chem.* **2010**, *20*, 844-857.

230. Schmid, A.; Dordick, J. S.; Hauer, B.; Kiener, A.; Wubbolts, M.; Witholt, B. *Nature* **2001**, *409*, 258-268.

231. Hartmann, M. *Chem. Mater.* **2005**, *17*, 4577-4593.

232. Yiu, H. H. P.; Wright, P. A. *J. Mater. Chem.* **2005**, *15*, 3690-3700.

233. Zhao, X. S.; Bao, X. Y.; Guo, W.; Lee, F. Y. *Mater. Today* **2006**, *9*, 32-39.

234. Gill, I.; Ballesteros, A. *J. Am. Chem. Soc.* **1998**, *120*, 8587-8598.

235. Lee, E. S.; Kwon, M. J.; Lee, H.; Kim, J. J. *Int. J. Pharm.* **2007**, *331*, 27-37.

236. Huo, Q.; Margolese, D. I.; Ciesla, U.; Feng, P.; Gier, T. E.; Sieger, P.; Leon, R.; Petroff, P. M.; Schüth, F.; Stucky, G. D. *Nature* **1994**, *368*, 317-321.

237. Attard, G. S.; Bartlett, P. N.; Coleman, N. R. B.; Elliott, J. M.; Owen, J. R.; Wang, J. H. *Science* **1997**, *278*, 838-840.

238. Ryoo, R.; Joo, S. H.; Jun, S. *J. Phys. Chem. B.* **1999**, *103*, 7743-7746.

239. Meng, Y.; Gu, D.; Zhang, F.; Shi, Y.; Yang, H.; Li, Z.; Yu, C.; Tu, B.; Zhao, D. *Angew. Chem. Int. Ed.* **2005**, *44*, 7053-7059.

240. Ispas, C.; Sokolov, I.; Andreescu, S. *Anal. Bioanal. Chem.* **2009**, *393*, 543-554.

241. Zhao, W.; Zhang, H.; He, Q.; Li, Y.; Gu, J.; Li, L.; Li, H.; Shi, J. *Chem. Commun.* **2011**, *47*, 9459-61.

242. Zhou, Z.; Taylor, R. N. K.; Kullmann, S.; Bao, H.; Hartmann, M. *Adv. Mater.* **2011**, *23*, 2627-2632.

243. Díaz, J. F.; Balkus Jr, K. J. *J. Mol. Catal. B: Enzym.* **1996**, *2*, 115-126.

244. Yiu, H. H. P.; Wright, P. A.; Botting, N. P. *Microporous Mesoporous Mater.* **2001**, *44–45*, 763-768.

245. Takahashi, H.; Li, B.; Sasaki, T.; Miyazaki, C.; Kajino, T.; Inagaki, S. *Chem. Mater.* **2000**, *12*, 3301-3305.

246. Takahashi, H.; Li, B.; Sasaki, T.; Miyazaki, C.; Kajino, T.; Inagaki, S. *Microporous Mesoporous Mater.* **2001**, *44–45*, 755-762.

247. Fadnavis, N. W.; Bhaskar, V.; Kantam, M. L.; Choudary, B. M. *Biotechnol. Prog.* **2003**, *19*, 346-351.

248. Lee, C. H.; Lang, J.; Yen, C. W.; Shih, P. C.; Lin, T. S.; Mou, C. Y. *J. Phys. Chem. B.* **2005**, *109*, 12277-12786.

249. Aburto, J.; Ayala, M.; Bustos-Jaimes, I.; Montiel, C.; Terrés, E.; Domínguez, J. M.; Torres, E. *Microporous Mesoporous Mater.* **2005**, *83*, 193-200.

250. Lee, C.-H.; Lin, T.-S.; Mou, C.-Y. *Nano Today* **2009**, *4*, 165-179.

251. Zhang, X.; Guan, R.-F.; Wu, D.-Q.; Chan, K.-Y. *J. Mol. Catal. B: Enzym.* **2005**, *33*, 43-50.

252. Salis, A.; Meloni, D.; Ligas, S.; Casula, M. F.; Monduzzi, M.; Solinas, V.; Dumitriu, E. *Langmuir* **2005**, *21*, 5511-5516.

253. Szymańska, K.; Bryjak, J.; Mrowiec-Białoń, J.; Jarzębski, A. B. *Microporous Mesoporous Mater.* **2007**, *99*, 167-175.

254. Kao, K.-C.; Lee, C.-H.; Lin, T.-S.; Mou, C.-Y. *J. Mater. Chem.* **2010**, *20*, 4653-4662.

255. Jung, D.; Streb, C.; Hartmann, M. *Int. J. Mol. Sci.* **2010**, *11*, 762-778.

256. Maier, K.; Wagner, E. *J. Am. Chem. Soc.* **2012**, *134*, 10169-10173.

257. Fried, D. I.; Schlossbauer, A.; Bein, T. *Microporous Mesoporous Mater.* **2011**, *147*, 5-9.

258.    Chen, Y.-P.; Chen, C.-T.; Hung, Y.; Chou, C.-M.; Liu, T.-P.; Liang, M.-R.; Chen, C.-T.; Mou, C.-Y. *J. Am. Chem. Soc.* **2013**, *135*, 1516-1523.

# 2    Characterization

Mesoporous silica materials can be characterized by various different techniques with regard to their structural and morphological parameters. X-ray diffraction, nitrogen physisorption, scanning electron microscopy (SEM) and transmission electron microscopy (TEM) were used to investigate the porous structure and the morphology of the nano-materials. Additionally, dynamic light scattering was employed to investigate mesoporous silica nanoparticles (MSNs) regarding their size and agglomeration behavior. Furthermore, zeta potential measurements were used to investigate the surface properties of the MSNs. Vibrational spectroscopy (IR- and Raman spectroscopy) in combination with magic angle solid state nuclear magnetic resonance spectroscopy (MAS ssNMR) gives detailed information about the chemical bonding of the nano-structured materials and was frequently used in this work. Additionally, thermogravimetric analysis (TGA) was used to evaluate the amount of organo-functionalities introduced to the mesoporous materials. Time-based fluorescence spectroscopy with fluorescent model drugs (calcein, propidium iodide, and fluorescein) was performed in order to obtain information about the capping behavior of different gatekeepers attached to the silica surface. Additionally, quenching experiments were carried out with fluorescence spectroscopy. UV-VIS spectroscopy was used for enzyme-catalyzed colorimetric reactions.

## 2.1    Dynamic Light Scattering

Dynamic light scattering (DLS) measurements are a valuable tool to determine the size of particles and molecules in solution as well as to investigate solution dynamics.[1,2] DLS is also referred to as photon correlation spectroscopy (PCS) or quasi-elastic light scattering (QELS).[3] Typically, a DLS instrument is composed of a laser source, a sample cell, a photodetector and a computer containing an autocorrelator (Figure 2.1).[4]
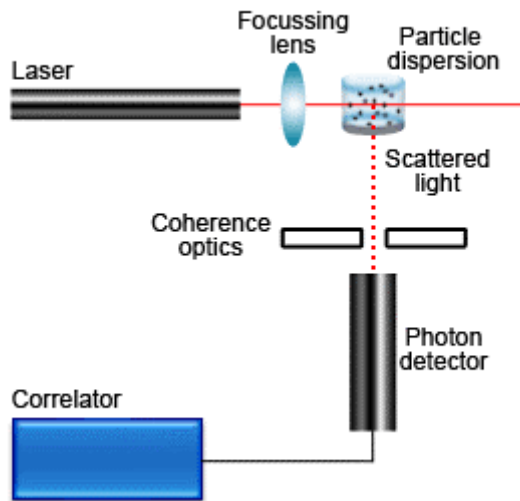
**Figure 2.1:** Schematic arrangement of a conventional DLS instrument.[4]

This technique is highly valuable for the analysis of nanometer-sized particles, typically with diameters between 1 – 1000 nm. The Brownian motion, which is a random movement of the particles in a liquid caused by constant collisions, is highly correlated to the particle size. Therefore, the particles in solution are in constant, random movement and the interparticle distance changes constantly, and so do the conditions for constructive and destructive interference of scattered light. This results in a time-dependent intensity fluctuation of the scattered light. Since the diffusion of large particles is slower than that of smaller particles, the intensity of the scattered light will change more slowly for larger particles and aggregates. During DLS measurements, these changes in intensity are recorded over a distinct time and can be evaluated afterwards. DLS measures the hydrodynamic diameter *d(H)* which is a value that is related to the diffusion properties of a particle in a liquid. The translational diffusion coefficient *D* depends on diverse parameters, including the ionic strength of the suspension, the texture of the particle surface, and the shape of the particles. Correlation analysis is used to calculate the diffusion coefficient, which is associated with the hydrodynamic diameter of colloidal spherical particles via the Stokes-Einstein equation:

$$d(H) = \frac{kT}{3\pi\eta D}$$

(2.1)

**Stokes-Einstein equation:** *d(H)* is the hydrodynamic diameter, *D* is the translational diffusion coefficient, *k* is the Boltzmann's constant, *T* is the temperature, $\eta$ is the viscosity.

## 2.2 Zeta Potential Measurements

Particles in suspension feature a zeta potential, which is the electrokinetic potential difference between a so-called stationary layer of ions in a solvent attached to the dispersed particle and the liquid medium in the surroundings. The zeta potential is also a force that mediates particle interactions.[5] Generally, particles dispersed in an aqueous solution possess a surface charge which results either from adsorption of charged species or from ionization of their surface groups. Both surface modifications lead to a surface charge that changes the distribution of the surrounding ions. As a consequence a layer different to the bulk solution with tightly bound ions (Stern layer) and loosely bound ions (slipping plane) is generated around the particle. Being a part of the particle, the interfacial double layer moves if the particle drifts due to Brownian motion within the solution. The potential at the point in this layer where it moves past the bulk solution is referred to as zeta potential (Figure 2.2). At this plane the charge is highly sensitive to the type of ions in solution as well as to their concentration.[6]
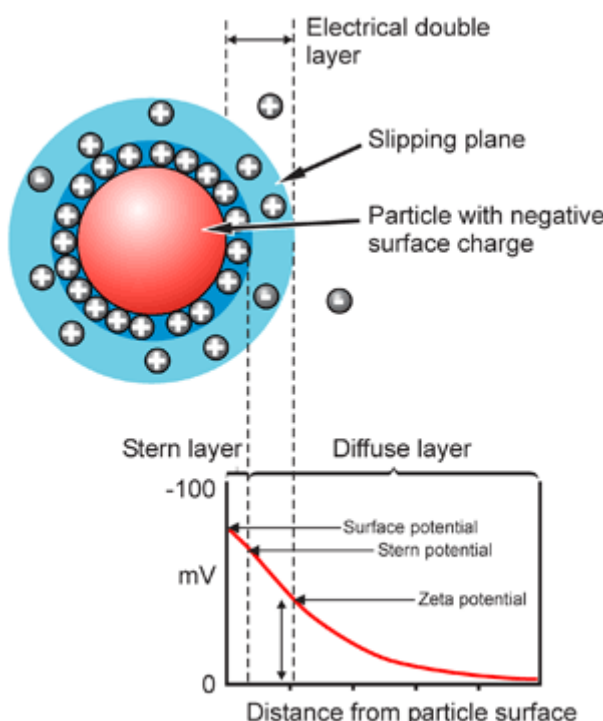


**Figure 2.2:** Schematic representation of the electric double layer around a negatively charged particle and location of the zeta potential.[7]

In order to measure the zeta potential of a sample, an electric field is applied across the dispersion and the electrophoretic mobility is observed. Particles inside the dispersion that possess a zeta potential will migrate towards the electrode of opposite charge whereby the

migration velocity is proportional to the magnitude of the zeta potential. Using the technique of laser Doppler anemometry, this velocity within the dispersion is measured. An incident laser beam striking one of the moving particles causes a frequency or phase shift that is recorded as the particle mobility. This mobility is transformed into zeta potential with the application of an appropriate theory together with the input of the dispersant's viscosity. The Henry equation (2.2) describes the relation between the electrophoretic mobility and the zeta potential.

$$U_E = \frac{2\varepsilon\zeta f(\kappa a)}{3\eta}$$

(2.2)

**Henry equation:** $U_E$ is the electrophoretic mobility, $\varepsilon$ is the dielectric constant of the sample, $\zeta$ is the zeta potential, *f(ka)* is the Henry function, and $\eta$ is the viscosity.

Specifically, to obtain the electrophoretic mobility, the velocity of the particles is determined by Laser Doppler Velocimetry (LDV).[8] The LDV applies an electrical field of known strength across the capillary cell which contains the colloidal particle solution. A shift in frequency is observed when the laser light (633 nm) passes the sample, determined by the velocity of the particles. Henry´s function is commonly set to f(Ka)=1.5, according to Smoluchowski´s approximation which is frequently used for particles larger than 200 nm and when the electric double layer is very thin compared to the particle diameter. Hückel's approximation uses f(Ka) = 1.0, this is frequently used for small particles in organic solvents.

## 2.3 Nitrogen Physisorption

Sorption measurements are an appropriate and commonly used technique to determine pore characteristics like pore size distribution, pore volume and pore width, as well as the surface area of various porous materials.[9] The nitrogen sorption process can be classified as physisorption, since only weak interactions including van-der-Waals forces occur during the sorption process. For nitrogen physisorption measurements, the obtained amount of the adsorbed nitrogen gas at different pressures and constant temperature (77 K) can be used to generate sorption isotherms (Figure 2.3).
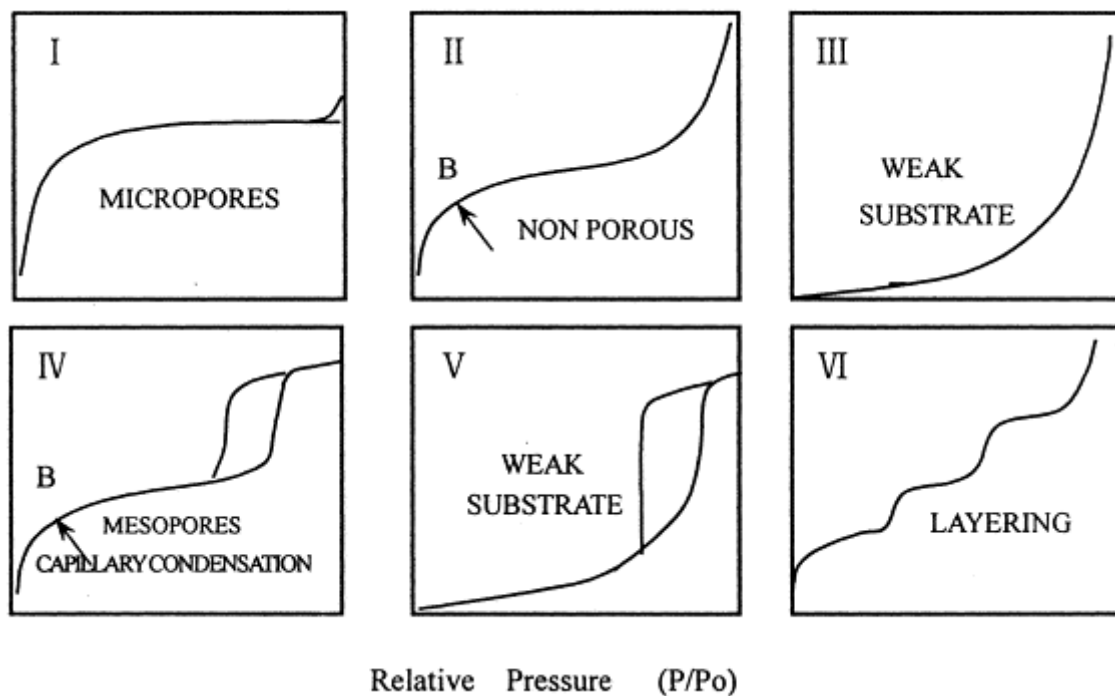
**Figure 2.3:** IUPAC classification of six different sorption isotherms.[10]

Six different types of sorption isotherms were classified by IUPAC.[11] The different types (I-VI) distinguish porous materials with respect to pore structure and size, and the interactions of the adsorbed gas molecules with the adsorbent.

**Table 2.1:** Types of sorption isotherms classified by IUPAC and the corresponding materials.[11]

| Isotherm Type | Corresponding Material |
| :---: | :--- |
| I | Microporous material with restricted micropore volume; Adsorbed amount of nitrogen reaches a constant value after pore filling |
| II | Macroporous or non-porous material; monolayer adsorption followed by unrestricted multilayer condensation |
| III | Fairly weak interactions between adsorbent and adsorbate |
| IV | Mesoporous material; hysteresis loop appearing due to capillary condensation inside the mesopores |
| V | Fairly weak interactions between adsorbent and adsorbate, but in contrast to Type III occurrence of a hysteresis loop |
| VI | Non-porous material; stepwise multilayer adsorption |

Mesoporous silica nanoparticles typically show type IV shaped isotherms. The arising hysteresis loop is assigned to high pressure hysteresis in the range of multilayer adsorption.[12]

Due to resulting van der Waals forces more energy has to be applied to remove the adsorbed gas molecules from the solid when the external pressure p is reduced during the desorption process. Hence, adsorption and desorption curves do not coincide.[13] Generally, a wide variety of shapes for hysteresis loops is known. The most common ones are presented in Figure 2.4.
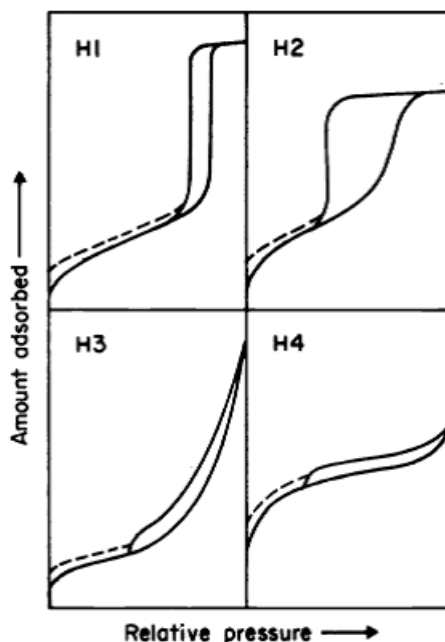


**Figure 2.4:** Different types of hysteresis loops.[11]

Several different methods exist to describe an isotherm. The simplest one was set up by Langmuir, but based on several approximations this approach oversimplifies the processes taking place in the experiment.[13] An enhancement of the Langmuir theory is represented by the Brunauer-Emmett-Teller (BET) approach, which is much more suitable to characterize an isotherm, as it takes processes such as multilayer condensation into account.[14]

### 2.3.1 Specific surface area

In mesopores, which have a pore size range of $2 - 50$ nm, van-der-Waals forces between adsorbate molecules as well as attractions between adsorbate and bulk surface cause capillary pore condensation. Gas forms a condensed phase at a pressure lower than the saturation

pressure $p_{sat}$. Depending on the shape of the pore and the surface tension, a meniscus is formed at the liquid-vapor interface in the pore. If the pore is not of ideal cylindrical shape, the pore opening can exhibit a smaller radius than the bottom of the pore. Considering the Kelvin equation (2.3) a lower partial pressure is required during the desorption process, leading to diverse isotherms.[5]

$$RT \cdot ln\frac{P_0^K}{P_0} = -\frac{2\gamma V_m}{r_c}$$
(2.3)

**Kelvin equation.** $R$: gas constant, $T$: temperature, $P_0^K$: equilibrium pressure, $P_0$: saturation vapor pressure, $\gamma$: surface tension, $V_m$: molar volume, $r_c$: reduced radius

Isotherm IV shows the resulting hysteresis, which reflects the different adsorption and desorption pathways (Figure 2.3). The obtained curves can be interpreted to obtain information on the porous features of the investigated sample.

There are different models to describe isotherms. The most common models are named after their developers, Langmuir (Langmuir isotherms) and Brunauer, Emmett and Teller (BET isotherms).[13,14] The Langmuir interpretation is the simplest characterization method and is based on the approximations that (i) the adsorption is leading at most to monolayer formation, (ii) the surface is uniform and (iii) all binding sites are equal. Furthermore, the ability of a molecule to bind at a specific surface site is independent of the occupancy of neighboring binding sites (no interactions between adsorbed molecules). The Langmuir equation is shown below (2.4).

$$\frac{n}{n_m} = \frac{K \cdot p}{1 + K \cdot p}$$
(2.4)

**Langmuir equation.** $n$: amount of adsorbate, $n_m$: capacity of one monolayer, $p$: pressure,
$K = k_{ad}/k_{des}$

If the initial adsorbate-layer acts as substrate for additional adsorption processes (physisorption), then the isotherms should not show a saturation value but continue to increase. This multilayer adsorption is described by Brunauer, Emmett and Teller (BET).[14,15]

The BET equation can be expressed as follows (2.5).

$$\frac{n}{n_m} = \frac{C \cdot \frac{p}{p_0}}{(1 - \frac{p}{p_0})(1 + C - \frac{p}{p_0})} \tag{2.5}$$

**BET equation.** *n*: amount of adsorbate, $n_m$: capacity of one monolayer, *C:* BET constant, *p*: equilibrium pressure, $p_0$: saturation vapor pressure of adsorbate

To calculate the specific surface area of a material, the linear part of the BET isotherm (at small p/p$_0$-values) can be used, as this part corresponds to monolayer formation.

### 2.3.2   Pore size calculation

Sorption data are further applicable to determine the pore volume and the pore size distribution of an analyzed sample. This method is based on the change of physical properties of gas molecules when being adsorbed in a porous material. The pore size distribution function is a very important characteristic of porous materials. The thermodynamic relation between the reduced pore radius $r_k$ and the relative vapor pressure *p/p$_0$* is described by Kelvin's equation (2.3)

Kelvin's equation frequently leads to inexact results as it tends to underestimate the pore size. An enhancement by Barrett-Joyner-Halenda (BJH) corrects the Kelvin radius $r_k$ by including the thickness *t* of the monolayer which is already adsorbed to the sample surface.[16] This method however is limited, as it disregards the impact of surface curvature on the formation of the film, it is only derived for cylindrical pores, it assumes formation of homogenous films and it does not explicitly account for surface forces between the film and the surface. Due to these limitations the BJH method is known to underestimate the pore size, especially for small pores. An approach that combines density functional theory (DFT) with the grand canonical Monte Carlo (GCMC) simulation method is frequently applied and usually gives the most exact results. In order to obtain the equilibrium density profile via DFT, the corresponding grand potential is minimized for a pore system in equilibrium with a bulk phase. The function contains terms describing attractive as well as repulsive solid-fluid and fluid-fluid interactions. Hypothetically, two different DFT methods exist, but in contrast to the applied non-local density functional theory (NLDFT) the local density functional theory (LDFT) is not applicable for narrow pores. The reason is that it cannot characterize short-range correlations inside the pores.[9] NLDFT in

combination with Monte Carlo simulations quite reliably describes the local fluid structure near curved solid walls. As the solid walls of mesoporous silica have an influence on the number density, NLDFT is used for calculating the pore size distribution in this work.

## 2.4   Infrared and Raman Spectroscopy

Infrared (IR) and Raman spectroscopy can be used to obtain information about functional groups present within the sample and offers the potential to study the properties of the chemical bonds in a molecule by exciting vibrational transitions.[17-19] Radiation in the mid-infrared (200 – 4000 cm$^{-1}$) region is predominantly used for IR spectroscopy. Today, usually Fourier transform (FT) IR spectroscopy is used for the analysis in which polychromatic IR light passes through a Michelson interferometer and subsequently through the sample. The spectra are background-corrected and the spectrum is calculated by FT from the interferogram.

The IR light interacts with the sample and the intensity of the scattered or transmitted light is measured; the energy of the IR absorption bands is often characteristic for a certain chemical bond and offers therefore the possibility of detailed analysis. It is important that the vibration itself is IR-active (the vibrational transition is allowed); a dipole moment that changes during the measurement is a prerequisite.

Compared to infrared spectroscopy, different selection rules apply for Raman spectroscopy, so that data from Raman spectra often complement data obtained with IR spectroscopy. The difference in the selection rules is based on the fact that the Raman process relies on scattering rather than a direct transition between two vibrational states as it is the case for IR. For Raman spectroscopy monochromatic light, usually generated by a laser, is used to characterize the sample. Through interaction with the electron shells in the sample, the sample is excited into a virtual energy level.[3] The two types of Raman scattering (Stokes and Anti-Stokes) and additional Rayleigh scattering are depicted in Figure 2.5.
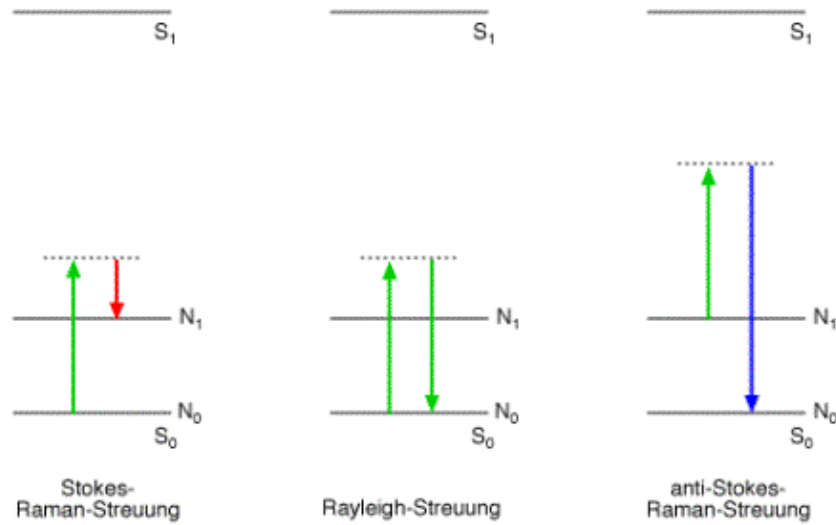
**Figure 2.5:** Energy states and scattering processes (Stokes-, Rayleigh-, and anti-Stokes scattering, respectively) occurring in a Raman experiment.[20]

Rayleigh scattering displays no change in frequency. As most molecules are located in the ground state at room temperature, Stokes shifts occur with higher intensity and are therefore commonly used for Raman measurements. The intensity of Raman signals is inversely proportional to the fourth power of the excitation wavelength, and Raman scattering comprises only a very small fraction of the scattered light.[3, 19]

## 2.5   UV-VIS Spectroscopy

In UV-Vis spectroscopy, the sample is irradiated with electromagnetic waves in the ultraviolet (10 – 400 nm) and visible range (400 – 750 nm). The UV-range can be divided in UV-A (400 – 320 nm), UV-B (320 – 280 nm) and UV-C (280 – 210 nm). Absorption of light leads to the excitation of valence electrons from the ground state ($S_0$) to an excited state ($S_1$), typically at higher vibrational states.

Accordingly, molecules with the same HOMO-LUMO energy difference can have different excitation energies. By spontaneous emission or stimulated emission (by a light ray), the excited electron can relax into the ground state, depending on the transition probability. For all electronic transitions selection rules have to be fulfilled. The spin selection rule implies that the total spin S or the multiplicity (M = 2S+1) cannot change during the transition. This implies

that singlet states cannot pass into triplet states. In centrosymmetric molecules, the inversion can be symmetric (even) or asymmetric (uneven). According to the Laporte rule, electronic transitions that conserve parity, either symmetric or asymmetric, are forbidden. However, due to atomic movements the symmetry can be degraded, which allows the transition to occur, albeit with low intensity.[19]

In UV-Vis spectroscopy the incoming light hits a homogeneous medium with a defined thickness $d$. The weakening of the light intensity by absorption (besides reflection and scattering losses) is given by the Beer-Lambert law (2.6).

$$A = \log\frac{I_o}{I} = \ \varepsilon\ \cdot c\ \cdot d \tag{2.6}$$

$A$: absorption, $I_0$: intensity of incident beam, $I$: intensity of emergent beam,
$\varepsilon$: molar absorption coefficient, $c$: concentration of diluted solution, $d$: sample thickness

The law is attributed to Bouguer (1728), Lambert (1760) and Beer (1852) and applies for monochromatic light and dilute solutions. In UV-Vis spectra, the absorbance is plotted against the wavelength of the incident light. Due to the energy width of the electronic levels (vibronic states), the observed spectrum is typically a band spectrum, which can be characterized by the position, intensity, shape and structure of the different bands.[19] This allows for the quantitative determination of different analytes, like transition metal ions, highly conjugated organic compounds or biological macromolecules.

## 2.6 Fluorescence Spectroscopy

Photoluminescence can be divided into phosphorescence and fluorescence, depending on the internal excitation mechanism and the resulting lifetimes of the excited states. According to the Franck-Condon rule, absorption of light results in a vertical electronic excitation. Typically, the excited molecule loses energy upon collisions with the environment until the vibrational ground state of the excited electronic state is reached. A schematic Jablonski diagram is depicted in Figure 2.5, which gives information about the three-stage process of fluorescence.
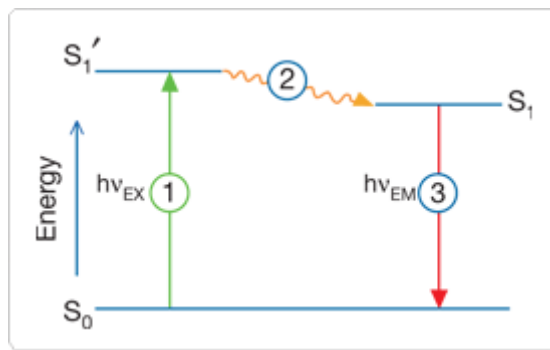
**Figure 2.6:** Jablonski diagram illustrating the three-stage process of fluorescence. **1)** Excitation of electron by external photon $h\nu_{ex}$, **2)** non-radiative relaxation, and **3)** emission of photon $h\nu_{em}$.[21]

**Excitation:** In a first step, a photon of certain energy ($h\nu_{ex}$) generated by an external source (incandescent lamp or laser light) is absorbed by the fluorophore, resulting in an excitation of the electon from the ground state ($S_0$) to the excited state ($S_1'$). This process is very fast, taking place within femtoseconds.

**Non-radiative relaxation:** The non-radiative transition of the electron from the excited state ($S_1'$) to the relaxed excited state ($S^1$) is caused by vibrational relaxation of the fluorophores and usually takes $1 - 10$ ns.

**Fluorescence emission:** In the third and last step, the excited electron falls back to the ground state ($S_0$) by emitting photons ($h\nu_{em}$) of a lower wavelength. Therefore, fluorescence features a red-shift of the emitted wavelength in comparison with the incident photons emitted by the external source. This bathochromic shift of the emission maximum compared to absorption is called Stokes shift. [15, 22]

In addition to fluorescence other processes can occur that cause a return of the excited molecules to the ground state, namely quenching, fluorescence energy transfer (FRET) and intersystem crossing (leading to phosphorescence).

## 2.7  Thermogravimetric Analysis

Thermogravimetric analysis (TGA) can be performed to determine the composition of a material that contains volatile or combustible components.[23, 24] TGA investigates the mass loss of a material with increasing temperature and yields information about the temperature stability of the sample. Typically, samples are placed into an adjustable oven and are heated to temperatures up to 900 °C. A controlled temperature program with a constant heating rate in inert gas atmosphere or synthetic air is applied to the sample, resulting in either desorption of adsorbed molecules or decomposition of the material, while its weight loss is measured as function of temperature. A sensitive thermobalance is connected to the specimen holder to detect small changes in mass (0.1 µg) during the heating process or while the sample is held at the required temperature.

## 2.8  Scanning Electron Microscopy

Scanning electron microscopy (SEM) is a technique using a focused beam of electrons that is raster-scanned over the surface of a solid sample. The highly energetic electrons focused onto the specimen interact with the surface atoms producing various signals that hold information about the shape, topography and composition of the material.[25] Compared to optical microscopy which uses visible light with a wavelength of about 400 – 800 nm, the resolution that can be achieved with an electron microscope is roughly four orders of magnitude higher. It is a versatile method for the analysis and examination of solid materials since it allows high resolution down to the nanometer range. Additionally, this method provides a large depth of field that is partly responsible for the three-dimensional appearance of the image.
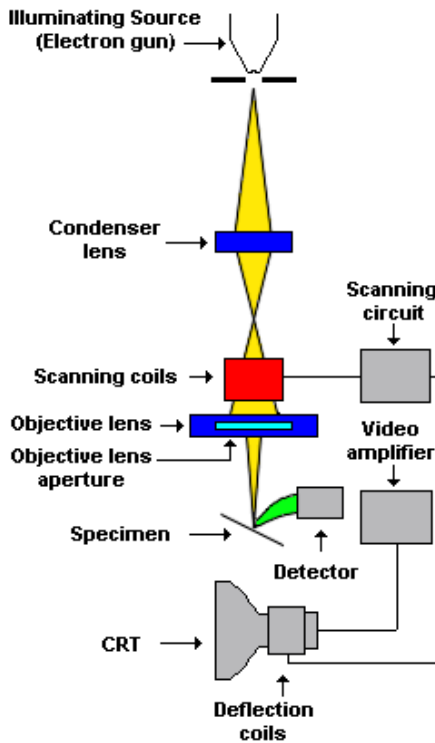
**Figure 2.7:** Scheme of a scanning electron microscope.[26]

In a scanning electron microscope primary electrons are accelerated by an anode and then focused by several coils on the specimen, scanning the latter line by line.[25] The electrons are generated from a tungsten filament inside the electron gun by thermionic emission or by field emission. Then they are accelerated by an anode. Through acceleration voltages in the range of $2 - 40\,kV$ within the SEM chamber, a beam of energetic electrons is generated. After focusing this electron beam onto the sample with the help of a condenser and objective lens, the so-called primary electrons (PE) interact with the specimen's surface producing secondary electrons (SE), back scattered electrons (BSE), X-rays, Auger electrons and cathodoluminescence. The condenser lens displays the image of the source on the condenser aperture. Subsequently, the collimated beam is focused by an objective lens and swept in a raster across the specimen employing scanning coils. These are controlled by varying the applied voltage on the scan coils generating a magnetic field which leads to a controlled deflection of the electron beam.[25] Depending on the nature of the sample and the energy of the primary electrons, different processes can occur when the electron beam hits the surface of the specimen. Importantly, electrostatic charging of the surface has to be avoided, as it leads to unstable secondary emission, which destroys the resolution and the image stability. Two possibilities to avoid

electrostatic charging are known, (1) using a low beam voltage, and (2) coating the sample with a thin layer of an electrically conducting film (Au, C).

## 2.9 Transmission Electron Microscopy

Transmission electron microscopy (TEM) is a powerful imaging technique for nanometer-sized materials offering a spatial resolution down to about 0.1 nm. Resolution of common light microscopes is limited by the wavelength of the used light and can reach values of 0.2 μm. Providing spatial resolution down to the range of Angstrom, TEM micrographs provide information about the elemental composition, the particle size distribution, the crystallography as well as the morphology of a sample. These (up to) atomic-resolution-images in combination with chemical and electronic properties make TEM a valuable instrument for the characterization of nanomaterials.[27]

In a conventional TEM, the electron beam is generated via heating a pin-shaped tungsten filament (cathode) that possesses a negative potential. Due to the strong interactions of electrons with matter the method requires ultrahigh vacuum, and limiting factors for high resolution are spherical aberrations, chromatic aberrations, and astigmatism. The emitted electrons are accelerated towards the positive anode and hence towards the sample by applying large voltages typically between 100 and 500 kV. Subsequently, the beam is tightly focused through the electromagnetic lens system whereby condenser lenses focus the beam to a small cylinder while the condenser aperture is used to remove electrons that are scattered at large angles. Having reached the specimen, the electron beam is scattered whereas a certain percentage of electrons is transmitted through the sample. Additionally, various processes occur upon electron irradiation of a material generating X-rays and a large variety of resulting electrons, namely secondary, backscattered, and so-called Auger electrons, which can be detected and are utilized for different techniques in electron microscopy including selected area electron diffraction (SAED), energy dispersive X-ray (EDX) analysis, and electron energy loss spectroscopy (EELS). Only electrons emitted at the bottom side of the sample are refocused by an objective lens. In TEM the transmitted electrons are detected by a fluorescent screen or by a CCD camera. This technique offers the investigation of the internal structure of the specimen.

Another possibility of imaging with a TEM is connected to electron beam scanning. This so-called scanning transmission electron microscopy (STEM) possesses the advantage of high contrast and absence of imaging artefacts.[27, 28]
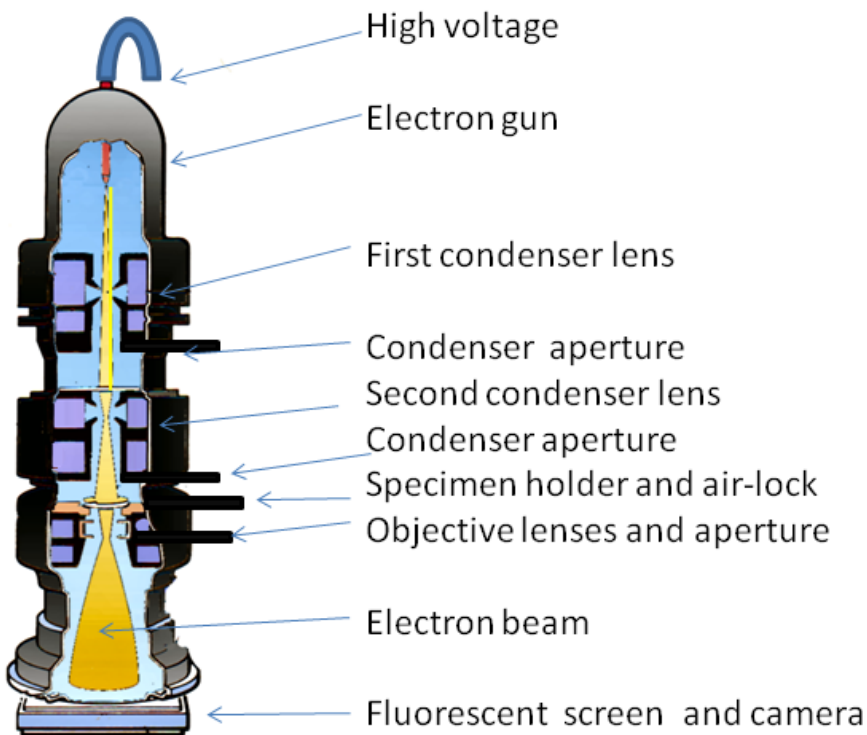


**Figure 2.8:** Schematic representation of a transmission electron microscope. The pathway of the electron beam is presented in yellow.[29]

TEM and STEM were used to investigate and characterize the morphology of mesoporous silica nanoparticles, especially their structure, wall thickness and pore dimensions.

## 2.10  Nuclear Magnetic Resonance

Nuclear magnetic resonance (NMR) spectroscopy can be applied to investigate the chemical environment of certain nuclear isotopes by applying a static magnetic field.[19] The analysis of

NMR data provides information about the structural properties and bonds of nuclear isotopes. Importantly, the investigated elements need to have a non-zero nuclear spin, which is present in, e.g., $^{1}$H, $^{13}$C, $^{19}$F, $^{29}$Si and $^{31}$P. By applying electromagnetic waves in the radio frequency region, transitions between different energetic states can be induced when the resonance condition is met. The measured difference between the strength of the local magnetic field and the applied external field gives insights about the electronic and chemical environment of the nuclei. The transition between these quantum states is induced by radiofrequency energy, typically ranging from a few kHz to several hundred MHz, in case of resonance conditions (2.7).

$$\omega = \gamma(B_0 + B_{int}) \qquad \textbf{(2.7)}$$

*$\omega$ is the frequency of electromagnetic radiation at resonance conditions, $\gamma$ is the gyromagnetic ratio, $B_0$ is the applied external magnetic field, and $B_{int}$ is the internal field arising from the electronic environment and surrounding magnetic moments.*

Nuclear magnetic resonance spectroscopy of liquids typically gives sharp spectra at high resolution, since the mobility of the nuclei in liquid samples creates an averaging process that leads to an intrinsic elimination of the line broadening related to dipole-dipole interactions. In comparison, the characterization of solid materials with solid state NMR (ssNMR) requires special methods to give comparable structural information.[30] The dipole-dipole interactions between the magnetic moments of nearby nuclei lead to line broadening in the spectra. Chemical shifts and spin-spin-coupling can no longer be observed. To solve this problem, the dipolar interaction has to be suppressed. In general, there are three methods available to solve this problem.

1)  If the specimen is dissolved, the thermal motion is much greater than in a solid. This so-called Brownian motion is even faster than the precession movement of the nuclear spins. As a result, the coupling is averaged out.

2)  Magic angle spinning (MAS).[31] At a certain angle ("magic angle", equation 2.9) that is between the interproton vector and the magnetic field $H_0$ the dipole-dipole interaction vanishes. Solid specimens can be rotated at this angle, and at typical rotation frequencies in the range of 10 kHz this averaging effect is observed.

$$cos^2(\theta magic) = \frac{1}{3} \qquad \textbf{(2.8)}$$

3)      Multi pulse sequence. The Carr-Purcell-Maiboom-Gill-sequence consists of a 90° pulse followed by a series of 180° pulses. Consequently, a number of spin-echoes can be detected with decreasing amplitudes with respect to time.

The "magic angle spinning" (MAS) technique provides a method to eliminate this anisotropic effect and to sharpen the obtained broad peaks in solid state NMR by rotating the sample at high velocity at an angle of 54.74 ° to the applied magnetic field. In this work, only magic angle spinning was used.

## 2.11  X-Ray Diffraction

X-ray diffraction measurements can be performed to characterize nanostructures and to gain information about the crystallinity of the investigated material. Additionally, the size of the nanomaterials, information about the pore structure, pore width and pore wall thickness can be obtained.[32] X-ray diffraction peaks for mesoporous silica materials appear in the low-angle range as the pore diameter is rather large in comparison to interatomic distances; therefore small angle X-ray scattering (SAXS)  ranging from $2\theta = 0.1 - 10$ ° was used in this work. X-ray radiation is emitted from a metal source, typically copper, with a characteristic wavelength (Cu-$K_\alpha$ is 1.54182 Å).[33] In order to obtain monochromatic X-ray radiation for X-ray diffraction (XRD) measurements, monochromators or blocking filters are used.[34] The wavelength of the monochromatic X-rays is in the Ångstrøm range, which is the same order of magnitude as interatomic distances in solids. Therefore, their diffraction on crystalline solid materials can be used to obtain structural information. The diffraction of X-rays on diffraction centers of the lattice leads to their reflection at sequential lattice planes. When X-rays hit the crystal with an incident angle of $\theta$, constructive interference occurs at the same exit angle if the Bragg equation is fulfilled (2.10).

$$\sin \theta = \frac{n\lambda}{2d}$$ 
(2.9)

**Bragg's relation:** $\theta$ is the angle of incidence, $d$ is the lattice plane distance, $\lambda$ is the wavelength, and $n$ is the order of interference.

## 2.12 References

1.   http://www.malvern.de/malvern/kbase.nsf/allbyno/KB000792/$file/MRK656-01_An_Introduction_to_DLS.pdf.

2.   Pecora, R. *Dynamic Light Scattering: Applications of Photon Correlation Spectroscopy*, Plenum Press, **1985**.

3.   Kalantar-Zadeh, K.; Fry, B., *Nanotechnology-Enabled Sensors*, Springer, **2008**.

4.   Skoog, D. A.; Holler, F. J., and Crouch, S. R. *Principles of instrumental analysis*, Thomson, **2007**.

5.   Butt, H.; Graf, K., and Kappl, M. *Physics and Chemistry of Interfaces*, Wiley VCH, **2003**.

6.   http://www.malvern.de/malvern/kbase.nsf/allbyno/KB000734/$file/MRK654-01%20An%20Introduction%20to%20Zeta%20Potential%20v3.pdf.

7.   http://www.malvern.com/labeng/technology/images/zeta_potential_schematic.png.

8.   Malvern Intruments, Zetasizer Nano Series - User Manual, **2003**.

9.   Lowell S.; Shields, J. E.; Thomas, M. A., and Thommes, M. *Characterization of Porous Solids and Powders: Surface Area, Pore Size and Density*. Springer, **2006.**

10.  Ryu, Z. Y.; Zheng, J. T.; Wang, M. Z.; Zhang, B. J. *Carbon* **1999**, *37*, 1257-1264.

11.  Sing, K. S. W.; Everett, D. H.; Haul, R. A. W.; Moscou, L.; Pierotti, R. A.; Rouquérol, J.; Siemieniewska, T. *Pure & Appl. Chem.* **1985**, *57*, 603-619.

12.  de Boer, J. H. *The Structures and Properties of Porous Materials*, Butterworth-Heinemann Limited, **1958**.

13.  Langmuir, I. *J. Am. Chem. Soc.* **1916**, *38*, 2221-2295.

14.  Brunauer, S.; Emmett, P. H.; Teller, E. *J. Am. Chem. Soc.* **1938**, *60*, 309-319.

15.  Atkins, P. W., *Physikalische Chemie*, Wiley-VCH, **2001**.

16.  Barrett, E. P.; Joyner, L. G.; Halenda, P. P. *J. Am. Chem. Soc.* **1951**, *73*, 373-380.

17.  Hollas, J. *Modern Spectroscopy*. Wiley, **2004**.

18. Brundle, C., Evans, C., and Wilson, S. *Encyclopedia of Materials Characterization: Surfaces, Interfaces, Thin Films*. Butterworth-Heinemann Limited, **1992**.

19. Hesse, M., Meier, H., and Zeeh, B. *Spektroskopische Methoden in der organischen Chemie*. Thieme Georg Verlag, **2005**.

20. http://www.raman.de/assets/images/energie.gif

21. http://www.lifetechnologies.com/content/dam/LifeTech/migration/en/images/ics-organized/references/the-handbook/intro-fluorescence-techniques.par.88992.image.275.171.1.s000100-intro-fluorescence-gif.gif.

22. Lakowicz, J. R. *Principles of Fluorescence Spectroscopy.* Plenum Press, **1983**.

23. Pang, L. S. K.; Saxby, J. D.; Chatfield, S. P. *J. Phys. Chem.* **1993**, *97*, 6941.

24. Sepe, M. P. *Thermal Analysis of Polymers*. Rapra Technology Limited, **1997**.

25. Goldstein, J.; Newbury, D. E.; Joy, D. C.; Lyman, C. E.; Echlin, P.; Lifshin, E.; Sawyer, L.; Michael, J. R. *Scanning Electron Microscopy and X-ray Microanalysis*. Springer, **2003**.

26. http://www.innerfidelity.com/content/hard-core-diy-scanning-electron-microscope

27. Williams, D. B., and Carter, C. B. *The Transmission Electron Microscope*. Springer, **1996**.

28. Vollath, D. *Nanomaterials: an introduction to synthesis, properties and application*. Wiley-VCH, **2008**.

29. http://edu.glogster.com/media/5/32/8/90/32089069.png

30. Duer, M. J. *Introduction to solid-state NMR spectroscopy*. Blackwell Science. **2008**.

31. Lowe, I. J. *Physical Review Letters* **1959**, *2*, 285-287.

32. Fratzl, P. *J. Appl. Crystallogr.* **2003**, *36*, 397.

33. Cullity, B. D., and Stock S. R. *Elements of X-Ray Diffraction.* Prentice Hall, **2001**.

34. Waseda, Y.; Matsubara, E., and Shinoda K. *X-Ray Diffraction Crystallography: Introduction, Examples and Solved Problems*. Springer, **2011**.

# 3 Cell Type Determines the Light-Induced Endosomal Escape Kinetics of Multifunctional Mesoporous Silica Nanoparticles

This chapter is based on the following publication:
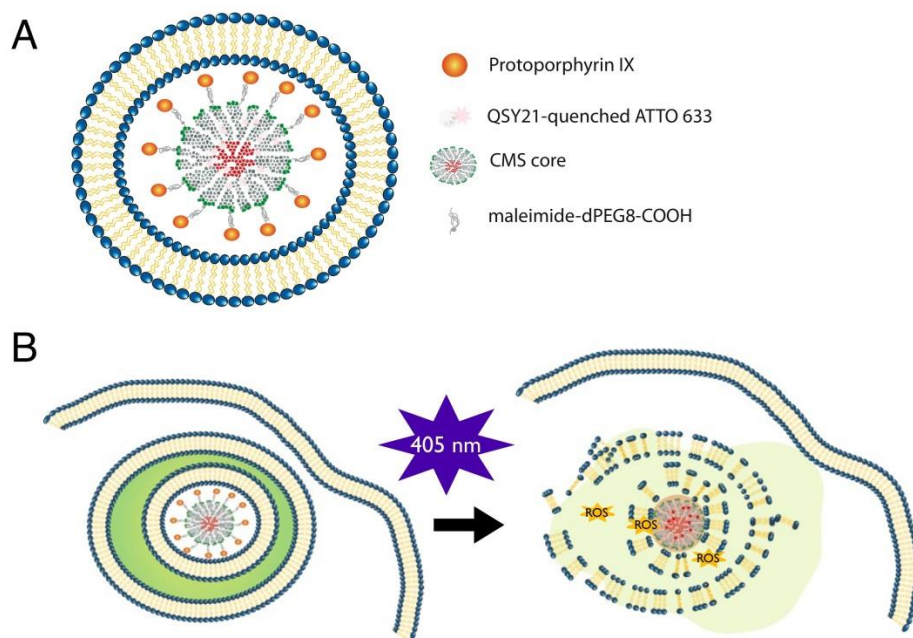
## Abstract

We investigated uptake and individual endosome lysis events in fibroblast, normal and carcinoma cell lines using a colloidal mesoporous silica nanoparticle (MSN)-based reporter system with a covalently attached photosensitizer. Endosome lysis was induced through the activation of protoporphyrin IX (PpIX). Surprisingly, this release on-demand system resulted in more broadly-distributed lysis times than expected, particularly for Renca, a renal carcinoma cell line. An analysis of the nanoparticle (NP) load per endosome, endosome size and uptake characteristics indicate that Renca cells not only take up a lower amount of NPs in comparison with the fibroblast cells, but also have larger endosomes, and a lower NP load per endosome. We then extended an existing stochastic pi calculus model of gold NP intracellular distribution to understand how much factors that cannot be directly measured, such as variations in the PpIX load per NP, affect the distributions. Model results indicate that the lysis time distribution is

primarily determined by the minimum of PpIX required to burst an endosome, a factor influenced by the NP load per endosome, as well as the endosome size.

## 3.1 Introduction

Endosomal escape has been identified as one of the main bottlenecks in gene and drug delivery.[1, 2] To date, however, there are few papers that investigate single endosome lysis in real time because of low signal-to-noise ratios[3]. Previous studies have recorded the intracellular trafficking of individual nanoparticles and various delivery vectors[4-6], measured endosome or cellular contents *ex vivo*[7, 8], or tracked individual viruses as they move across the cell.[9] In these protocols, individual components of the virus or the vector, as well as cellular components, are labeled.[10] In all studies involving delivery vector tracking[4-6], confocal laser scanning microscopy was used, since dye localization on a single plane is insufficient to definitely establish particle internalization;[11] it was reported in Akita *et al.* that at least 20 z-slice images were required for their method, and that at least 30 cells were needed to be imaged in this manner to obtain statistically meaningful results.[4] If this method were translated into a 30-hour observation period, as in employed by Schwake and co-workers[11], this would entail the capture, consolidation and analysis of 216.000 images. Due to such limitations, most of the studies have concentrated on the spatial distribution of the material,[6, 12] or on the trafficking mechanisms used instead.[4, 9] Endosome escape efficiency is inferred from a minimal amount of sampling points.[4] Uptake events are likewise rarely recorded in real time, again due to the low signal-to-noise ratio; real time recording frequently requires confocal or total internal reflection microscopy.[9] It is more common for endosomal escape rates to be estimated from data fits.[8] Combining direct analysis of uptake and endosomal escape will not only yield time distributions of the escape events, but also information on the vector load per endosome, and the influence of endosome size on escape. Availability of such information for vectors tested on different cell lines would be important in evaluating their performance. To obtain real-time information on individual lysis events, it would be highly desirable to have a reporter system that could be co-delivered with, or be used itself as a delivery vector. An ideal detector system should have distinct signals for each target compartment, and the signals produced should not immediately diffuse into the cytosolic milieu. Given these considerations, we chose to modify a recently

designed colloidal mesoporous silica nanoparticle (MSN) system to create a fluorometric detector.

MSNs are non-toxic and biocompatible,[14, 15] possess a controllable and well-defined uniform porosity, offer large surface areas, pore volumes, multifunctionality and are small in size, a critical feature for endosomal uptake.[16-19] The surface of these nanoparticles (NPs) can be modified by inorganic and organic functionalization to give multifunctional hybrid materials.[20-22] MSNs can be functionalized with polymers such as polyethylene glycol (PEG)[23, 24] and polyethyleneimine (PEI)[25], which increase colloidal stability by preventing non-specific protein adsorption.[23, 26-29] In addition, controlled release from MSNs can be implemented using various stimuli-responses to these cap systems.[30-33] The opening stimulus can be a change in pH[34], UV irradiation[35], or redox-activity.[36] MSNs can also be enclosed in supported lipid bilayers (SLB@MSN)[37], created by a solvent exchange induced self-assembly of lipids around the MSNs.[38] NP-supported lipid bilayers exhibit a narrower size distribution and enhanced stability compared to liposomes.[39-41] Combining SLB@MSNs with photochemical internalization (PCI)[42, 43] and photosensitizers (PS) leads to a highly potent drug delivery system.[39] PS generate reactive oxygen species (ROS) upon light-activation, leading to membrane rupture.[44] Recently, multifunctional MSNs have been equipped with an on-board photosensitizer, namely amino-modified protoporphyrin IX (PpIX-NH$_2$). This system has already been tested in different cell lines.[43] Here we combine PCI with a covalently bound blue-light sensitive photosensitizer and the redox-labile disulfide-bridge approach to create highly potent, multifunctional MSNs acting as fluorimetric reporter vectors in different cell lines (Figure 3.1).
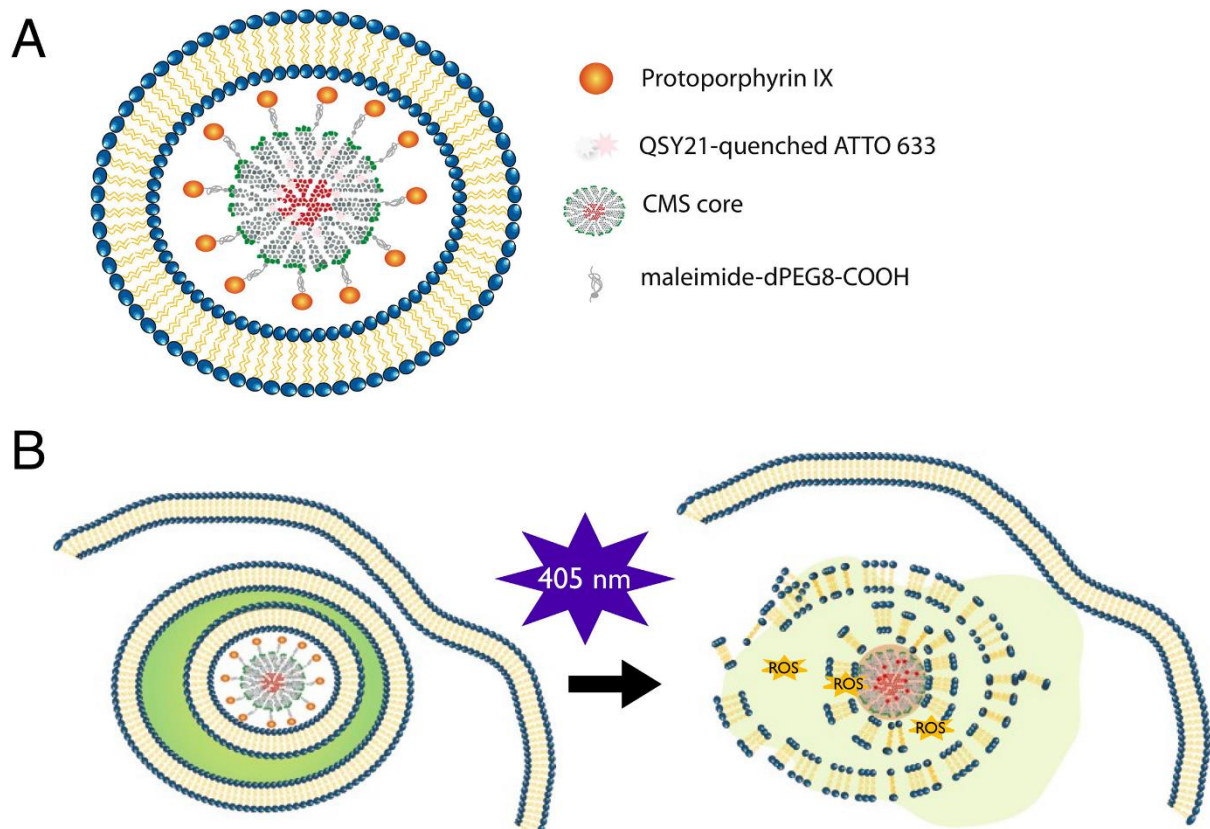
**Figure 3.1:** MSN-based endosome lysis detector system **(A).** MSNs to which inactive protoporphyrin IX (PpIX) and the quenched dye Atto633 are covalently attached (CMS core), are encapsulated in a lipid bilayer. Cells are incubated with NPs for at least 6 hours prior to a lysis experiment together with a fluid-phase marker, AlexaFluor Dextran 488. Endosome lysis is induced by activating PpIX with 405 nm light. **(B)** The reactive oxygen species (ROS) produced by this reaction oxidize double bonds in the lipid tails in both the SLB surrounding the NPs, as well as of the endosome. Following membrane disruption, the reductive intracellular milieu cleaves the bonds between the quencher and Atto633, leading to localized fluorescence at the site of lysis.

Apart from the construction of a reporter system, it is useful to construct a model that can be used to understand variations in the lysis time distributions, especially the contributions of factors that could not be directly quantified, such as the PpIX load per NP. We have previously created a stochastic pi calculus model for describing the intracellular distribution of NPs and NP aggregates.[45] Here, we extended the model to include the PpIX-mediated endosome lysis reaction. The model is executed using SPiM (http://research.microsoft.com/en-us/projects/spim/), developed by Andrew Philips and Luca Cardelli, at Microsoft Research, Cambridge.[45, 46] SPiM uses the Gillespie algorithm to describe the time evolution of the system

by selecting the reaction that will occur, as well as its duration, with a probability proportional to the base rate of reaction and reactant availability.[47] Model results indicate that for a PpIX-dependent NP system, the lysis time distribution depends heavily on cell specific uptake parameters, rather than any inter-NP variability in PpIX load, provided that the PpIX load is not too low. In this paper, we demonstrate that the use of this reporter system for generating time distributions of lysis events, coupled with an appropriate stochastic model, is a powerful method for evaluating and analyzing the efficiency of delivery vectors.

## 3.2    Results and Discussion

**Multifunctional mesoporous core-shell silica nanoparticles**

The multifunctional core-shell MSNs were synthesized following a previously reported procedure.[16, 17] We use a so-called delayed co-condensation approach to selectively introduce different functionalities on the inner and outer particle surface. This synthesis employs tetraethyl orthosilicate (TEOS) as silica source, 3-aminopropyl triethoxysilane (APTES) and 3-mercaptopropyl triethoxysilane as functionalized silica precursors and cetyltrimethylammonium chloride (CTAC) as structure directing agent. The polyalcohol triethanolamine (TEA) slows down the condensation rate of TEOS and leads to a small size distribution and radial growth of MSNs. Functionalized MSNs with 3-mercaptopropyl moieties in the shells of the particles and 3-aminopropyl groups in the core were synthesized according to this procedure giving the sample multifunctional MSNs (sample CMS_$NH_{2in}$_$SH_{out}$) after template removal (cf. experimental section), offering the possibility for post-synthesis modification due to the reactive nature of the groups. The MSNs were characterized in detail before further post-synthesis functionalization was carried out. The nitrogen sorption data revealed a type IV isotherm for the sample CMS_$NH_{2core}$_$SH_{shell}$ typical for mesoporous materials (Figure 3.2A). A high Brunauer-Emmett-Teller (BET) surface area of 1160 $m^2g^{-1}$ was derived from the data. Additionally, the pore size of the MSNs was calculated from the nitrogen physisorption data (Figure 3.2B). The pore size distribution derived from non-local density functional theory shows a narrow pore size distribution of 3.7 nm. Additionally, transmission electron microscopy was employed for further characterization, revealing spherically shaped nanoparticles of about 70 nm with a homogenous mesoporsity (cf. appendix 3.12).
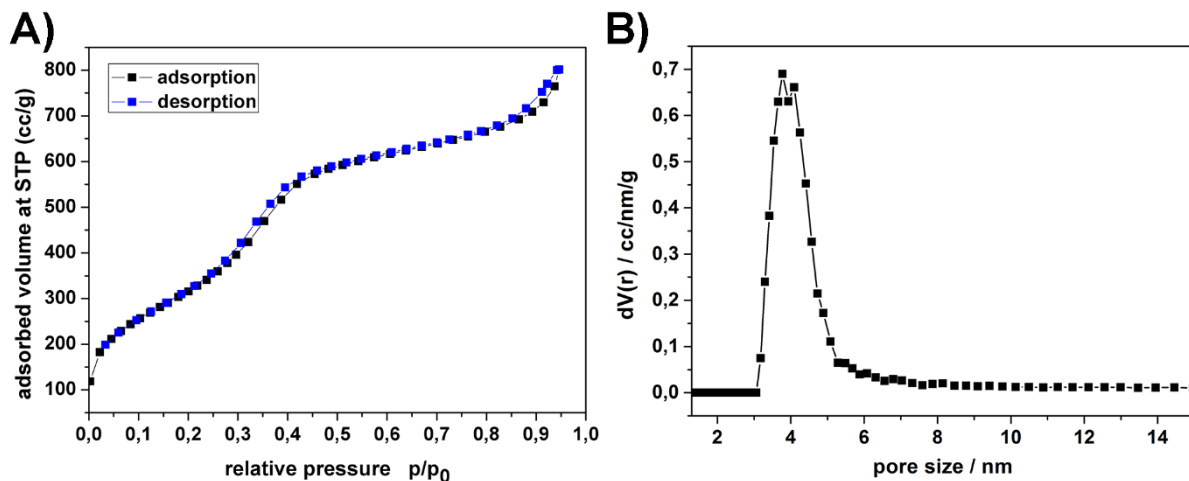
**Figure 3.2:** Nitrogen sorption data of template-free multifunctional MSNs (sample CMS_NH$_{2core}$-SH$_{shell}$). **A)** Nitrogen sorption isotherms and **B)** pore size distribution.

**MSN based detector system.** Figure 3.2-A shows the post-synthesis functionalization of the outer surface of the MSNs. In a first reaction step the thiol-moieties on the outer shell of the MSNs were reacted with a short, bi-functional polyethyleneglycol linker (maleimide-dPEG8-COOH, (1-maleimido-3-oxo-7,10,13,16,19,22,25,28-octaoxa-4-azahen-triacontan-31-oic acid), which increases the monodispersity of the sample in water and avoids pore blocking by the relatively large photosensitizer. The thiol moiety forms a stable bond with the maleimide functionalization of the PEG-linker in a Michael addition whereas the carboxy-functionality remains accessible for further modification. The amino-modified photosensitizer protoporphyrin-IX (PpIX-NH$_2$) was synthesized according to a modified literature procedure to allow covalent attachment to the carboxy-terminated PEG-linker on the outer surface of the MSNs.[48] This precursor was covalently attached to the carboxy-functions at the particle surface via an $N$-(3-dimethylaminopropyl-)$N'$-ethylcarbodiimide (EDC) assisted amidation to give the photosensitizer-modified MSN sample (CMS_NH$_{2in}$_PEG-PpIX$_{out}$).
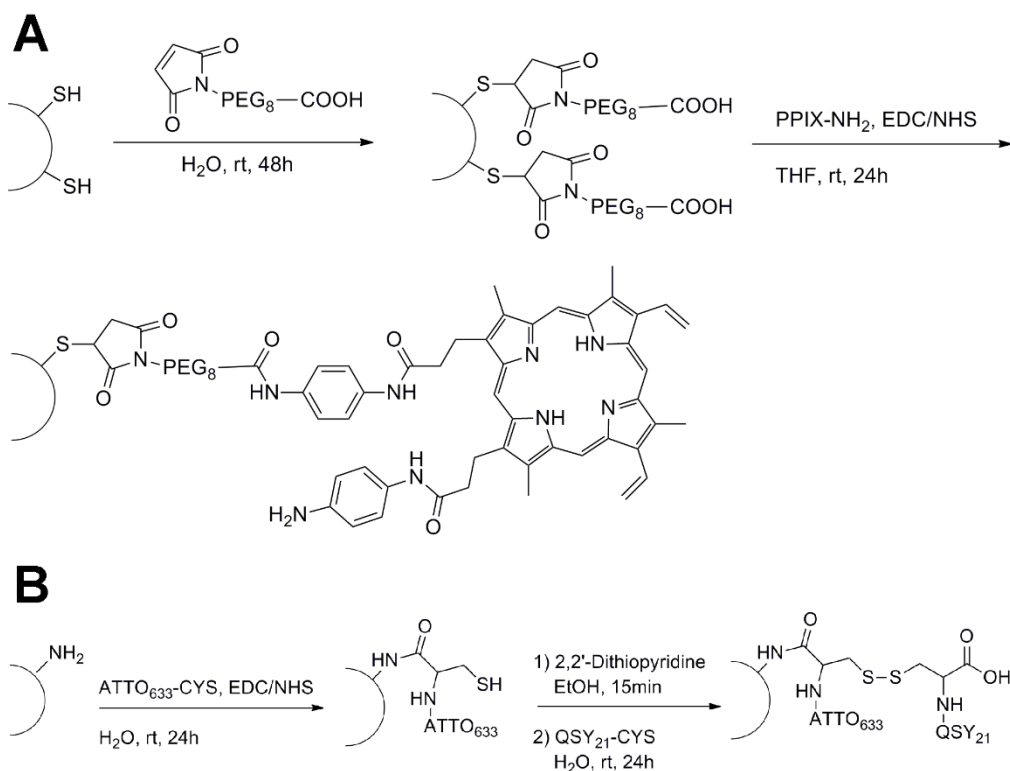
**Figure 3.3:** Reactions of MSNs. **A)** Shell reaction: 1) PEGylation 2) PpIX-NH$_2$ attachment via EDC-amidation. **B)** Core reactions: 1) Atto633-CYS attachment via EDC-amidation 2) The 2,2'-dithiopyridine attachment to the SH-group of Atto633Cys is followed by the bonding of QSY21Cys via a redox-labile disulfide bridge.

The core of the silica nanoparticles was modified according to Figure 3.3-B. We designed a redox-sensitive fluorimetric dye-quencher system for the MSN core. In the first step the highly reactive ATTO633-NHS ester was covalently attached to the amino group of cysteine (CysATTO633). Subsequently, CysATTO633 was reacted with the aminopropyl-functionality in an EDC assisted amidation to give the sample CMS_CysATTO633$_{in}$_PEG-PpIX$_{out}$. The thiol group of cysteine was activated with 2,2'-dithiopyridine, and cysteine-modified QSY21 (CysQSY21) was added. This resulted in a disulfide bridged dye-quencher system in the particle core and yielded the final sample CMS_CysATTO633-CysQSY21$_{in}$_PEG-PpIX$_{out}$.

The multi-step shell functionalization of the MSNs was monitored with dynamic light scattering (DLS) measurements, revealing homogeneous nanoparticles with a narrow size distribution (Figure 3.4). The modification with PEG leads to a slightly smaller particle sizes in water, whereas the attachment of PpIX leads to a broader size distribution; this can be explained by the hydrophobic nature of the photosensitizer.
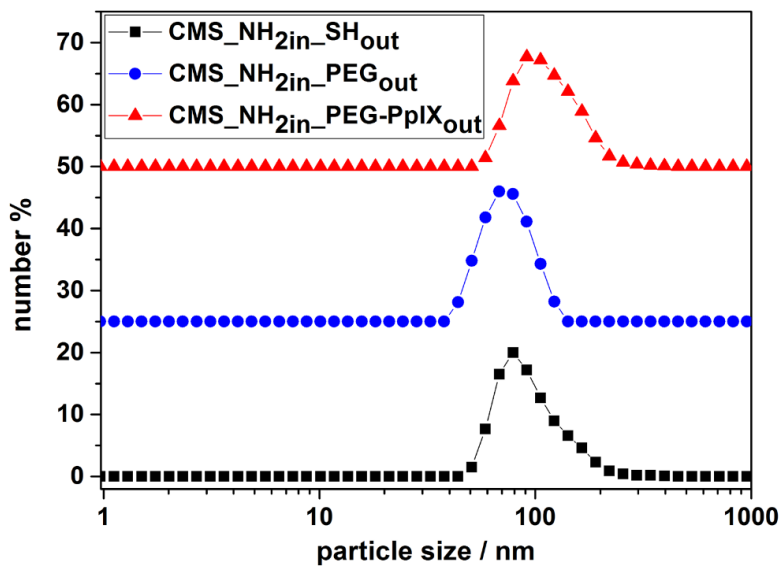
**Figure 3.4:** Dynamic light scattering (DLS) measurement of samples CMS_NH$_{2in}$_SH$_{out}$ (black curve), CMS_NH$_{2in}$_PEG$_{out}$ (blue curve) and CMS_NH$_{2in}$_PEG-PpIX$_{out}$ (red curve). For clarity reasons curves for CMS_NH$_{2in}$_PEG$_{out}$ (blue) and CMS_NH$_{2in}$_PEG-PpIX$_{out}$ (red) were shifted along the y-axis by a value of 25 each.

To demonstrate the efficiency of our disulfide bridged dye/quencher system in the sample CMS_CysATTO633-QSY21Cys$_{in}$-_PEG-PpIX$_{out}$ the NPs were investigated with fluorescence spectroscopy (Figure 3.5). The disulfide bridge between the two cysteine moieties is cleaved upon the addition of 10 mM L-glutathione (GSH) which corresponds to the strength of the reductive milieu. As a result, the covalently attached quencher CysQSY21 can diffuse out of the pores, resulting in a fluorescence of ATTO633.
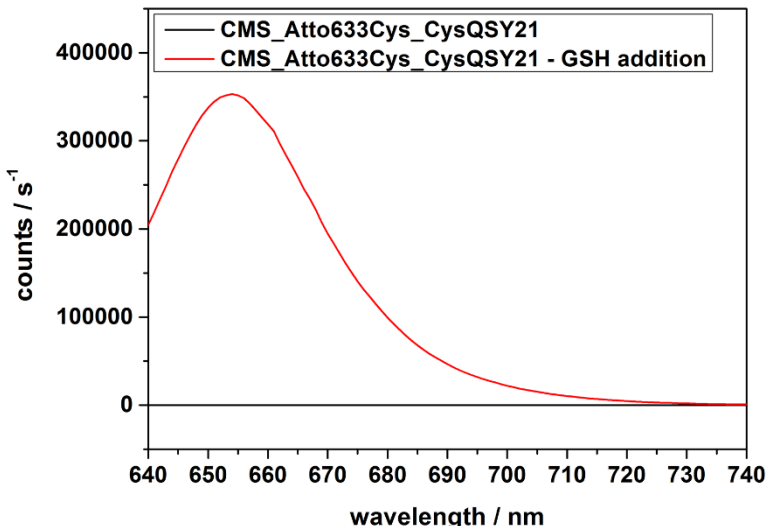
**Figure 3.5:** Fluorescence emission spectra of the sample CMS_CysATTO633-QSY21Cys$_{in}$_PEG-PpIX$_{out}$ (black curve) and 60 seconds after the addition of 10 mM L-glutathione (red curve), allowing the quencher to diffuse out of the mesopores.

**Lipids.** 1,2-dioleoyl-sn-glycero-3-phosphocholine (DOPC) and 1,2-Dioleoyl-sn-glycero-3-phospho-ethanolamine (DOPE), were chosen for the study. Both lipids bear a sufficiently high number of double bonds with which the singlet oxygen produced upon PpIX activation can react to destabilize the membrane structure.[49] Additionally, both lipids have been previously reported to form stable, fluid bilayers on the MSN core in their pure form.[50, 51] DOPE is known to possess fusogenic properties because of its ability to adopt an inverted hexagonal phase[52], influencing the curvature and structural integrity of a lipid bilayer[53], and can fuse with cell membranes better than DOPC.[52-54] The multifunctional MSNs were covered with SLBs comprised of either pure DOPC (DOPC@MSN) or pure DOPE (DOPE@MSN) lipid membranes labelled with 1 mol% Texas Red 1,2-dihexadecanoyl-sn-glycero-3-phosphoethanolamine, triethylammonium salt (TR-DHPE). The quality of the membrane was previously assessed using confocal microscopy and correlation spectroscopy, and was shown to prevent cargo release before it reaches the delivery target[55], or before controlled release is initiated. Additionally, the tight closure of the system was studied with time-based fluorescence release experiments (cf. appendix 3.13). Here, we provide further characterization of the system using single-cell uptake experiments and single-endosome lysis experiments.

**Supported lipid bilayer (SLB) deposition on MSNs through solvent exchange.** SLBs were deposited on MSNs particles as previously described[50]. Briefly, post-synthesis modified MSNs in solution are centrifuged at 13000 rpm for five minutes. The supernatant is discarded and the

particles are re-dispersed in a 2.5 mg/mL lipid solution in 40 vol% ethanol : 60 vol% water; this solution was subsequently titrated with water until a 95% vol water content is reached. The solution is allowed to equilibrate for 15 minutes, in the process forming the SLB on individual particles[56]; the NPs are separated from excess lipid by centrifugation, and subsequently re-suspended in a smaller volume comprised of 50 vol% complete cell culture medium: 50 % vol water solution. In this alcohol-free environment, the SLB is fully stabilized. The aggregation of NPs in this solution is minimized by brief sonication followed by filtration.

**Uptake experiments.** DOPC@MSN were tested on non-phagocytic cell lines whose interactions with NPs were of interest: Beas2B, a human normal bronchial epithelium cell line; Huh7, a human hepatocarcinoma cell line; Renca-LacZ, a transformed murine renal carcinoma cell line; and 3T3, a mouse embryonic fibroblast cell line. Cells were plated to a density of $0.75 \times 10^4$ cells/cm$^2$ on 8-well ibiTreat-coated Ibidi chambers 3 - 4 days before the start of the experiment. Cells were subsequently incubated with 50 µg/cm$^2$ DOPC@MSN over two-hour intervals up to eight hours and washed with PBS five times post-incubation. External fluorescence was additionally quenched with a wash using 0.4 % w/w trypan blue.[57, 58] Cells were then fixed with 2% formaldehyde in Leibovitz medium, reported to reduce cellular fluorescence[59], supplemented with 10% FCS for a total of two hours. Internalized NPs were visualized using fluorescence microscopy at 40x magnification, and recorded at an exposure time of 1 s and a density power of 0.12 W/cm2. For each setup, eight random viewfields were chosen. Experiments were performed in triplicate. The relative number of particles taken up by each cell was approximated by taking the mean gray values across the area occupied by the cell. Analysis was done semi-automatically in ImageJ using an in-house program.[60] Control experiments were performed using 30 nm, fluorescein labeled Latex NPs (Sigma Aldrich).

**Lysis experiments.** For *in vitro* lysis experiments, cells were incubated for 12 hours with DOPC@MSN or DOPE@MSNs functionalized with PpIX and ATTO633-QSY21 to ensure completion of uptake. Lysis experiments were performed on 3T3 and Renca-LacZ cells, which appear to exhibit the highest and lowest uptake characteristics for DOPC@MSN particles. AlexaFluor Dextran 488 (MW=10 kDa) was used as a fluid-phase marker for endocytosis. Following incubation, cells were washed with PBS five times post-incubation, or until most of the fluorescence from the AlexaFluor Dextran was removed; washing with 0.4% w/w trypan blue was performed to quench any remaining external fluorescence. PpIX was activated by a

one or two minute exposure to a 405 nm laser prior to imaging. Fluorescence images were taken every second with an exposure time of 200 ms over a period of two minutes per view field. NP and endosome fluorescence were monitored using the following excitation/emission filter sets: 488 nm/525 nm (AlexaFluor dextran); 560 nm/645 nm (Texas Red); and 640 nm/690 nm (ATTO633) (Chroma Technology). A negative control composed of DOPC@MSNs or DOPE@MSN functionalized with ATTO633-QSY21, but not PpIX, was used in parallel with all setups. Single endosome lysis events were detected using the same ImageJ plugin described previously. Briefly, images are segmented based on the fluid-phase marker channel (Figure 3.6). Discontinuities that occur in both the red and green channels were recorded as an endosome lysis event, and the time distribution of these events was collected for the different experimental setups. Apart from lysis times, the endosome area and NP colocalization intensity, based on the mean gray values in the red channel, are recorded.
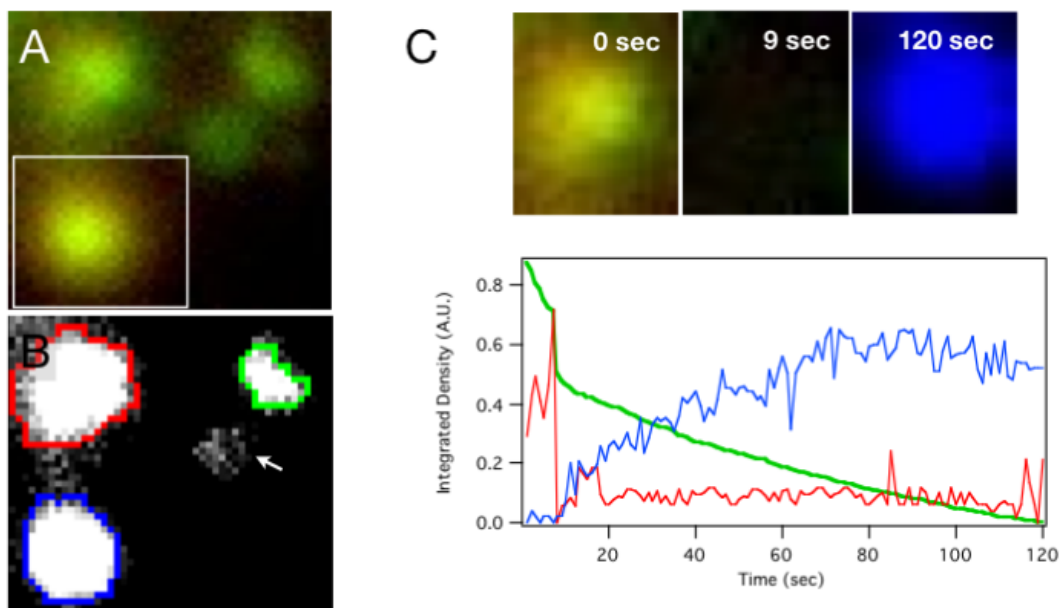


**Figure 3.6:** Single-endosome lysis time evaluation. Individual endosomes **(A)** are identified using automatic segmentation[59] performed on the green channel, which is able to identify three out of four endosomes; the arrow indicates an endosome that was not properly segmented, and that had to be manually added. Colors represent automatically-defined ROIs, and not RGB channels **(B)** ATTO633 fluorescence is artificially colored blue. For each endosome, the lysis time is determined through the occurrence of discontinuities in the time course in the red and green channels, as well as an increase in fluorescence in the long red channel **(C)**.

**Modelling.** To systematically evaluate the factors that influence lysis time distributions, we extended the generic stochastic pi calculus model that we have created for gold NP uptake and intracellular movement.[61] Specifically, we included PpIX and activated PpIX (Act_PpIX) counts as attributes of each NP process; an activation reaction, coupled with preconditions for lysis in the form of a minimum amount of Act_PpIX per endosome, also replaces the simple endosome lysis rate. We also redefine the aggregate size restrictions for 100 nm MSNs, instead of 4 nm gold NPs. Finally, we made uptake rates variable to represent cell specific responses. Each simulation was carried out with a starting value of 10000 NPs per cell; the PpIX load assigned to each NP was taken from a normal distribution with a mean of 50 PpIX per NP, and a width of 5. Sensitivity analysis was performed to identify the critical parameters of the model. We used code for SPiM v.0.05, which is run automatically using a Perl script that also permits parameter alteration. We omit the events downstream of endosomal escape, which we do not consider in this study.

**Statistics from single-endosome PpIX-mediated lysis with different lipids, cell types, and PpIX activation times.** We investigated the time distribution of endosome lysis as a function of PpIX activation time, lipid coat, and cell type. Our results generally show that DOPE@MSN exhibit marginally earlier lysis times than DOPC@MSN. An interesting observation is that the activation time appears to play a more prominent role in Renca-LacZ than in 3T3, as evinced by the bigger shift in the distribution when the activation time is decreased (Figure 3.7A-D, Table 3.1). Furthermore, the distribution of lysis times after a two-minute PpIX activation is considerably more spread than in 3T3, which could be an indication of cell-specific dependence of endosome lysis.
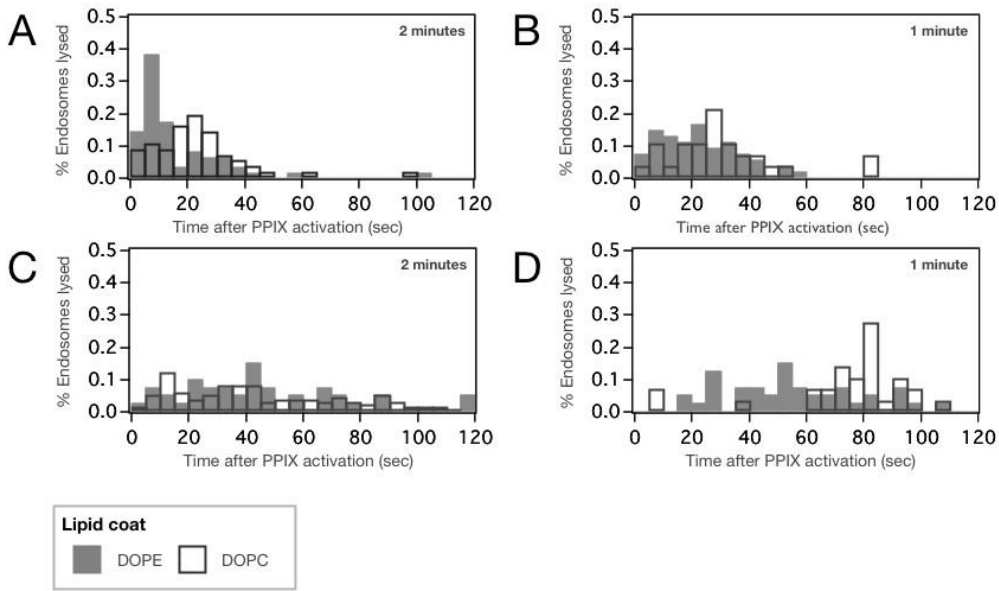
**Figure 3.7: A and B)** Time distributions of endosome lysis events after PpIX-activation in 3T3 and **C and D)** Renca-LacZ cells. PpIX-functionalized DOPC@MSN and DOPE@MSN were incubated overnight, then activated for either one or two minutes. Results generally show marginally earlier lysis times for DOPE@MSN. It is interesting to note that lysis appears to be more concentrated towards earlier times for 3T3 cells than for Renca-LacZ; furthermore, the shift in the lysis times when activation is shorter is less prominent in 3T3.

**Table 3.1.** Selected gauss fit parameters of endosomal escape data for DOPC@MSN and DOPE@MSN in 3T3 and Renca-LacZ cultures.

| Sample | Activation time (min) | Mean | Width |
|---|---|---|---|
| DOPC@MSN, 3T3 | 2 | $17.4 \pm 0.9$ | $17.0 \pm 1.5$ |
| DOPC@MSN, 3T3 | 1 | $23.7 \pm 1.8$ | $17.2 \pm 2.9$ |
| DOPE@MSN, 3T3 | 2 | $5.3 \pm 0.3$ | $5.2 \pm 0.4$ |
| DOPE@MSN, 3T3 | 1 | $15.4 \pm 1.6$ | $24.0 \pm 2.7$ |
| DOPC@MSN, Renca-LacZ | 2 | $25.9 \pm 7.3$ | $39.3 \pm 15.6$ |
| DOPC@MSN, Renca-LacZ | 1 | $77.6 \pm 1.9$ | $13.6 \pm 3.0$ |
| DOPE@MSN, Renca-LacZ | 2 | $31.1 \pm 5.3$ | $28.0 \pm 10.1$ |
| DOPE@MSN, Renca-LacZ | 1 | $49.8 \pm 5.0$ | $35.0 \pm 15.2$ |

In order to check if there were cell-specific differences that may have influenced the lysis events, we analyzed the size distribution of endosomes, demarcated by the AlexaFluor Dextran 488. We also obtained the red channel intensity within the area occupied by the endosome as a rough approximation of the endosome load. Although the colocalization intensity distribution appears to have a similar range (Figure 3.8B), the disparities in the endosome area are relatively marked (Figure 3.8A), with Renca-LacZ cells displaying more size variation, and tending towards larger endosomes. When a correlation is made between individual endosomes and corresponding mean gray values (Figure 3.8C), it becomes evident that 3T3 cells have a higher NP load per endosome on average.

A possible reason for this is the higher expression and/or a longer lifetime of Rab5 in Renca-LacZ, a protein that controls endosome fusion, and consequently endosome size distribution.[62] Expression profiles of 3T3 cells and differentiated counterparts show an increase in Rab5 expression in differentiated cells; Rab5 has also been reported to be overexpressed in several carcinoma cell lines, including lung adenocarcinoma[63] and HeLa.[64] One way of clarifying the results would be to use a Rab5 tag to have an approximation of both its expression and lifetime in the cell types tested.
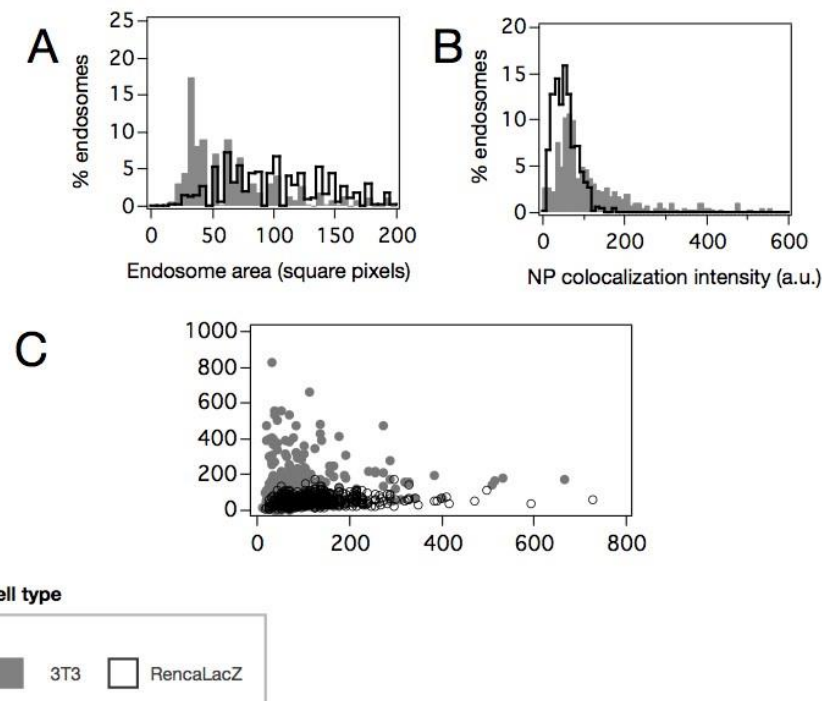
**Figure 3.8:** Endosome size and colocalization intensity data for 3T3 and Renca-LacZ cells. Endosomes appear to have more varied sizes in Renca-LacZ cells than in 3T3 cells **(A)**, as well as a lower MSN reporter load **(B)**. The variation in endosome size may be a result of differences in Rab5 expression.

**Cell-type dependence of NP uptake.** Another interesting observation was that Renca-LacZ cells generally took up a smaller amount of MSNs than 3T3 (Figure 3.9). To confirm this, we conducted time-course uptake experiments using 3T3 and Renca cells, as well as two additional cell lines. From these experiments, we gathered information for between 500 and 1000 cells for each time point and each cell line. We ran a parallel experiment using 30 nm fluorescently-labeled Latex NPs as a form of control. Our results confirm that 3T3 cells take up more DOPC@MSN than Renca-LacZ on average (Figure 3.10, Table 3.2). Additionally, the cell-to-cell uptake variation in Renca-LacZ cells appears to be at least twice of what could be expected from 3T3. Table 3.2 summarizes selected parameters from Gaussian fits of the uptake data eight hours post-incubation. The cell-specific uptake features can also be observed with Latex NPs, with Renca-LacZ cells being able to take up the highest amount, followed by 3T3 and Huh7.
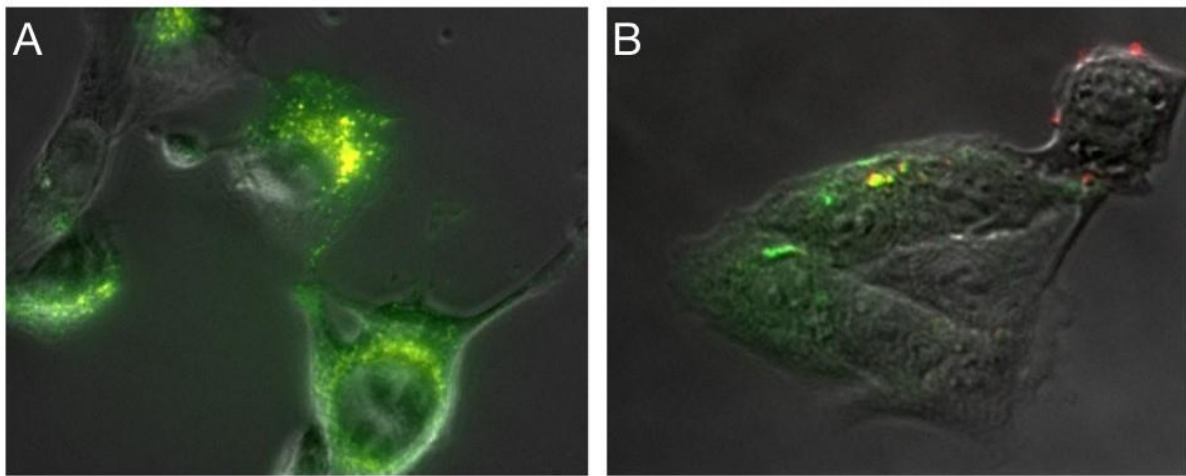
**Figure 3.9:** Uptake of MSNs in 3T3 cells **A)** appears to be higher than in Renca-LacZ **B)** after 12 hours of incubation with DOPC@MSN. Note that individual cells of the same type appear to take up a widely variable numbers of NPs. NPs (red) were incubated together with Alexa-Fluor Dextran 488 (green). NPs inside endosomes appear as yellow spots. Images are taken at 40x.
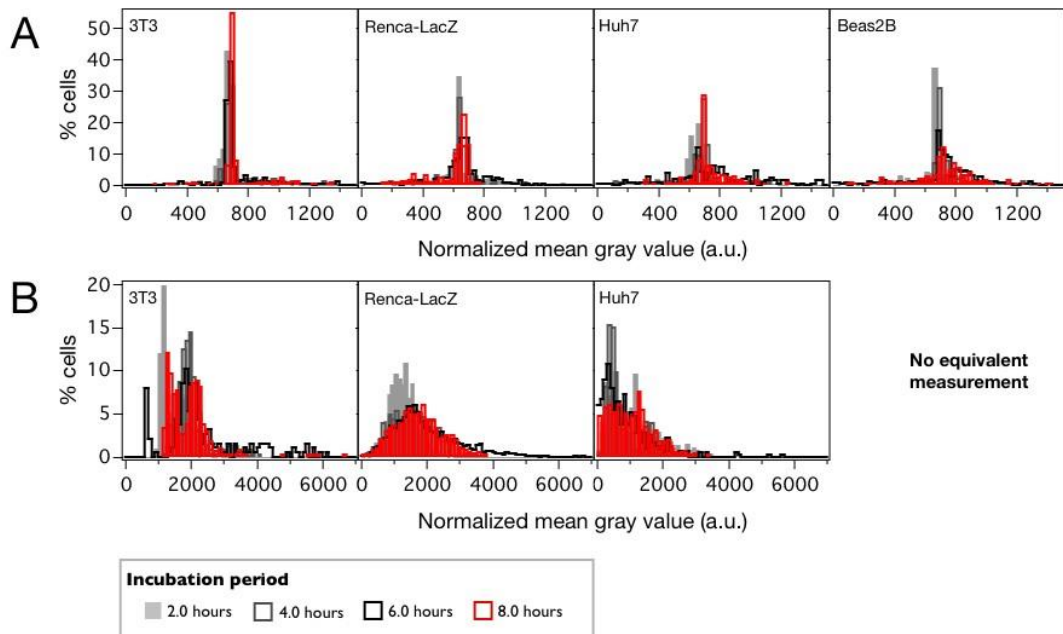


**Figure 3.10:** Cell type differences in reporter system uptake. Uptake of DOPC@MSN **A)** in 3T3, Renca-LacZ, Huh7 and Beas2B cells. The numbers of NPs taken up were approximated using the mean fluorescence intensity across a cell. A parallel experiment was performed using commercially available 30 nm latex nanoparticles **B)** for 3T3, Renca-LacZ and Huh7 cells.

**Table 3.2:** Selected Gauss fit parameters of cell-type specific NP uptake profiles at eight hours post-incubation.

| Sample | Activation time (min) | Mean |
|:---:|:---:|:---:|
| DOPC@MSN, 3T3 | $675.7 \pm 0.3$ | $17.2 \pm 0.2$ |
| DOPC@MSN, Renca-LacZ | $644.5 \pm 1.7$ | $41.7 \pm 2.4$ |
| DOPC@MSN, Huh7 | $673.9 \pm 1.2$ | $20.9 \pm 1.1$ |
| DOPC@MSN, Beas2B | $726.9 \pm 9.4$ | $132.5 \pm 14.3$ |
| Latex, 3T3 | $1314.1 \pm 29.9$ | $227.8 \pm 43.3$ |
| Latex, Renca-LacZ | $1603.54 \pm 19.3$ | $1065.7 \pm 31.6$ |
| Latex, Huh7 | $613.4 \pm 69.4$ | $1314.5 \pm 102.0$ |

It is not the first time that cell type uptake dependence for non-functionalized NPs was reported. Non-functionalized silver NPs, for instance, are taken up better by peripheral monocytes, but not by T-cell populations.[64] A recent paper also indicates that apart from uptake differences resulting from cell surface properties, there are also cell-type specific cytoplasmic and nuclear pore penetration constraints.[65] Our results, together with other recent reports on cell-type dependent uptake specificity, indicate the need to investigate this phenomenon more closely, and to take results as a consideration in NP design and dosage.

**Stochastic pi calculus model of endosomal escape.** We extended the gold NP model to be able to systematically study the factors that influence endosomal escape. For a release on-demand system such as PpIX, we expected a very narrow distribution of endosome lysis times. Considering the time window, which is two minutes post-PpIX activation, the spread is of course insignificant compared to non-release on-demand systems. However, what was striking is the disparity of the distributions in 3T3 and Renca cells. In order to check how much of the spread is caused by noise inherent to the reporter system, we added PpIX and Act_PpIX parameters to each NP, through which we can vary the PpIX load distribution per NP. As indicated in the methods section, we made the initial assumption that the NPs had a normally distributed PpIX load with a mean of 50, and a width of 5, which we changed in the course of the sensitivity analysis. For the first run, we also made the assumption that the binding and aggregation rates are the same as those used for gold NPs. Other parameters were also subjected to sensitivity analysis, results of which are summarized in Figure 3.11. Interestingly, the model is most sensitive to the minimum number of PpIX required to burst an endosome. Although the current version of SPiM does not permit us to dynamically create endosomes that are assigned

an unfixed size parameter (taken from a distribution as in Figure 3.11), this result is logical in that this minimum number is intimately linked with the NP load per endosome, as well as endosome size, which we have shown experimentally to be the main difference between the two cells.
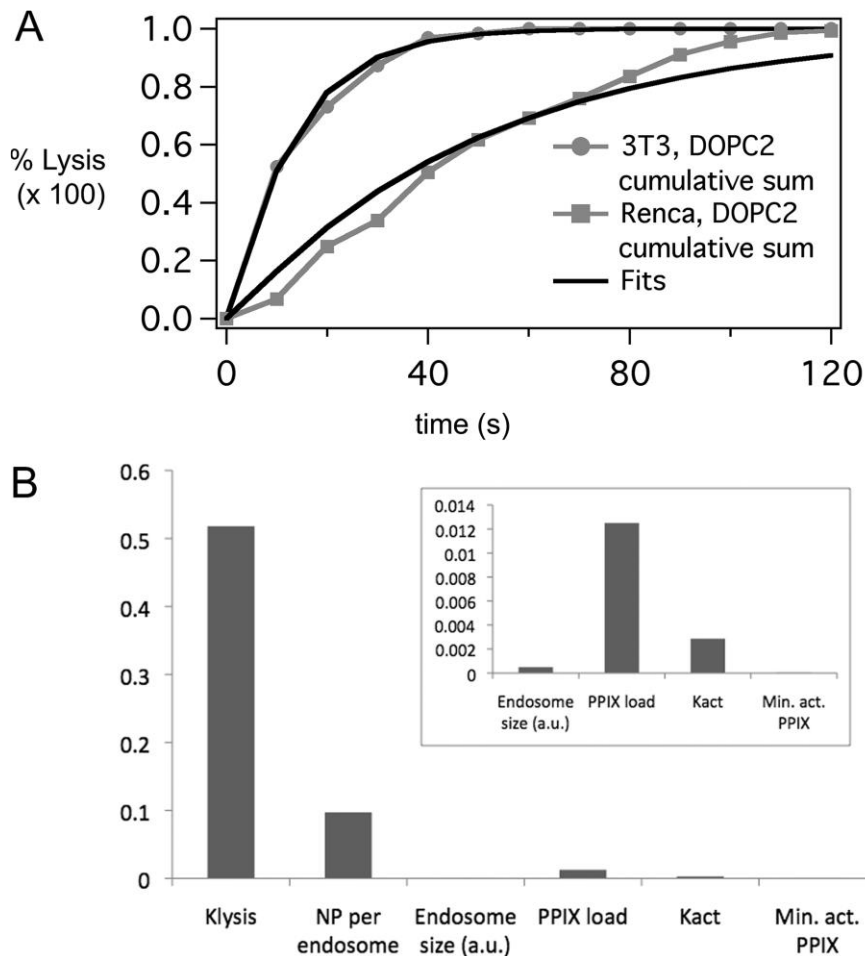


**Figure 3.11:** Fits of representative 3T3 and Renca data (DOPC-coated, 2-min PpIX activation) presented as a cumulative sum **(A)** and sensitivity analysis of the different model parameters **(B)** indicate that the cell associated parameter, klysis, causes most of the data spread, followed by the NP load per endosome. $k_{lysis}$ was assumed to decrease by a factor proportional to the endosome size, represented in arbitrary units (a.u.).

## 3.3 Conclusion

A reporter system based on colloidal mesoporous silica nanoparticles (MSNs) was developed. The MSNs were covalently modified with a blue-light sensitive photosensitizer, protoporphyrin IX (PpIX) and capped with a supported DOPC lipid bilayer (SLB). In this study, photochemical internalization (PCI) with an on-board photosensitizer and the redox-labile disulfide-bridge approach (of a corresponding dye-quencher system) was combined to create highly potent multifunctional MSNs as fluorimetric reporter vector. The photosensitizer allows to overcome endosomal entrapment through the formation of highly reactive singlet oxygen which is followed by the subsequent disintegration of both membranes in a cascaded manner. Endosomal uptake of the SLB-capped MSNs and individual endosome lysis events were studied in three different cell lines (a fibroblast, normal and carcinoma cell line). The release on-demand system resulted in more broadly distributed lysis times than expected, particularly for Renca, a renal carcinoma cell line. An analysis of the nanoparticle load per endosome, endosome size and uptake characteristics indicate that Renca cells not only take up a lower amount of NPs in comparison with the fibroblast cells, but also have larger endosomes, and a lower NP load per endosome. An existing stochastic pi calculus model of the gold nanoparticle intracellular distribution was extended to our reporter-system, enabling to understand how different factors (e.g. PpIX load per NP) affect the distributions. Model results indicate that the lysis time distribution is primarily determined by the minimum net PpIX required to burst an endosome, a factor influenced by the NP load per endosome, as well as the endosome size.

## 3.4 Experimental

*Chemicals.* Tetraethyl orthosilicate (TEOS, Fluka, >99%), (3-mercaptopropyl)-triethoxysilane (MPTES, Gelest, 95%), (3-aminopropyl)-triethoxysilane (APTES, Sigma, 98%), cetyltrimethylammonium chloride (CTAC, Fluka, 25wt% in $H_2O$), phenyltriethoxysilane (PhTES, Sigma, 98%), triethanolamine (TEA, Aldrich, 98%), Atto633-NHS ester (Atto-Tec), QSY21 succinimidyl ester (Invitrogen), tetrahydrofuran (THF, Acros, 99.8%), protoporphyrin IX (Sigma, >95%), *p*-phenylenediamine (Sigma, 95%), triethylamine (Sigma, 99%), ethyl chloroformate (Fluka, >98%), ammonium nitrate (Sigma, 99%), conc. hydrochloric acid (Aldrich, >95%, 37wt%) 1-maleinimido-3-oxo-7,10,13,16,19,22,25,28-octaoxa-4-azahentriacontan-31-oic acid (mal-dPEG(8)-COOH, Iris Biotech), sulfo-N-hydroxysuccinimide (sulfo-NHS, Aldrich, 98%), N-(3-dimethylaminopropyl)-N′-

ethylcarbodiimide (EDC, Sigma, 97%), toluene (Aldrich, 99.8 %), ethanol (EtOH, Aldrich, >99.5%), fluorescein disodium salt dihydrate (Acros, >95%), L-glutathione (Aldrich, >98%), 2,2'-dithiopyridine (DTP, Sigma, >99%), L-cysteine (Cys, Sigma, >97%), anhydrous N,N-dimethylformamide (DMF, Sigma, >99.8%). All chemicals were used as received without further purification. Doubly distilled water from a Millipore system (Milli-Q Academic A10) was used for all synthesis and purification steps. The lipids 1,2-dioleoyl-sn-glycero-3-phosphocholine (DOPC) and 1,2-Dioleoyl-sn-glycero-3-phospho-ethanolamine (DOPE) were purchased from Avanti polar lipids.

**Synthesis procedures**

**Synthesis of core-shell CMS_NH$_{2in}$_SH$_{out}$.** Bi-functional core-shell colloidal mesoporous silica was synthesized following the previously published method.[66] A mixture of TEOS (1.63 g, 9.22 mmol), PhTES (57 mg, 0.24 mmol), APTES (53.1 mg, 0.24 mmol) and TEA (14.3 g, 95.6 mmol) was heated at 90 °C for 20 min under static conditions in a polypropylene reactor. Then a solution of CTAC (25 % in water, 2.41 mL, 1.83 mmol) in water (21.7 g, 1.21 mol) was preheated to 60 °C and added quickly. The reaction mixture was stirred at room temperature for 20 minutes. TEOS (138.2 mg, 0.92 mmol) was added in four equal increments every three minutes. This step was followed by 30 minutes of stirring at room temperature. For the shell functionalization a mixture of TEOS (19.3 mg, 92.5 μmol) and MPTES (22 mg, 92.5 μmol) was added to the reaction. The resulting mixture was then allowed to stir at room temperature for 12 hours. After the addition of 100 mL ethanol, the MSNs were collected by centrifugation, re-dispersed in 100 mL of ethanol and extracted according to the procedure described below.

**Extraction of CMS_NH$_{2in}$_SH$_{out}$.** Extraction of the surfactant from the MSNs was performed by heating 250 mg for 45 minutes under reflux at 90 °C in a solution containing 2 g ammonium nitrate in 100 mL ethanol, followed by 45 minutes under reflux in a mixture of 4 g conc. hydrochloric acid (37 wt%) in 100 mL ethanol. The CMS nanoparticles were separated by centrifugation and washed with ethanol after each extraction step. MSN materials were obtained as colloidal suspensions.

**PEGylation of CMS_NH$_{2in}$_SH$_{out}$ with bi-functional Mal-PEG(8)-COOH to the sample CMS_NH$_{2in}$_PEG$_{out}$.** An ethanolic suspension containing 1 mg of CMS_NH$_2$_SH$_{out}$ was centrifuged and re-dispersed in 1 mL of water. This washing step was repeated twice. Next, the MSNs were suspended in 500 μL of water and 100 μL of a solution of Mal-dPEG(8)-COOH (10 mg/mL) was added under stirring. The reaction mixture was stirred for 48 hours at room temperature. In order to remove the excess of Mal-dPEG(8)-COOH, the particles were washed five times with 1 mL of water to remove unbound PEG. All washings steps were followed by centrifugation. Finally, the sample CMS_NH$_{2in}$_PEG$_{out}$ was re-dispersed in 500 μL ethanol.

**Synthesis of protoporphyrin-IX-bis(phenyleneaminoamide) (PpIX-NH$_2$).** Protoporphyrin-IX-bis(phenyleneaminoamide) was prepared according to a modified literature procedure.[43, 48] In a dry and darkened 100 mL three-neck flask, protoporphyrin-IX (100 mg, 0.178 mmol, 1 eq.) was dissolved in 20 mL anhydrous tetrahydrofuran and cooled to 0 °C under nitrogen atmosphere. Triethylamine (2.45 mL, 17.7 mmol, 100 eq.) was added with a syringe to the solution. Ethyl chloroformate (1.7 mL, 17.9 mmol, 100 eq.) was subsequently added over a time of 30 minutes via a dropping funnel. The resulting mixture **1** was stirred for 2 hours at 0 °C. In a second flask, finely powdered *p*-phenylene diamine (1.95 g, 17.9 mmol, 100 eq.) was dissolved in 10 mL anhydrous THF under nitrogen atmosphere. Mixture **1** was slowly added with a syringe. The resulting reaction mixture was stirred for 24 hours at room temperature in the dark. The solvent was removed *in vacuo*, the resulting precipitate suspended in 15 mL of ice-cold water. The precipitate was filtered off and washed three times with 15 mL of ice-cold water each. PpIX-NH$_2$ was obtained as a brown precipitate (85 mg, 0.114 mmol, 64%).

**Attachment of PpIX-NH$_2$ to CMS_NH$_{2in}$_PEG$_{out}$ to the sample CMS_NH$_{2in}$_PEG-PpIX$_{out}$.** 1 mg of CMS_NH$_{2in}$_PEG$_{out}$ was re-suspended in 1 mL THF before PpIX-NH$_2$ (2 mg, 2.7 μmol) was added. The mixture was stirred for 5 minutes. Subsequently, EDC (3.5 μL, 20 μmol) and *sulfo*-NHS (4.3 mg, 20 μmol) were added and the reaction was stirred for 14 hours in the dark. The sample was washed five times with 1 mL of THF to remove unbound PpIX-NH$_2$ and three times with a total amount of 3 mL water.

**Fluorescence labeling procedure for the amino group of L-cysteine (CysAtto633).** L-Cysteine (Cys, 1 mg, 8.25 μmol) was dissolved in 100 μL of freshly prepared 0.1 M sodium bicarbonate buffer (pH 8.3). Then, 10 μL (26.7 nmol) of a solution of Atto633-NHS (1 mg dissolved in 500 μL anhydrous DMF) was added. The large excess of Cys is intended to

minimize the amount of remaining free dye, since no purification of the product was performed. The resulting mixture was stirred for 2 hours in the dark to give CysAtto633.

**Attachment of Cys-Atto633 to the core of CMS_NH$_{2in}$_PEG-PpIX$_{out}$.** A solution of 1 mg Cys-Atto633 in water was added to a colloidal suspension of 1 mg CMS_NH$_{2in}$_PEG-PpIX$_{out}$ in water. The reaction mixture was stirred for 5 minutes in the dark before EDC (3.5 µL, 20 µmol) and *sulfo*-NHS (4.3 mg, 20 µmol) were added. The reaction was stirred for 14 hours in the dark. The sample was washed two times with 1 mL water and then five times with 1 mL ethanol each to remove unbound dye.

**Quencher QSY21 labeling procedure for the amino group of L-cysteine (CysQSY21).** L-Cysteine (Cys, 1 mg, 8.25 µmol) was dissolved in 100 µL of freshly prepared 0.1 M sodium bicarbonate buffer (pH 8.3). Then, 21.8 µL (26.7 nmol) of a solution of QSY21-NHS (1 mg/mL in anhydrous DMF) was added. The large excess of Cys is intended to minimize the amount of remaining free quencher, since no purification of the product was performed. The resulting mixture was stirred for 2 hours in the dark to give CysQSY21.

**Attachment of Cys-QSY21 via a disulfide bond to the Cys-Atto633 moiety in the core of CMS_NH$_{2in}$_PEG-PpIX$_{out}$.** 150 µL of an ethanolic suspension of the sample CMS_NH$_{2in}$_PEG-PpIX$_{out}$ containing 1 mg particles was adjusted to the total volume of 1 mL by adding 850 µL absolut ethanol. Then, 2,2'-dithiopyridine (DTP, 1 mg, 4.5 µmol) was added. The sample was stirred for 15 minutes in the dark. Three washing steps with 1 mL ethanol each were followed by subsequent centrifugation. The DTP-activated MSNs were re-suspended in 500 µL water and a solution containing 1 mg CysQSY21 in 100 µL water was added. The reaction mixture was stirred 14 hours in the dark. Unbound CysQSY21 was removed by five washing steps with 1 mL ethanol each.

**Fluorescence spectroscopy of the sample CMS_CysAtto633-QSY21Cys$_{in}$-_PEG-PpIX$_{out}$** Fluorescence spectroscopy was performed on a PTI spectrofluorometer with a photomultiplier detection system (model 810/814). The sample included 0.5 mg of the sample CMS_CysAtto633-QSY21Cys$_{in}$-_PEG-PpIX$_{out}$ suspended in 2 mL of water. GSH (2 mg, 6.51 µmol) was added under continuous stirring. The obtained spectra derived from excitation at 633 nm can be found in Figure 3.5.

**Characterization.** Centrifugation was performed using a Sorvall Evolution RC equipped with a SS-34 rotor or an Eppendorf centrifuge 5418 for small volumes (1.5 mL maximum). Dynamic light scattering (DLS) were performed on a Malvern Zetasizer-Nano instrument equipped with a 4 mW He-Ne laser (633 nm) and an avalanche photodiode. DLS measurements were directly recorded on ethanolic colloidal suspension at a constant concentration. Transmission electron microscopy (TEM) and Scanning TEM were performed on a FEI Titan 80-300 kV microscope operating at 300 kV. Nitrogen sorption measurements were performed on a Quantachrome Instruments NOVA 4000e. All three samples (15 mg each) were heated to 393 K for 12 h *in vacuo* to outgas the samples before nitrogen sorption was measured at 77 K. For calculations of pore sizes and volumes a non-local density functional theory (NLDFT) equilibrium model of nitrogen on silica was used. The Brunauer-Emmett-Teller (BET) model was applied to evaluate the surface areas. Fluorescence time-based release experiments were recorded on a PTI fluorescence system featuring a PTI 814 photomultiplier detector and a PTI A1010B Xenon arclamp driven by a PTI LPS-220B lamp power supply. For temperature settings, a Quantum Northwest TC 125 sample holder was used. Our previously described custom-made release cuvette system was employed for all experiments. All samples were measured at a temperature of 37 °C with slits of 1-1.2-1-1-1.

## 3.5 Appendix
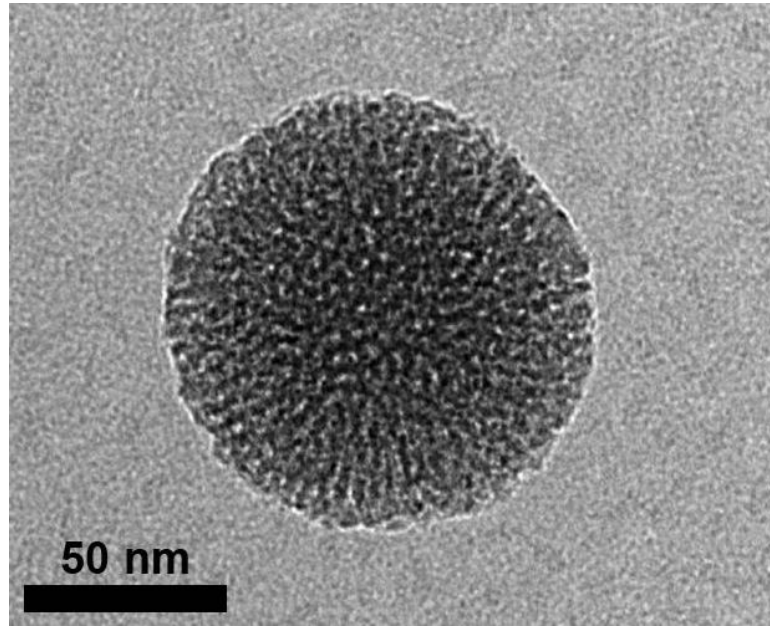


**Figure 3.12:** Transmission electron micrograph of the multifunctional MSNs (sample CMS_NH$_{2in}$_SH$_{out}$).
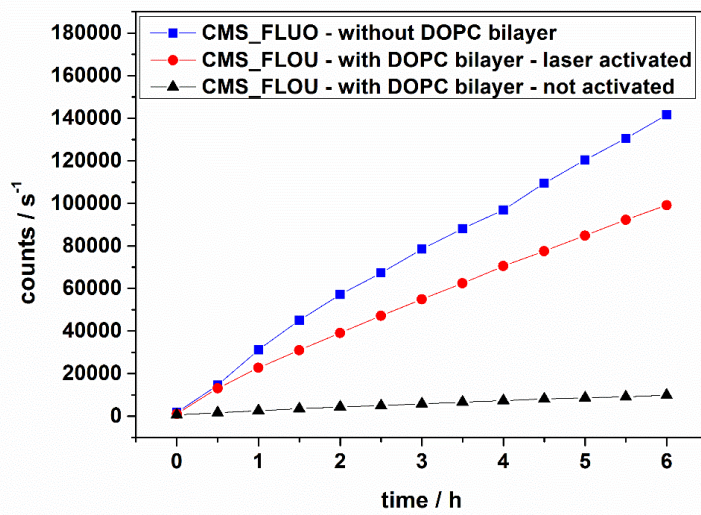


**Figure 3.13:** Time-based fluorescence release curves with fluorescein as cargo for the MSN samples CMS_NH$_{2in}$_PEG-PpIX$_{out}$ (blue), laser activated DOPC@CMS_NH$_{2in}$_SH$_{out}$ (red) and tightly capped, non-activated DOPC@CMS_NH$_{2in}$_SH$_{out}$ (black).

## 3.6   References

1.      Douglas, K. L. *Biotechnol. Prog.* **2008**, *24*, 871-883.

2.      Varga, C. M.; Tedford, N. C.; Thomas, M.; Klibanov, A. M.; Griffith, L. G.; Lauffenburger, D. A. *Gene Ther.* **2005**, *12*, 1023-1032.

3.      Jin, H.; Heller, D. A.; Strano, M. S. *Nano Lett.* **2008**, *8*, 1577-1585.

4.      Akita, H.; Ito, R.; Khalil, I. A.; Futaki, S.; Harashima, H. *Mol. Ther.* **2004**, *9*, 443-451.

5.      Chen, H. H.; Ho, Y.-P.; Jiang, X.; Mao, H.-Q.; Wang, T.-H.; Leong, K. W. *Mol. Ther.* **2008**, *16*, 324-332.

6.      Hama, S.; Akita, H.; Ito, R.; Mizuguchi, H.; Hayakawa, T.; Harashima, H. *Mol. Ther.* **2006**, *13*, 786-794.

7.      Brabec, M.; Schober, D.; Wagner, E.; Bayer, N.; Murphy, R. F.; Blaas, D.; Fuchs, R. *J. Virol.* **2005**, *79*, 1008-1016.

8.      Brandenburg, B.; Zhuang, X. *Nat. Rev. Microbiol.* **2007**, *5*, 197-208.

9.      Rust, M. J.; Lakadamyali, M.; Brandenburg, B.; Zhuang, X. *Cold Spring Harb. Protoc.* **2011**, *2011*.

10.     Brandenburg, B.; Zhuang, X. *Nat. Rev. Microbiol.* **2007**, *5*, 197-208.

11.     Schwake, G.; Youssef, S.; Kuhr, J.; Gude, S.; David, M.; Mendoza, E.; Frey, E.; Rädler, J. O. *Biotechnol. Bioeng.* **2009**, *105*, 805-813.

12.     Chen, H. H.; Ho, Y. P.; Jiang, X.; Mao, H. Q.; Wang, T. H.; Leong, K. W. *Mol. Ther.* **2008**, *16*, 324-332.

13.     Radin, S.; El-Bassyouni, G.; Vresilovic, E. J.; Schepers, E.; Ducheyne, P. *Biomaterials* **2005**, *26*, 1043-1052.

14.     Kortesuo, P.; Ahola, M.; Karlsson, S.; Kangasniemi, I.; Yli-Urpo, A.; Kiesvaara, J. *Biomaterials* **2000**, *21*, 193-198.

15.     Möller, K.; Kobler, J.; Bein, T. *Adv. Funct. Mater.* **2007**, *17*, 605-612.

16.     Kecht, J.; Schlossbauer, A.; Bein, T. *Chem. Mater.* **2008**, *20*, 7207-7214.

17.     Cauda, V.; Schlossbauer, A.; Kecht, J.; Zürner, A.; Bein, T. *J. Am. Chem. Soc.* **2009**, *131*, 11361-11370.

18.     Muhammad, F.; Guo, M.; Qi, W.; Sun, F.; Wang, A.; Guo, Y.; Zhu, G. *J. Am. Chem. Soc.* **2011**, *133*, 8778-8781.

19.     Argyo, C.; Cauda, V.; Engelke, H.; Rädler, J.; Bein, G.; Bein, T. *Chem. Eur. J.* **2012**, *18*, 428-432.

20.     Rosenholm, J. M.; Meinander, A.; Peuhu, E.; Niemi, R.; Eriksson, J. E.; Sahlgren, C.; Lindén, M. *ACS Nano* **2009**, *3*, 197-206.

21.   Zhao, W.; Zhang, H.; He, Q.; Li, Y.; Gu, J.; Li, L.; Li, H.; Shi, J. *Chem. Commun.* **2011**, *47*, 9459-9461.

22.   Cauda, V.; Argyo, C.; Bein, T. *J. Mater. Chem.* **2010**, *20*, 8693-8699.

23.   He, Q.; Zhang, J.; Shi, J.; Zhu, Z.; Zhang, L.; Bu, W.; Guo, L.; Chen, Y. *Biomaterials* **2010**, *31*, 1085-1092.

24.   Xia, T.; Kovochich, M.; Liong, M.; Meng, H.; Kabehie, S.; George, S.; Zink, J. I.; Nel, A. E. *ACS Nano* **2009**, *3*, 3273-3286.

25.   Kim, J.; Kim, H. S.; Lee, N.; Kim, T.; Kim, H.; Yu, T.; Song, I. C.; Moon, W. K.; Hyeon, T. *Angew. Chem. Int. Ed.* **2008**, *47*, 8438-8441.

26.   Ogris, M.; Brunner, S.; Schüller, S.; Kircheis, R.; Wagner, E. *Gene Ther.* **1999**, *6*, 595-605.

27.   Cauda, V.; Schlossbauer, A.; Bein, T. *Microporous Mesoporous Mater.* **2010**, *132*, 60-71.

28.   Cauda, V.; Engelke, H.; Sauer, A.; Arcizet, D.; Bräuchle, C.; Rädler, J.; Bein, T. *Nano Lett.* **2010**, *10*, 2484-2492.

29.   Giri, S.; Trewyn, B. G.; Lin, V. S. Y. *Nanomedicine*  **2007**, *2*, 99-111.

30.   Yang, P.; Gai, S.; Lin, J. *Chem. Soc. Rev.* **2012**, *41*, 3679.

31.   Lee, C. H.; Cheng, S. H.; Huang, I. P.; Souris, J. S.; Yang, C. S.; Mou, C. Y.; Lo, L. W. *Angew. Chem. Int. Ed.* **2010**, *49*, 8214-8219.

32.   Lu, J.; Liong, M.; Sherman, S.; Xia, T.; Kovochich, M.; Nel, A. E.; Zink, J. I.; Tamanoi, F. *Nanobiotechnology* **2007**, *3*, 89-95.

33.   Giri, S.; Trewyn, B. G.; Lin, V. S. Y. *Nanomedicine* **2007**, *2*, 99-111.

34.   Yang, P.; Gai, S.; Lin, J. *Chem. Soc. Rev.* **2012**, *41*, 3679-3698.

35.   Lai, C.-Y.; Trewyn, B. G.; Jeftinija, D. M.; Jeftinija, K.; Xu, S.; Jeftinija, S.; Lin, V. S.-Y. *J. Am. Chem. Soc.* **2003**, *125*, 4451-9.

36.   Meng, H.; Xue, M.; Xia, T.; Zhao, Y.-L.; Tamanoi, F.; Stoddart, J. F.; Zink, J. I.; Nel, A. E. *J. Am. Chem. Soc.* **2010**, *132*, 12690-12697.

37.   Khashab, N. M.; Trabolsi, A.; Lau, Y. A.; Ambrogio, M. W.; Friedman, D. C.; Khatib, H. A.; Zink, J. I.; Stoddart, J. F. *Eur. J. Org. Chem.* **2009**, *2009*, 1669-1673.

38.   Ambrogio, M. W.; Pecorelli, T. A.; Patel, K.; Khashab, N. M.; Trabolsi, A.; Khatib, H. A.; Botros, Y. Y.; Zink, J. I.; Stoddart, J. F. *Org. Lett.* **2010**, *12*, 3304-3307.

39. Radu, D. R.; Lai, C.-Y.; Jeftinija, K.; Rowe, E. W.; Jeftinija, S.; Lin, V. S. Y. *J. Am. Chem. Soc.* **2004**, *126*, 13216-13217.

40. Gan, Q.; Lu, X.; Yuan, Y.; Qian, J.; Zhou, H.; Shi, J.; Liu, C. *Biomaterials* **2011**, *32*, 1932-1942.

41. Mal, N. F., M; Tanaka, Y. *Nature* **2003**, *421*, 350-353.

42. Schlossbauer, A.; Sauer, A. M.; Cauda, V.; Schmidt, A.; Engelke, H.; Rothbauer, U.; Zolghadr, K.; Leonhardt, H.; Bräuchle, C.; Bein, T. *Adv. Healthcare Mater.* **2012**, *1*, 316-320.

43. Sauer, A. M.; Schlossbauer, A.; Ruthardt, N.; Cauda, V.; Bein, T.; Bräuchle, C. *Nano Lett.* **2010**, *10*, 3684-3691.

44. Cardelli, L.; Phillips, A. *Procs. BioConcur* **2004**, *90*.

45. Gillespie, D. T. *J. Phys. Chem.* **1977**, *81*, 2340–2361.

46. Maziere, J. C.; Santus, R.; Morliere, P.; Reyftmann, J. P.; Candide, C.; Mora, L.; Salmon, S.; Maziere, C.; Gatt, S.; Dubertret, L. *J. Photochem. Photobiol. B, Biol* **1990**, *6*, 61-68.

47. Sahoo, S. K.; Sawa, T.; Fang, J.; Tanaka, S.; Miyamoto, Y.; Akaike, T.; Maeda, H. *Bioconjugate Chem.* **2002**, *13*, 1031-1038.

48. Khalil, I. A.; Kogure, K.; Akita, H.; Harashima, H. *Pharmacol. Rev.* **2006**, *58*, 32-45.

49. Hohner, A. O.; David, M. P. C.; Rädler, J. O. *Biointerphases* **2010**, *5*, 1-8.

50. Hafez, I. M.; Cullis, P. R. *Adv. Drug Delivery Rev.* **2001**, *47*, 139-148.

51. Koltover, I.; Salditt, T.; Rädler, J. O.; Safinza, C. R. *Science* **1998**, *281*, 78-81.

52. Bailey, A. L.; Cullis, P. R. *Biochemistry* **1997**, *36*, 1628-1634.

53. Rejman, J.; Oberle, V.; Zuhorn, I. S.; Hoekstra, D. *Biochemical Journal* **2004**, 1, 159-169.

54. Cauda, V.; Engelke, H.; Sauer, A.; Arcizet, D.; Rädler, J.; Bein, T. *Nano Lett.* **2010**, *10*, 2484-2492.

55. Liu, J.; Stace-Naughton, A.; Jiang, X.; Brinker, C. J. *J. Am. Chem. Soc.* **2009**, *131*, 1354-1355.

56. Hed, J.; Hallden, G.; Johansson, S.; Larsson, P. *J. Immunol. Methods* **1987**, *101*, 119-125.

57. Xiao, J., *Handbook of Single-Molecule Biophysics*. Springer: New York, **2009**.

58. Youssef, S.; Gude, S.; Rädler, J. O. *Integr. Biol.* **2011**, *3*, 1095-1101.

59. Dobay, M. P.; Dobay, A.; Bantang, J.; Mendoza, E. *Molecular bioSystems* **2011**, *7*, 2741-2749.

60.     Li, G.; Qian, H. *Traffic* **2002**, *3*, 249-255.

61.     Li, Y.; Meng, X.; Feng, H.; Zhang, G.; Liu, C.; Li, P. *Chin. Med. Sci. J.* **1999**, *14*, 96-101.

62.     Duclos, S.; Diez, R.; Garin, J.; Papadopoulou, B.; Descoteaux, A.; Stenmark, H.; Desjardins, M. *J. Cell Science* **2000**, *113*, 3531 - 3541.

63.     Greulich, C.; Diendorf, J.; Geßmann, J.; Simon, T.; Habijan, T.; Eggeler, G.; Schildhauer, T. A.; Epple, M.; Köller, M. A*cta Biomater.* **2011**, *7*, 3505-3514.

64.     Williams, Y.; Sukhanova, A.; Nowostawska, M. G.; Davies, A. M.; Mitchell, S.; Oleinikov, V.; Gun'ko, Y.; Nabiev, I.; Kelleher, D.; Volkov, Y. *Small* **2009**, *5*, 2581-2588.

65.     Cauda, V.; Schlossbauer, A.; Kecht, J.; Zürner, A.; Bein, T. *J. Am. Chem. Soc.* **2009**, *131*, 11361-11370.

# 4 Targeted Drug Delivery in Cancer Cells with Red Light Photoactivated Mesoporous Silica Nanoparticles

This chapter is based on the following publication:
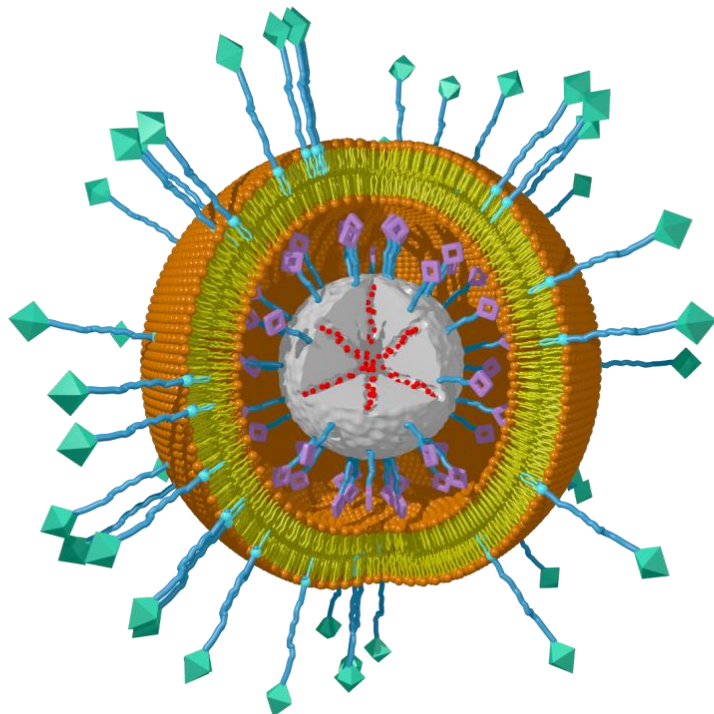
## Abstract

The development of mesoporous nanoparticles for drug delivery has made significant progress, but improvements are still necessary regarding targeting efficiency and endosomal release. We present a system based on colloidal mesoporous silica nanoparticles with targeting ligands and a covalently attached red-light photosensitizer. This nanoparticle system provides spatial and temporal control of the release of the model drug into the cytosol of cancer cells. The system can be loaded with different cargos within a certain size range and adapted for multiple cancer cell types in regard to their overexpressed receptors.

## 4.1 Introduction

The delivery of large amounts of cancer therapeutics specifically into the cytosol of cancer cells still faces significant challenges. Promising approaches in the field of drug delivery encompass the utilization of various types of nanoparticles such as polyplexes,[1-3] dendrimers,[4-6] gold nanoparticles,[7] and colloidal mesoporous silica (CMS, also named mesoporous silica nanoparticles, MSNs).[8-11] Each of these systems has its inherent advantages and disadvantages. Usually, they are either optimized for specific uptake by cancer cells, amount of cargo delivered, release of cargo into the cytosol or ease of synthesis of the system itself. However, often they do not perform well in all of these required areas. Notably, release of the drug from the endosome poses a significant hurdle on the way towards drug delivery with high efficacy. In this paper, we will present a system that provides solutions for all of these aspects. In particular, a photoactivatable drug delivery system, based on core-shell colloidal mesoporous silica nanoparticles (MSNs) will be employed, which allows exact spatial and temporal control of the release of the cargo from both the MSN and the endosome.[12-14] Core-shell MSNs are more suitable than regular MSNs for this task because they can have different functionalization in the core and the shell. This allows to optimize the core functionalization, e.g. for cargo uptake or covalent binding of the cargo to the core by disulfide bridges.[15] Moreover, the surface functionalization can be chosen to implement various gating mechanisms, such as surrounding the MSNs with a lipid bilayer to enclose the cargo in it.[13, 16] Previously, our groups published a photoactivatable drug delivery system performing most of the above-mentioned tasks well.[16] The current system is improved in 3 key areas. The used photosensitizer (PS) is activated by red light instead of blue light, the synthesis is significantly simplified and targeting ligands have now been added to the system. The function of the photosensitizer is to solve the problem of endosomal entrapment. Other approaches addressing this issue such as taking advantage of the proton sponge effect,[17-19] employing fusogenic or endosomolytic peptides[20-23] and others have been used.[24] There, the endosomal escape occurs at a less defined time point and for all particles regardless of their location in healthy or cancerous cells. In contrast, the photoactivation approach offers a solution for both of these shortcomings by initiating the cargo release through an external stimulus in form of a laser beam. The laser beam can be directed into the cancer tissue and activated at the right time point. The activation of the photosensitizer with red light instead of blue light reduces the phototoxicity and significantly increases the depth of tissue penetration,[25] which will be crucial when activation *in vivo* is required as shown by the Kataoka

group.[26] In comparison to regular photochemical internalization and other photoactivatable systems our system exhibits specific uptake by cancer cells due to the presence of targeting ligands. Schlossbauer *et al.*[16] presented MSNs with photosensitizers that allowed free choice and controlled release of the cargo. However, the issue of the targeting capability of the system was not addressed. Febvay *et al.*[27] used MSNs with photosensitizers in their studies as well, but the cargo had the role of the photosensitizer, i.e. the cargo selection was very limited. Moreover, the photosensitizer, i.e. cargo, was covalently bound to the MSN core and hence a suitable release mechanism was not present. In the current approach, we covalently link the photosensitizer molecule (PS) to the MSN surface and encapsulate the MSN with a supported lipid bilayer (SLB) to retain the drug. This allows for choosing a drug different from the PS and implementing a gating mechanism as well. Furthermore, the targeting mechanism presented by Febvay *et al.* was based on a streptavidin coated nanoparticle and a cell surface that was stained with the antibody P-gp.[27] While this demonstrates the targeting effect in principle, this specific targeting system is rather rare for cancer cells. Here we introduce the choice between two targeting ligands to our MSNs namely folic acid (FA) and epidermal growth factor (EGF), where both are relevant for cancer cells. For this purpose, targeting ligands (TL) are inserted into the SLB by diffusion to achieve specific uptake of the drug delivery vehicle by cancer cells. In the following, we will first discuss the synthesis and characteristics of our drug delivery system. Subsequently, live cell microscopy studies will be presented to evaluate the functionality of the employed targeting ligands and the release of the cargo from the MSNs by photoactivation.

## 4.2   Results and Discussion

**Synthesis and characterization of the drug delivery vehicle.**

The core-shell MSN were synthesized via a modified sol-gel method using tetraethyl orthosilicate (TEOS) as silica source and CTAC as pore template.[14] Kruk and co-workers showed the positive effect of ammonium fluoride on the particle morphology and pore size enlargement by employing 1,3,5-triisopropylbenzene (TiPB) as micellar expander for  the synthesis of SBA-15.[28, 29] A distinct amount of both components was introduced into the core-shell MSN synthesis (cf. experimental). The MSN core was functionalized with thiol groups and the surface with cyano groups, allowing for various post-synthesis modifications.
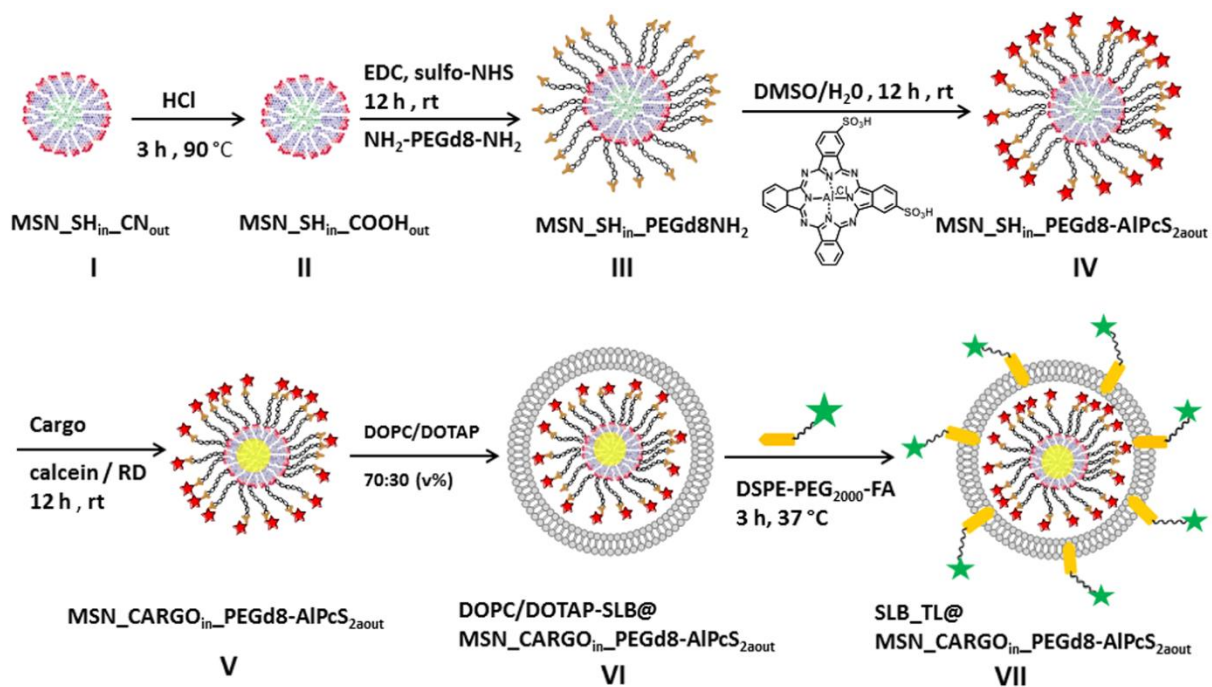
**Figure 4.1:** Synthesis pathway of core (green) shell (red) MSN with covalently linked AlPcS$_{2a}$ (red star) via PEG linker (black chain), and surrounded by DOPC/DOTAP supported lipid bilayer with targeting ligand (green star, TL). Before the formation of the SLB, the MSN core is loaded with a cargo (yellow), in our case calcein or a rhodamine derivative. Drawing is not to scale.

In the first reaction step, the surface cyano-groups of the MSN (**I**) are hydrolyzed to carboxyl groups (**II**), and subsequently the PEG linker is attached to the MSN surface via EDC amidation (**III**). To promote endosomal escape and subsequent delivery of the cargo into the cytosol, we employ a photoactivation approach. Therefore, a red-light sensitive photosensitizer, aluminum phthalocyanine disulfonate (AlPcS$_{2a}$), is covalently linked to the surface of the MSN via an octamer PEG linker. The PEG linker is functionalized with amino groups on both ends.
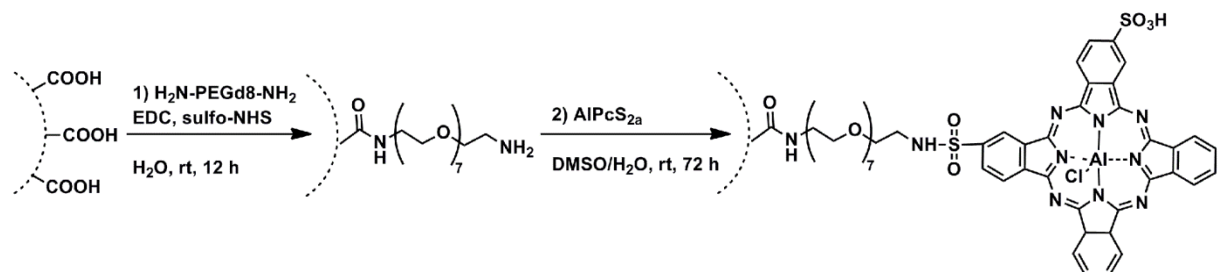


**Figure 4.2:** Shell reactions of MSN_SH$_{in}$_COOH$_{out}$ nanoparticles. 1) PEGylation reaction and 2) covalent attachment of photosensitizer AlPcS$_{2a}$.

The transmission electron microscope (TEM) image of the MSNs (species **I** in Figure 4.1) shows spherical particles with a mean diameter of 70 nm (Figure. 4.3a and cf. appendix 4.12). The mesoporous channel structure radiating from the particle center is apparent in the micrograph. It was proven that the conversion of the cyano-moieties to carboxy-groups and the subsequent PEGylation does not lead to a destruction of the mesostructure (cf. appendix 4.13). From dynamic light scattering (DLS) a mean particle size of 69 nm was obtained. In particular, it appears that the presence of carboxyl- or sulfonyl groups, either directly on the MSN surface or on the AlPcS$_{2a}$, results in an increase of the effective particle size (red circles and blue inverse triangles in Figure 4.3b, respectively). In contrast, the presence of PEG molecules on the MSN surface as well as the presence of the SLB results in a decrease of the effective particle size (green triangles and cyan diamonds in Figure 4.3b). In both cases, the origin of the size decrease can be attributed to the weaker interactions between the particles caused by steric or electrostatic stabilization.
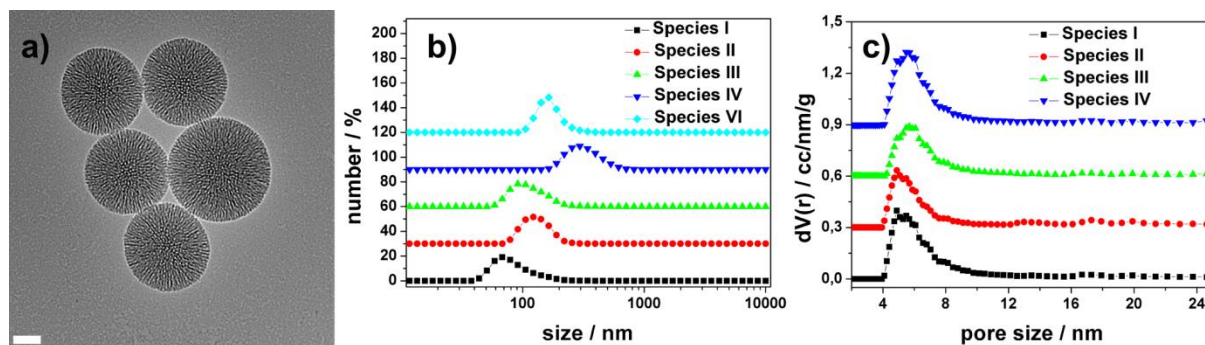


**Figure 4.3: a)** The TEM image shows bare MSN (I). The scale bar is 20 nm. **b)** Particle sizes of species I – VI in Figure 4.1 obtained by DLS measurements. All curves, except of MSN_SH$_{in}$_CN$_{out}$, are shifted by a value of 22 along the y-axis for clarity reasons. **c)** Pore size distributions of species I – IV. The exact values of the maxima are given in Table 4.1. Data are shifted by a value of 0.3 along the y-axis for clarity reasons.

The nitrogen sorption isotherms of the samples MSN_SH$_{in}$_CN$_{out}$ (**I**, black squares), MSN_SH$_{in}$_COOH$_{out}$ (**II**, red circles), MSN_SH$_{in}$_PEGd8NH$_{2out}$ (**III**, green up triangles), and MSN_SH$_{in}$_PEGd8-AlPcS$_{2aout}$ (**IV**, blue inverted triangles) can be seen in Figure 4.4, exhibiting typical type IV isotherms for mesoporous materials. The Brunauer-Emmett-Teller (BET) surface areas for each sample are calculated from the corresponding nitrogen sorption isotherm in the range p/p$_0$ = 0.05 − 0.2 and are summarized in Table 4.1. All samples feature a high specific surface area typical for our MSN. We assume that the reduced BET surface area in the

sample MSN_SH$_{in}$_COOH$_{out}$ (**II**) in comparison with MSN_SH$_{in}$_CN$_{out}$ (**I**) comes from the more condensed silica network and pore shrinkage resulting from the hydrolysis of the cyano-moiety in hydrochloric acid. The decrease of the specific surface area in the sample MSN_SH$_{in}$_PEGd8NH2$_{out}$ (**III**) can be explained by the addition of non-porous PEG and the blocking of some pores by frozen PEG-linker in the surface layer of the MSN. This effect is relatively small due to the short length of the flexible spacer. In contrast, the BET surface area of the sample MSN_SH$_{in}$_PEGd8-AlPcS$_{2aout}$ is with 918 m$^2$/g significantly higher than the BET surface area for MSN_SH$_{in}$_COOH$_{out}$ (**II**) and MSN_SH$_{in}$_PEGd8NH2$_{out}$ (**III**). We suppose that this effect comes from interstitial pore volume occurring upon attachment of AlPcS$_{2a}$ onto the particle shell. Considering phthalocyanines are large, sterically hindered molecules that lack the flexibility of a PEG-linker, a covalent attachment of them to the MSN surface will result in voids at liquid nitrogen temperatures. The mean pore size of MSN_SH$_{in}$_CN$_{out}$ was calculated to 5.2 nm, indicating the successful employment of the micellar expander (black squares in Figure 4.3c). This value is an enlargement of 25% compared to our standard MSNs. The pore size distributions for the post-synthesis functionalized samples derived from NLDFT calculations are given in Figure 4.3c and the values are summarized in Table 4.1. The pore size changes little upon PEGylation and photosensitizer attachment, indicating that the mesopores are still accessible for guest molecules. Furthermore, it proves the selective functionalization of the particle shell.
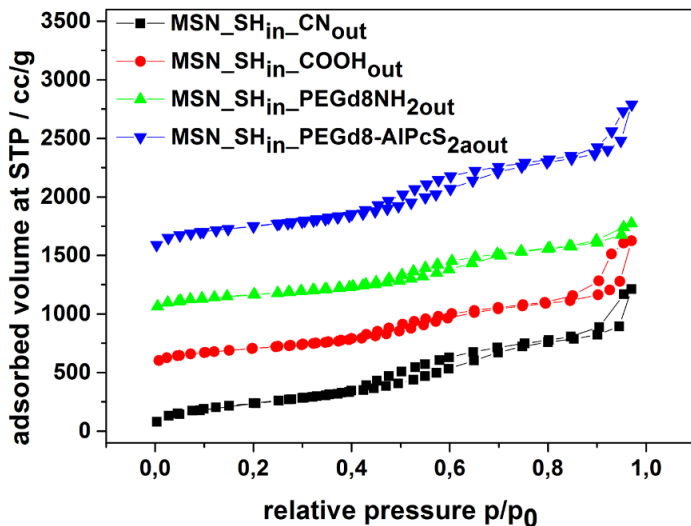
**Figure 4.4:** Nitrogen sorption isotherms for the samples MSN_SH$_{in}$_CN$_{out}$ (black squares), MSN_SH$_{in}$_COOH$_{out}$ (red circles), MSN_SH$_{in}$_PEGd8NH$_{2out}$ (green up triangles) and MSN_SH$_{in}$_PEGd8-AlPcS$_{2aout}$ (blue down triangles). For clarity reasons curves for MSN_SH$_{in}$_COOH$_{out}$, MSN_SH$_{in}$_PEGd8NH$_{2out}$, and MSN_SH$_{in}$_PEGd8-AlPcS$_{2aout}$ are shifted along the y-axis by a value of 500 each.

The $^{13}$C solid state NMR (ssNMR) shows the successful implementation of these three steps (Figure 4.5a). The resonance of the carboxyl group appears at 180 ppm upon hydrolysis of the cyano-groups (red trace in Figure 4.5a). Following EDC amidation, the carboxyl group disappears and the C-O and CH$_2$ resonances, both from the PEG linker, appear at 70 and 42 ppm, respectively (green trace in Figure 4.5a). The other resonances originate from the functionalized silanes of the MSNs. The different surface functionalization, including the attachment of the PEG linker, are apparent in the final relative mass levels of the thermogravimetric analysis (TGA) curves as well (Figure 4.5b and Table 4.1). Species **III** with the PEG linker has a significantly greater mass loss than species **I** and **II**. The slightly lower mass loss of species **II** in comparison to species **I**, originates from a more stable silica network that is formed during the 3 h heating in HCl, where the cyano is converted to carboxylic acid groups. The more stable silica network is apparent from the reduced BET surface area, as measured by N$_2$ sorption experiments, as well (isotherms shown in Figure 4.4). Subsequently, AlPcS$_{2a}$ is attached to the free remaining amino group of the PEG linker by linking the PEG-NH$_2$ group with one of the two sulfonate groups of AlPcS$_{2a}$ (**IV**). The PEG linker is required here because direct attachment of the AlPcS$_{2a}$ to the MSN surfaces results in a significantly reduced pore accessibility and particle aggregation. The successful attachment of

$AlPcS_{2a}$ is inferred from the IR spectrum (Figure 4.7) and the TGA (blue curve in Figure 4.5b). The mass loss for species **IV** is comparably large due to the high molecular mass of $AlPcS_{2a}$. In particular, the ratio of the mass loss going from species **III** to **IV** and from species **II** to **III** is 2. This can be related to the molecular mass ratio of the PS and the PEG, which is 2 as well.

To utilize the above multifunctional nanoparticles as drug delivery vehicles, a cargo was loaded into the MSN pores and the entire nanoparticle was enclosed by a supported lipid bilayer to prevent premature release of the cargo from the MSN core. The cargo was loaded into the MSN by incubating them in a concentrated solution of the cargo overnight. Afterwards, the SLB was formed around the nanoparticle via the solvent exchange method as published by Cauda *et al.*[13] The SLB consists of a lipid mixture of 70 v% of 1,2-dioleoyl-sn-glycero-3-phosphocholine (DOPC) and 30 v% of 1,2-dioleoyl-3-trimethylammonium-propane (DOTAP). We note that the length of the PEG linker, as described above, should not be too long because otherwise the formation of the SLB around the nanoparticle can be difficult. The DLS data (Figure 4.2b) show that the modifications of the MSN surface, the attachment of the PEG linker, the linking of the photosensitizer, and the formation of the 70 v% DOPC / 30 v% DOTAP shell (SLB) result in colloidal systems with slightly varying hydrodynamic particle sizes (Figure 4.3b and Table 4.1). We note that the hydrodynamic sizes can also reflect a weak agglomeration behavior.
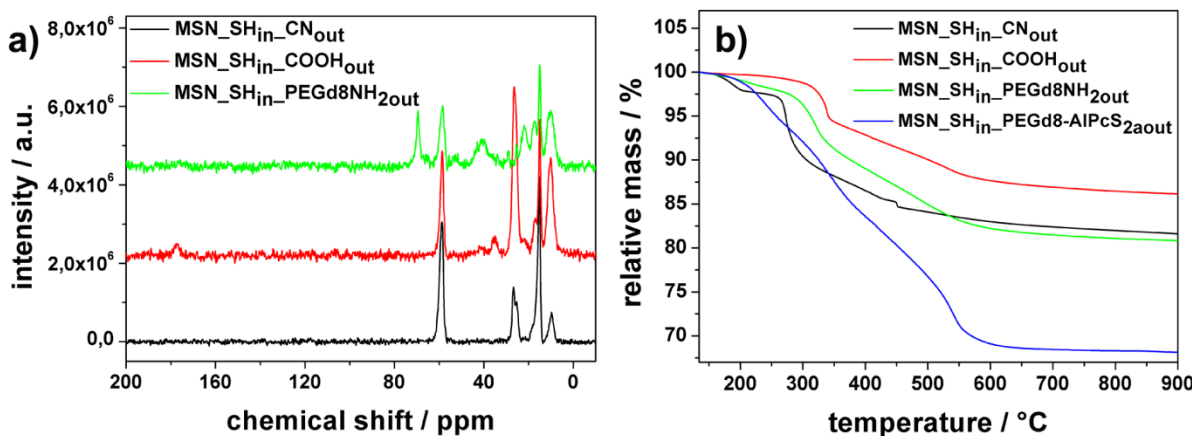


**Figure 4.5: a)** Solid state $^{13}$C NMR spectra of species **I – III.** It shows the successful conversion of the surface cyano-groups to carboxyl groups and the subsequent linkage of the $PEG_8$ linker to the MSN shell. Spectra for $MSN\_SH_{in}\_COOH_{out}$ (red) and $MSN\_SH_{in}\_PEGd8NH_{2out}$ (green) are shifted by a value of $2 \cdot 10^6$ each for clarity reasons. **b)** Thermogravimetric analysis of species **I – IV.** The relative mass losses are given in Table 4.1.

The cyanopropyl-groups of the sample MSN_SH$_{in}$_CN$_{out}$ (**I**, black squares) are uncharged at high or low pH values, resulting in a zeta potential curve that is similar to the one of unfunctionalized MSN (Figure 4.6). The successful attachment of NH$_2$-PEGd8-NH$_2$ to the sample MSN_SH$_{in}$_COOH$_{out}$ results in a higher zeta potential value due to protonation of the amino groups at low pH values (green). The sample MSN_SH$_{in}$_PEGd8_AlPcS$_{2aout}$ (**IV**) couldn't be measured because the laser wavelength of 633 nm leads to an excitation of the photosensitizer, resulting in oxygen production with bubble formation on the electrode. Shorter measurement times did not lead to sufficient results.
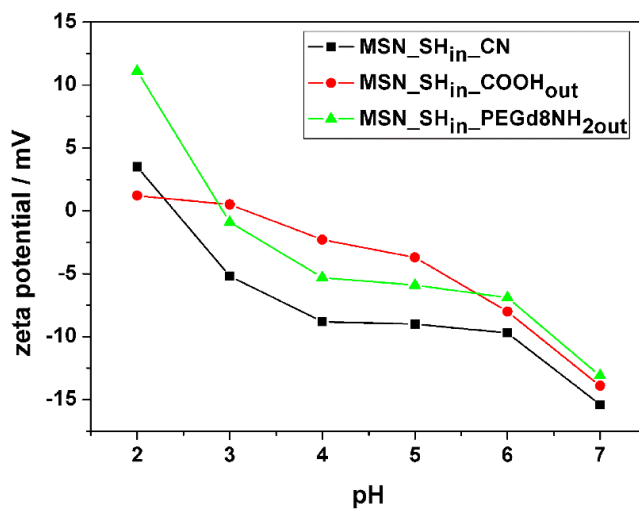


**Figure 4.6:** Zeta potential measurements of the samples MSN_SH$_{in}$_CN$_{out}$ (black squares), MSN_SH$_{in}$_COOH$_{out}$ (red circles), MSN_SH$_{in}$_PEGd8NH$_{2out}$ (green up triangles).

In order to prove the functionality of our designed MSN carrier system, IR spectroscopy was carried out (Figure 4.7). The CH$_2$ stretching vibrations of the organic functionality (mercaptopropyl- and cyanopropyl) are visible between 2800 cm$^{-1}$ and 2850 cm$^{-1}$. Furthermore, several peaks at 2900 cm$^{-1}$ (C-H stretching vibrations) and at 1400 cm$^{-1}$ (C-H bending vibrations) are visible. The intensity of these vibrations decreases after the carboxylation of the cyanide groups. Further condensation of the silica framework was achieved through the hydrolysis of the cyano-moiety and therefore the content of ethoxygroups was reduced. The cyanide vibration at 2253 cm$^{-1}$ for the species **I** disappears completely after hydrolysis while the new -COOH vibration at 1707 cm$^{-1}$ (MSN_SH$_{in}$_COOH$_{out}$) arises. After PEGylation by EDC amidation the C=O stretching vibration mode is moved to higher vibrational energies (1616 cm$^{-1}$) resulting from the newly formed amide bond. Also the N-H bending vibrations appear at 1530 cm$^{-1}$. The band between 1300 cm$^{-1}$ and 900 cm$^{-1}$ can be attributed to silica framework vibrations and is visible in all spectra. The peak at 1332 cm$^{-1}$ represents the

asymmetric stretching of the -$SO_2$ group in AlPcS$_{2a}$. The peak arising at 904 cm$^{-1}$ in the spectra of MSN_SH$_{in}$_PEGd8-AlPcS$_{2aout}$ can be assigned to the stretching vibration of the newly formed N-S bond between the terminal amino-group of the PEG-linker and AlPcS$_{2a}$. The two peaks at 743 cm$^{-1}$ and 720 cm$^{-1}$ correspond to the non-planar deformation vibrations of the C-H bonds of benzene rings.
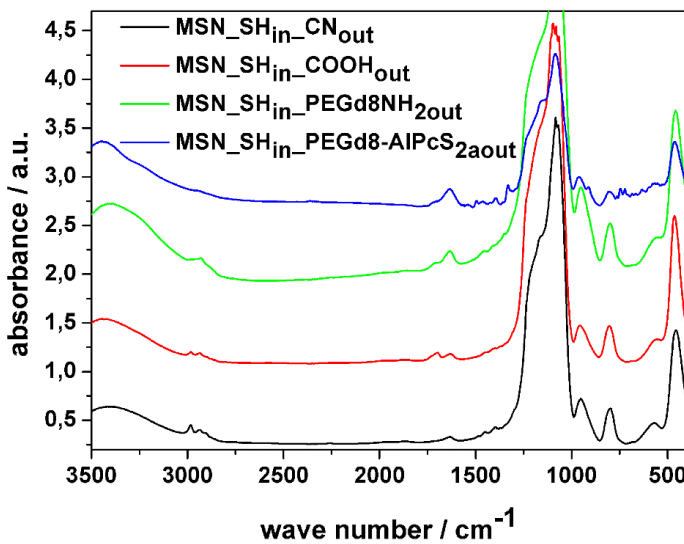


**Figure 4.7:** IR spectra of MSN_SH$_{in}$_CN$_{out}$ (black), MSN_SH$_{in}$_COOH$_{out}$ (red curve), MSN_SH$_{in}$_PEGd8NH$_{2out}$ (green curve) and MSN_SH$_{in}$_PEGd8-AlPcS$_{2aout}$ (blue curve). For clarity reasons curves for MSN_SH$_{in}$_COOH$_{out}$ (red curve), MSN_SH$_{in}$_PEGd8NH$_{2out}$ (green curve) and MSN_SH$_{in}$_PEGd8-AlPcS$_{2aout}$ (blue) were shifted along the y-axis by a value of 0.8 each for clarity reasons.

The accessible pore size as obtained by nitrogen sorption measurements is barely affected by the various surface modifications, as expected for particles that feature true core-shell spatially distributed functionalities (Figure 4.2c).

**Table 4.1:** Particle size, specific BET surface area, pore size and relative mass loss derived from dynamic light scattering, nitrogen physisorption and thermogravimetric analysis.

| Sample | Particle size[a] [nm] | BET surface area [m²/g] | Pore size[b] [nm] | Relative mass loss[c] [%] |
|---|---|---|---|---|
| **MSN_SH$_{in}$_CN$_{out}$** | 69 | 934 | 5.2 | 17 |
| **MSN_SH$_{in}$_COOH$_{out}$** | 125 | 746 | 5.1 | 12 |
| **MSN_SH$_{in}$_PEGd8NH$_{2out}$** | 98 | 615 | 5.6 | 18 |
| **MSN_SH$_{in}$_PEGd8-AlPcS$_{2aout}$** | 294 | 918 | 5.5 | 31 |
| **DOPC/DOTAP_SLB@MSN** | 160 | n.a. | n.a | n.a |

[a]Particle size refers to the peak value derived from DLS [b]DFT pore size refers to the peak value of the pore size distribution. [c]Relative mass loss obtained by TGA; all curves are normalized to 130 °C.

The permeability of the SLB and the opening of the SLB by photoactivation were examined *in situ* with a cuvette, containing a semipermeable membrane (cf. experimental section).[30] Figure 4.8 shows the release of cargo, either calcein (blue triangles) or a rhodamine derivative (RD) (black squares), from the MSN–PS–SLB (**VI**).
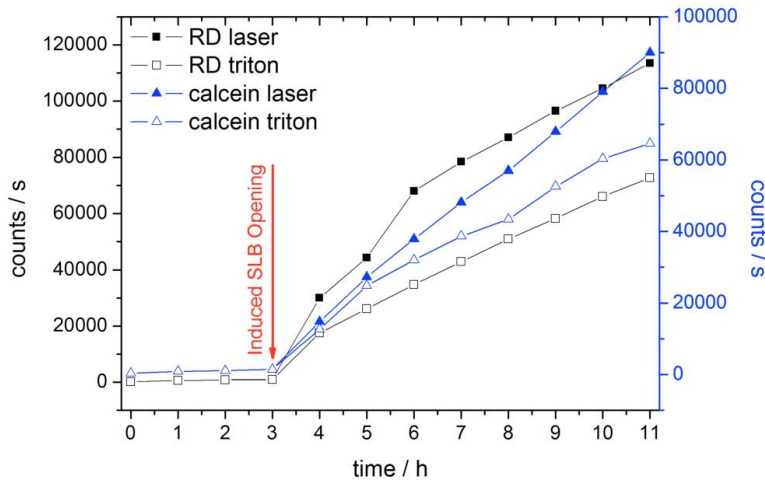


**Figure 4.8:** Release kinetics of calcein (solid blue triangle) and a rhodamine derivative (RD, solid black squares) before and after photoactivation at 3 h with light of $\lambda = 639$ nm and 0.55 mW/mm$^2$ for 1 min. of MSN-PS-SLB measured *in situ*. Analogous, the SLB can be open by addition of triton to the MSN solution after a 3 h time period. For both calcein (open blue triangles) and the RD (open black squares) the release by triton is slower as compared to the opening of the SLB by photoactivation.

The amount of released cargo over a 3 h time period before opening the SLB is minimal, demonstrating the integrity of the SLB. After 3 h in the cuvette the SLB was opened either by photoactivation or triton addition. To open the SLB through photoactivation the MSN-PS-SLB particles were exposed to 639 nm light with a power density of 0.55 mW / mm$^2$ for 1 min., resulting in an activation of the photosensitizer and singlet oxygen production. The singlet oxygen reacts with the double bonds of the DOPC and opens the SLB. This is apparent from the strong increase of fluorescence starting after 3 h, originating from the release of the cargo from the MSN core (solid symbols in Figure 4.8). Alternatively, the SLB can be opened by triton addition (open symbols in Figure 4.8). A strong increase of fluorescence for calcein (open blue triangles) and RD (open black squares) is apparent. However, the SLB opening via photoactivation seems to be more efficient, judging from the release rate of the cargos after induced SLB opening. Besides the prevention of premature release of the cargo from the MSN core, the SLB offers the opportunity to add various targeting ligands to our nanoparticle system. In the following section, we will discuss how our MSN-PS-SLB system can be modified with two different targeting ligands, namely folic acid (FA) and epidermal growth factor (EGF). The efficient modification of our drug delivery system with various targeting ligands as the final step in the synthesis allows for tuning of our multifunctional nanoparticles for a wide range of cancer types without constructing a completely new system for each type of cancer.

**Targeting.** Most cancer cells have specific receptors overexpressed on their surface. These receptors are only present in small concentrations or not at all on the surface of healthy cells. Ideally, a drug delivery system can be easily modified to make it specific for multiple cancer cell types. The system presented above offers this opportunity because the MSN-PS-SLB (**VI**) is only modified at the very end of the synthesis with a specific targeting ligand (TL). The basic building block for adding the targeting ligand to the MSN-PS-SLB (**VI**) is a DSPE-PEG$_{2000}$-TL conjugate molecule. This building block is inserted into the SLB by incubating the MSN-PS-SLB (**VI**) with DSPE-PEG$_{2000}$-TL at 37 °C for 3 h (FA) and 12 h (EGF), respectively (final step in Figure 4.1). In the studies presented here, we chose FA and EGF as targeting ligands because their receptors are commonly overexpressed on a wide range of cancer cells.[31, 32] FA receptors are overexpressed on various cell lines such as HeLa cells and KB cells,[31] and the EGF receptor is abundant on HuH7 cells, for example.[33] The functionality of the targeting ligands on our nanoparticle system was evaluated by performing competition

experiments and by evaluating the MSN-PS-SLB-TL (**VII**) uptake with live cell confocal fluorescence microscopy.
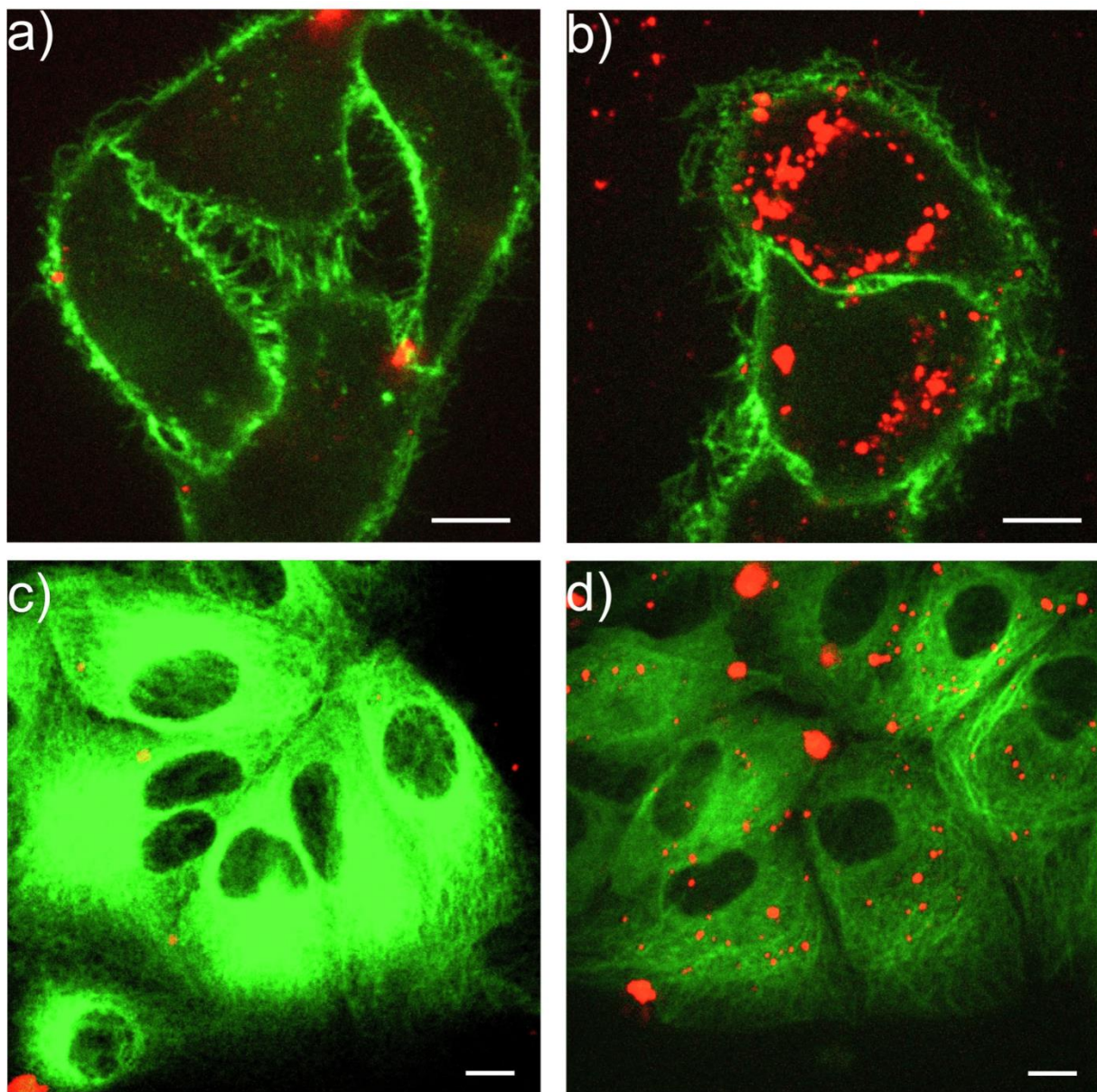


**Figure 4.9:** Unspecific and receptor-mediated endocytosis of MSN-PS-SLB particles with folic acid ligand (MSN-PS-SLB-FA) by KB cells, and MSN-PS-SLB particles with EGF ligand (MSN-PS-SLB-EGF) by HuH7 cells with GFP tagged tubulins (HuH7tub), respectively. **a)** Incubation of MSN-PS-SLB-FA particles with FA pre-incubated KB cells for 3 h at 37 °C. **b)** Incubation of MSN-PS-SLB-FA particles with KB cells, not FA pre-incubated, for 3 h at 37 °C. **c)** Internalization of MSN-PS-SLB-EGF particles by HuH7tub with EGF pre-incubated, and **d)** non-pre-incubated HuH7tub cells. The KB cell membrane is shown in green and the particles in red. For HuH7tub the GFP tagged tubulins are shown in green and the particles in red. Images were taken with live KB cells and HuH7tub cells. The scale bar is 10 μm.

In a competition experiment the MSN-PS-SLB-TL (**VII**) are incubated with cells that were either previously incubated with free targeting ligand or not. Pre-incubation of cells with free targeting ligand will block the specific receptors on the cell surface. Consequently, uptake of the MSN-PS-SLB-TL (**VII**) should only happen unspecific and therefore is expected to take much longer than receptor-mediated endocytosis. To evaluate the functionality of the FA ligand, KB cells were used. In the experiments shown in Figure 4.9a the cells were pre-incubated with FA for 2 h at 37 °C before the MSN-PS-SLB-FA (**VII**) particles were added to the cells and incubated for 3 h at 37 °C. Recording z-stacks of the cells with a spinning disk confocal fluorescence microscope allows us to indicate MSNs inside or outside the cell. A typical cut through the cell is shown in Figure 4.9. It shows that in KB cells only a few individual particles are present inside the cell (Figure 4.9a), whereas full stacks emphasize the quasi absence of nanoparticles inside the cell, independent of the chosen focal plane. In contrast, incubation of MSN-PS-SLB-FA (**VII**) with KB cells that were not pre-incubated with FA before resulted in significant uptake of particles (Figure 4.9b). The nanoparticles appear in the single representative z-slice as well as in the full stack, through the entire height of the cell. This clearly demonstrates that the particles are taken up by receptor-mediated endocytosis and that unspecific uptake of the particles by KB cells is small after 3 h incubation time (cf. appendix 4.19).

In the case of the EGF ligand, we synthesized the DSPE-PEG$_{2000}$-EGF conjugate as described in Figure 4.14 (cf. appendix). Similar to the FA experiments, we performed competition experiments with the EGF ligand. Experiments were performed with HuH7 cells, which are known to overexpress the EGF receptor.[33] Figure 4.9c shows that in the case of pre-incubation of HuH7 cells with EGF almost no MSN-PS-SLB-EGF (**VII**) particles are endocytosed by the HuH7 cells after 3 h. In contrast, a significant number of the particles is present inside the cells when the cells were not pre-incubated with EGF (Figure 4.9d). Again typical slices of the z-stacks are shown in Figure 4.9c and d (cf. appendix 4.20). The above results demonstrate that our MSN-PS-SLB nanoparticles can be modified efficiently to meet the specific requirements of various cancer types and to ensure a specific receptor-mediated uptake. In addition, in the two cell types discussed here the unspecific uptake of the NPs is very small after 3 h. Both are important factors for successful drug delivery vehicles in order to prevent damage of healthy cells by cancer therapeutics. Furthermore, the targeting ligand is introduced after the completion of the synthesis of the actual nanoparticle system. This offers more flexibility to separately

synthesize both the nanoparticle system and the DSPE-PEG$_{2000}$-TL because possible incompatible reaction conditions can be avoided. This allows for selecting the synthesis strategies for both components more freely, which is considered a significant advantage for the incorporation of fragile peptides into these systems. Besides the specific uptake of the drug delivery vehicle by cancer cells, it is of key importance for efficient drug delivery to release the drug into the cytosol, and ideally to do so with spatial and temporal control. In the following, we will show that our system provides the means to achieve this.

**Cargo Release by Photoactivation.** One of the main challenges for drug delivery with high efficacy is to overcome the endosomal entrapment in order to release the drug into the cytosol. In combination with MSNs, three strategies have been pursued so far to solve this issue, namely employing cationic lipids,[10] fusion or endosomolytic proteins[19-21] or photosensitizers.[16, 26, 27] In the case of MSNs coated with a cationic lipid, targeting capabilities were shown but release of cargo was not and no gating mechanism, to keep the drug enclosed, was presented.[10] The fusion or endosomolytic protein approach is a rather complicated and costly strategy, but it works well as has been demonstrated.[19-21] However, for both methods an external control of the exact location and time of the cargo release is not possible. A photoactivation approach provides both of these capabilities. In the studies where MSNs and photosensitizers were used, the photosensitizer was either loaded as a cargo into MSNs[27] or covalently attached to them.[15] The covalent attachment of the photosensitizer is advantageous compared to loading it into the MSN pores. The ratio of MSN to photosensitizer is more easily controlled, the loading capacity of the MSNs can be completely used for the drug, and a spatial separation between drug and photosensitizer exists. This could be important considering that the singlet oxygen, produced by photoactivation of the photosensitizer, will most likely damage the drug when not spatially separated from it. In previous work from our group,[16] the photosensitizer had to be excited by blue light, which cannot penetrate the tissue very deeply.[25] Moreover, the attachment of the used photosensitizer to the MSN surface was synthetically more involved. Here we have improved both of these aspects by using a different photosensitizer, namely AlPcS$_{2a}$. First, it is photoactivatable with red light and thereby the phototoxicity caused by light activation with blue light is reduced. Additionally, the potential depth of tissue penetration of the activation laser is increased by a factor of about 5. The latter feature will become important if this drug delivery system is tested *in vivo*. Nishiyama *et al.* demonstrated this by using AlPcS$_{2a}$ for a transfection of the conjunctival tissue in rat eyes.[25] Finally, AlPcS$_{2a}$ can be more easily attached

to the MSN surface than the previously used photosensitizer because a sulfonate group can be directly linked to an amino group.

To verify that the drug delivery mechanism works *in vitro*, we incubated MSN-Calcein-PS-SLB-FA nanoparticles for 3 h with HeLa cells. In comparison to the incubation with free calcein, the incubation of the nanoparticles containing calcein as a cargo produces a significantly higher calcein concentration inside the cell (Figure 4.10a). The uptake of free calcein by KB cells is negligible (cf. appendix 4.17). This demonstrates that our drug delivery system can be used to efficiently transport membrane impermeable cargos into the cell. Before photoactivation, the calcein and the photosensitizer are co-localized (yellow color in Figure 4.10c) and exhibit a dot-like pattern, indicating that the calcein and the MSN-PS-SLB-FA particles are still inside the endosomes (Figure 4.10a - c). This demonstrates that the escape from the endosome does not happen automatically and that a mechanism is required to overcome this key challenge in the field of drug delivery.
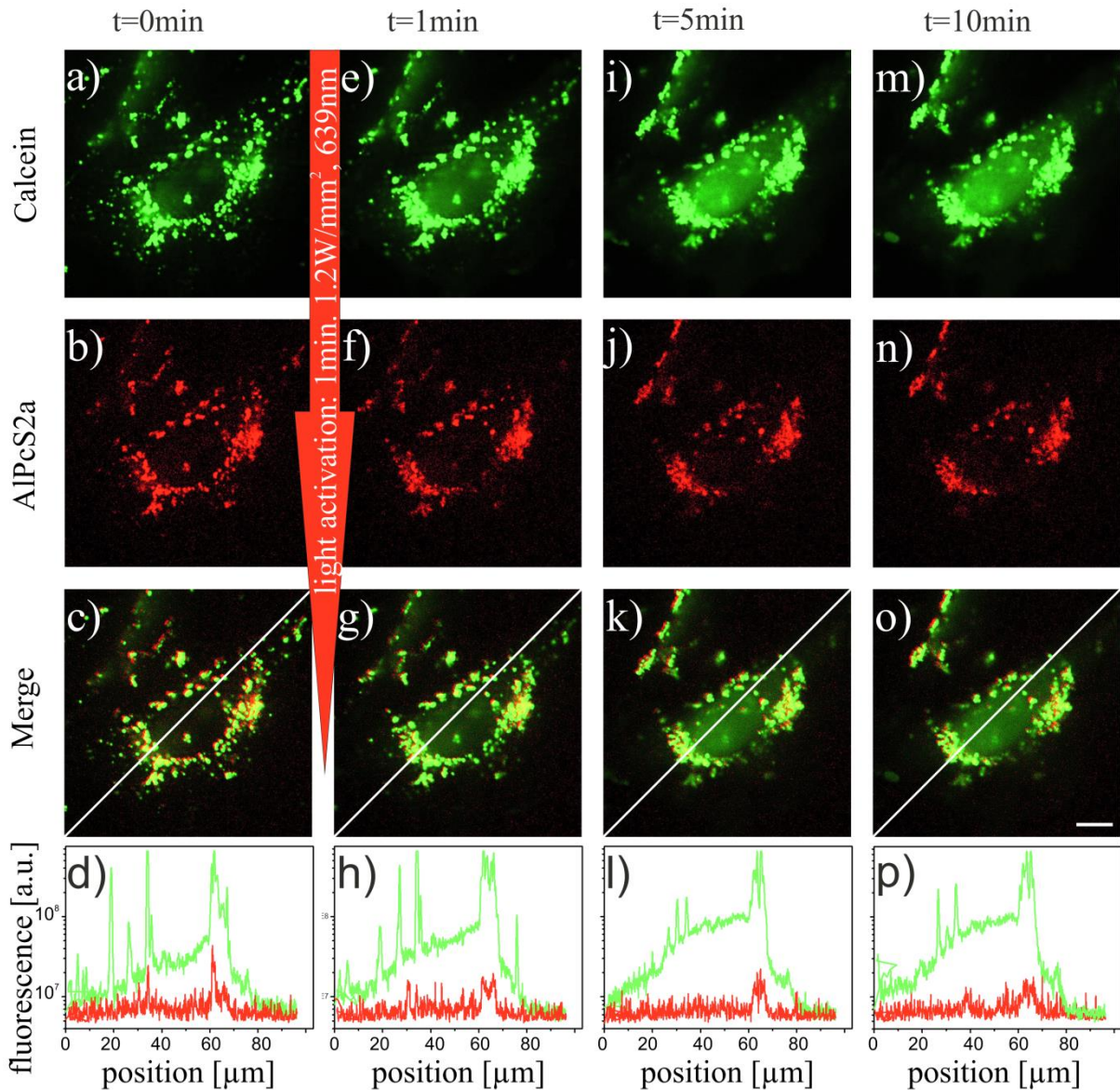
**Figure 4.10:** Fluorescence microscopy of MSN-PS-SLB-FA nanoparticles loaded with calcein inside HeLa cells, after an incubation time of 16 h. **a – c)** Calcein (green) and AlPcS$_{2a}$ (red) are co-localized (yellow) prior to photoactivation. **d)** Intensity profile along the white line in the merged image for both. **e – h)** 1 min after photoactivation, **i – l)** 5 min and **m – p)** 10 min. after photoactivation. The scale bar is 10 μm.

To induce endosomal escape, we activated the integrated photosensitizer AlPcS$_{2a}$ with 1.2 W / mm$^2$ of 639 nm light for 1 min., at similar conditions as those used for the *in situ* experiment in Figure 4.8. As a result, 1 min. after activation an increase of the green fluorescence caused by calcein through the entire cell and in particular in the nucleus can be observed (Figure 4.10 e and h). In contrast, no change of the red fluorescence originating from

the photosensitizer is observed. This trend continues over time as is apparent from the images taken at 5 min. (Figure 4.10 i – k) and at 10 min. (Figure 4.10 m – o) after photoactivation. In the merged image after 1, 5, and 10 min. (Figure 4.10g, k and o), the presence of the green signal becomes dominant, indicative of a lower colocalization between calcein and photosensitizer due to the spreading of the calcein in the cell. The green fluorescence is observed in particular inside the cell nucleus. This time-series of images shows that photoactivation can open the SLB and the endosome via an activation cascade, resulting in the release of the calcein into the cytosol. While the green fluorescence from calcein is present through the entire cytosol after photoactivation (Figure 4.10 e, i and m), the dot-like pattern of the red fluorescence, caused by the PS on the MSN, does not change (Figure 4.10 f, j and h). This shows that in contrast to calcein, the MSN does not escape from the endosomes. The reason for this behavior is unknown, but has been observed before.[27] However, we note that free PS in endosomes does spread after photoactivation (cf. appendix 4.18).

In addition to calcein, our multifunctional system can be loaded with various cargos. For example, we loaded the MSN core (**IV**) with a rhodamine derivative (RD). Subsequently, the loaded MSN core (**V**) was surrounded by an SLB and FA was inserted into the SLB, resulting in MSN-RD-PS-SLB-FA (**VII**).
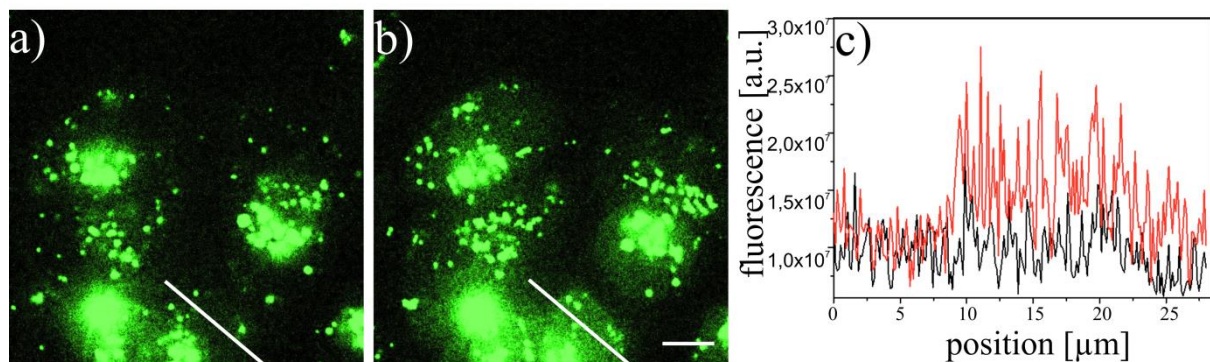


**Figure 4.11:** MSN-PS-SLB-FA nanoparticles loaded with RD (green) inside KB cells. **a)** Before and **b)** 10 min after photoactivation. **c)** Intensity profile along the white line in **a** and **b**. Post-photoactivation (red line) a significantly higher fluorescence signal is apparent in the positions $10 - 20\,\mu m$ in comparison to pre-photoactivation (black line). The scale bar is $10\,\mu m$.

The nanoparticles were incubated on KB cells for 22 h at 37 °C under a 5% $CO_2$ humidity atmosphere. Similar to calcein, the fluorescence from RD-loaded particles in the cells exhibits a dot-like pattern before photoactivation (Figure 4.11a). 10 min after the photoactivation an evenly spread fluorescence in addition to the dot-like pattern is observed (Figure 4.11b). The increase of the evenly spread fluorescence is apparent when measuring the intensity profile in a region that had low fluorescence before photoactivation. Figure 4.11c shows the fluorescence intensity along the white line in Figure 4.11a and b. After photoactivation, a strong increase of the fluorescence is observed. Thus, we conclude that 10 min after photoactivation some of the RD has been released from the MSN core and from the endosome as well and subsequently has spread through the cytosol. For both types of cargo the release into the cytosol occurs shortly after photoactivation, emphasizing the precise temporal control that is provided by the photoactivation approach. In addition, before photoactivation no spreading of the cargo is observed, i.e. photoactivation is required for release of cargo into the cytosol. As a result, our system provides means to spatially control the release of cargo by applying laser light at specific areas, in particular the cancer tissue. This spatial control is available in addition to the ligand-based targeting ability of our particles and should further reduce unintentional exposure of healthy cells to cancer therapeutics. Therefore, the selectivity of drug release should be enhanced in comparison to the cases where only the proton sponge effect or fusogenic/endosomolytic peptides are used.

## 4.3 Conclusion

We have developed a drug delivery system based on mesoporous silica nanoparticles that addresses some of the key issues in the field of drug delivery involving high selectivity and drug delivery with high efficacy. The combination of the high loading capacity of MSN, the supported lipid bilayer for controlled release, the addition of targeting ligands, and overcoming of endosomal entrapment by photoactivation makes this system a potent drug delivery vehicle. Employing fluorescence microscopy, we were able to demonstrate the selective uptake of our nanoparticles by various cancer cell lines and the release of different cargos *in vitro*. Furthermore, we have demonstrated that the red light-based photoactivation approach has many advantages compared to other approaches used in the field. In particular, by covalently linking the PS to the MSN surface and using a PS that can be excited by red light, negative side-effects of the PS can be minimized and activation of the PS *in vivo* is feasible. Moreover,

photoactivation for cargo release enhances the spatial selectivity of where the drug is released as compared to using targeting ligands only. We anticipate that the integration of all these strategies into one multifunctional drug delivery vehicle as well as the efficient synthesis and modification of the nanoparticles for multiple cancer cell types will hold promise for wide-ranging applications in cancer therapy.

## 4.4   Experimental

**Materials.** Tetraethyl orthosilicate (TEOS, Fluka, >99%), (3-mercaptopropyl)-triethoxysilane (MPTES, Gelest, 95%), (3-cyanopropyl)-triethoxysilane (CN-TES, ABCR, 98%), cetyltrimethylammonium chloride (CTAC, Fluka, 25wt% in $H_2O$), triethanolamine (TEA, Aldrich, 98%), ammonium fluoride ($NH_4F$, Sigma, >98%), $\alpha,\omega$-bis-amino octa (ethylene glycol) ($NH_2$-PEGd8-$NH_2$, Iris Biotech), Al(III) phthalocyanine chloride disulfonic acid (AlPcS$_{2a}$, Frontier Scientific), ammonium nitrate (Sigma, 99%), conc. hydrochloric acid (Aldrich, >95%, 37 wt%), 1,3,5-triisopropylbenzene (TiPB, Fluka, 96%), sulfo-N-hydroxysuccinimide (sulfo-NHS, Aldrich, 98%), N-(3-dimethylaminopropyl)-N′-ethylcarbodiimide (EDC, Sigma, 97%), calcein (CAL, Sigma), dimethyl sulfoxide (DMSO, Sigma, >99.5%), ethanol (EtOH, Aldrich, >99.5%), 1,2-dioleoyl-sn-glycero-3-phosphocholine (DOPC, Avanti Polar Lipids), 1,2-distearoyl-*sn*-glycero-3-phosphoethanolamine-N-[folate(polyethylene glycol)-2000] (ammonium salt) (DSPE-PEG$_{2000}$-FA, Avanti Polar Lipids), 1,2-distearoyl-*sn*-glycero-3-phosphoethanolamine-N-[maleimide(polyethylene glycol)-2000] (ammonium salt) (DSPE-PEG2000-maleimide, Avanti Polar Lipids), 2-Iminothiolane hydrochloride (Traut's reagent, Sigma-Aldrich), 5(6)-Carboxy-X-rhodamine (RD, Sigma), Wheat germ agglutinin (WGA) Alexa Fluor 488 conjugate (Invitrogen), epidermal growth factor (EGF, PeproTech, >98%), Folic acid (FA, Sigma, >97%).

All chemicals were used as received without further purification. Doubly distilled water from a Millipore system (Milli-Q Academic A10) was used for all synthesis and purification steps.

**Synthesis of core-shell MSN_SH$_{in}$_CN$_{out}$.** Bi-functional core-shell colloidal mesoporous silica nanoparticles were synthesized according to a slightly modified published method.[12] A mixture of TEOS (1.63 g, 9.22 mmol), MPTES (112 mg, 0.48 mmol) and TEA (14.3 g, 95.6 mmol) was heated under static conditions at 90 °C for 20 min in a polypropylene reactor. Then a solution of CTAC (25 wt% in water, 2.41 mL, 1.83 mmol), NH$_4$F (100 mg, 2.70 mmol) and TiPB (2.54 g, 12.4 mmol) in water (21.7 g, 1.21 mol) was preheated to 60 °C and added quickly. The reaction mixture was stirred vigorously (1000 rpm) at room temperature for 20 minutes. Subsequently TEOS (138.2 mg, 0.922 mmol) was added in four equal increments every three minutes. This step was followed by 30 minutes of stirring at room temperature. For the shell functionalization a mixture of TEOS (19.3 mg, 92.5 μmol) and CN-TES (21.4 mg, 92.5 μmol) was added to the reaction. The resulting mixture was then allowed to stir at room temperature for 12 h. After the addition of 100 mL ethanol, the MSNs were collected by centrifugation (15 min, 20500 rpm, 50228 rcf), re-dispersed in 100 mL of ethanol and extracted according to the procedure described below.

**Extraction of MSN_SH$_{in}$_CN$_{out}$.** Extraction of the surfactant was performed by heating 250 mg of MSN for 45 minutes under reflux at 90 °C in a solution containing 2 g ammonium nitrate in 100 mL ethanol. This extraction step was performed twice. The template-free MSN were separated by centrifugation (15 min, 20500 rpm, 50228 rcf) and washed with ethanol after each extraction step. MSN_SH$_{in}$_CN$_{out}$ were obtained as colloidal suspension in EtOH.

**Conversion of MSN_SH$_{in}$_CN$_{out}$ to MSN_SH$_{in}$_COOH$_{out}$.** 250 mg of MSN_SH$_{in}$_CN$_{out}$ in EtOH were collected by centrifugation and washed with H$_2$O once. The particles were re-dispersed in 10 mL H$_2$O and 30 mL hydrochloric acid (37 wt%) was added carefully. The reaction mixture was heated to reflux for 3 h. After cooling down, 20 mL H$_2$O were added and the synthesis was stirred at room temperature overnight. The resulting colloidal suspension of MSN_SH$_{in}$_COOH$_{out}$ was diluted further with 100 mL H$_2$O, collected by centrifugation (15 min, 20500 rpm, 50228 rcf), and re-dispersed in 100 mL of water. This washing step was repeated twice with both water and ethanol. MSN_SH$_{in}$_COOH$_{out}$ were obtained as an ethanolic suspension.

**PEGylation of MSN_SH$_{in}$_COOH$_{out}$ with bi-functional NH$_2$-PEGd8-NH$_2$ to the sample MSN_SH$_{in}$_PEGd8NH$_{2out}$.** An ethanolic suspension containing 20 mg of MSN_SH$_{in}$_COOH$_{out}$ was centrifuged (15 min, 20500 rpm, 50228 rcf) and re-dispersed in 60 mL of water. This washing step was repeated twice. EDC (0.85 μL, 4.6 μmol, 1.2 eq) was

added at room temperature to a diluted suspension of $MSN\_SH_{in}\_COOH_{out}$ in 40 mL of water. The reaction mixture was stirred for 5 min before sulfo-NHS (1 mg, 4.6 µmol, 1.2 eq) was added. A second solution, containing bi-functional $NH_2$-PEGd8-$NH_2$ (7.05 mg, 19.2 µmol, 5 eq.) dissolved in 2 mL water was prepared. The EDC-activated $MSN\_SH_{in}\_COOH_{out}$ were added dropwise to the PEG-containing solution. Afterwards, the pH was adjusted with two drops of hydrochloric acid (37 wt%) to a value pH < 7 and the reaction mixture was stirred for 12 h at ambient temperature. In order to remove the excess of the PEG-linker, the reaction mixture was washed five times with 30 mL of water to remove unbound PEG. All washing steps were followed by centrifugation (15 min, 20500 rpm, 50228 rcf). Finally, the sample $MSN\_SH_{in}\_PEGd8NH_{2out}$ was re-dispersed in 10 mL ethanol.

**Attachment of the photosensitizer $AlPcS_{2a}$ to $MSN\_SH_{in}\_PEGd8NH_{2out}$ yielding the sample $MSN\_SH_{in}\_PEGd8\text{-}AlPcS_{2aout}$.** 1 mg of $MSN\_SH_{in}\_PEGd8NH_{2out}$ in ethanolic solution was centrifuged and re-suspended in a 500 µL water/DMSO mixture (2:1). Subsequently, 40 µL of an $AlPCS_{2a}$ stock solution (2 mg in 1 mL DMSO) were added to the MSN. The reaction mixture was stirred in the dark at room temperature for 72 h. The resulting $MSN\_SH_{in}\_PEGd8\text{-}AlPcS_{2aout}$ were extensively washed by centrifugation (4 min, 14000 rpm, 16873 rcf) with water/DMSO (1:1) in order to remove excess photosensitizer. All supernatants were investigated with a Nanodrop UV-VIS in order to monitor the content of free photosensitizer. In order to remove DMSO from the mesopores the sample was washed three times with water after no free PS could be detected (cf. appendix 4.15 and 4.16). The colloidal solution of sample $MSN\_SH_{in}\_PEGd8\text{-}AlPcS_{2aout}$ was used for further experiments immediately.

**Adsorption of the the dyes calcein and a rhodamine derivative (RD) into the mesopores of $MSN\_SH_{in}\_PEGd8\text{-}AlPcS_{2aout}$.** 0.5 mg of the sample $MSN\_SH_{in}\_PEGd8\text{-}AlPcS_{2aout}$ in ethanol were centrifuged (4 min, 14000 rpm, 16873 rcf) and re-dispersed in 1 mL water. This washing step was repeated twice. Then, the suspension was centrifuged again and re-dispersed in 500 µL calcein in water (1 mM stock solution in water) or RD (1 mM stock solution in water), respectively. The mixture was stirred over night in the dark yielding the sample $MSN\_CARGO_{in}\_PEGd8\text{-}AlPcS_{2aout}$.

**Supported DOPC/DOTAP lipid bilayer (SLB) around MSN_CARGO$_{in}$_PEGd8-AlPcS$_{2aout}$.** 0.5 mg of MSN_CARGO$_{in}$_PEGd8-AlPcS$_{2aout}$ in 1 mL dye solution were centrifuged (4 min, 14000 rpm, 16873 rcf) and the supernatant discarded. Afterwards, a mixture of 70 µL DOPC and 30 µL DOTAP (each 2.5 mg/mL in 60:40 H$_2$O : EtOH) were added to the resulting pellet, mixed extensively, and sonicated for 10 s. To form the supported lipid bilayer around the MSN via solvent exchange method, 700 µL of water were added. The resulting suspension was mixed and sonicated for 10 s, yielding DOPC/DOTAP@MSN_Cargo$_{in}$_PEGd8-AlPcS$_{2aout}$.

**Diffusion of the targeting ligand (TL) construct, DSPE-PEG$_{2000}$-TL, into the SLB of DOPC/DOTAP@MSN_CARGO$_{in}$_PEGd8-AlPcS$_{2aout}$.**

0.5 mg of DOPC/DOTAP@MSN_CARGO$_{in}$_PEGd8-AlPcS$_{2aout}$ in 800 µL water were incubated with 6 µL of DSPE-PEG$_{2000}$-TL for 3 h (for DSPE-PEG$_{2000}$-Folate) or 12 h respectively (for DSPE-PEG$_{2000}$-EGF) at 37 °C. The resulting sample DOPC/DOTAP@MSN_CARGO$_{in}$_PEGd8-AlPcS$_{2aout}$-TL was used without further purification for confocal microscopy studies.

**Time-based fluorescence release experiments of the sample DOPC/DOTAP@ MSN_CARGO$_{in}$_PEGd8-AlPcS$_{2aout}$.** Fluorescence time-based release experiments were recorded on a PTI fluorescence system featuring a PTI 814 photomultiplier detector and a PTI A1010B Xenon arclamp driven by a PTI LPS-220B lamp power supply. For temperature settings, a Quantum Northwest TC 125 sample holder was used. Our previously described custom-made release cuvette system was used for all experiments.[30] All samples were measured at a temperature of 37 °C with slits of 2/2.2/2/2. For RD an excitation wavelength of 575 nm was used (emission maximum at 597 nm), whereas calcein was excited with 495 nm and with an emission maximum at 516 nm. Results are given in Figure 4.8.

For all experiments, 0.5 mg of DOPC/DOTAP@MSN_Cargo$_{in}$_PEGd8-AlPcS$_{2aout}$ were used. 200 µL of the particle suspension was filled into the reservoir cap sealed with a dialysis membrane (Molecular weight cut-off 14000 g/mol) allowing released dye molecules to pass into the fluorescence cuvette. In order to monitor the release of adsorbed dyes upon membrane rupture with singlet oxygen, the sample was excited with 0,56 W/mm$^2$ of 633 nm light for 1 minute prior the measurement. For triton-mediated release, 5 µL of a 1 mM stock solution of TritonX100 was added to the particle solution.

**Characterization.** Centrifugation was performed using a Sorvall Evolution RC equipped with a SS-34 rotor or an Eppendorf centrifuge 5418 for small volumes. All samples were investigated with a FEI Titan 80-300 operating at 300 kV with a high-angle annular dark field detector. A droplet of the diluted MSN solution in ethanol absolute was dried on a carbon-coated copper grid. Nitrogen sorption measurements were performed on a Quantachrome Instruments NOVA 4000e. All four samples (15 mg each) were heated to 393 K for 12 h in vacuum (10 mTorr) to outgas the samples before nitrogen sorption was measured at 77 K. For calculations of pore sizes and volumes a non-local density functional theory (NLDFT) equilibrium model of nitrogen on silica was used. Dynamic light scattering (DLS) measurements were performed on a Malvern Zetasizer-Nano instrument equipped with a 4 mW He-Ne laser (633 nm) and an avalanche photodiode. The hydrodynamic radius of the particles was determined by dynamic light scattering in ethanolic suspension. For this purpose, 100 µL of an ethanolic suspension of MSN particles (ca. 10 mg/mL) was diluted with 3 mL of ethanol prior to the measurement. Zeta potential measurements of the samples were performed on a Malvern Zetasizer-Nano instrument equipped with a 4 mW He-Ne laser (633 nm) and an avalanche photodiode. For determination of the zeta potential curves, two drops of the ethanolic MSN suspension (~ 3 %wt.) was mixed with 1 mL commercial Hydrion Buffer solution of the appropriate pH prior to measurement. IR measurements were performed on a Bruker Equinox 55 FTIR/FTNIR Spectrometer in absorbance mode (spectra were background substracted). Thermogravimetric analysis of the bulk samples $MSN\_SH_{in}\_CN_{out}$, $MSN\_SH_{in}\_COOH_{out}$, $MSN\_SH_{in}\_PEGd8NH_{2out}$ and $MSN\_SH_{in}\_PEGd8\text{-}AlPcS_{2aout}$ was performed on a Netzsch STA 440 C TG/DSC with a heating rate of 10 K / min in a stream of synthetic air of about 25 mL/min. The mass was normalized to 100% at 133.8 °C for all samples and the resulting data is presented in Figure 4.5b. Cross-polarized $^{13}C$ solid-state NMR (ssNMR) measurements were performed on a Bruker DSX Avance500 FT spectrometer in a 4 mm $ZrO_2$ rotor. The spinning rate was 10 kHz and a total number of up to 8000 scans were recorded. UV-VIS spectra were recorded with a NanoDrop ND 1000 spectrometer. Usually, 2 µL of sample were used and all presented spectra are background corrected for water absorption.

**Cell Culture.** KB cells were grown in folic acid deficient Roswell Park Memorial Institute 1640 medium (RPMI 1640, Invitrogen) supplemented with 10% FCS at 37 °C in a 5% $CO_2$ humidified atmosphere. The cells were seeded on ibidiTreat µ-Slide (IBIDI). HuH7 cells were grown in Dulbecco's modified Eagle's medium (DMEM):F12 (1:1) (Invitrogen) medium

supplemented with 10% fetal bovineserum (FBS) at 37 °C in a 5% $CO_2$ humidified atmosphere. To reduce autofluorescence of the cells, the medium was changed to DMEM:F12(Invitrogen) supplemented with 10% B-27 two days before seeding. The cells were seeded on collagen A-coated LabTek chambered cover glass (Nunc). HeLa cells were grown in Dulbecco's modified Eagle's medium (DMEM):F12 (1:1) (Invitrogen) with Glutamax I medium supplemented with 10% fetal bovineserum (FBS) at 37 °C in a 5% $CO_2$ humidified atmosphere. The cells were seeded on collagen A-coated LabTek chambered cover glass (Nunc). For live cell imaging the cells were seeded 24 or 48 h before measuring, at a cell density of 2x104 or 1x104 cells/cm$^2$.

**Uptake studies.** To evaluate the functionality of the folic acid ligand, KB cells were incubated with nanoparticles for 3 h at 37 °C under a 5% $CO_2$ humidified atmosphere. In the case of live cell imaging the cell membrane was stained afterwards by adding 4 µL of 1 mg/mL wheat germ agglutinin Alexa Fluor 488 or 633 conjugate (WGA488, WGA633, Invitrogen) to 400 µL of cell medium. After 1 min, the cell medium was removed, the cells were washed twice with cell medium, and imaged immediately. In the case of fixed cells the cells were washed three times after the 3 h incubation time with PBS (Invitrogen). Afterwards 200 µL of 4% paraformaldehyde (PFA, Science Service) were added for 15 minutes. After removing PFA the cells were washed three times with PBS and stained by adding 4 µL of 1 mg/mL WGA 488 to 400 µL of PBS. After 1 min the cell medium was removed, the cells were washed twice with PBS and imaged. In control experiments, the FA receptors on the KB surface were blocked by pre-incubation of the cells with 3 mM folic acid (Sigma) for 2 h at 37 °C under a 5% $CO_2$ humidified atmosphere, before particle were added. In the case of EGF, HuH7 cells with GFP tagged tubulin were used in addition to staining the cell membrane. In the case of HuH7 tubulin the cell medium was exchanged with $CO_2$-independent medium (Invitrogen) and imaged immediately after incubation with cells. After incubation with nanoparticles, the cell medium was exchanged with $CO_2$-independent medium (Invitrogen) and imaged immediately. The wildtype HuH7 cells were treated equivalent to the live cell imaging of the KB cells. For the control experiments, EGF receptors on the HuH7 surface were saturated by pre-incubating the cells with 0.2 µM EGF (PeproTech, >98%) for 2 h at 37 °C under a 5% $CO_2$ humidified atmosphere, before particle addition.

**Cargo Release Experiments.** Cells were incubated 16 − 22 h prior to the measurements at 37 °C under a 5% $CO_2$ humidified atmosphere. Shortly before imaging, the medium was replaced by $CO_2$-independent medium (Invitrogen). During the measurements all cells were kept on a heated microscope stage at 37 °C. The photosensitizer $AlPcS_{2a}$ was activated by

1.2 W/mm$^2$ of 639 nm light for 1 min. The subsequent imaging was performed as described in the Spinning disk confocal microscopy section.

**Spinning disc confocal microscopy.** Confocal microscopy for live-cell imaging was performed on a setup based on the Zeiss Cell Observer SD utilizing a Yokogawa spinning disk unit CSU-X1. The system was equipped with a 1.40 NA 100x Plan apochromat oil immersion objective from Zeiss. For all experiments the exposure time was 0.1 s and the frame rate varied between 3 frames/s and 1 frame/30s, depending on the specific requirements of the experiment. Calcein and WGA488 were imaged with approximately 0.4 W/mm$^2$ of 488 nm excitation light. The rhodamine derivative (RD) was excited with 1.2 W/mm$^2$ of 561 nm light. AlPcS$_{2a}$ was excited with 0.12 W/mm$^2$ of 639 nm for imaging and for photoactivation with 1.2 W/mm$^2$. In the excitation path a quad-edge dichroic beamsplitter (FF410/504/582/669-Di01-25x36, Semrock) was used. For two color detection of calcein and AlPcS$_{2a}$ and accordingly WGA 488 and AlPcS$_{2a}$, a dichroic mirror (660 nm, Semrock) and band-pass filters 525/50 and 690/60 (both Semrock) were used in the detection path. In case of RD a band-pass filter 629/60 (Semrock) was used. Separate images for each fluorescence channel were acquired using two separate electron multiplier charge coupled devices (EMCCD) cameras (PhotometricsEvolveTM).

## 4.5 Appendix
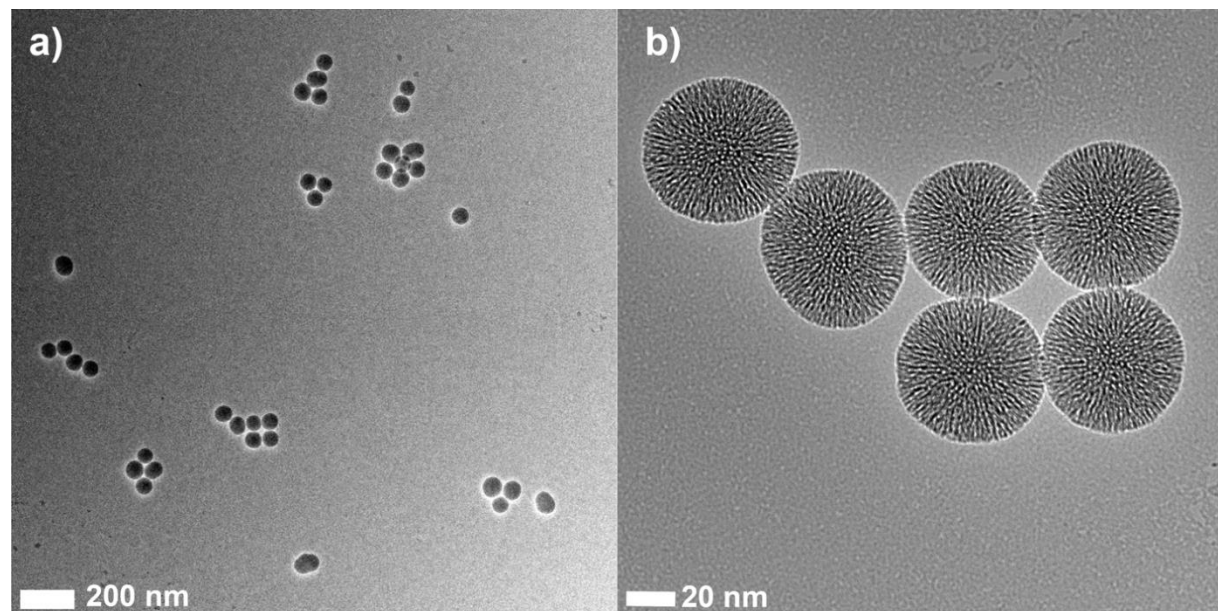


**Figure 4.12:** TEM images of the template-extracted core-shell MSN_SH$_{in}$_CN$_{out}$.
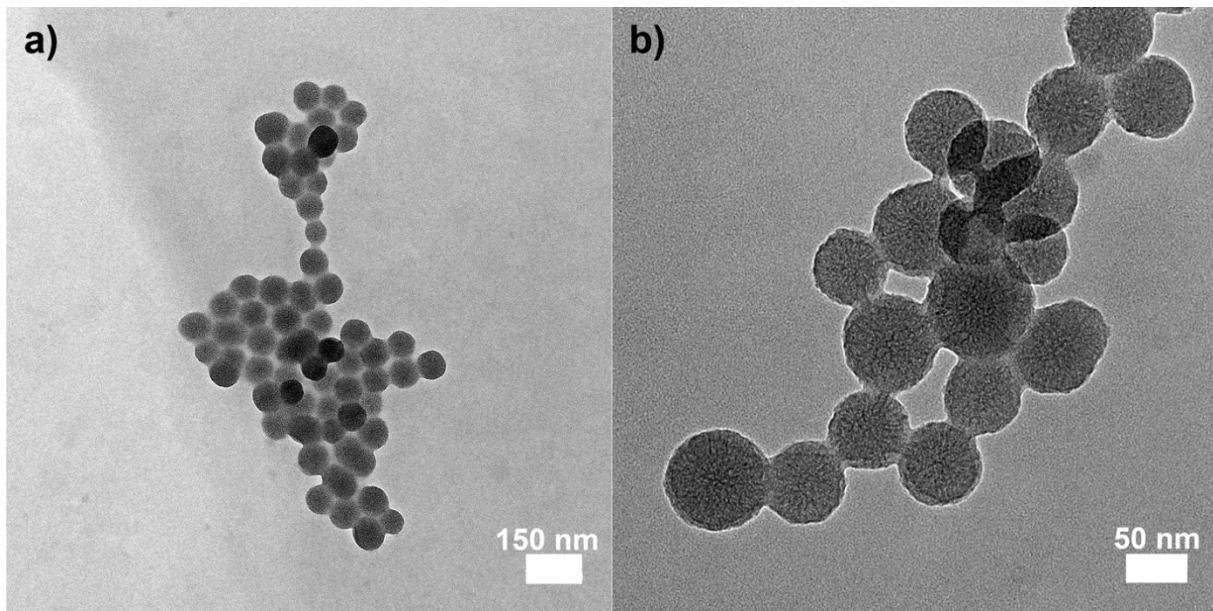
**Figure 4.13:** TEM micrographs at different of the sample MSN_SH$_{in}$_PEGd8NH$_{2out}$.

The homogeneity of the sample and the mesostructure of the MSN are preserved during the hydrolysis of the cyano-groups and the PEGylation step. The size of around 70 nm is in good agreement with the results from the dynamic light scattering experiments. In comparison to Figure 4.12, the mesoporous structure of the nanoparticles is hardly detectable due to the additional organic layer attached to the MSN shell. The mild white-greyish halo is a focus artifact caused by electron beam exposure and ultrahigh vacuum.
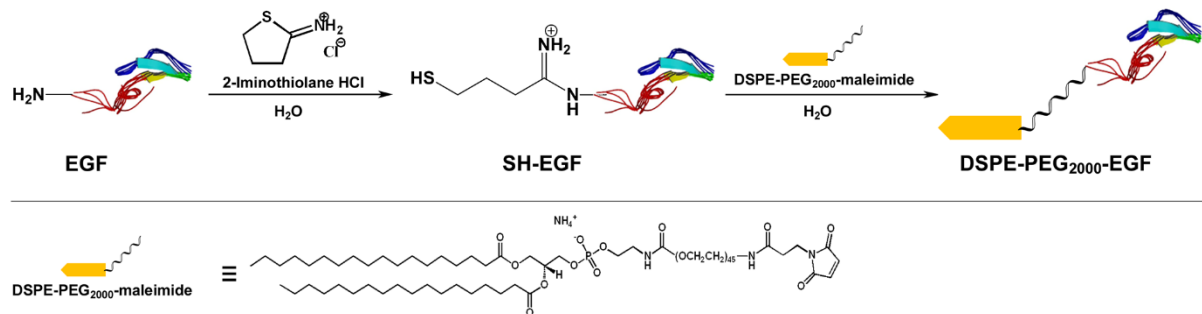


**Figure 4.14:** Chemical modification of the EGF targeting ligand via the Traut's reagent (2-iminothiolane) to achieve thiolation of the N-termius of EGF. In a second step the lipid DSPE-PEG$_{2000}$-maleimide covalently binds to the modified EGF.

To utilize EGF as another targeting ligand beside folic acid, we synthesized a lipid-EGF construct, where the EGF (50 µg) is covalently attached to the lipid DSPE-PEG$_{2000}$-maleimide (Figure 4.14). In a first step, the N-terminus of the targeting peptide was modified via the

Traut's reagent (2-Iminothiolane, 2 equiv., 16 nmol) in an aqueous solution by stirring for 1 h at room temperature. This resulted in a terminal thiol group which can be used for further functionalization. Subsequently, the modified EGF was covalently attached to the lipid DSPE-PEG$_{2000}$-maleimide (3.5 μL of a 10 mg/mL 60/40 H$_2$O/EtOH v%). The final DSPE-PEG$_{2000}$-EGF construct can be further utilized to use as targeting ligand on the nanoparticle as described below.



**Figure 4.15:** Supernatants of the washing procedure of the sample MSN_SH$_{in}$_PEGd8-AlPcS$_{2aout}$.
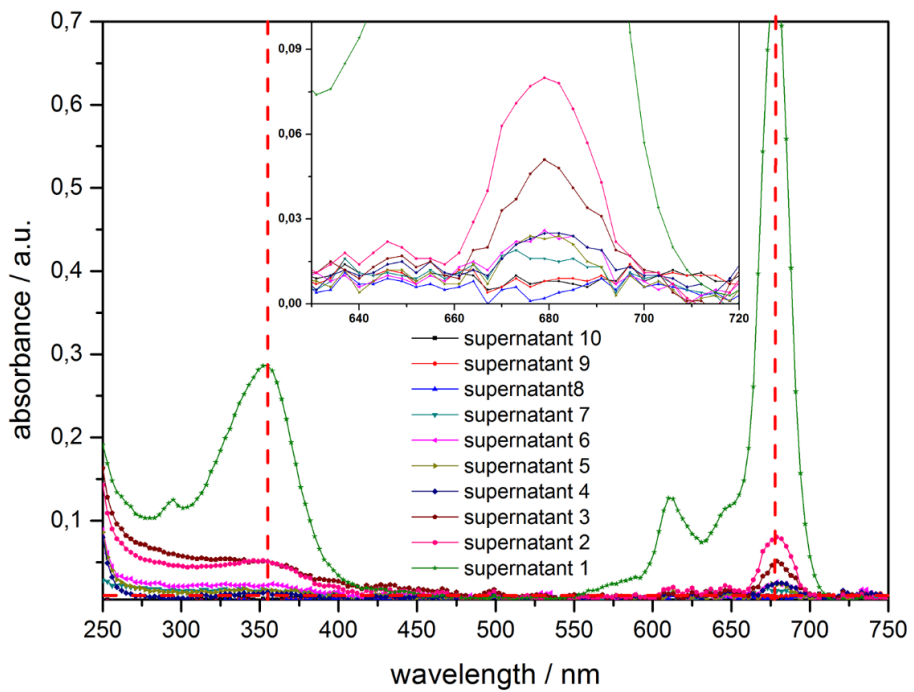
**Figure 4.16:** UV-VIS data obtained from the supernatants of the washing procedure of the sample MSN_SH$_{in}$_PEGd8-AlPcS$_{2aout}$. No free photosensitizer could be detected in supernatants $8 - 10$.

**Uptake of free calcein and MSN loaded with calcein by KB cells**
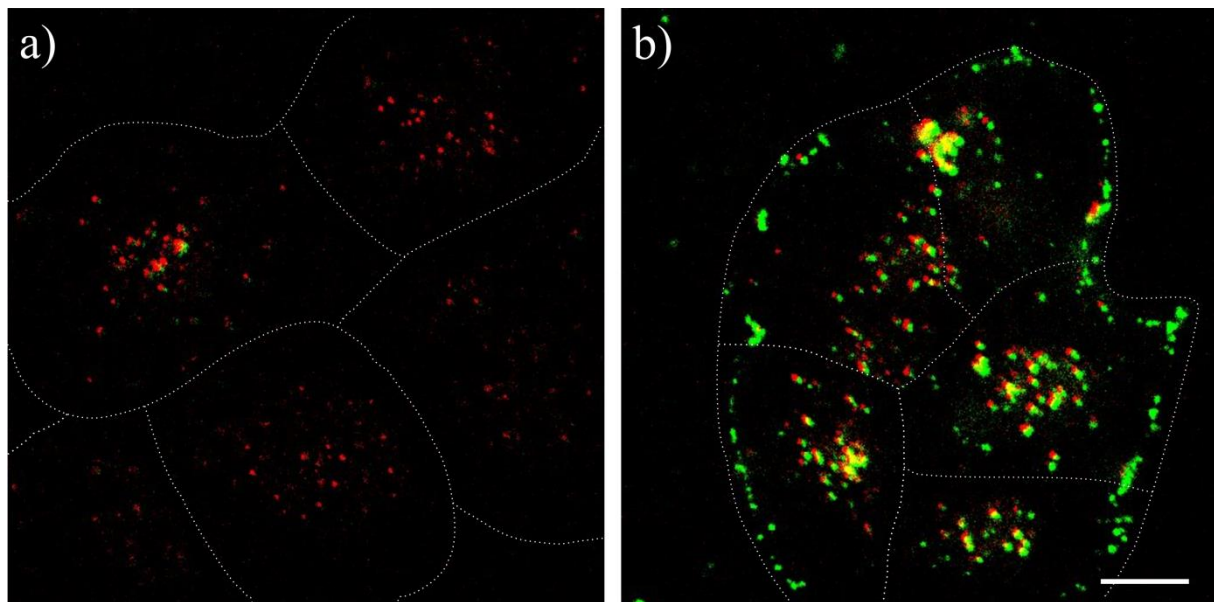


**Figure 4.17: a)** Uptake of free calcein (green) and free $AlPcS_{2a}$ (red) by KB cells after 20 h incubation at 37 °C under 5% $CO_2$ humidified atmosphere. **b)** Uptake of MSN loaded with calcein (green), covalent attached $AlPcS_{2a}$ (red) and SLB after 20 h incubation at 37 °C under 5% $CO_2$ humidified atmosphere. Intensity scale is the same in both images. The fluorescence of calcein and $AlPcS_{2a}$ is slightly shifted against each other to show the colocalization clearer. Calcein is only transported into the cell in significant amounts when it is loaded into the MSN. Scale bar: 10 μm.

**Uptake of free $AlPcS_{2a}$ by HeLa cells and spreading after photoactivation**
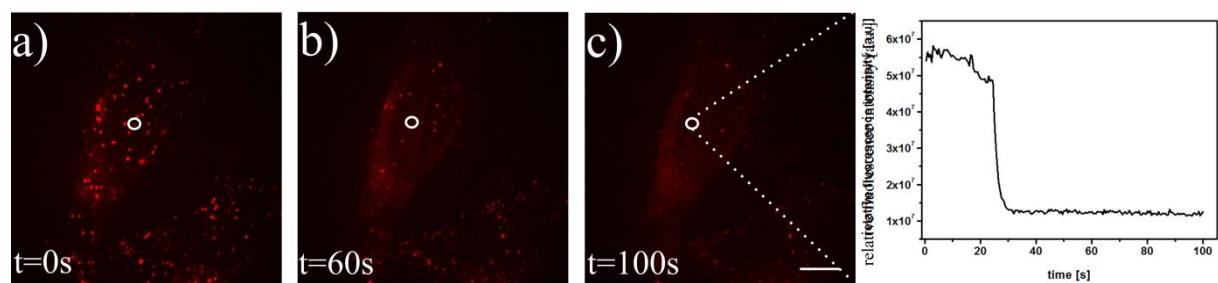


**Figure 4.18:** Uptake of free $AlPcS_{2a}$ by HeLa cells after 20 h incubation at 37 °C under 5% $CO_2$ humidified atmosphere. **a)** Before photoactivation **b)** 60s after photoactivation with 1.2 W / $mm^2$ of 639 nm light **c)** 100 s after photoactivation. The spreading of the $AlPcS_{2a}$ is apparent. d) Intensity trace of one endosome marked by white circle in a – c. Scale bar: 10 μm.

**Uptake of MSN-PS-SLB-FA particles with folic acid ligand by KB cells, imaging after fixation of cells**
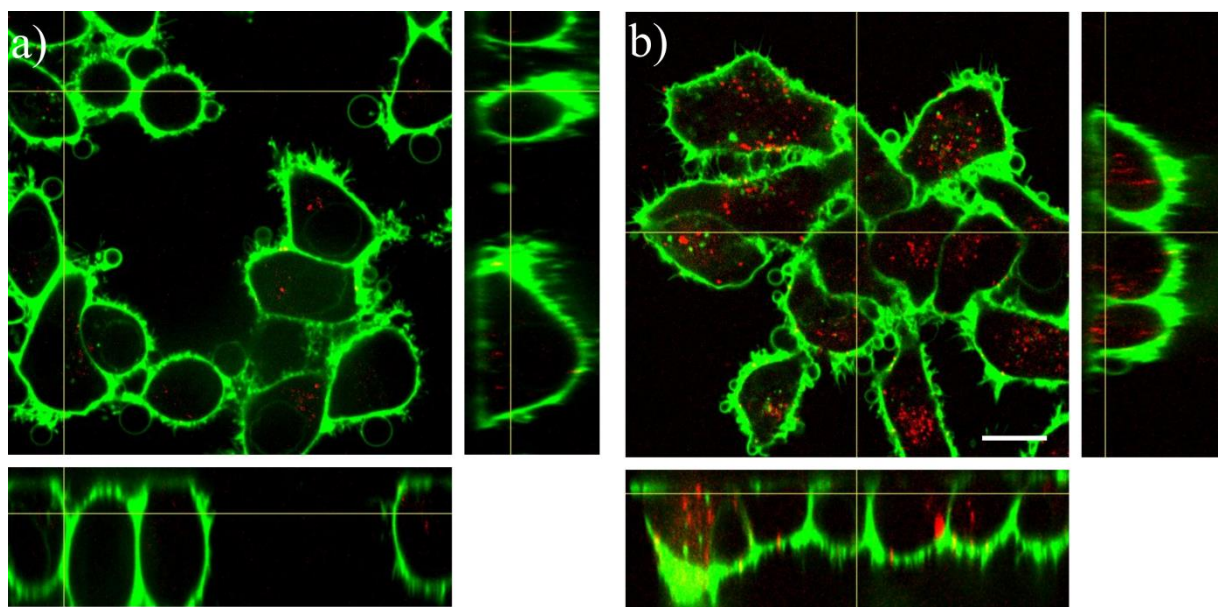


**Figure 4.19:** Unspecific and receptor mediated endocytosis of MSN-PS-SLB-FA particles with folic acid ligand by KB cells. Cells are fixed with paraformaldehyde after an incubation of 3h and the cell membrane is stained with a cell membrane stain (WGA 488). **a)** Incubation of MSN-PS-SLB-FA particles with FA pre-incubated KB cells for 3 h at 37 °C. **b)** Incubation of MSN-PS-SLB-FA particles with KB cells, not FA pre-incubated, 3 h at 37 °C. For both **a)** and **b)** the orthogonal view in xz and yz plane is shown on the bottom and right side of the main image. The KB cell membrane is shown in green and the particles in red. The particles are imaged over the photosensitizer, and even after fixation one can see the particles in a dot-like structure which indicates that the photosensitizer is not separated from the particles. The scale bar is 10 μm.

**Uptake of MSN-PS-SLB-EGF particles with folic acid ligand by HuH7 cells**
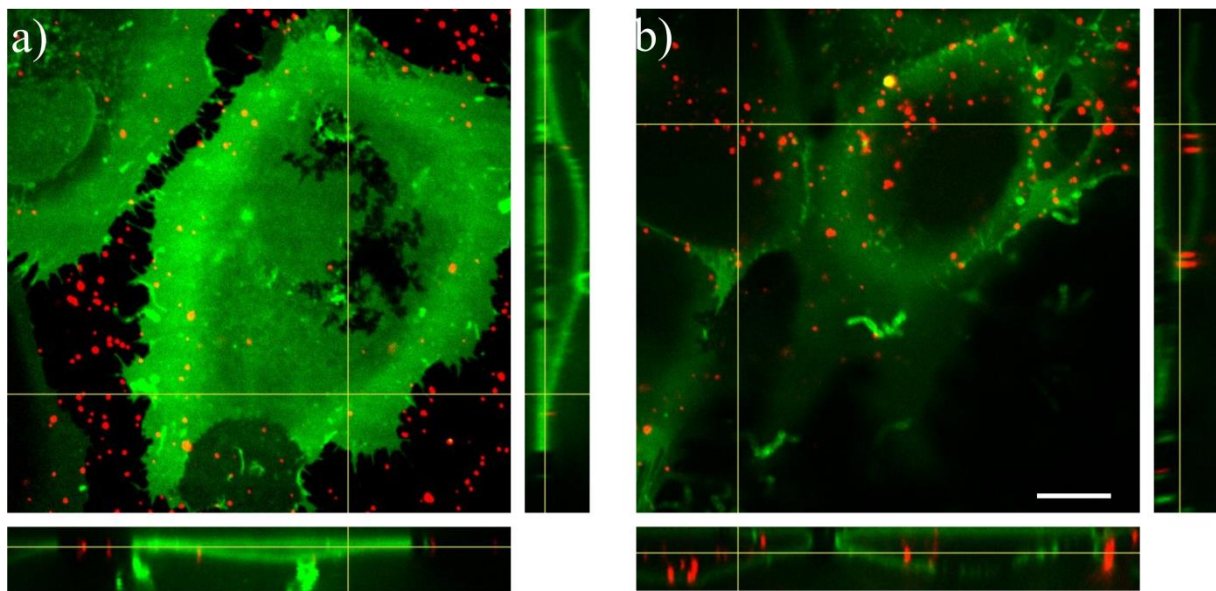


**Figure 4.20:** Unspecific and receptor mediated endocytosis of MSN-PS-SLB-EGF particles with EGF ligand by HuH7 cells. Cells are incubated for 3 h and the cell membrane is stained with a cell membrane stain (WGA 633). **a)** Incubation of MSN-PS-SLB-EGF particles with EGF pre-incubated HuH7 cells for 3 h at 37 °C. **b)** Incubation of MSN-PS-SLB-EGF particles with EGF cells, not EGF pre-incubated, 3 h at 37 °C. For both **a)** and **b)** the orthogonal view in xz and yz plane is shown on the bottom and right side of the main image. The HuH7 cell membrane is shown in green and the particles in red. The scale bar is 10 μm.

## 4.6 References

1. Pack, D. W.; Hoffman, A. S.; Pun, S.; Stayton, P. S. *Nature reviews. Drug discovery* **2005**, *4*, 581-593.

2. Fröhlich, T.; Wagner, E. *Soft Matter* **2010**, *6*, 226-234.

3. Miyata, K.; Nishiyama, N.; Kataoka, K. *Chem. Soc. Rev.* **2012**, *41*, 2562-2574.

4. Gillies, E. R.; Fréchet, J. M. J. *Drug Discov. Today* **2005**, *10*, 35-43.

5. Svenson, S.; Tomalia, D. A. *Adv. Drug Deliv. Rev.* **2005**, *57*, 2106-2129.

6. Lee, C. C.; MacKay, J. A.; Frechet, J. M. J.; Szoka, F. C. *Nat. Biotech.* **2005**, *23*, 1517-1526.

7. Ghosh, P. S.; Kim, C.-K.; Han, G.; Forbes, N. S.; Rotello, V. M. *ACS Nano* **2008**, *2*, 2213-2218.

8. Vivero-Escoto, J. L.; Slowing, I. I.; Trewyn, B. G.; Lin, V. S. Y. *Small* **2010**, *6*, 1952-1967.

9. Rosenholm, J. M.; Sahlgren, C.; Linden, M. *Nanoscale* **2010**, *2*, 1870-1883.

10. Rosenholm, J. M.; Meinander, A.; Peuhu, E.; Niemi, R.; Eriksson, J. E.; Sahlgren, C.; Linden, M. *ACS Nano* **2009**, *3*, 197-206.

11. Liong, M.; Lu, J.; Kovochich, M.; Xia, T.; Ruehm, S. G.; Nel, A. E.; Tamanoi, F.; Zink, J. I. *ACS Nano* **2008**, *2*, 889-896.

12. Cauda, V.; Schlossbauer, A.; Kecht, J.; Zürner, A.; Bein, T. *J. Am. Chem. Soc.* **2009**, *131*, 11361-11370.

13. Cauda, V.; Engelke, H.; Sauer, A.; Arcizet, D.; Bräuchle, C.; Rädler, J.; Bein, T. *Nano Lett.* **2010**, *10*, 2484-2492.

14. Kecht, J.; Schlossbauer, A.; Bein, T. *Chem. Mater.* **2008**, *20*, 7207-7214.

15. Sauer, A. M.; Schlossbauer, A.; Ruthardt, N.; Cauda, V.; Bein, T.; Bräuchle, C. *Nano Lett.* **2010**, *10*, 3684-3691.

16. Schlossbauer, A.; Sauer, A. M.; Cauda, V.; Schmidt, A.; Engelke, H.; Rothbauer, U.; Zolghadr, K.; Leonhardt, H.; Bräuchle, C.; Bein, T. *Adv. Healthcare Mater.* **2012**, *1*, 316-320.

17. Behr, J.-P. *Chimia* **1997**, *51*, 34-36.

18. Sonawane, N. D.; Szoka, F. C.; Verkman, A. S. *J. Biol. Chem.* **2003**, *278*, 44826-44831.

19. Robson Marsden, H.; Elbers, N. A.; Bomans, P. H. H.; Sommerdijk, N. A. J. M.; Kros, A. *Angew. Chem. Int. Ed.* **2009**, *48*, 2330-2333.

20. Ashley, C. E.; Carnes, E. C.; Phillips, G. K.; Padilla, D.; Durfee, P. N.; Brown, P. A.; Hanna, T. N.; Liu, J.; Phillips, B.; Carter, M. B.; Carroll, N. J.; Jiang, X.; Dunphy, D.

R.; Willman, C. L.; Petsev, D. N.; Evans, D. G.; Parikh, A. N.; Chackerian, B.; Wharton, W.; Peabody, D. S.; Brinker, C. J. *Nat. Mater.* **2011**, *10*, 389-397.

21. Ashley, C. E.; Carnes, E. C.; Epler, K. E.; Padilla, D. P.; Phillips, G. K.; Castillo, R. E.; Wilkinson, D. C.; Wilkinson, B. S.; Burgard, C. A.; Kalinich, R. M.; Townson, J. L.; Chackerian, B.; Willman, C. L.; Peabody, D. S.; Wharton, W.; Brinker, C. J. *ACS Nano* **2012**, *6*, 2174-2188.

22. Meyer, M.; Dohmen, C.; Philipp, A.; Kiener, D.; Maiwald, G.; Scheu, C.; Ogris, M.; Wagner, E. *Mol. Pharm.* **2009**, *6*, 752-762.

23. Schlossbauer, A.; Dohmen, C.; Schaffert, D.; Wagner, E.; Bein, T. *Angew. Chem. Int. Ed.* **2011**, *50*, 6828-6830.

24. Varkouhi, A. K.; Scholte, M.; Storm, G.; Haisma, H. J. *J. Control. Release* **2011**, *151*, 220-228.

25. Anderson, R. R.; Parrish, J. A. *J. Investig. Dermatol.* **1981**, *77*, 13-19.

26. Nishiyama, N.; Iriyama, A.; Jang, W.-D.; Miyata, K.; Itaka, K.; Inoue, Y.; Takahashi, H.; Yanagi, Y.; Tamaki, Y.; Koyama, H.; Kataoka, K. *Nat. Mater.* **2005**, *4*, 934-941.

27. Febvay, S. b.; Marini, D. M.; Belcher, A. M.; Clapham, D. E. *Nano Lett.* **2010**, *10*, 2211-2219.

28. Cao, L.; Man, T.; Kruk, M. *Chem. Mater.* **2009**, *21*, 1144-1153.

29. Cao, L.; Kruk, M. *Colloids Surf., A* **2010**, *357*, 91-96.

30. Schlossbauer, A.; Kecht, J.; Bein, T. *Angew. Chem. Int. Ed.* **2009**, *48*, 3092-3095.

31. Ladino, C. A.; Chari, R. V. J.; Bourret, L. A.; Kedersha, N. L.; Goldmacher, V. S. *Int. J. Cancer* **1997**, *73*, 859-864.

32. Clark, A. J.; Ishii, S.; Richert, N.; Merlino, G. T.; Pastan, I. *Proc. Natl. Acad. Sci. U. S. A.* **1985**, *82*, 8374-8378.

33. Mickler, F. M.; Möckl, L.; Ruthardt, N.; Ogris, M.; Wagner, E.; Bräuchle, C. *Nano Lett.* **2012**, *12*, 3417-3423.

# 5 Multifunctional Polymer-Capped Mesoporous Silica Nanoparticles for pH-Responsive Targeted Drug Delivery
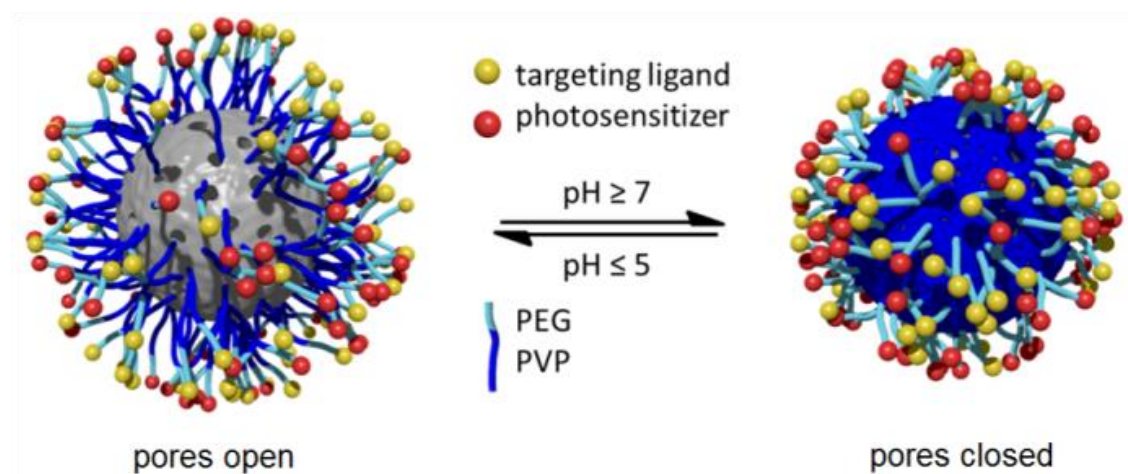
## Abstract

A highly stable modular platform, based on the sequential covalent attachment of different functionalities to the surface of core-shell mesoporous silica nanoparticles (MSNs) for targeted drug delivery is presented. As drug release mechanism poly(2-vinylpyridine) (PVP) was used as a pH-responsive cap system. Our platform offers (i) tuneable interactions and release kinetics with the cargo drug in the mesopores based on chemically orthogonal core-shell design, (ii) an extremely robust and reversible closure and release mechanism based on endosomal acidification of the covalently attached PVP polymer block, (iii) high colloidal stability due to a covalently coupled PEG shell, and (iv) the ability to covalently attach a wide variety of dyes, targeting ligands and other functionalities at the outer periphery of the PEG shell.

The functionality of the system was demonstrated in several cell studies, showing pH-triggered release in the endosome, light-triggered endosomal escape with an on-board photosensitizer, and efficient folic acid-based cell targeting.

## 5.1 Introduction

Polymers can be attractive for biological applications due to their biocompatibility, tuneable properties and production from sustainable sources.[1, 2] Therefore, polymers are widely used as responsive coatings of surfaces for selective ion-permeability,[3] surface patterning[4, 5] and drug delivery with polyplexes,[1, 6] hybrid dendrimers,[7, 8] and other drug-polymer conjugates.[9, 10] Regarding drug-polymer conjugates, which offer relatively small particle sizes and good biocompatibility, possible issues may arise from low loading capacities and potentially poor stability, depending on the strength of the drug-polymer interactions.[11] The drug-polymer interactions need to be optimized for different kinds of drugs to ensure stable drug-polymer conjugates. Aimed at creating a more general delivery platform, much effort has been made towards the development of inorganic nanoparticles such as mesoporous silica nanoparticles (MSNs) for the delivery of bioactive compounds to cells and tumors.[12-16] MSNs have a high loading capacity and can be functionalized internally and on the external surface.[17] To prevent premature release from these mesoporous systems, different strategies including covalent attachment of the cargo inside the mesopores[18, 19] or complete capping of the whole particle[20-23] have been developed. The release mechanisms include changes in reduction potential,[24] pH,[18, 20] temperature,[25] and irradiation with light.[14, 19, 26]

Combining the high loading capacity and stability of mesoporous nanoparticles with the biocompatibility and tuneable properties of polymers offers the possibility to create stimuli-responsive and reversible delivery systems. For instance, You *et al.* showed the release behavior of poly(*N*-isopropylacrylamide) coated mesoporous silica at different temperatures.[27] Drug delivery vehicles based on nanoparticles in a size range of around 100 nm are likely to be taken up by cells via endocytosis.[28] During this process, the endosome is acidified by the action of proton pumps.[29, 30] Therefore, pH-responsive polymer coatings around mesoporous silica nanoparticles offer the possibility to use the changes in pH during endocytosis as trigger for controlled release. For instance, attachment of poly(acrylic acid)[31] or poly(2-(diethylamino)ethyl methacrylate)[32] showed the ability of pH-responsive functional polymer coatings around mesoporous silica nanoparticles for release applications. Liu *et al.* reported on different release kinetics from mesoporous silica by the use of poly(4-vinylpyridine) as pH-responsive shell created by multipoint anchoring.[20] Poly(2-vinylpyridine) (PVP) has also been used for the pH-sensitive functionalization of

surfaces, due to the pronounced transition between hydrophilicity and hydrophobicity upon protonation and deprotonation.[4] Here, we describe a multifunctional drug delivery vehicle that combines the high loading capacity of a mesoporous silica core with the 'intelligence' towards internal stimuli of a pH-responsive polymer.

As shown in Figure 5.1, at low pH, the protonated polymer is in a hydrophilic state and therefore, cargo molecules are able to diffuse into and out of the mesoporous silica nanoparticle. At pH values around 5.5 or higher, the polymer is deprotonated, leading to a hydrophobic state which is subsequently followed by a collapse of the polymer onto the silica surface, thus preventing premature release of the cargo. The pH-responsive switching behavior of the polymer introduces a site-specific release mechanism to the delivery vehicle. After endosomal uptake of the particles by a cell, the endosomes are acidified by proton pumps present in the endosomal membrane.[29] The change in pH leads automatically to a switch of the particle into its open state, and therefore triggers the release of cargo into the endosomal compartment. A major advantage of this delivery vehicle is offered by the reversibility of the cap system. Once the particles have been exocytosed by the cell before having released all of their cargo, the cap system will return into the closed state due to the environment (pH > 7) outside of the cell.[29] To maintain colloidal dispersibility, even in the hydrophobic closed state, poly(ethylene glycol) blocks were attached to the ends of the PVP cap system. In this context, the use of α-ω-bis-functionalized polymers offers the possibility for anchoring any functionality of interest (photosensitizers, targeting ligands) step by step (Figure 5.1).
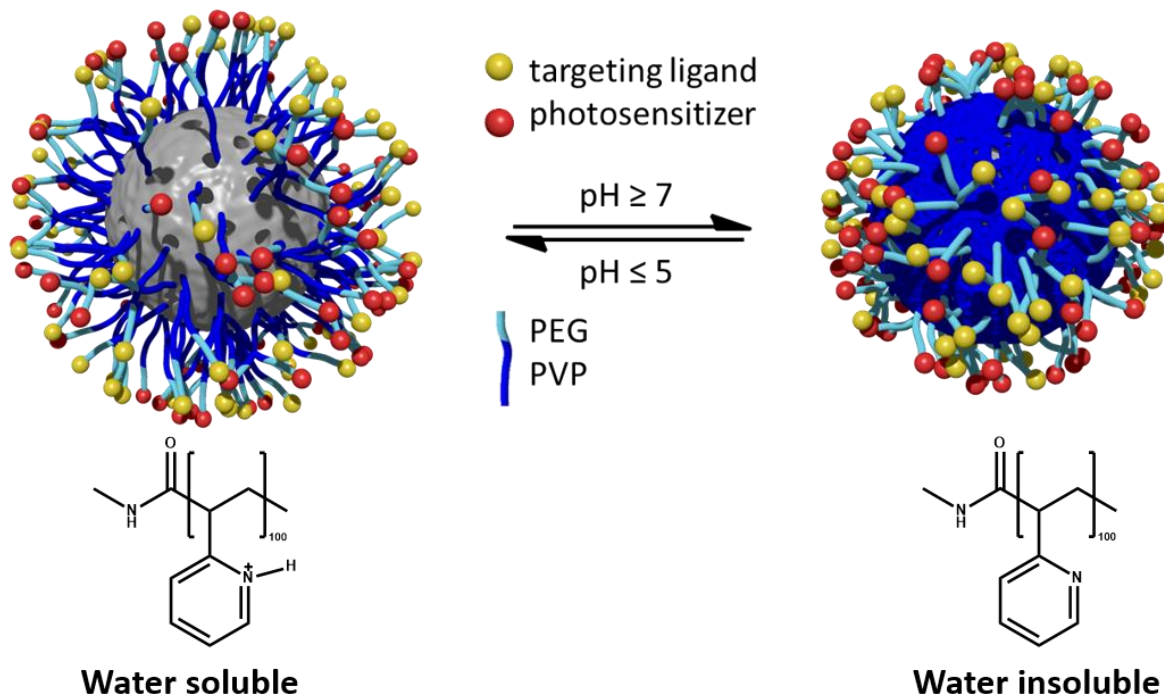
**Figure 5.1:** Concept of the MSN-based pH-responsive drug delivery system. The pores can be reversibly opened and closed through changes in the hydrophilicity of the polymer.

## 5.2   Results and Discussion

Colloidal core-shell mesoporous silica nanoparticles (MSNs) with amino-moieties on the shell were synthesized via a delayed co-condensation approach according to a published synthesis procedure with CTAB as structure directing agent and TEOS as silica source.[17] The outer surface of the template-free MSNs were subsequently modified with bi-functional poly(2-vinylpyridine) (PVP) via an EDC-assisted amidation reaction (cf. appendix 5.8). The bi-functionality of the polymer allows the subsequent attachment of PEG, fluorescent dyes and targeting ligands. As proved by transmission electron microscopy (TEM), the shell functionalized mesoporous silica nanoparticles show an average particle diameter of 90 nm with a wormlike pore structure (cf. figure 5.3A). The stepwise functionalization of the MSNs with poly(2-vinylpyridine) and PEG was monitored with several methods (dynamic light scattering, nitrogen adsorption and zeta potential, Figure 5.2A-C; further characterization: cf. appendix 5.9, 5.10 and 5.11) and is discussed in the following section. Dynamic light scattering (DLS) measurements revealed the need for PEG as stabilizing agent; the

hydrodynamic diameter of amino shell-functionalized MSNs in aqueous media reveals an average particle size of 160 nm (Figure 5.2A, black curve), whereas the polymer-modified sample MSN-PVP-NH$_2$ (red curve) shows strong aggregation in water due to the hydrophobicity at pH 7, indicated by an apparent size increase to 550 nm. However, subsequent PEGylation of PVP recovers the colloidal nature of the system, which is indicated by a decrease of the average particle size (blue curve). Additionally, the covalent functionalization of the mesoporous silica nanoparticles was monitored with thermogravimetric analysis (TGA, Figure 5.2B). While the shell functionalized nanoparticles (MSN-NH$_2$) show a relative mass loss of 14.6% (2.97 mmol per gram silica), the relative mass loss of 61.6% for MSN-PVP-NH$_2$ corresponds to 0.14 mmol PVP per gram silica. From these data, it can be concluded that only 4.7% of the amino-groups present at the MSN-surface have reacted with the polymer. Based on the mass loss of 80.4% in the sample MSN-PVP-PEG, the amount of 1.3 mmol PEG per gram silica could be determined. This result indicates, that additional attachment of PEG to the shell of the MSNs must have occurred besides the attachment to the end of the polymer cap system. Additionally, zeta potential titration experiments of the samples MSN-NH$_2$ and MSN-PVP-NH$_2$ were carried out to prove the functionalization of the synthesized inorganic-organic hybrid material (cf. appendix 5.9). The high zeta potential (+50 mV) of MSN-PVP-NH$_2$ at low pH reflects the polymer cap system in its fully protonated and thus open state. At pH = 5.5, close to the pk$_a$ value of protonated pyridine, deprotonation of the polymer cap system occurs, leading to a significant drop in zeta potential with increasing pH. Together with the zeta potential, DLS measurements were performed simultaneously at the same pH values. For MSN-PVP-NH$_2$ the particles showed good colloidal dispersability as long as the polymer remained in its protonated state. Upon deprotonation, the polymer collapses at the particle surface, forming a hydrophobic shell around the particles, which is revealed in the increase in size due to agglomeration. In contrast, attachment of PEG to the PVP-functionalized particles led to the suppression of aggregation, as no changes in size were observed over the whole pH-range for MSN-PVP-PEG. Infrared spectroscopy was carried out to prove the functionality of the designed MSN carrier system and to monitor the subsequent reaction steps on the outer shell of the MSNs (cf. appendix 5.10). The signals between 2850 cm$^{-1}$ and 2800 cm$^{-1}$ can be attributed to the CH$_2$ stretching vibrations arising from the organic functionality (aminopropyl-moieties) and are present in each sample. Furthermore, several peaks at 2900 cm$^{-1}$ (C-H stretching vibrations) and at 1400 cm$^{-1}$ (C-H bending vibrations) are visible. The peaks at 1590 cm$^{-1}$ and 1570 cm$^{-1}$ correspond to the C=C stretch vibrations of the aromatic pyridine ring and are present in each spectra after the attachment of PVP to the surface of MSN-NH$_2$. Additionally, peaks at

1474 cm$^{-1}$ and 1430 cm$^{-1}$ are present after covalent attachment of the boc-protected polymer to the shell of the MSNs and can be assigned to the C=N stretch vibrations of the aromatic pyridine ring. In order to successfully enable additional covalent attachment of functionalities (e.g. PEG or targeting ligands), the boc-protection group at the polymer end was subsequently removed (cf. appendix 5.8). After deprotection of MSN-PVP-NH$_2$-Boc and conversion of the amino group into a carboxy-functionality with oxalic acid, a peak at 1677 cm$^{-1}$ arises which can be attributed to the asymmetric C=O stretching vibration of MSN-PVP-COOH. This band shifts after PEGylation, implying a successful attachment of PEG. In order to show the ability of poly(2-vinylpyridine) to act as a pH responsive cap system, nitrogen sorption measurements were performed (Figure 5.2C). To observe the open form (MSN-PVP$_{open}$), the particles where dried from a 0.01 M HCl dispersion at 60 °C; this was expected to keep the protonated PVP functionalized MSN in an open state. The closed state could be measured after drying from a dispersion in millipore water (pH 7). In the open state, the mesopores are highly accessible, whereas the polymer completely blocks the pores in the closed state, even for very small molecules like nitrogen. The BET surface area of 51 m$^2$/g in the closed state is in very good accordance with an estimated external BET surface area of 45 m$^2$/g of dense spheres with similar density and diameter. The BET surface area of 51 m$^2$/g for MSN-PVP$_{closed}$ corresponds to a reduction in surface area of 95% compared with MSNs without polymer cap system (MSN-NH$_2$), indicating that the surface of the pore walls after blocking is not even accessible for nitrogen. The key features of the different MSNs are summarized in Table 5.1.

**Table 5.1:** Nitrogen physisorption data of MSN-NH$_2$ and MSN-PVP.

| Sample | BET surface area [m²/g] | Pore size[a] [nm] | Pore volume[b] [cm³/g] |
|---|---|---|---|
| MSN-NH$_2$ | 1097 | 3.8 | 0.79 |
| MSN-PVP$_{open}$ | 617 | 3.4 | 0.36 |
| MSN-PVP$_{closed}$ | 51 | - | - |

[a]DFT pore size refers to the peak value of the pore size distribution. [b]Pore volume is calculated up to a pore size of 8 nm to remove the contribution of interparticle porosity.

The decrease of the specific surface area in the sample MSN_PVP$_{open}$ can be explained by the addition of non-porous PVP and the blocking of some pores by frozen polymer on the surface layer of the MSNs. This effect is comparably large due to the length of the PVP.
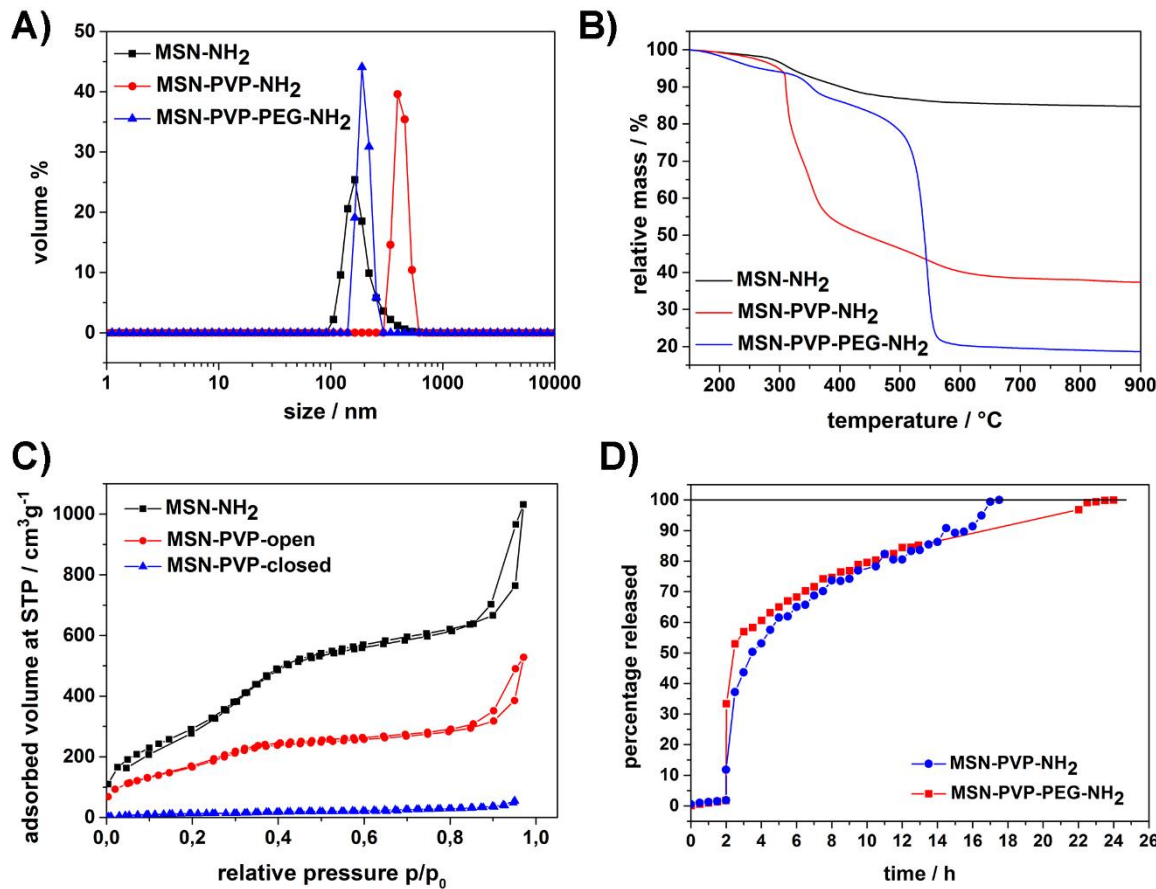


**Figure 5.2:** Characterization of the MSN system **A)** Dynamic light scattering data of MSN-NH$_2$ (black), MSN-PVP-NH$_2$ (red) and MSN-PVP-PEG-NH$_2$ (blue) **B)** Thermogravimetric analysis of MSN-NH$_2$ (black), MSN-PVP-NH$_2$ (red) and MSN-PVP-PEG-NH$_2$ (blue). The curves are normalized at 150 °C, **C)** Nitrogen physisorption measurements of MSN-NH$_2$ (black), MSN-PVP in the open state of the polymer (red) and MSN-PVP-closed (blue). **D)** Time-based fluorescence release experiment of MSN-PVP-NH$_2$ (blue) and MSN-PVP-PEG-NH$_2$ (red) with fluorescein as cargo.

***In vial* fluorescence release experiments.** The pH-responsive opening of the polymer cap system was demonstrated by time-based fluorescence release experiments with our custom-made release set-up.[33] Therefore, a distinct amount of fluorescein-loaded MSN-PVP-NH$_2$ (Figure 5.2D, blue curve, or MSN-PVP-PEG-NH$_2$ (red), respectively) were measured in the closed state of the polymer for 2 h before the sample was acidified, allowing a subsequent opening of the pores and the diffusion of cargo molecules. All intensity values are normalized to the highest obtained fluorescence counts of the respective sample. Therefore, the

highest amount released is set to 100% relative release. The pH-dependent release curves show the striking capping effect of the poly(2-vinylpyridine) cap system. At pH 7, the polymer is in its hydrophobic state and thus successfully blocks the pores of the MSNs until the release is triggered by decreasing the pH. In acidic media, the polymer changes into its water soluble hydrophilic state through protonation, which allows the cargo to diffuse out of the pores. No significant changes in release kinetics are observed by further attachment of PEG compared with sample MSN-PVP (Figure 5.2D). Long-term release experiments showed that even after 16 h, the premature release is less than 4% in the closed state of the polymer (cf. appendix 5.13).

**Stability tests of the nanoparticles**

Previous studies on the effect of functionalizations of MSNs on the bio-degradation demonstrated the fast degradation of unfunctionalized MSNs in simulated body fluids. The attachment of poly(ethylene glycol) increased the stability drastically up to days, whereas the un- or organo-silane functionalized MSNs lost their porosity in the first hours of incubation. During the partial hydrolysis and dissolution of the silica material, hydroxyapatite layers precipitated on the surface of the silica by adsorption of $Ca^{2+}$ ions in the porous system and via hydrogen bonding of $PO_4^{3-}$ ions.[10, 34] The functionalization with PEG already exhibited a very good improvement of the MSN stability, but the PEG-layer does not close the pores of the MSNs. Therefore, the protection of the pores relies on a shielding mechanism, whereas in the case of PVP the particles are completely protected from the environment as long as they stay in neutral or basic milieu. The stability of the MSNs was tested i) in bio-fluids and ii) for storage purposes in order to estimate shelf life. Biostability assays were performed to test whether the polymer cap system will prevent the mesoporous silica nanoparticles from degradation. This was done using Dulbecco's Modified Eagle's Medium (DMEM) at 37 °C at two different pH values (5 and 7). As a widely used basal medium for growing many mammalian cells, DMEM contains various amino acids, vitamins and inorganic salts, among other ingredients and is used to simulate a biological environment. A certain amount of sample was removed after specific times (2 h, 4 h and 24 h), washed thoroughly and dried. The nanoparticles were then characterized with transmission electron microscopy and nitrogen sorption. TEM images show significant degradation of the nanoparticle structure for unfunctionalized MSNs after 24 h immersion at pH 7 (Figure 5.3B), which is in good accordance with results of similar

experiments reported earlier.[10] In contrast, nanoparticles functionalized with PVP offer very good stability in DMEM at pH 7 (Figure 5.3C). At this pH, the polymer cap system forms a tight, hydrophobic, and therefore impermeable shield against water, proteins and salts around the MSNs. Additionally, the polymer shell also improves the stability of the MSNs in DMEM at pH 5, where the cap system is in its open state (Figure 5.3D). In comparison with uncoated nanoparticles, MSN-PVP-PEG particles show less degradation, which was also confirmed by nitrogen sorption experiments (Figure 5.4). In both cases, in the open and the closed state of the cap system, no changes in the pore size distribution were observed, indicating that the pores are not affected by the medium and no degradation of the mesoporous framework did occur.
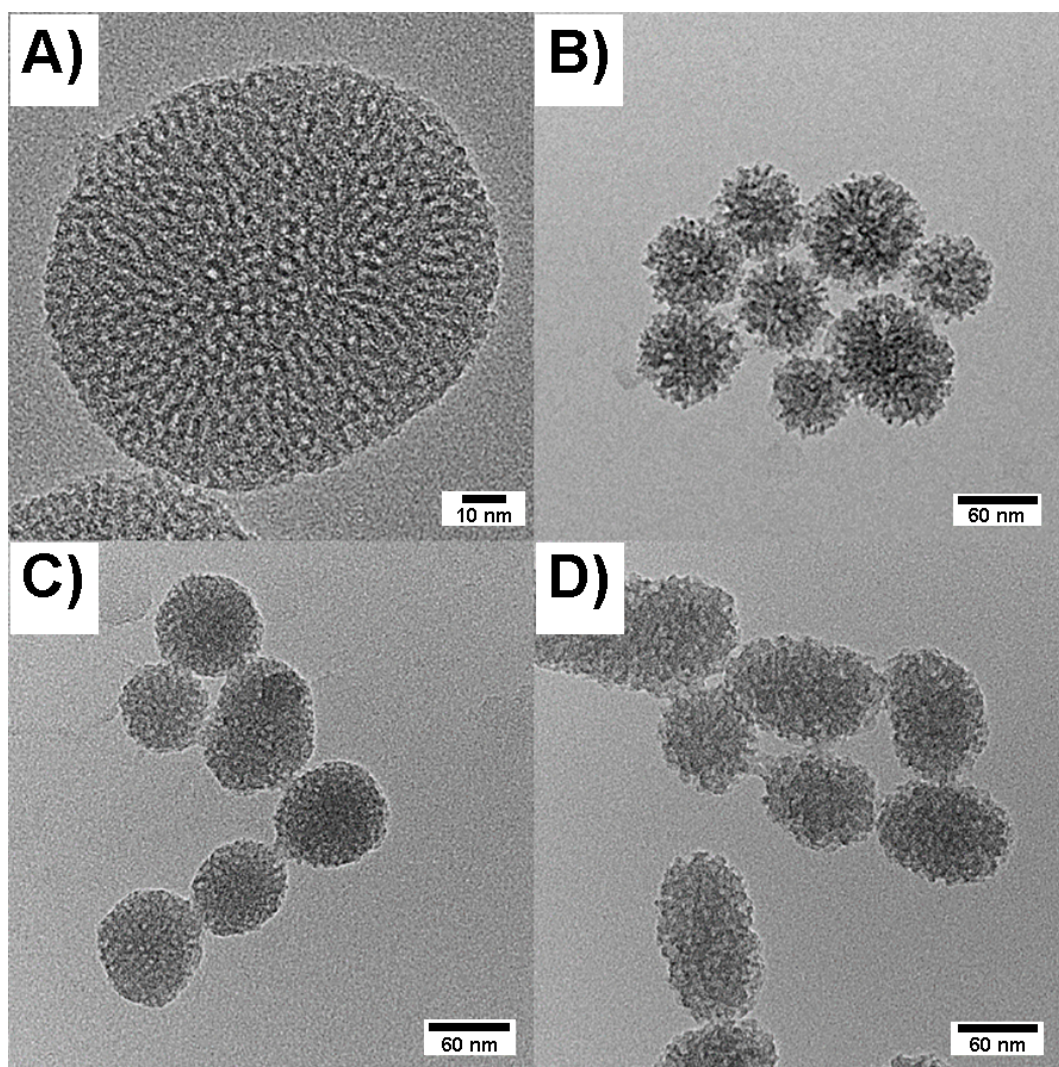


**Figure 5.3:** TEM micrographs of **A)** template-free, untreated MSN-NH$_2$, **B)** MSN-NH$_2$ after 24 h incubation in DMEM, **C)** MSN-PVP-PEG at pH 7 (closed state) after 24 h in DMEM and **D)** MSN-PVP-PEG incubated in DMEM at pH 5 (open state) after 24 h.
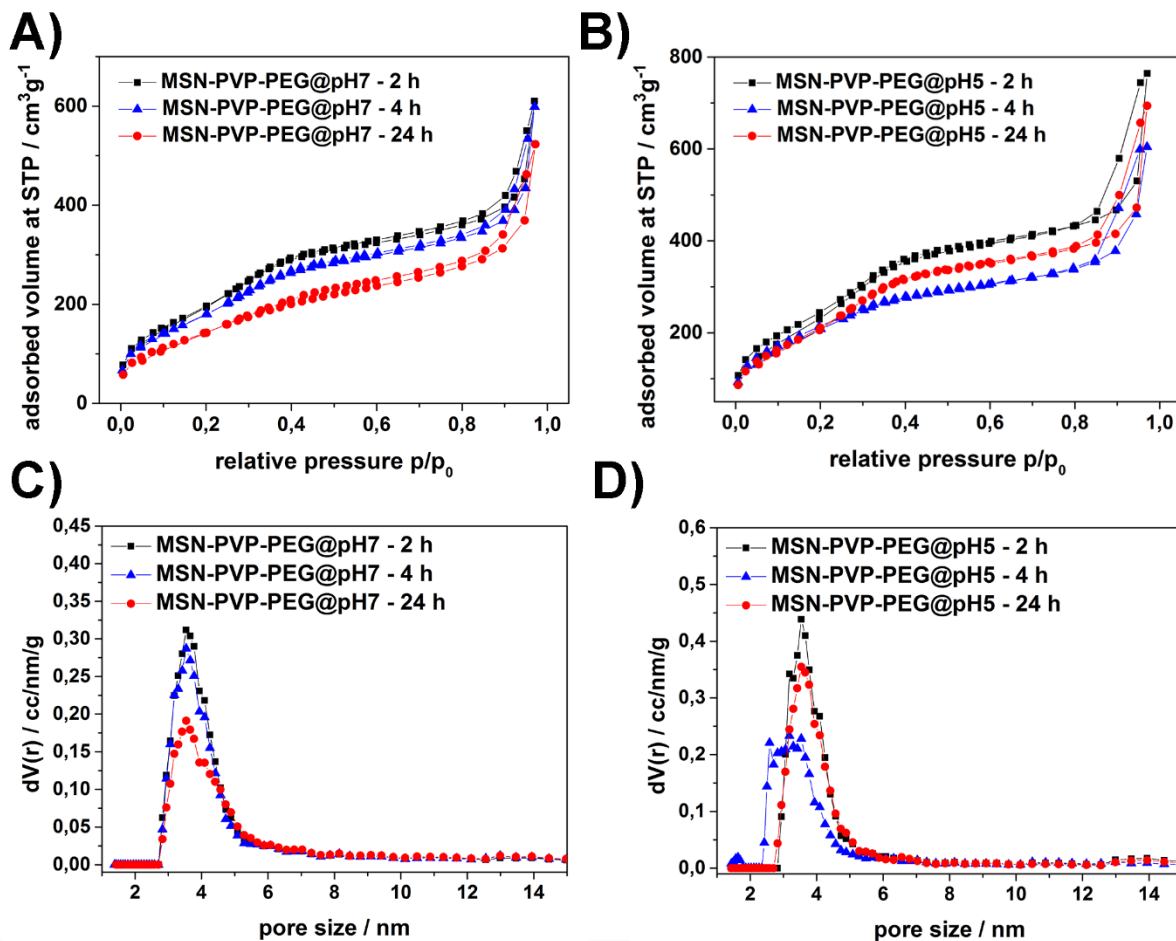
**Figure 5.4:** Nitrogen physisorption data of MSN-PVP-PEG after immersion in DMEM at different pH values after 2 h (black), 4 h (blue) and 24 h (red). **A)** Nitrogen sorption isotherms of MSN-PVP-PEG at pH 7, **B)** nitrogen sorption isotherms after immersion in DMEM at pH 5, **C)** pore size distributions of MSNs for different immersion times in DMEM at pH 7 and **D)** at pH 5 after distinct times.

In order to test the stability of the MSNs under storage conditions, the functionality of 4-week-old particles (stored at 4 °C) could be verified with *in vitro* release experiments (cf. appendix 5.13). After storage in water (and therefore in a closed state of the PVP) the particles retain the same calcein release behavior in cells (cf. appendix 5.15). Additionally, drying and re-dispersion of MSN-PVP-PEG-NH$_2$ in water exhibits no significant agglomeration of the particles or any other visible change of their solution behaviour (DLS cf. appendix 5.16). This remarkable behavior is exceptional for mesoporous silica nanoparticles; the common response to drying is serious agglomeration that cannot even be broken with ultrasound. Based on the re-dispersibility of the nanoparticles after drying, a long shelf life of the nanoparticles is expected.

**Targeting.** To design an effective drug delivery system, a targeting system is highly desirable. Generally one can distinguish between passive and active targeting. Modifications such as attaching PEG at the surface of the delivery system provide shielding against undesired interactions, and therefore favor the enhanced permeability and retention effect (passive targeting). Active targeting, on the other hand, takes advantage of the overexpression of certain receptors on diseased cells by attachment of the corresponding targeting ligand to the delivery vehicle.[35] Accordingly, active targeting was shown *in vitro* using the example of folic acid (FA) receptor targeting on KB cells.

***In vitro* cellular model.** The attachment of active targeting ligands is important for creating a functional drug delivery system.[35] Folic acid was chosen as targeting ligand because it is an ideal model system for targeting with a small molecule and is also believed to be a promising candidate for clinical applications.[36] Furthermore, the covalent binding of folic acid to the particles can be achieved with an EDC-mediated coupling and could be easily substituted by other targeting ligands without changing the coupling chemistry. To demonstrate the functionality of the particles, they were incubated with KB cells, which are known to overexpress FA-receptors.[36] In a competition experiment, with either free folic acid to block the FA-receptors or with uninhibited FA-receptors, the uptake of MSN-PVP-PEG-NH$_2$-FA particles and hence the targeting abilities were monitored. For the visualization of nanoparticle-uptake, z-stacks of the cells were recorded with a spinning disk confocal fluorescence microscope, which allowed to detect MSNs inside or outside the cells after staining the cell membrane.
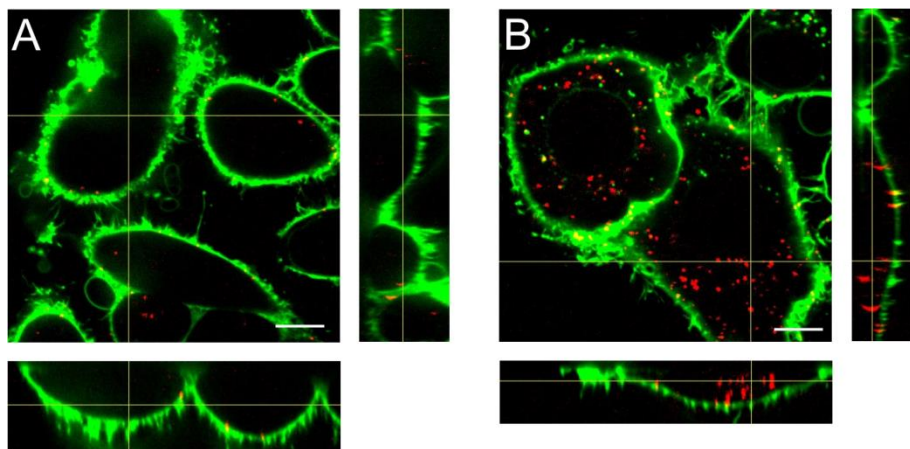
**Figure 5.5:** Unspecific and receptor-mediated uptake of MSN-PVP-PEG-NH$_2$-FA particles by KB cells. **A)** Incubation of MSN-PVP-PEG-NH$_2$-FA particles with FA pre-incubated KB cells for 2 h at 37 °C. **B)** Incubation of MSN-PVP-PEG-NH$_2$-FA particles with KB cells, no free FA in cell culture medium, for 2 h at 37 °C. The KB cell membrane is shown in green (dye WGA 488) and the particles in red (dye Atto-633). Orthogonal views are given to illustrate the uptake more clearly. The scale bars represent 10 μm.

In Figure 5.5, typical confocal cuts through the cells together with the orthogonal projection are shown. In the case of pre-incubation with free folic acid, only a few individual particles are present inside the cells (Figure 5.5A), and also in the full stacks the quasi-absence of nanoparticles is noted, independent of the chosen focal plane. In contrast, incubation of MSN-PVP-PEG-NH$_2$-FA on KB cells without pre-incubation of FA resulted in significant uptake of particles (Figure 5.5B). The particles appear in the representative z-slice as well as in the entire height of the cell as shown in the orthogonal views. In the case of blocked receptors, only unspecific uptake is expected to occur, therefore the results demonstrate the specific folate-receptor mediated endocytosis within two hours with only a minor rate of unspecific uptake.

**Release experiments.** To verify the release properties of the particle-system, several experiments were performed. First, as already described above, the pH dependency was tested *in vial* with time-based fluorescence spectroscopy at pH 7 and pH 5 (Figure 5.2D). In a second approach, the multifunctional MSNs were tested *in vitro*. For these experiments, membrane-permeable (DAPI) and impermeable (calcein) dyes were adsorbed in the mesopores of the MSNs and the dye-loaded nanoparticles were incubated with cells to prove the

functionality of the system on a cellular level. Membrane-impermeable cargos can't escape the endosomal compartments, therefore a photosensitizer (AlPcS$_{2a}$) was covalently attached to the outer surface of the sample MSN-PVP-PEG.[14]

*In vitro.* The controlled release of cargo inside the desired tissue is one of the greatest challenges in drug delivery. Many systems have been developed and characterized, including fusion, redox-sensitive systems and photoactivation.[30] Some of these systems already exhibit a good temporal and spatial control of the cargo release. But once they are activated, the release of the cargo is continuous, even if the particles leave the tissue of interest. One advantage of our newly developed system is the reversibility of the pore opening. If the pH of the environment turns neutral again, it is assumed that PVP will seal the pores again and the delivery system can circulate safely inside the blood system.

**By photoactivation.** In the first experiments, MSN-PVP-PEG particles loaded with calcein were incubated on HeLa cells for 20 h. The incubation time is long enough to allow the endosomal acidification.[37] However, the fluorescence colocalization of the membrane-impermeable cargo calcein and the covalently bound dye Atto-633 remained (cf. appendix 5.19). Calcein is a membrane impermeable cargo and therefore is not able to exit intact endosomal compartments without external trigger, but it should be released inside the endosomal compartment. For membrane-impermeable cargos the system had to be further enhanced to induce endosomal escape. Thus the photosensitizer AlPcS$_{2a}$ (PS) was covalently linked to the PEG-chains, in addition to the pH-sensitive polymer on the particle surface. Endosomal escape was expected to occur after acidification of the endosomes and activation of the photosensitizer with red laser light. After activation with red laser light (639 nm, 1.2 W/mm$^2$) singlet oxygen is produced, which can destroy the endosomal membrane. We emphasize that the lifetime of the singlet oxygen is very short (around $2 \times 10^{-7}$ s)[38], thus its diffusion range is limited and therefore the cargo and also the cell membrane should stay intact, due to the spatial separation of cargo, cell membrane and PS. Moreover, the red light used for activation of the photosensitizer is in a useful region for medical applications and is already used in photodynamic therapy.[39] For the photoactivated release experiment, MSN-PVP-PEG-AlPcS$_{2a}$/FA particles were incubated on HeLa cells for 18 h. Calcein and PS are perfectly co-localized (yellow spots, Figure 5.6C) after endocytosis of the MSNs. Directly after 1 min photoactivation with 1.2 W/mm$^2$ of 639 nm light, calcein-spreading over the whole cell can be observed, and the calcein-fluorescence gets brighter over time due to de-quenching

of the dye upon escape from the MSN host (Figure 5.6C, I, M). In comparison to the emission from calcein, the fluorescence of the photosensitizer stays localized in the same dot-like pattern as prior to the photoactivation, only the intensity is reduced because of photobleaching effects after the activation (Figure 5.6F, J, N). The intensity profile along the white line, indicated in the merged pictures, depicts the fluorescence increase due to calcein more clearly (Figure 5.6D, H, L, P). The cargo release can also be visualized with a constant PS-activation and simultaneous observation of calcein fluorescence (over a period of 8 min; cf. appendix 5.18). Strikingly, a significant part of the cargo appears to be released inside the cell already within two minutes.
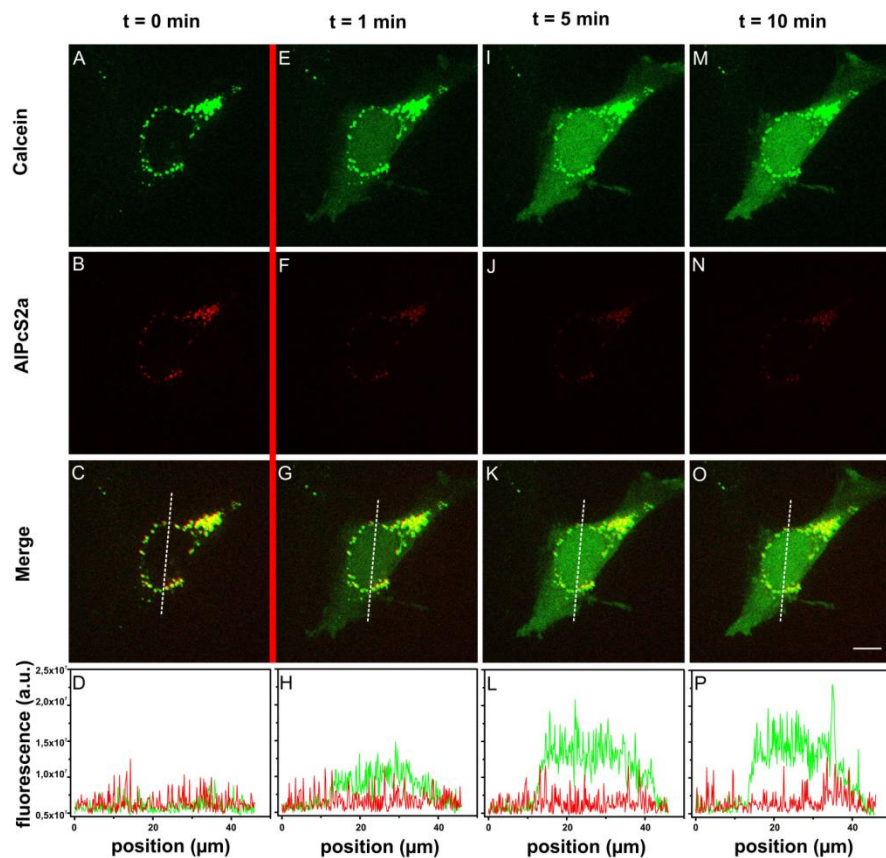


**Figure 5.6:** Fluorescence microscopy of MSN-PVP-PEG-AlPcS$_{2a}$-FA nanoparticles loaded with calcein after 18 h incubation on a HeLa cell. **A-C)** Calcein (green) and AlPcS$_{2a}$ (red) are co-localized (yellow) prior to photoactivation. **D)** Intensity profile along the white line in the merged image. The red line indicates photoactivation with 1.2 W/mm$^2$ of red light (639 nm). **E-H)** after 1 min photoactivation, **I-L)** 5 min after photoactivation, **M-P)** 10 min after photoactivation. The scale bar represents 10 µm.

The above results were compared to those of incubation experiments of cells with a solution of free calcein and PS. We also observe that the free PS is spreading over the whole cell. If the PS is not covalently bound to the nanoparticles, the molecules can diffuse inside the entire cell and can cause much more damage to the cell membrane and other organelles due to their greater proximity.

**By pH-sensitivity with membrane-permeable cargos.** To safely deliver membrane-permeable cargos like DAPI[40] or colchicine[41] inside cells with our newly developed system, the implementation of additional endosomal escape mechanisms is not necessary. It is anticipated that the particles will be taken up in endosomal compartments, and in the following the endosomes get acidified. This drop in pH from around 7 to approximately 5 results in the solvation of poly(2-vinyl pyridine) and thus in release of the cargo from the pores into the endosome, and consequently into the cytosol if it diffuses through the endosomal membrane. On the other hand, if the particles get exocytosed the pH will increase and poly(2-vinyl pyridine) will turn insoluble again. In this case the cargo will stay inside the particles and the latter can circulate again and possibly find a new target cell. DAPI and colchicine were used as model systems to examine the delivery of membrane permeable cargo. DAPI preferentially stains dsDNA and thereby produces a fluorescence enhancement of around 20-fold.[42] Figure 5.7 shows the staining of the nucleus after several time intervals. Shortly after incubation only a weak staining of the nucleus can be seen, after 15 h the nucleus is clearly visible and after 46 h even the region of the endoplasmic reticulum gets stained. Because of the slowly increasing and very strong DAPI-fluorescence signal after several hours of incubation, it could be excluded that the staining is due to free DAPI in the particle solution. In the case of free DAPI in the solution, the staining would be expected to be detectable shortly after addition, as the typical incubation time for nucleus staining with free DAPI in solution is only between 1 - 5 minutes.
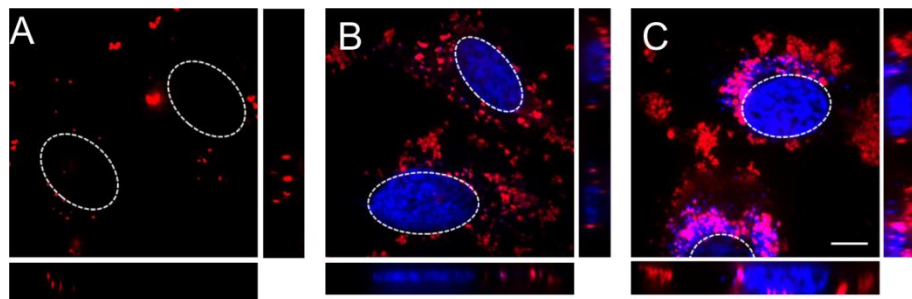
**Figure 5.7:** Fluorescence microscopy of HeLa cells incubated with DAPI-loaded MSN-PVP-PEG. MSN-PVP-PEG loaded with DAPI (blue) and labeled with Atto 633 (red) after **A)** 15 min **B)** 15 h and **C)** 46 h incubation with the cells. The nucleus region is indicated with dashed white lines. The scale bar represents 10 μm.

## 5.3 Conclusion

In this work, we have developed a multifunctional drug delivery vehicle based on polymer-functionalized mesoporous silica nanoparticles. This system combines attractive features such as the high loading capacity of MSNs with the tuneable functionality of a polymer. The use of bi-functionalized polymer blocks allowed us to covalently attach step-by-step many functionalities of interest. We demonstrate that covalently bound poly(2-vinylpyridine) in combination with a PEG-block acts as a pH-responsive cap system for MSNs. With this system, we show the successful delivery of different cargos into cells. Membrane permeable cargos were delivered without any external trigger, because such cargos can penetrate the endosomal membrane. Covalent attachment of a red-light-photosensitizer offered the possibility to open the endosome through irradiation with laser light, and to deliver membrane-impermeable cargos. Effective targeting of folic acid receptor expressing cells was enabled by the covalent attachment of folic acid. Stability tests revealed the effectiveness of poly(2-vinylpyridine) not only as cap system, but also as a highly effective protecting agent for MSNs against aggressive body fluids. Strikingly, the polymer-coated nanoparticles can even be dried and then re-dispersed in water without agglomeration. This extraordinary feature bodes well for a long shelf life of the dried particles. Biodistribution experiments *in vivo* revealed no particle agglomeration and showed preferred liver accumulation. The modified and unmodified MSN particles were well tolerated in mice without causing side-effects. With this new system we have developed a multifunctional toolbox based on MSNs that is able to open and close its cap

system depending on the environment. One major advantage of our system derives from the covalent attachment of all components, which allows the system to operate for several cycles. We anticipate that the possible integration of almost any functionality of interest as well as the efficient synthesis make this system promising for wide-ranging biological and medical applications, especially in cancer therapy.

## 5.4 Experimental

**Chemicals**

All reagents were purchased from commercial suppliers: tetraethyl orthosilicate (TEOS, Fluka, >98%), cetyltrimethylammonium bromide (CTAB, Aldrich, 95%), (3-aminopropyl) triethoxysilane (APTES, Fluka, 95%), (3-mercaptopropyl)triethoxysilane (ABCR), $N$-(3-dimethylaminopropyl)-$N$-ethylcarbodiimide hydrochloride (EDC, Fluka, 97%), α-amino-ω-carboxy terminated poly(2-vinylpyridine) (NH$_2$-PVP-COOH, Polymer source, M$_n$ = 10000, PDI = 1.08), α,ω-polyethyleneglycolbisamine (NH$_2$-PEG-NH$_2$, Aldrich, M$_n$ = 2000), Boc anhydride (Aldrich, 95%), folic acid (Sigma, 99%), aluminum (lll) phthalocyanine chloride tetrasulfonic acid (AlPcS$_{2a}$, Frontier Scientific), $N$-hydroxysulfosuccinimide sodium salt (Sulfo-NHS, Aldrich, 98%), 4,6-diamidino-2- phenylindole dihydrochloride (DAPI, ≥98%), Bis[N,N−bis(carboxymethyl) aminomethyl] fluorescein (calcein), Folic Acid (FA, >97 %). Doubly distilled water from a Millipore system (Milli-Q academie A-10) was used for all syntheses and purification steps. All solvents and buffer contents above were purchased from Sigma-Aldrich. Wheat germ agglutinin (WGA) Alexa Fluor 488 conjugate (Invitrogen), Atto-633 maleimide (ATTO-TEC). Unless otherwise noted, all reagents were used without further purification.

**Synthesis procedures.**

**Preparation of shell-functionalized colloidal mesoporous silica nanoparticles (MSN-NH$_2$).**
MSN nanoparticles were prepared by a delayed co-condensation approach as described earlier by Cauda et al.[1] In detail, a two phase mixture of TEA (14.3 g) and TEOS (1.9 g, 9.12 mmol) was heated at 90 °C for 20 minutes without stirring. After removal of the oil bath, a preheated (60 °C) solution of CTAC (2.14 mL, 1.62 mmol, 25 wt% in H$_2$O) and water (21.7 g) was added and stirred afterwards at 500 rpm for 30 min at room temperature. Subsequently, a mixture of 3-aminopropyltriethoxysilane (22.5 µL, 96 µmol) and TEOS (20.5 µL, 92 µmol) was added.

The resulting solution was stirred overnight at room temperature at 500 rpm. Extraction of the organic template was achieved by heating the ethanol-suspended sample (10 mg/mL) under reflux at 90 °C for 1 h in a mixture of 2 g ammonium nitrate and 100 mL ethanol. Afterwards, the sample was centrifuged for 20 min (19000 rpm, 43146 rcf), re-dispersed in ethanol and heated under reflux at 90 °C in a solution of 8 mL concentrated HCl and 32 mL ethanol for 45 minutes. After centrifugation, the particles were re-dispersed in ethanol, resulting in a colloidal suspension.

**Protection of NH$_2$-PVP-COOH (Boc-PVP-COOH).** To a solution of NH$_2$-PVP-COOH (500 mg, 5 µmol) in  10 mL dry dichloromethane, triethylamine (15 µL, 0.11 mmol) and Boc anhydride (15 mg, 6.9 µmol) were added. The solution was stirred overnight and extracted several times with brine. The organic phase was dried over MgSO$_4$ and the solvent removed *in vacuo* to yield the Boc protected polymer. The polymer was used without further purification.

**General procedure for the attachment of poly(2-vinyl pyridine) to MSN-NH$_2$ (MSN-PVP-Boc).** To a colloidal solution of MSN-NH$_2$ (50 mg), tetrahydrofuran (THF, 10 mL) and the Boc protected polymer (60 mg, 5.6 µmol) dissolved in 1.5 mL THF was added. The amidation was activated by the addition of EDC (10 µL, 57.2 µmol) and *sulfo*-NHS (1.3 mg, 6 µmol). The mixture was stirred at room temperature for 12 h. Afterwards the particles were separated by centrifugation (19000 rpm, 43146 rcf, 20 min) and washed 3 times by repeated centrifugation and re-dispersion in 30 mL THF.

**Deprotection of MSN-PVP-Boc (MSN-PVP-NH$_2$).** Deprotection of the polymer was achieved through stirring 10 mg polymer functionalized particles in a mixture of 2 mL trifluoroacetic acid and 8 mL water for 24 h. After deprotection, the particles were extensively washed by centrifugation (19000 rpm, 43146 rcf, 20 min) and re-dispersion in a mixture of 0.01 M HCl and EtOH.

**Conversion of MSN-PVP-NH$_2$ to MSN-PVP-COOH.** 10 mg MSN-PVP-NH$_2$ in 2 mL EtOH were reacted with a large excess of oxalic acid (5 mg, 55 µmol) and EDC (9 µL, 51 µmol) for 1 h. Afterwards, the particles were extensively washed by centrifugation (19000 rpm, 43146 rcf, 20 min) and re-dispersion in a mixture of 0.01 M HCl and EtOH.

**PEGylation of MSN-PVP-COOH (MSN-PVP-PEG-NH$_2$).** To a colloidal solution of MSN-PVP-COOH (1 mg) in 500 µL EtOH, NH$_2$-PEG-NH$_2$ (2 mg, 100 nmol – dissolved in

500 µL bi-distilled water) was added, Afterwards, EDC (0.5 µL, 2.8 µmol) was added and the reaction was allowed to stir at ambient temperature for 1 h. The sample was purified by subsequent centrifugation (4 min, 14000 rpm, 16873 rcf) with a mixture of EtOH:water (1:1). The washing step was repeated three times with 1 mL each.

**Attachment of folic acid to MSN-PVP-PEG-NH$_2$ (MSN-PVP-PEG-NH$_2$-FA).** The amino functionalities of MSN-PVP-PEG-NH$_2$ (1 mg, in 1 mL EtOH:water 1:1) were partially reacted with folic acid (0.44 µg, 1 nmol). Subsequently, EDC (0.5 µL, 2.8 µmol) and a catalytic amount of *sulfo*-NHS (~1 mg) was added. After 1 h, the sample was washed 3 time by subsequent centrifugation (4 min, 14000 rpm, 16873 rcf) and re-dispersion with a mixture of EtOH:water 1:1.

**Attachment of AlPcS$_{2a}$ to residual amino groups of MSN-PVP-PEG-NH$_2$-FA (MSN-PVP-PEG-FA- AlPcS$_{2a}$).** To the sample MSN-PVP-PEG-NH$_2$-FA (1 mg) in 1 mL DMSO:water 1:1 20 µL of AlPcS$_{2a}$ (1 mg/mL in DMSO) were added. The resulting mixture was stirred at room temperature in the dark for 24 hours. The sample was washed extensively with DMSO:water 1:1 by repeated centrifugation (4 min, 14000 rpm, 16873 rcf) and re-dispersion until no photosensitizer could be detected in the supernatant.

**Release experiments:**

**Drug/dye loading.** 1 mg MSN-PVP-PEG-NH$_2$ were dispersed in 500 µL of a 1 mM drug/dye solution in water. To open the pores and enable the uptake, 50 µL of citrate buffer (pH 2) were added. The particles were stirred overnight, centrifuged, and re-dispersed in 1 mL SSC buffer (pH 7) to trigger closure of the polymer shell. The particles were washed extensively with SSC buffer until no fluorescence was detected in the supernatant.

***In vial* fluorescein release:** 1 mg fluorescein loaded MSN-PVP-NH$_2$ or MSN-PVP-PEG-NH$_2$ were re-dispersed in 200 µL SSC buffer and transferred to the cap of the fluorescence cuvette. This cap was sealed with a dialysis membrane (molecular weight cutoff of 16000 g/mol) and placed on top of the fluorescence cuvette, which was also filled with SSC buffer. The "release" of fluorescein out of the closed particles was monitored for 2 h ($\lambda_{ex}$ = 490 nm, $\lambda_{em}$ = 512 nm). Subsequently, the cap was removed and the particles were centrifuged and re-dispersed in 200 µL citrate-phosphate buffer (pH 5), before being put into the cap of the release setup. The fluorescence cuvette was also filled with citrate-phosphate buffer (pH 5). After reassembling

the release setup, the release of fluorescein was continuously measured for 10 h. For comparison of the obtained curves, calibration curves of fluorescein in SSC buffer (pH 7) and in citrate-phosphate buffer (pH 5) were recorded.

**Characterization.** All samples were investigated with a FEI Titan 80-300 operating at 300 kV with a high-angle annular dark field detector. A droplet of the diluted MSN solution in absolute ethanol was dried on a carbon-coated copper grid. Nitrogen sorption measurements were performed on a Quantachrome Instruments NOVA 4000e. All samples (15 mg each) were heated to 60 °C for 12 h in vacuum (10 mTorr) to outgas the samples before nitrogen sorption was measured at 77 K. Pore size and pore volume were calculated by a NLDFT equilibrium model of $N_2$ on silica, based on the desorption branch of the isotherms. In order to remove the contribution of the interparticle textural porosity, pore volumes were calculated only up to a pore size of 8 nm. A BET model was applied in the range of $0.05 - 0.20$ $p/p_0$ to evaluate the specific surface area of the samples. Centrifugation was performed using a Sorvall Evolution RC equipped with a SS-34 rotor or an Eppendorf centrifuge 5418 for small volumes. Raman spectra were recorded on a Jobin Yvon Horiba HR800 UV Raman microscope using a He-Ne laser emitting at $\lambda = 633$ nm. Dynamic light scattering (DLS) measurements were performed on a Malvern Zetasizer-Nano instrument equipped with a 4 mW He-Ne laser (633 nm) and an avalanche photodiode. The hydrodynamic radius of the particles was determined by dynamic light scattering in ethanolic suspension. For this purpose, 100 µL of an ethanolic suspension of MSN particles (ca. 10 mg/mL) was diluted with 3 mL of ethanol prior to the measurement. Zeta potential measurements of the samples were performed on a Malvern Zetasizer-Nano instrument equipped with a 4 mW He-Ne laser (633 nm) and an avalanche photodiode. Zeta potential measurements were performed using the add-on Zetasizer titration system (MPT-2) based on diluted NaOH and HCl as titrants. For this purpose, 1 mg of the particles was diluted in 10 mL bi-distilled water. IR measurements were performed on a Bruker Equinox 55 FTIR/FTNIR Spectrometer in absorbance mode (spectra were background substracted). Thermogravimetric analysis was performed on a Netzsch STA 440 C TG/DSC with a heating rate of 10 K / min in a stream of synthetic air of about 25 mL/min. The mass was normalized to 100% at 150 °C for all samples. UV-VIS spectra were recorded with a NanoDrop ND 1000 spectrometer. Usually, 2 µL of sample were used and all presented spectra are background corrected for water absorption.

## Cell culture and *in vitro* Experiments

**Cell culture.** KB cells were grown in folic acid deficient Roswell Park Memorial Institute 1640 medium (RPMI 1640, Invitrogen) supplemented with 10% fetal bovine serum (FBS). HeLa cells were grown in Dulbecco's modified Eagle's medium (DMEM):F12 (1:1) (Invitrogen) with Glutamax I medium supplemented with 10 % FBS. Tubulin-GFP expressing HuH7 cells were grown in Dulbecco's modified Eagle's medium : F12 (1:1) supplemented with 10% FBS. All cells were cultured at 37 °C in a 5% $CO_2$ humidified atmosphere. KB cells were seeded on ibidiTreat µ-Slides (IBIDI). HeLa and tubulin GFP expressing HuH7 cells were seeded on collagen A - coated LabTek chambered cover glass (Nunc). For live cell imaging the cells were seeded 48 or 24 h before measuring, at a cell density of $1x10^4$ or $2x10^4$ cells / $cm^2$, respectively.

**Spinning disc confocal microscopy.** Live-cell imaging was performed on a confocal setup based on the Zeiss Cell Observer SD, utilizing a Yokogawa spinning disc unit CSU-X1. The system was equipped with a 1.40 NA 100x or 63x Plan apochromat oil immersion objective from Zeiss. The exposure time was 0.1 s for all experiments und the frame rate varied between 3 frames / s and 1 frame / 30 s, depending on the experiment. Calcein, WGA 488 and GFP were imaged with approximately 0.39, 0.29 and 1.1 W/$mm^2$ of 488 nm excitation light. Atto-633 was imaged with approximately 0.06 W/$mm^2$ of 639 nm excitation light and DAPI with 0.16 W/$mm^2$, respectively. The photosensitizer AlPcS$_{2a}$ was excited with approximately 0.12 W/$mm^2$ at 639 nm for imaging and with 1.2 W / $mm^2$ for photoactivation. A quad-edge dichroic beamsplitter (FF410/504/582/669-Di01-25xx36, Semrock) was used in the excitation path. For the two-color detection of calcein and AlPcS$_{2a}$, WGA 488 and Atto 633 or GFP and Atto 633, a dichroic mirror (660 nm, Semrock) and band-pass filters 525 / 50 and 690 / 60 (both semrock) were used in the detection path. Separate images for each fluorescence channel were acquired using two separate electron multiplier charge coupled device (EMCCD) cameras (Photometrics Evolve$^{TM}$)

**Uptake studies.** The functionality of the folic acid targeting ligand was evaluated in a receptor competition experiment. For this purpose, one part of the KB cells was preincubated with 3 mM folic acid (Sigma), to block the receptors, for 2 h at 37 °C under a 5% $CO_2$ humidified atmosphere. Then the KB cells were incubated with particles (MSN-PVP-PEG-FA, covalently labeled with Atto 633; 25 µg / mL) for 2 h at 37 °C under a 5% $CO_2$ humidified atmosphere. After the incubation the cells were washed three times with PBS (Invitrogen), and 4% paraformaldehyde (PFA, Science Service) was added for 15 min. The PFA was removed and

the cells were washed again three times with PBS. For staining the cell membrane, the cells were incubated with a final concentration of 10 μg/mL wheat germ agglutinin Alexa Fluor 488 conjugate (WGA 488, Invitrogen) for one minute. The cells were washed once with PBS and imaged.

**Cargo release Experiments.** To measure the photoactivated cargo release the cells were incubated with particles (MSN-PVP-PEG-AlPcS$_{2a}$-FA, 25 μg/mL) for 16-20 h at 37 °C under a 5% $CO_2$ humidified atmosphere. For imaging the medium was replaced by $CO_2$-independent medium (Invitrogen), during the measurements the cells were kept on a heated microscope stage at 37 °C. For activation of the photosensitizer, the cells were irradiated with 1.2 W/mm$^2$ of 639 nm light for 1 min. The release of cell-membrane permeable cargo due to pH-dependent opening of the PVP-coating inside the endosomes was also measured.

## 5.5 Appendix
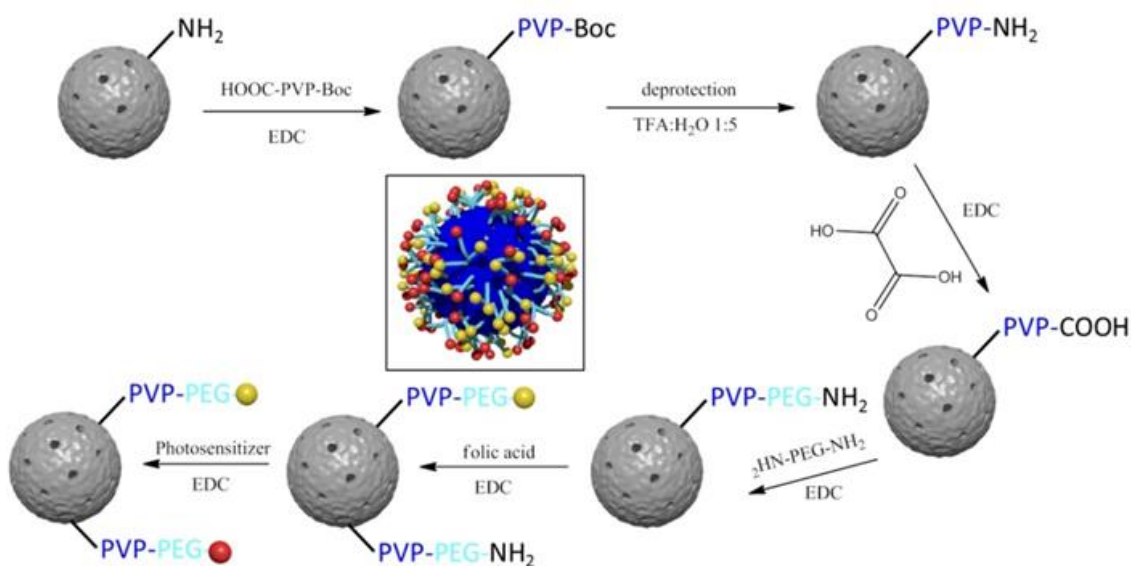


**Figure 5.8:** Synthesis pathway of a fully functionalized mesoporous silica nanoparticle.
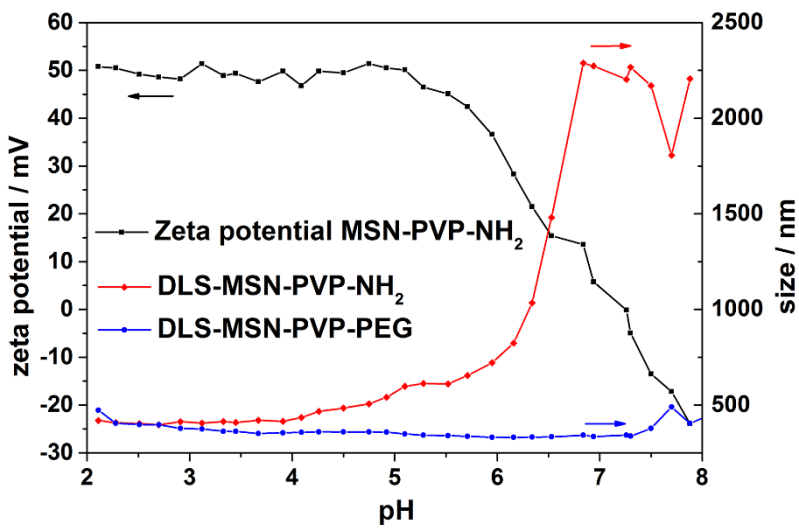
**Figure 5.9:** Titration experiments showing the zeta potential of MSN-PVP (black), and dynamic light scattering of MSN-PVP (red) and MSN-PVP-PEG (blue), respectively.
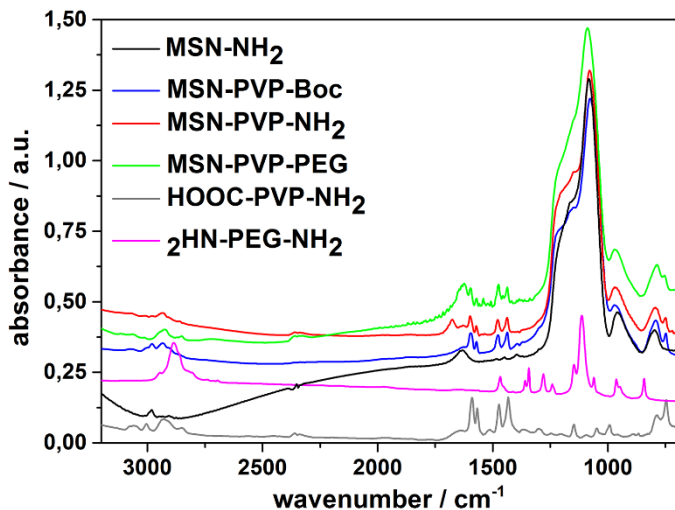


**Figure 5.10:** IR spectra of MSN-NH$_2$ (black), MSN-PVP-Boc (blue), MSN-PVP-COOH (red), MSN-PVP-PEG (green), HOOC-PVP-NH$_2$ (grey) and NH$_2$-PEG-NH$_2$ (magenta).
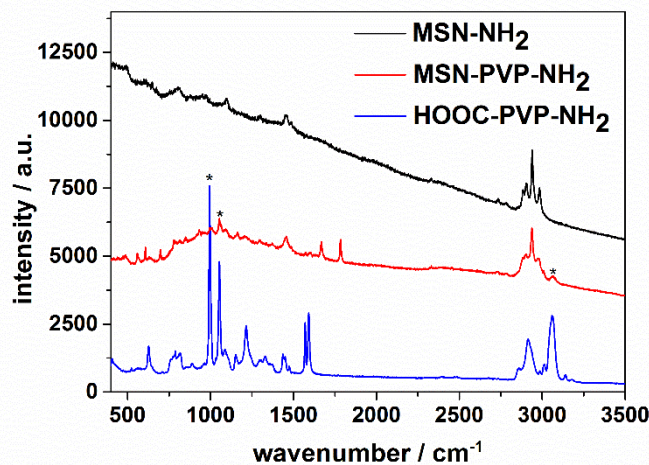
**Figure 5.11:** Raman spectra of MSN-NH$_2$ (black), MSN-PVP-NH$_2$ (red) and HOOC-PVP-NH$_2$ (blue).

In addition, Raman spectroscopy was used to monitor the attachment of HOOC-PVP-NH$_2$ (blue curve) to MSN-NH$_2$ (black curve) resulting in MSN-PVP-NH$_2$ (red curve). Bands at 3062 cm$^{-1}$ (*) (C-H stretching vibration of aromatic rings (pyridine)) and 1054 & 995 cm$^{-1}$ (*) (ring stretching vibration of mono-substituted pyridines) are typical for the pyridine groups of poly-2-vinylpryridine. The signals from the polymer appear in the MSN sample after attachment of PVP to MSN and are marked with an asterisk.

**Experimental Setup of fluorescence release experiments.**

Fluorescence experiments were performed to show the time-dependent release of fluorescein from the mesopores of colloidal mesoporous silica spheres. The measurements were recorded on a PTI fluorescence system featuring a PTI 814 photomultiplier detector and a PTI A1010B Xenon arc lamp driven by a PTI LPS-220B lamp power supply. For temperature settings, a Quantum Northwest TC 125 sample holder was used. Fluorescein was excited with 490 nm and emission was detected at 512 nm (excitation slit 1.0 mm, emission slit 1.0 mm, 1 point per 30 min). For the release experiment, a ROTH Visking Typ 8/32 dialysis membrane with a molecular cut-off of 14000 g/mol was used.

**Figure 5.12:** Custom made release experiment setup featuring a 200 µL Teflon tube **(a)** which is closed by a dialysis membrane **(b).** This setup is put onto a fluorescence cuvette filled with the desired buffer **(c).**

For the release experiment, the particles were re-dispersed in 200 µL SSC buffer pH 7 and put into a container that was subsequently closed by a dialysis membrane. The closed container was then put onto a fluorescence cuvette, which was completely filled with SSC buffer pH 7. The released dye is able to pass through the applied membrane while the relatively larger particles are retained. After 16 h, the particles were centrifuged and re-dispersed in 200 µL Mc Ilvaine's buffer pH 5, put into the container and closed by the dialysis membrane. The closed container was then put onto the fluorescence cuvette, which was completely filled with Mc Ilvaine's buffer pH 5. The release was measured every 30 min until no further release was observed (Figure 5.13).
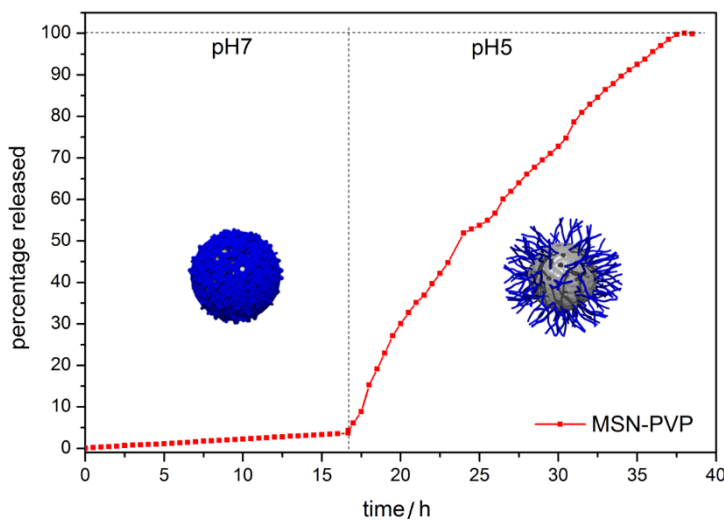


**Figure 5.13:** Long term release curve (normalized fluorescence intensity).

As the fluorescence of fluorescein is strongly dependent on the pH, calibration curves at pH 7 and pH 5 were recorded (Figure 5.14) to be able to compare fluorescence signals in the closed and open state.
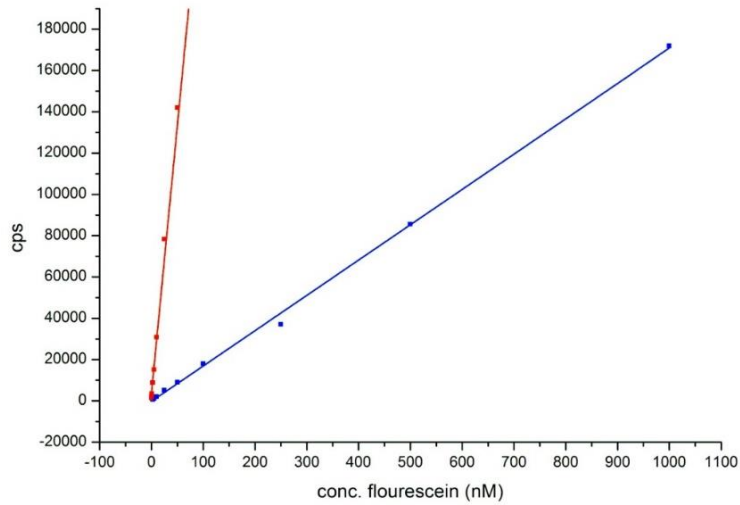


**Figure 5.14:** Calibration curves of fluorescein at pH 7 (red) and pH 5 (blue).

**Release in cells with three week old particles**

Cell experiments also revealed the good stability of the system. Even after storage of the ready-for-use particles for four weeks at 4 °C the release behavior stays the same, as can be seen in Figure 5.15. This test is in good agreement with the stability tests that are described above. It clearly demonstrates the good shielding of the silica core by the polymer layer.
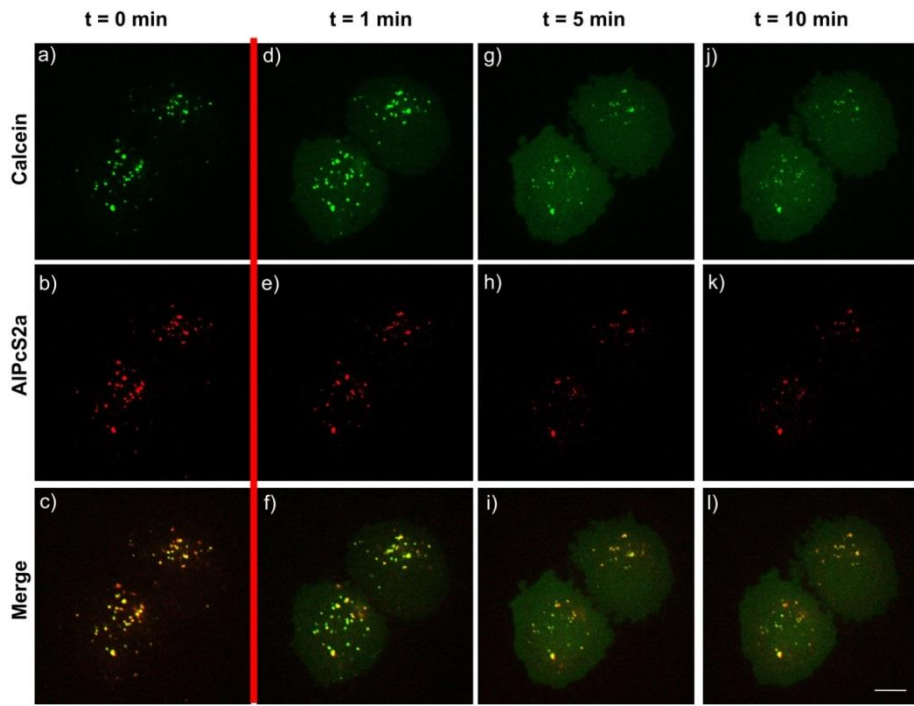
**Figure 5.15:** Fluorescence microscopy of MSN-PVP-PEG-AlPcS$_{2a}$-FA nanoparticles loaded with calcein inside KB cells; particles had been stored three weeks at 4 °C. **a-c)** Calcein (green) and AlPcS$_{2a}$ (red) are co-localized (yellow) prior to photoactivation. The red line indicates photoactivation with 1.2 W/mm$^2$ of red light (639 nm). **d-f)** after 1 min. photoactivation, **h-i)** 5 min. after photoactivation, **j-l)** 10 min. after photoactivation. The scale bar represents 10 μm.
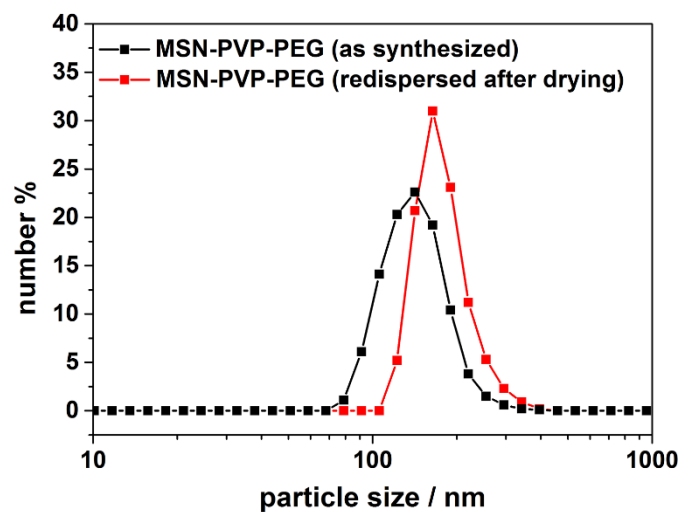


**Figure 5.16:** Dynamic light scattering of MSN-PVP-PEG as synthesized (black curve) and after drying the particles followed by re-dispersion in water (red curve). There is only a small apparent size increase from around 142 nm to around 164 nm, which demonstrates good re-dispersability

**Release behavior of the membrane impermeable cargo calcein.**

Even after 20 h of incubation the cargo stays co-localized with the MSN-fluorescence. In the absence of photosensitizer no release could be detected.
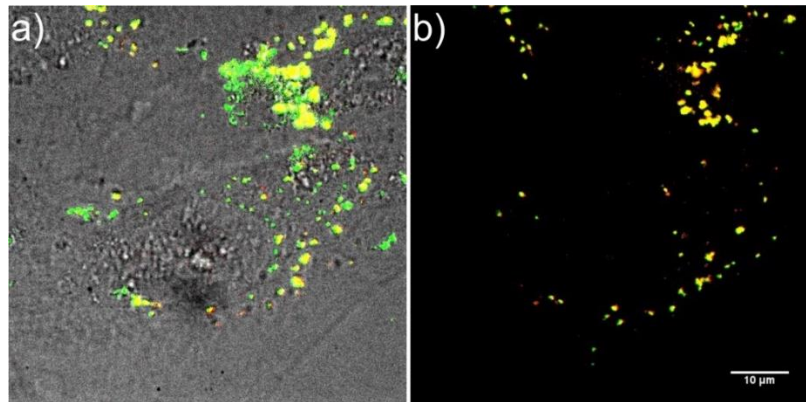


**Figure 5.17:** Fluorescence microscopy of MSN(Atto633)-PVP-PEG (25 µg/mL) nanoparticles loaded with calcein inside HeLa cells after 20 h incubation. **a)** Merge of brightfield image and fluorescence image. **b)** Fluorescence image of calcein (green) and Atto633 (red) are co-localized (yellow), no spreading of calcein can be observed, thus no endosomal escape has occurred. The scale bar represents 10 µm.
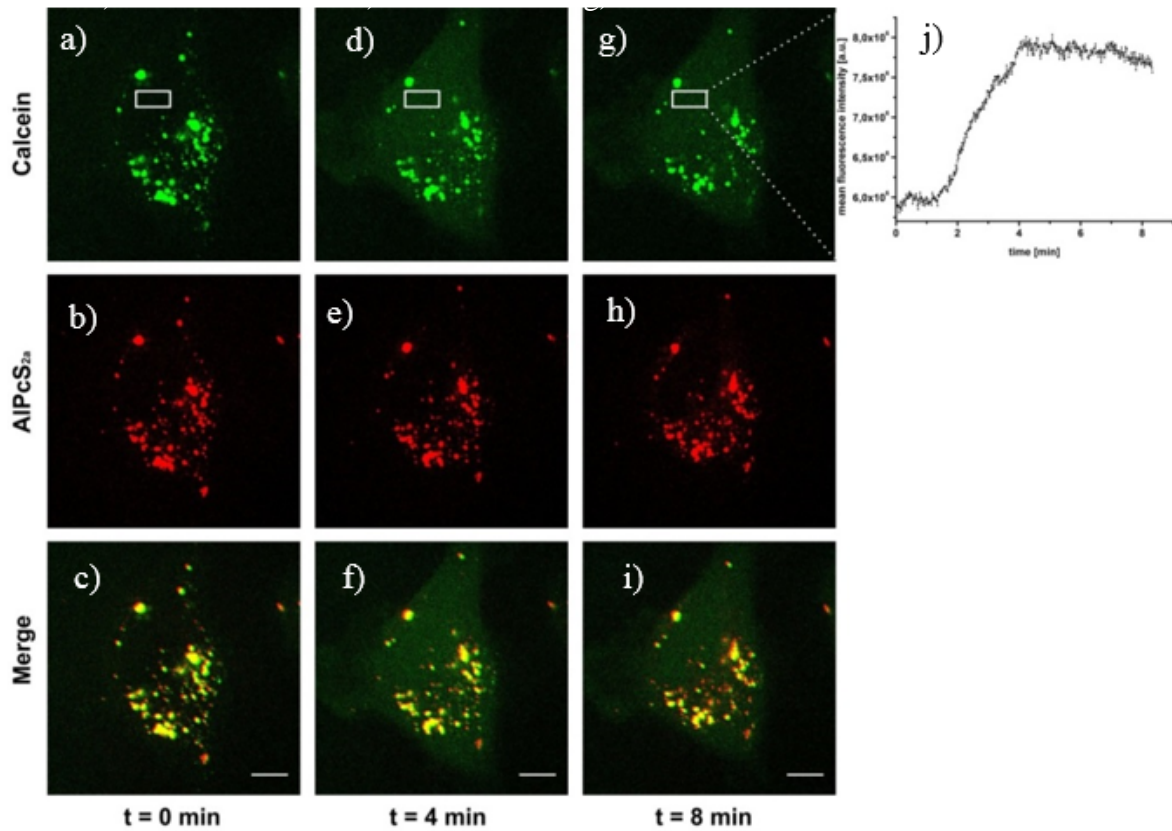
**Figure 5.18:** Fluorescence microscopy of MSN-PVP-PEG-AlPcS$_{2a}$-FA (25 µg/mL) nanoparticles loaded with calcein inside HeLa cells after 24 h incubation. **a-c)** Calcein (green) and AlPcS$_{2a}$ (red) are co-localized (yellow) prior to photoactivation. The cell was constantly monitored with a frame rate of 1 frame/s and 0.6 W/mm$^2$ of red light (639 nm). **d-i)** example images after different time points; spreading of calcein can be clearly seen over time, whereas AlPcS$_{2a}$ stays at the same location. **j)** Intensity of calcein fluorescence inside the cytosol over time in the indicated rectangle, after approximately 2 min an increase can be monitored. The scale bar represents 10 µm.

In comparison to Figure 5.18, the incubation of cells with free photosensitizer and free calcein (Figure 5.19) does not lead to the same effect. It is possible to detect calcein in the beginning of the experiment, but the endocytosed amount is too low to be detected after some time and therefore no spreading could be observed. In contrast to the dot-like pattern of the particle-bound photosensitizer in Figure 5.17, the spreading of the free photosensitizer can be detected in Figure 5.18.
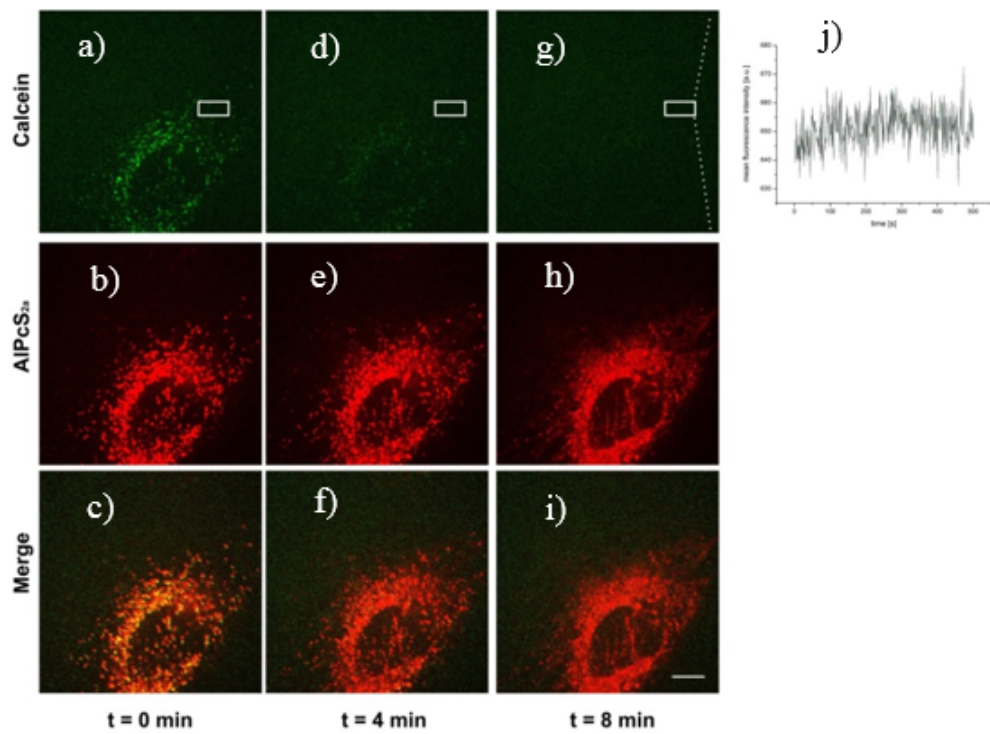
**Figure 5.19:** Fluorescence microscopy of free calcein and free $AlPcS_{2a}$ (each 2.5 µg/mL) inside HeLa cells after 24h incubation. **a-c)** Calcein (green) and $AlPcS_{2a}$ (red) are co-localized (yellow) prior to photoactivation. The cell was constantly monitored with a frame rate of 1frame/s and 0.6 W/mm$^2$ of red light (639 nm). **d-i)** example images after different time points, spreading of $AlPcS_{2a}$ can be clearly seen over time, whereas the calcein fluorescence is too weak to be detected after some time. **j)** Intensity of calcein fluorescence inside the cytosol over time in the indicated rectangle; no increase inside the cytosol can be detected. The scale bar represents 10 µm.

## 5.6   References

1.  Brewer, E.; Coleman, J.; Lowman, A. *J. Nano Mat.* **2011**, 1-10.

2.  Shu, J. Y.; Panganiban, B.; Xu, T. *Annu. Rev. Phys. Chem.* **2013**, *64*, 631-657.

3.  de Groot, G. W.; Santonicola, M. G.; Sugihara, K.; Zambelli, T.; Reimhult, E.; Vörös, J.; Vancso, G. J. *ACS Appl. Mater. Interfaces* **2013**, *5*, 1400-1407.

4.  Synytska, A.; Stamm, M.; Diez, S.; Ionov, L. *Langmuir* **2007**, *23*, 5205-5209.

5.  Hotta, J.-i.; Uji-i, H.; Hofkens, J. *Opt. Express* **2006**, *14*, 6273-6278.

6.  Meyer, M.; Dohmen, C.; Philipp, A.; Kiener, D.; Maiwald, G.; Scheu, C.; Ogris, M.; Wagner, E. *Mol. Pharm.* **2009**, *6*, 752-762.

7.  Vetter, A.; Virdi, K. S.; Espenlaub, S.; Rödl, W.; Wagner, E.; Holm, P. S.; Scheu, C.; Kreppel, F.; Spitzweg, C.; Ogris, M. *Mol. Pharm.* **2013**, *10*, 606-618.

8.  Minard-Basquin, C.; Weil, T.; Hohner, A.; Rädler, J. O.; Müllen, K. *J. Am. Chem. Soc.* **2003**, *125*, 5832-5838.

9.  Arpicco, S.; Stella, B.; Schiavon, O.; Milla, P.; Zonari, D.; Cattel, L. *Int. J. Pharm.* **2013**, *454*, 653-659.

10. Cauda, V.; Argyo, C.; Bein, T. *J. Mater. Chem.* **2010**, *20*, 8693-8699.

11. Zhou, Z.; Ma, X.; Jin, E.; Tang, J.; Sui, M.; Shen, Y.; Van Kirk, E. A.; Murdoch, W. J.; Radosz, M. *Biomaterials* **2013**, *34*, 5722-5735.

12. Coti, K. K.; Belowich, M. E.; Liong, M.; Ambrogio, M. W.; Lau, Y. A.; Khatib, H. A.; Zink, J. I.; Khashab, N. M.; Stoddart, J. F. *Nanoscale* **2009**, *1*, 16-39.

13. Slowing, I. I.; Trewyn, B. G.; Giri, S.; Lin, V. S. Y. *Adv. Funct. Mat.* **2007**, *17*, 1225-1236.

14. Mackowiak, S. A.; Schmidt, A.; Weiss, V.; Argyo, C.; von Schirnding, C.; Bein, T.; Bräuchle, C. *Nano Lett.* **2013**, *13*, 2576-83.

15. Tarn, D.; Ashley, C. E.; Xue, M.; Carnes, E. C.; Zink, J. I.; Brinker, C. J. *Acc. Chem. Res.* **2013**, *46*, 792-801.

16. Zhang, F.; Lees, E.; Amin, F.; Rivera-Gil, P.; Yang, F.; Mulvaney, P.; Parak, W. J. *Small* **2011**, *7*, 3113-3127.

17. Cauda, V.; Schlossbauer, A.; Kecht, J.; Zürner, A.; Bein, T. *J. Am. Chem. Soc.* **2009**, *131*, 11361-11370.

18. Schlossbauer, A.; Dohmen, C.; Schaffert, D.; Wagner, E.; Bein, T. *Angew. Chem. Int. Ed.* **2011**, *50*, 6828-6830.

19.     Strassert, C. A.; Otter, M.; Albuquerque, R. Q.; Höne, A.; Vida, Y.; Maier, B.; De Cola, L. *Angew. Chem. Int. Ed.* **2009**, *48*, 7928-7931.

20.     Liu, R.; Liao, P.; Liu, J.; Feng, P. *Langmuir* **2011**, *27*, 3095-3099.

21.     Tarn, D.; Xue, M.; Zink, J. I. *Inorg. Chem.* **2013**, *52*, 2044-2049.

22.     Ashley, C. E.; Carnes, E. C.; Phillips, G. K.; Padilla, D.; Durfee, P. N.; Brown, P. A.; Hanna, T. N.; Liu, J.; Phillips, B.; Carter, M. B.; Carroll, N. J.; Jiang, X.; Dunphy, D. R.; Willman, C. L.; Petsev, D. N.; Evans, D. G.; Parikh, A. N.; Chackerian, B.; Wharton, W.; Peabody, D. S.; Brinker, C. J. *Nat. Mater.* **2011**, *10*, 389-397.

23.     Cauda, V.; Engelke, H.; Sauer, A.; Arcizet, D.; Bräuchle, C.; Rädler, J.; Bein, T. *Nano Lett.* **2010**, *10*, 2484-2492.

24.     Slowing, I. I.; Vivero-Escoto, J. L.; Wu, C.-W.; Lin, V. S. Y. *Adv. Drug Delivery Rev.* **2008**, *60*, 1278-1288.

25.     Croissant, J.; Zink, J. I. *J. Am. Chem. Soc.* **2012**, *134*, 7628-7631.

26.     Vivero-Escoto, J. L.; Slowing, I. I.; Wu, C.-W.; Lin, V. S. Y. *J. Am. Chem. Soc.* **2009**, *131*, 3462-3463.

27.     You, Y.-Z.; Kalebaila, K. K.; Brock, S. L.; Oupický, D. *Chem. Mater.* **2008**, *20*, 3354-3359.

28.     Harush-Frenkel, O.; Debotton, N.; Benita, S.; Altschuler, Y. *Biochem. Biophys. Res. Commun.* **2007**, *353*, 26-32.

29.     Lakadamyali, M.; Rust, M. J.; Babcock, H. P.; Zhuang, X. *Proc. Natl. Acad. Sci. U.S.A.* **2003**, *100*, 9280-9285.

30.     Varkouhi, A. K.; Scholte, M.; Storm, G.; Haisma, H. J. *J. Control. Rel.* **2011**, *151*, 220-228.

31.     Hong, C.-Y.; Li, X.; Pan, C.-Y. *J. Mater. Chem.* **2009**, *19*, 5155-5160.

32.     Sun, J.-T.; Hong, C.-Y.; Pan, C.-Y. *J. Phys. Chem. C* **2010**, *114*, 12481-12486.

33.     Schlossbauer, A.; Kecht, J.; Bein, T. *Angew. Chem. Int. Ed.* **2009**, *48*, 3092-5.

34.     Cauda, V.; Schlossbauer, A.; Bein, T. *Microporous Mesoporous Mater.* **2010**, *132*, 60-71.

35.     Huynh, N. T.; Roger, E.; Lautram, N.; Benoît, J.-P.; Passirani, C. *Nanomedicine* **2010**, *5*, 1415-1433.

36.     Salazar, M. A.; Ratnam, M. *Cancer Metastasis Rev.* **2007**, *26*, 141-152.

37.     Huotari, J.; Helenius, A. *Embo. J.* **2011**, *30*, 3481-3500.

38.    Salokhiddinov, K. I.; Byteva, I. M.; Gurinovich, G. P. *J. Appl. Spectrosc.* **1981**, *34*, 561-564.

39.    Brasseur, N.; Ouellet, R.; La Madeleine, C.; van Lier, J. E. *Br. J. Cancer* **1999**, *80*, 1533-41.

40.    Zink, D.; Sadoni, N.; Stelzer, E. *Methods* **2003**, *29*, 42-50.

41.    Lalande, M. E.; Ling, V.; Miller, R. G. *Proc. Natl. Acad. Sci. U. S. A.* **1981**, *78*, 363-7.

42.    Kapuscinski, J. *J. Histochem. Cytochem.* **1990**, *38*, 1323-9.

# 6 Fluorocarbon Surfactant-mediated Synthesis of Small Mesoporous Silica Nanoparticles with Ultra-large Pores

This chapter is based on the work in collaboration with:

Martina Lichtnecker and Kathrin Bader
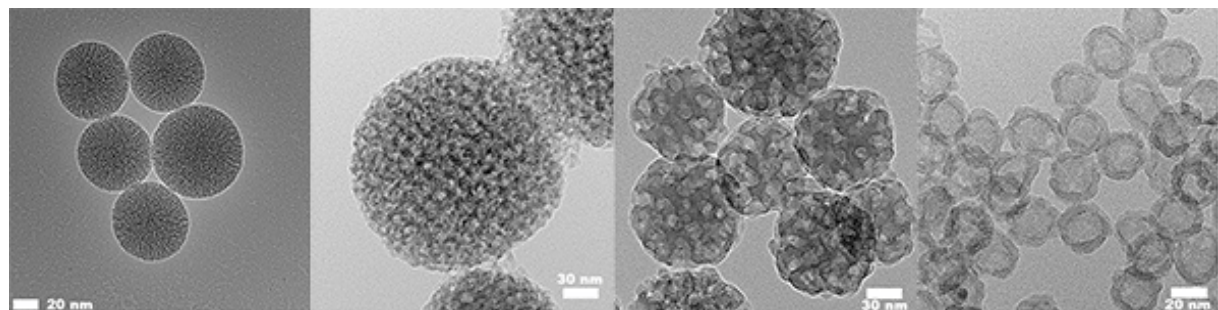
**Abstract**

Colloidal mesoporous silica nanoparticles (MSNs) have attracted great attention in recent years as versatile vehicles for advanced drug delivery applications.[1-3] In this context, MSNs are highly interesting due to the possibility to tailor structural and textural parameters (e.g. pore sizes and morphologies) while introducing a multiplicity of different functionalities within the mesoporous framework for selective post-synthetic modification.[2-4] Recently, we have developed several bare and modified colloidal mesoporous silica systems, for example MSNs functionalized with numerous organic moieties.[3-5] However, the synthesis of MSNs with large pores (LP_MSNs) and defined small particle sizes is still challenging since the pore size of conventional silica nanoparticles (around 4 nm) is inappropriate for the adsorption of larger biomolecules such as small interfering RNA (siRNA) or enzymes. In this chapter, the optimization of the pore diameter with regard to the adsorption of large biomolecules and the molecular functionalization of the mesopores in order to allow the facile diffusion and attachment of guest molecules into the host is demonstrated. An increase in pore diameter to values larger than 5 nm was achieved with various swelling agents that were incorporated into the surfactant aggregates and were used as structure-directing agents during the MSN synthesis. Moreover, large molecular weight surfactants (Pluronic F127) and novel fluorinated co-surfactants,[6, 7] distinct low temperature synthesis protocols and the impact of hydrothermal

treatment steps on the pore diameter were investigated in this study. Additionally, the impact of different organo-silanes bearing functional groups such as amino- and thiol-moieties on the mesostructure and morphology of the MSNs will be discussed.

## 6.1    Introduction

Considerable effort has been made in the past decade regarding the synthesis of mesoporous silica nanoparticles (MSNs) with a focus on mesostructural diversity, compositional flexibility and morphological control.[3, 4, 6-8] These multifunctional MSNs have recently been widely studied as promising nano-carriers for anti-cancer drugs such as doxorubicin[9, 10] or paclitaxel[11] both *in vitro* as well as *in vivo*.[12, 13] However, for the application of MSNs as host systems for larger molecules, such as enzymes, proteins and nucleic acids, larger mesopores than those available in conventional MSN systems are of key importance for a successful uptake into the host-system. An attractive application of LP_MSNs is the adsorption of small interfering RNA (siRNA) into their ultra-large pores. Artificially generated siRNA is a promising therapeutic agent in gene therapy since it can be specifically designed to knock down the targeted mRNA and therefore inhibit the translation of a target protein that is known to cause a certain disease.[14-16] Hom *et al.* attached siRNA to the external surface of PEI-modified MSNs and observed an effective gene silencing of enhanced green fluorescent protein (EGFP).[17] However, it would be advantageous to incorporate the fragile and expensive molecules within the mesoporous channels of the drug delivery vehicles to prevent premature degradation and undesired leakage. Two different studies showed a successful delivery of oligonucleotides (pDNA and siRNA, respectively) to cells with amino-functionalized LP_MSNs.[7, 18] Gao *et al.* used post-synthesis amino-modified LP_MSNs for pDNA adsorption[7], whereas Hartono *et al.* modified the outer silica shell with the cationic polymer poly-L-lysine.[18]. Cationic polymers are widely used for the generation of polyplexes for efficient gene delivery due to their electrostatic interaction with the negative backbone of the oligonucleotides.[19-21] A well-established representative of mesoporous silica materials is the Santa Barbara Amorphous 15 (SBA-15), which was introduced by Stucky and co-workers in 1998, exhibiting high hydrothermal stability and large, tuneable pore sizes (4.9 – 30 nm).[22, 23] Kruk and co-workers showed that the substitution of 1,3,5-trimethylbenzene (TMB) by 1,3,5-triisopropylbenzene (TiPB) leads to an increase in pore size for SBA-15 particles,[24, 25] and Bräuchle, Bein and

co-workers already showed the impact of this micellar expander on multifunctional core-shell MSNs, increasing their pore size by 25% to 5 nm.[3] However, we note that in addition to large pore sizes, a distinctly small particle size (within a size range of $50-300$ nm) of the nano-carrier is of great importance for cell experiments and *in vivo* applications such as drug delivery since the endosomal uptake of nanoparticles is highly size dependent.[26] In addressing this issue, recently several strategies for the synthesis of LP_MSNs with a particle diameter of $70-300$ nm and very large pores (up to 17 nm) using fluorocarbon surfactant FC-4 and triblock copolymers (Pluronic F127, P123 and P65) have been published by different groups.[6, 7, 27] Gao *et al.* developed a novel strategy based on the publication of Han *et al.*[6] to synthesize LP_MSNs at low temperatures (10 °C) applying a dual surfactant system consisting of Pluronic F127 together with fluorocarbon surfactant FC-4 and TMB as micellar expander to generate spherical MSNs with large pores.[7] In all published syntheses, the fluorocarbon surfactant seems to play a crucial role to keep the size of the LP_MSNs small, but it did not contribute to the mesostructure formation. One missing feature of the above-mentioned LP_MSN synthesis protocols is the incorporation of organo-functionalizations into the mesoporous framework, which is a key prerequisite for the attachment of external triggers such as targeting ligands and/or stimuli-responsive capping mechanisms. Organo-functionalization can be introduced into the LP_MSNs via post-synthesis grafting, yet this post-modification requires an additional synthesis step under dry conditions, and control over the exact amount of organo-silane that is grafted onto the silica surface is challenging.

Here we describe the successful development of novel organo-functionalized LP_MSNs by employing a dual surfactant system consisting of the triblock copolymer F127 and fluorocarbon surfactant FC-4. Low synthesis temperatures (10 °C and 30 °C) and two different micellar expanders (1,3,5-trimethylbenzene and 1,3,5-triisopropylbenzene) were applied to generate uniform LP_MSNs. We were able to introduce multiple organo-functionalizations (thiol-, azide- and amino/phenyl-moieties) into the mesoporous framework by a co-condensation approach under mildly acidic conditions.

## 6.2 Results and Discussion

The synthesis procedure described by Gao *et al.*[7], carried out at low temperatures (10 °C) with Pluronic F127 as organic template, fluorocarbon surfactant FC-4 as co-surfactant and 1,3,5-trimethylbenzene (TMB) as micellar expander served as a starting point for this work. The impact of different hydrothermal treatment steps in acidic media on the pore size of the synthesized nanoparticles was investigated with nitrogen adsorption measurements (cf. appendix 6.22) and transmission electron microscopy (cf. appendix 6.23). It was shown that non-hydtrothermally treated particles exhibit smaller pore sizes than those synthesized with the typical hydrothermal treatment. Hydrothermal treatment leads to an increase in entropy and an additional expansion effect on the micelles by the organic swelling agent. It proved mandatory to employ slightly more acidic conditions for the second hydrothermal treatment (0.2 M hydrochloric acid); it is assumed that the presence of the diluted hydrochloric acid leads to an additional 'etching' of the pore entrances. TEM micrographs of the unfunctionalized, hydrothermally treated MSNs with large pores (LP_MSN-bare) are shown in Figure 6.1.
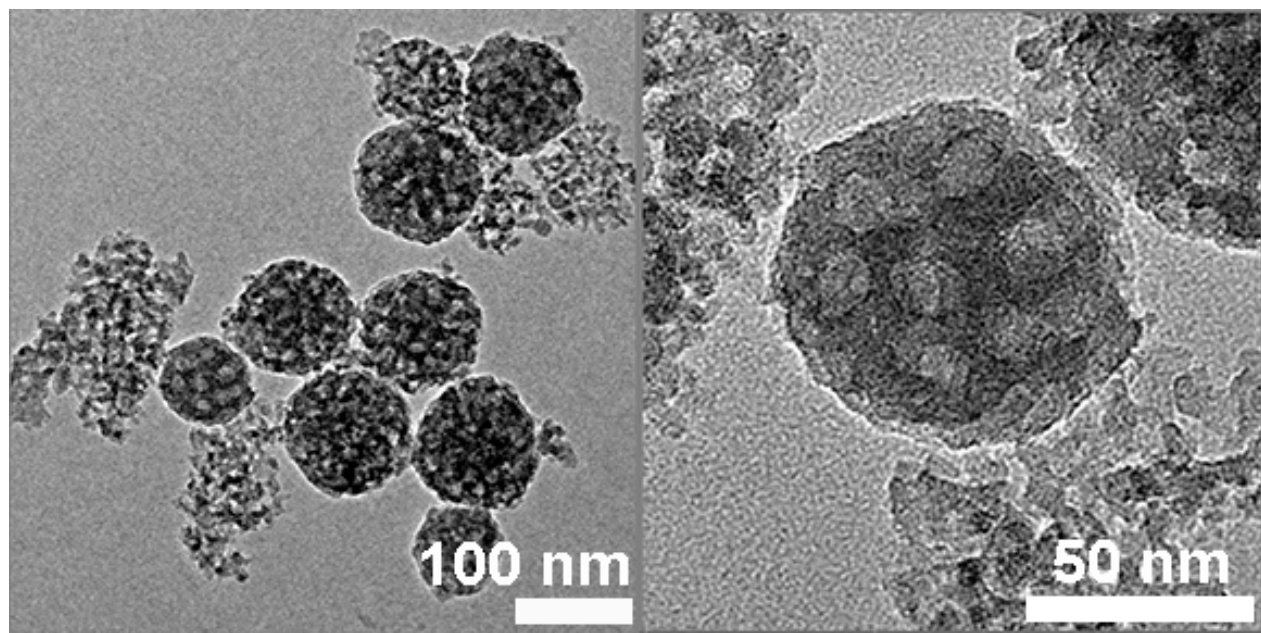


**Figure 6.1:** TEM micrographs of unfunctionalized LP_MSNs synthesized with TMB at 10 °C.

The TEM micrographs show spherically shaped particles within a size range of 70 – 100 nm and large pores of 10 – 15 nm. The pores are regularly arranged over the entire nanoparticle. Besides the particles a small amount of impurities is present in the sample. Kruk and co-workers

reported that the pore size of SBA-15 particles can be increased by the substitution of TMB by 1,3,5-triisopropylbenzene (TiPB)[24, 25] and we had successfully shown a similar increase of the pore size for core-shell MSNs (cf. chapter 4).[3] Therefore, the impact of TiPB as micellar expander on the synthesis of unfunctionalized LP_MSNs was investigated.

### 6.2.1 Synthesis of unfunctionalized large pore silica nanoparticles

**Synthesis of LP_MSNs with TiPB as micellar expander at 10 °C**

In brief, a modified synthesis protocol based on the publication of Gao *et al.* was employed for the synthesis of LP_MSNs with TiPB as micellar expander.[7] The mildly acidic surfactant solution consisting of the dual surfactant system Pluronic F127 and fluorocarbon surfactant FC-4, together with a distinct amount of TiPB (same molar amount previously applied for TMB), was allowed to stir for 2 h at 10 °C to induce micelle formation. After this time period, tetraethyl orthosilicate (TEOS) was introduced drop-wise into the surfactant solution as silica source and the reaction mixture was allowed to stir over night at 10 °C. The as-synthesized LP_MSNs were hydrothermally treated for one day at 150 °C in the synthesis solution. Subsequently they were centrifuged and re-suspended in 0.2 M hydrochloric acid. A second hydrothermal treatment step (140 °C, 2 d) was employed afterwards. The structure-directing agent was removed by solvent extraction in a mixture of ethanol, acetone and hydrochloric acid to maintain the colloidal behavior of the nanoparticles. In order to study the impact of TiPB on the mesostructure, the template-free, unfunctionalized LP_MSNs (LP_MSN-bare-TiPB) were compared with LP_MSNs generated with TMB (LP_MSN-bare-TMB). The hydrothermal treatment and template removal was identical for both samples. The resulting samples (LP_MSN-bare) were investigated with small angle X-ray diffraction (SAXS). The diffraction pattern for LP_MSN-bare-TiPB shows a reflection at 2θ = 0.55° (cf. appendix 6.24). Additionally, for both samples nitrogen physisorption measurements were performed (Figure 6.2).
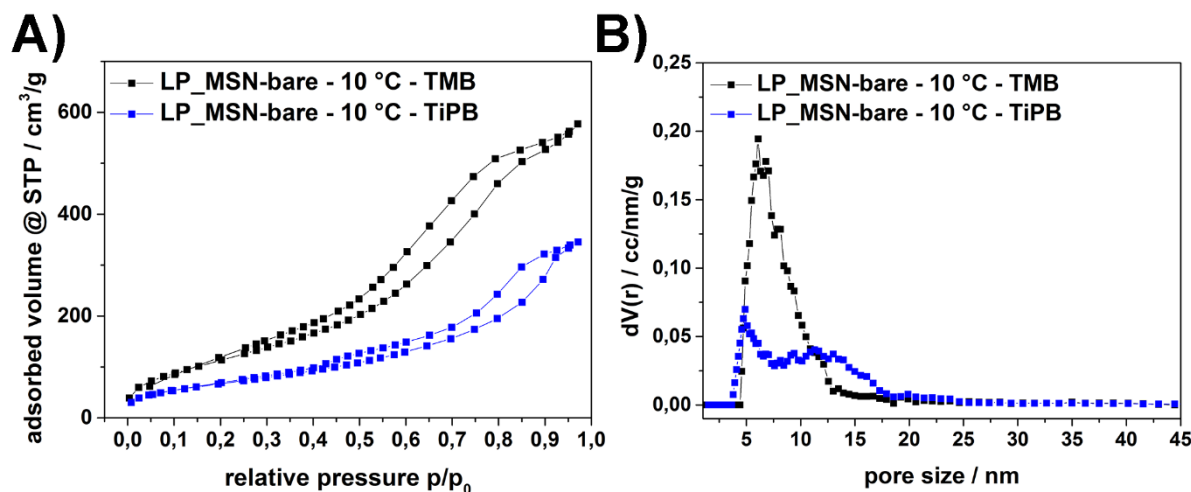
**Figure 6.2:** Nitrogen sorption data for LP_MSN-bare synthesized at 10 °C with 1,3,5-trimethylbenzene (LP_MSN-bare **-** 10 °C **-** TMB, black) and 1,3,5-triisopropylbenzene (LP_MSN-bare - 10 °C - TiPB, blue) as micellar expander. **A)** Nitrogen sorption isotherms and **B)** calculated NLDFT pore size distributions of template-free LP_MSNs.

The isotherm of LP_MSN-bare-TMB (black curve) represents a type IV isotherm with an H3 hysteresis indicating a significant degree of textural porosity in the macroporous regime. The isotherm of LP_MSN-bare-TiPB (blue curve) shows the same characteristic but with lower values of adsorbed volumes. A monolayer formation of the adsorbate can be observed between $p/p_0 = 0$ and 0.02, followed by multilayer adsorption over a broad range. Both isotherms show a relatively flat slope during capillary condensation at $p/p_0 = 0.5$–0.8, resulting in broad pore size distributions (PSD) for both samples (Figure 6.2B). In addition, the slope is notably flatter for LP_MSN-bare - 10 °C - TiPB resulting in an even wider PSD than was observed for LP_MSN-bare - 10 °C - TMB; a distinct maximum cannot be obtained for the LP_MSNs synthesized with TiPB. Both isotherms do not reach a saturation plateau at high $p/p_0$ values indicating the presence of either impurities within the sample or textural porosity. The resulting BET surface areas, pore volumes and pore sizes are summarized in Table 6.1.

**Table 6.1:** Nitrogen sorption data of LP_MSN-bare synthesized with different micellar expanders.

| Sample | BET surface area (m²/g) | Pore volume (cm³/g) | Pore size (nm) |
|--------|--------|--------|--------|
| LP_MSN-bare – 10 °C – TMB | 431 | 0.84 | 5–17 |
| LP_MSN-bare – 10 °C – TiPB | 249 | 0.51 | 6–13 |

Compared to conventional MSNs[4, 28] and SBA-15 materials[22, 24], the BET surface area is rather low for both obtained nanoparticles, but in the typical range of LP_MSNs generated with FC-4 reported by Gao *et al.* ($A_s = 201 - 561$ m²/g, dependent on the synthesis employed).[7] From the shape of the pore size distribution it can be concluded that the formation of the mesostructure is, at least partly disrupted by the TiPB at the applied synthesis conditions. The scanning electron microscopy image of LP_MSN-bare synthesized with TiPB shows a broad particle size distribution with spherical nanoparticles in the size range of $50 - 300$ nm, allowing us to assume that the particle morphology itself is not disrupted by the micellar expander (Figure 6.3). It can be concluded that the synthesis approach with TiPB at low temperatures is not favorable for the generation of well-defined LP_MSNs without organo-functionality.
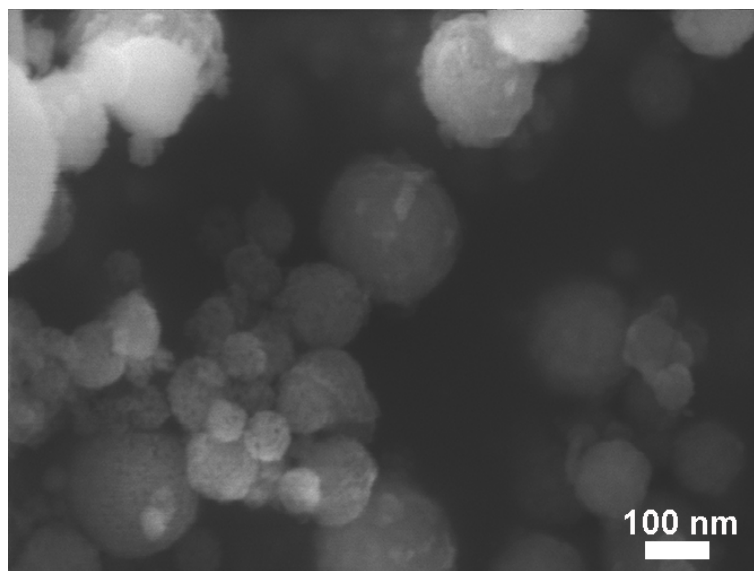


**Figure 6.3:** Scanning electron micrograph of LP_MSN-bare synthesized at 10 °C with TiPB.

**Synthesis of unfunctionalized large pore silica nanoparticles with TiPB at 30 °C**

As the synthesis approach at 10 °C with TiPB does not lead to the desired result but partly disrupted the mesostructure, a higher synthesis temperature was examined. The synthesis of unfunctionalized LP_MSN-bare at 30 °C was based on the previously described procedure reported by Gao *et al.*[7] In comparison to the aforementioned synthesis we used TiPB at a distinct synthesis temperature of 30 °C for the synthesis of LP_MSNs. TEOS was hydrolyzed in a mildly acidic reaction mixture containing the tri-block copolymer Pluronic F127, fluorocarbon surfactant FC-4 and TiPB in an overnight reaction which yielded the LP_MSNs as white precipitate. For all samples the two step post-synthetic hydrothermal treatment (1 d at 150 °C, 2 d at 140 °C) introduced by Gao *et al.* was applied.[7]
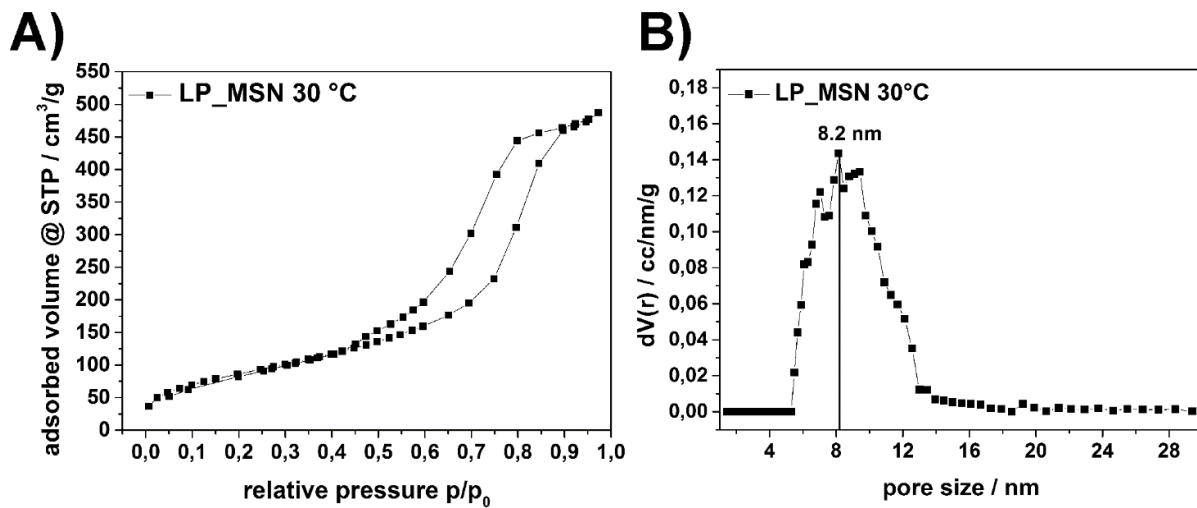


**Figure 6.4:** Nitrogen physisorption data of unfunctionalized LP_MSN-bare synthesized at 30 °C with TiPB **A)** Nitrogen sorption isotherm and **B)** calculated NLDFT pore size distribution.

The nitrogen adsorption isotherm (Figure 6.4A) reveals a type IV isotherm typical for mesoporous materials. The first part of the isotherm at relative pressures between 0 and 0.2 $p/p_0$ shows a nearly logarithmic slope that can be assigned to monolayer adsorption of nitrogen. Monolayer adsorption is followed by linearly increasing multilayer adsorption taking place at $p/p_0$ values of 0.2–0.42. At $p/p_0$ values between 0.42 and 0.92 the isotherm ascends steeply and a hysteresis occurs between the adsorption and the desorption branch resulting from capillary condensation. At relative pressures higher than 0.92, the isotherm almost reaches a plateau indicating that pore saturation occurs. NLDFT pore size distribution calculated from nitrogen sorption data gave an average pore diameter of 8.2 nm for the LP_MSNs with a narrow

distribution pattern comparable to LP_MSNs synthesized at 10 °C with TMB. The XRD diffraction pattern (cf. appendix 6.25) showed a (1 0 0) reflection at $2\theta = 0.64°$, which gave a calculated d-spacing of $d_{100} = 13.8$ nm. Dynamic light scattering (DLS) measurements in ethanolic media feature an average particle size of 145 nm with a narrow particle size distribution (Figure 6.5). No agglomeration of LP_MSNs occurred in ethanolic suspensions and the sample showed good colloidal stability.
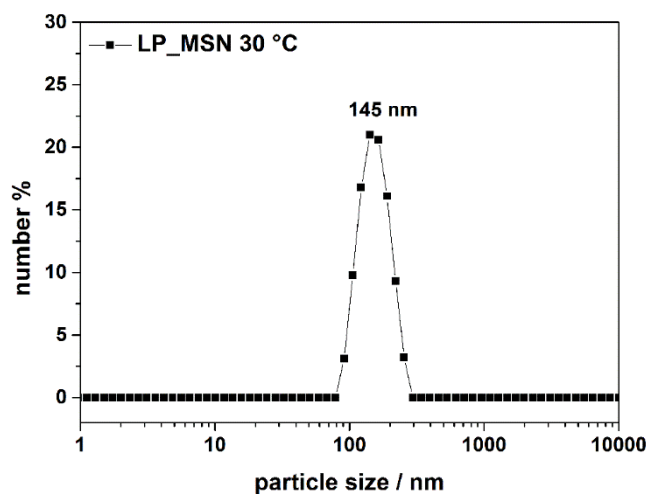


**Figure 6.5:** Dynamic light scattering (DLS) measurement of large pore mesoporous silica nanoparticles (LP_MSNs) without organo-functionalization synthesized at 30 °C with TiPB as micellar expander in ethanol.

The key features of LP_MSN-bare obtained with nitrogen sorption measurements and dynamic light scattering are summarized in Table 6.2. The unfunctionalized LP_MSNs exhibit a high pore volume and a BET surface area typical for large pore silica nanoparticles. We note that the BET surface area for LP_MSN-bare synthesized with TiPB at 30 °C is lower than for LP_MSNs generated with TMB ($A_s = 421$ m$^2$/g).

**Table 6.2:** Structural parameters of LP_MSN-bare synthesized with TiPB at 30 °C.

| Sample | Particle size[a] (nm) | BET surface area (m²/g) | Pore volume (cm³/g) | Pore size[b] (nm) |
|---|---|---|---|---|
| **LP_MSN-bare 30 °C** | 145 | 321 | 0.72 | 8.2 |

[a]Average particle size refers to the peak value of the particle size distribution derived from DLS measurements in ethanolic solution; [b]DFT pore size refers to the peak value of the pore size distribution.

Transmission electron microscopy (TEM) was conducted in order to obtain a detailed overview of the morphology of the synthesized, template-extracted LP_MSNs.
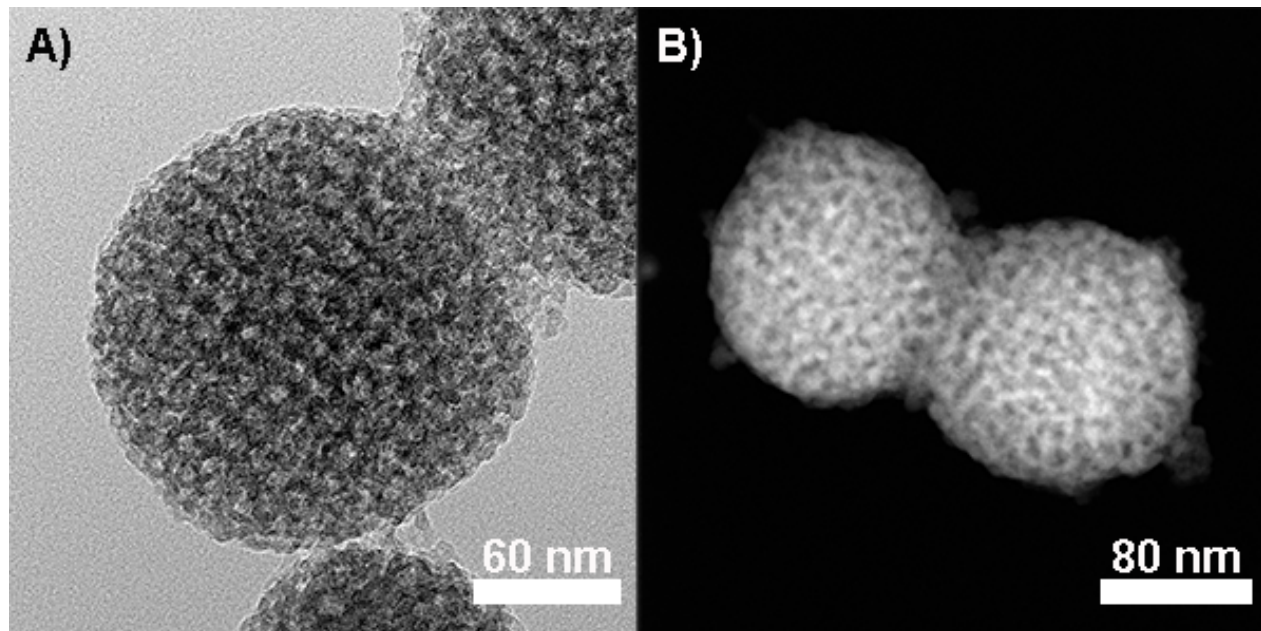


**Figure 6.6:** Unfunctionalized mesoporous silica nanoparticles synthesized with TiPB as micellar expander at 30 °C. **A)** TEM micrograph and **B)** STEM micrograph of LP_MSN-bare. The images show spherically shaped and uniform particles.

The representative TEM micrograph (Figure 6.6A) shows a homogenously composed sample with spherically shaped particles having an average diameter of about 120 nm, which is in good accordance with the data obtained from dynamic light scattering. The slightly higher value derived from DLS can be explained by the hydrodynamic radius of the measured sample and weak agglomeration. The mesopores are clearly visible and evenly distributed over the entire nanoparticle and in good accordance with the data obtained from nitrogen physisorption. It can be noted that the synthesized LP_MSNs, compared to standard MSNs (cf. chapter 4 and 5) and unfunctionalized LP_MSNs synthesized at 10 °C, seem to exhibit an entirely different growth mechanism visible by transmission electron microscopy (cf. chapter 4 and Figures 6.1 and 6.6). TEM data of the standard MSNs suggest a typical radial growth mechanism, resulting in a worm-like mesoporous network. Additionally, scanning transmission electron microscopy (STEM) images were recorded to gain an even better contrast of the mesoporous framework of the LP_MSNs (Figure 6.6 B).

In summary, we were able to successfully synthesize spherical, homogenous LP_MSN-bare with TiPB as micellar expander and a synthesis temperature of 30 °C; the data show that the higher temperature combined with TiPB has a positive effect on the mesostructure formation of unfunctionalized LP_MSNs. Compared to the samples generated at 10 °C with TMB, less impurities were observed and the LP_MSNs exhibit a narrower pore size distribution. Additionally, the nanoparticles are of well-defined spherical shape and homogeneous within the sample.

## 6.2.2  Synthesis of organo-functionalized large pore mesoporous silica nanoparticles

One major goal of this work was the synthesis of organo-functionalized LP_MSNs synthesized with a direct co-condensation approach. To date, organo-modified large-pore silica nanoparticles are only available by applying a post-synthesis grafting step after the original synthesis, which has certain drawbacks (e.g., additional modification step under dry conditions). It is desirable to achieve good control over the amount of functional groups introduced and to obtain a homogenous distribution of organic moieties;[4, 28] therefore we investigated co-condensation reactions with different organo-silanes (3-mercaptopropyl triethoxysilane, 3-azidopropyl triethoxysilane and 3-aminopropyl triethoxysilane : phenyl triethoxysilane (1:1 mixture)) with the two above-mentioned micellar expanders at different synthesis temperatures (10 °C and 30 °C).

### Synthesis of LP_MSN with thiol-functionality at different temperatures

For the synthesis of mesoporous silica nanoparticles with ultra-large pores and organo-functionalization (LP_MSN-SH) a modified sol-gel method at mildly acidic conditions with Pluronic F127 as structure directing agent and an increased amount of fluorocarbon surfactant FC-4 as co-surfactant was employed.[7] We chose to introduce a low amount of thiol-functionalization (1 mol% of the original TEOS amount) via a co-condensation method to LP_MSNs in order to obtain a homogeneous distribution of the organic-moieties within the silica material. The silica source TEOS was mixed with the respective amount of 3-mercaptopropyl triethoxysilane before the resulting solution was introduced drop-wise into an acidic template solution consisting of Pluronic F127, FC-4 and the respective micellar expander. The reaction mixture was stirred at the desired temperature (10 °C or 30 °C, respectively – dependent of the employed micellar expander) for 14 h. Afterwards, a two-step hydrothermal treatment of the as-synthesized material in acidic media was carried out to yield

two different samples of LP_MSN-SH (cf. experimental section).[7]. Small angle XRD measurements (cf. appendix 6.26A for LP_MSN-SH-30 °C and 6.26B for LP_MSN-SH-10 °C) were carried out to yield information about the structural nature of LP_MSN-SH. The sample LP_MSN-SH-30 °C shows a sharp reflection (2 theta = 0.65 °) whereas the sample LP_MSN-SH-10 °C shows a broadened reflection at 2 theta = 0.68 °. These results are in good accordance with the data obtained from nitrogen sorption measurements (cf. Figure 6.7B).

The isotherm of the template-extracted sample LP_MSN-SH-30 °C (Figure 6.7A, black curve) exhibits a steeper slope in the range of $p/p_0$ = 0.5–0.8 compared to LP_MSN-SH-10 °C (blue curve). Accordingly, the calculated pore size distribution of the sample synthesized at 30 °C is considerably narrower (Figure, 6.7B maximum at 9.4 nm) compared to the pore size distribution of LP_MSN-SH-10 °C. In the case of the 30 °C sample, pore saturation is indicated at $p/p_0$ values beyond 0.9, while the remaining upwards slope hints at additional textural porosity. The latter is more pronounced in the case of the 10 °C sample. Dynamic light scattering (DLS) measurements of the template-extracted silica nanoparticles after size separation centrifugation in ethanol yielded rather similar size distributions with maxima at 164 nm (LP_MSN-SH-30 °C, Figure 6.7C, black curve) and 142 nm (LP_MSN-SH-10 °C, blue curve). A narrow particle size distribution was observed for both samples, indicating the absence of aggregates. Zeta potential measurements gave information about the successful incorporation of organo-functionalization on the outer surface, although thiol-moieties do not show distinctly higher values than unfunctionalized LP_MSNs (Figure 6.7D). Thiol-groups need to be located at the outer surface of the silica nanoparticle to influence the zeta potential of the LP_MSNs. The zeta potential of both samples is negative within the pH range of 2–7, since the mercapto moieties cannot be protonated at low pH values. The decrease of the zeta potential with increasing pH value is a result of the deprotonation of the mercapto-groups.
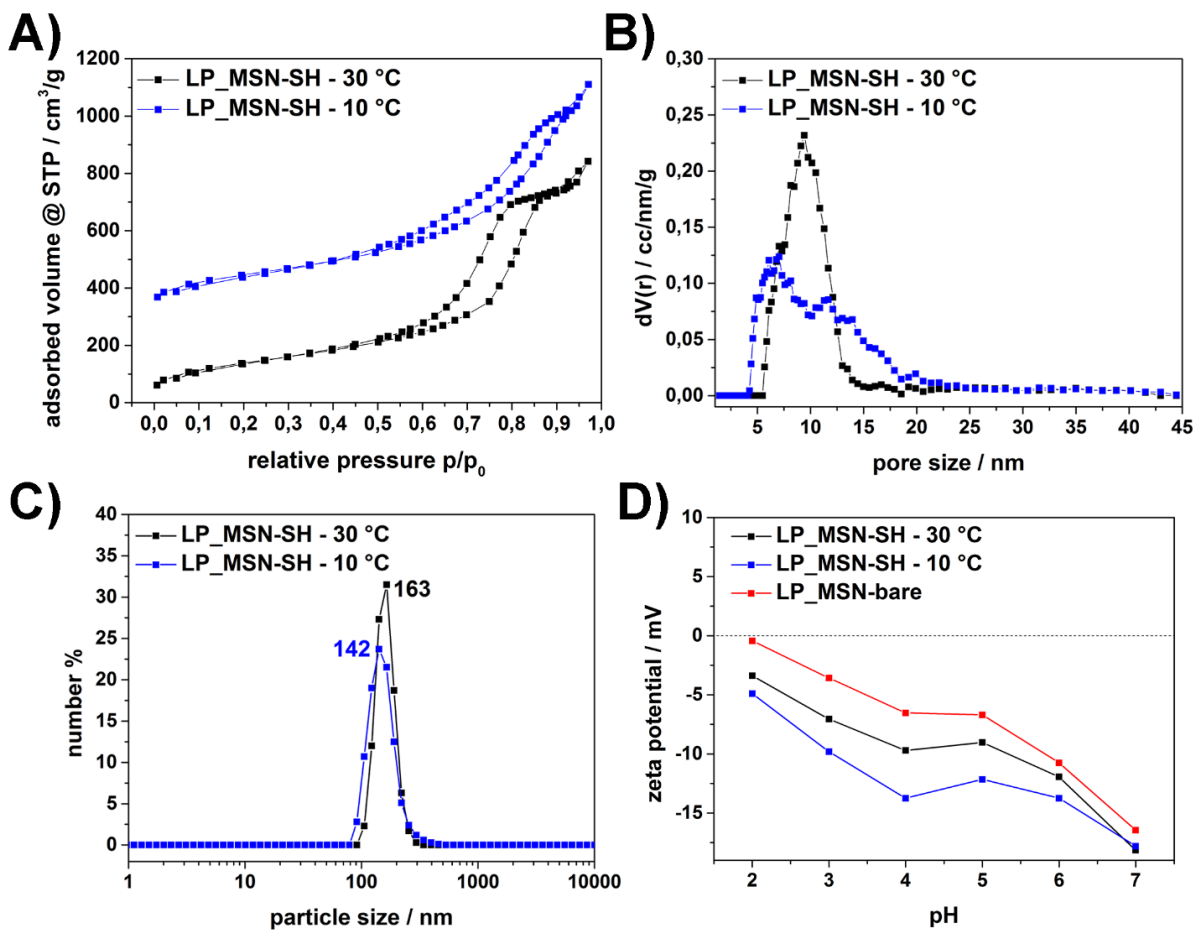
**Figure 6.7:** Analysis of LP_MSN-SH synthesized with different synthesis procedures; synthesized with 1,3,5-triisopropylbenzene as micellar expander at 30 °C (black) and TMB at 10 °C (blue). **A)** Nitrogen sorption isotherms of template-free LP_MSNs – the isotherm of LP_MSN-SH-10 °C was shifted by a value of 200 along the y-axis for clarity reasons. **B)** NLDFT pore size distribution. **C)** Dynamic light scattering (DLS) data of the template-extracted nanoparticles in ethanol, and **D)** zeta potential measurements of LP_MSN-SH-30 °C (black), LP_MSN-SH-10 °C (blue) and LP_MSN-bare (LP_MSNs without organo-functionality, red).

The larger pore size of LP_MSN-SH-30 °C results in a lower BET surface area of 492 m²/g compared to 521 m²/g for the sample LP_MSN-SH-10 °C. The pore volume is not changed in both samples. The key features of the LP_MSN-SH obtained by dynamic light scattering and nitrogen adsorption are summarized in Table 6.3.

**Table 6.3:** Dynamic light scattering (DLS) results after size separation centrifugation and nitrogen sorption data of LP_MSN-SH synthesized at different temperatures.

| Sample | Particle size[a] (nm) | BET surface area (m²/g) | Pore volume (cm³/g) | Pore size[b] (nm) |
|---|---|---|---|---|
| LP_MSN-SH – 30 °C (TiPB) | 163 | 492 | 1.2 | 9.4 |
| LP_MSN-SH – 10 °C (TMB) | 142 | 521 | 1.2 | 7.0 |

[a]Average particle size refers to the peak value of the particle size distribution derived from DLS measurements in ethanolic solution; [b]DFT pore size refers to the peak value of the pore size distribution

We note that despite the different pore sizes of the LP_MSN-SH, the pore volume and the BET surface area are similar for both samples, as are the particle sizes obtained from DLS measurements. Vibrational spectroscopy gives information about organic moieties within the sample and was thus used to obtain insights about the functionality of the samples.
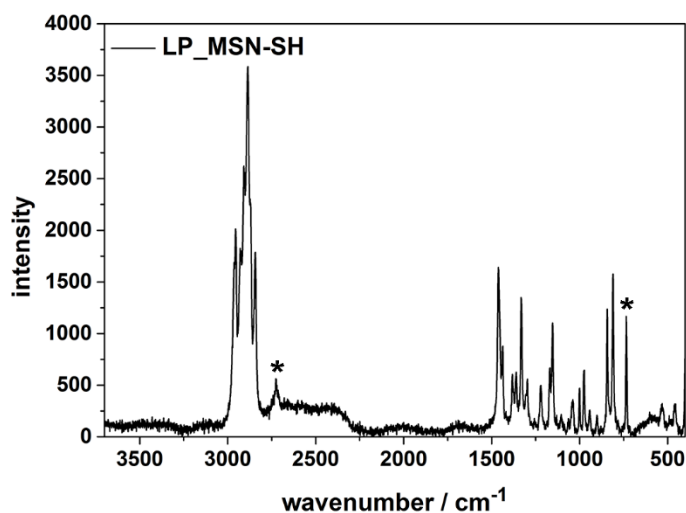


**Figure 6.8:** Raman spectrum of template-free LP_MSN-SH–10 °C.

Distinct bands arise (marked with an asterisk in Figure 6.8) at 2725 cm$^{-1}$ (-CH$_2$-SH, stretching vibration) and 734 cm$^{-1}$ (-C-SH, stretching vibration) indicating a successful organo-functionalization with thiol-moieties. Additionally, the C-H stretching vibration modes of the alkyl chains (including ethoxy-groups on the silica framework) are present at 2952, 2874 and 2848 cm$^{-1}$. From these data, we conclude that thiol-groups were successfully incorporated into the mesoporous framework of LP_MSNs via the co-condensation approach. The

morphology and pore structure of both LP_MSN samples was investigated with transmission electron microscopy after size separation centrifugation. The nanoparticles of sample LP_MSN-SH-30 °C (Figure 6.9A and B) are of spherical shape with particle diameters within a size range of 70 – 120 nm. The mesopores are visible and evenly distributed within each particle of the sample LP_MSN-SH. The pores appear in a size range of 8 – 10 nm (data taken from the micrograph), which is in good accordance with the nitrogen adsorption results for LP_MSN-SH-30 °C. We note that the mesoporous structure of the sample synthesized at 10 °C with TMB (LP_MSN-SH-10 °C, Figure 6.9C and D) appears to be slightly less ordered than LP_MSN-SH-30 °C. The majority of the nanoparticles in the sample after size separation centrifugation is of spherical shape with a particle size between 90 – 170 nm, which is in good accordance with the DLS measurements.
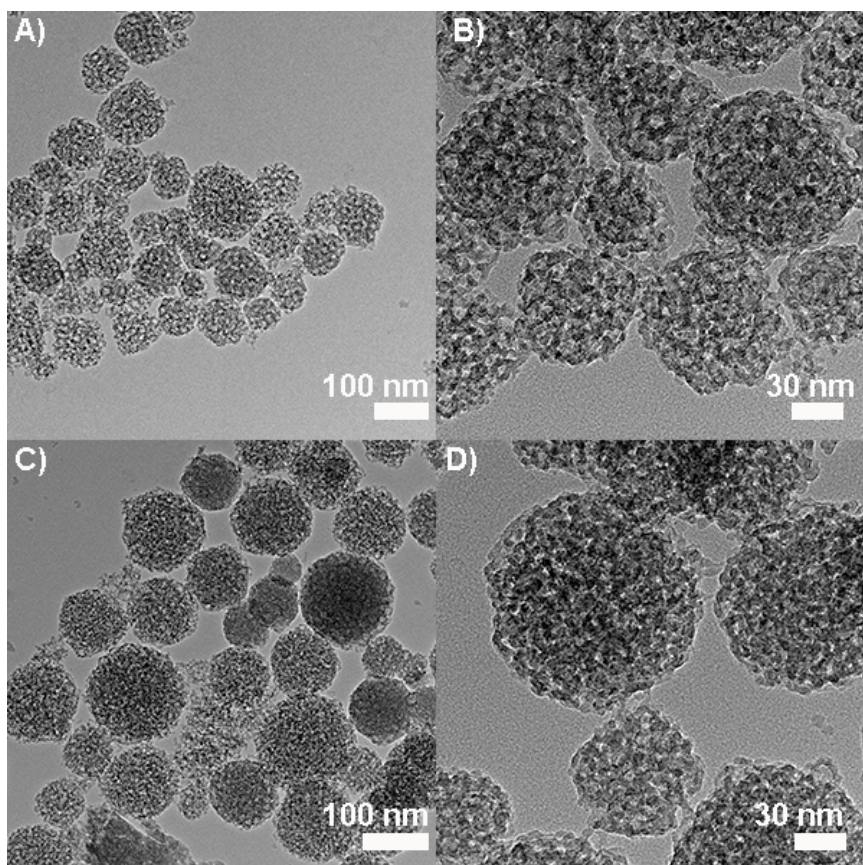


**Figure 6.9:** Transmission electron micrographs after size separation centrifugation of two differently synthesized, template-extracted LP_MSN-SH, **A) and B)** synthesized with TiPB as micellar expander at 30 °C (sample LP_MSN-SH-30 °C). **C) and D)** LP_MSN-SH synthesized with the same molar amount of TMB and a synthesis temperature of 10 °C (sample LP_MSN-SH-10 °C).

From all the obtained data it can be concluded that both synthesis approaches yield LP_MSN-SH of a distinct small size suitable for post-synthesis modifications.

**Synthesis of LP_MSNs with azide-functionality at 10 °C with TMB as micellar expander**

Azide-functionalized mesoporous silica nanoparticles with ultra-large pores (LP_MSN-N$_3$) were successfully synthesized employing a modified sol-gel method at mildly acidic conditions and low temperatures (10 °C).[7]These LP_MSNs are suitable for the immobilization of alkyne-functionalized enzymes by a click chemistry approach. In brief, a co-condensation approach was chosen to introduce low amounts (1 mol% of the original TEOS amount) of azide-functionality into the mesoporous framework of the LP_MSNs and to obtain a homogeneous distribution of organic-moieties within the silica material. For this purpose, the silica source TEOS was mixed with freshly synthesized 3-azidopropyl triethoxysilane (AzTES)[29] before the resulting solution was introduced into an acidic solution consisting of the dual surfactant system Pluronic F127 and an increased amount of FC-4 (1.4 g), together with TMB). We applied a hydrothermal treatment of the as-synthesized material in acidic media developed by Gao *et al.* in order to obtain LP_MSN-N$_3$ (cf. experimental section).[7] The key features of the newly generated LP_MSN-N$_3$ are summarized below.

**Table 6.4:** Dynamic light scattering (DLS) after size separation centrifugation and nitrogen sorption data of LP_MSN-N$_3$.

| Sample | Particle size[a] (nm) | BET surface area (m²/g) | Pore volume (cm³/g) | Pore size[b] (nm) |
|---|---|---|---|---|
| **LP_MSN-N$_3$** | 220 | 150 | 0.7 | 11.8 |

[a]Average particle size refers to the peak value of the particle size distribution after size separation centrifugation derived from DLS measurements in ethanolic solution; [b]DFT pore size refers to the peak value of the pore size distribution.

Transmission electron microscopy (Figure 6.10A) and scanning TEM images (Figure 6.10B) after size separation centrifugation show spherically shaped nanoparticles with a narrow particle size distribution within a size range of 80 – 150 nm. The large pores are present in each LP_MSN-N$_3$ nanoparticle and evenly distributed over the entire particle.
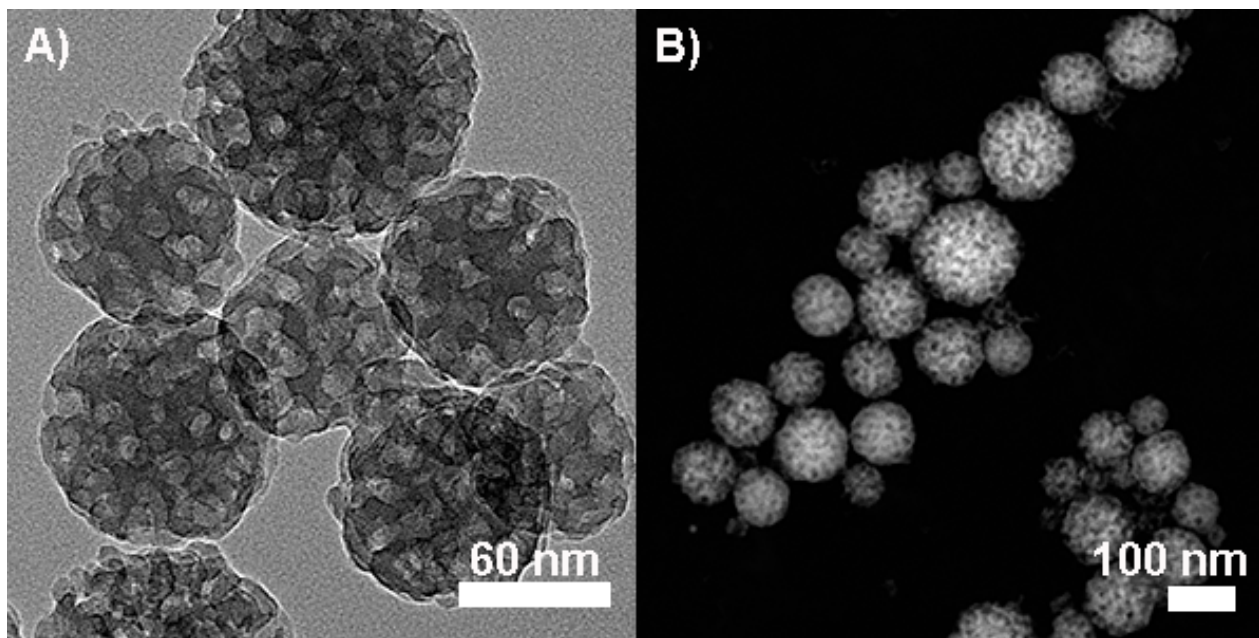
**Figure 6.10: A)** Transmission electron micrograph of LP_MSN-N$_3$ after size separation centrifugation and **B)** scanning transmission electron micrograph of LP_MSN-N$_3$.

The detailed analysis and discussion of the sample LP_MSN-N$_3$ is given in Chapter 7, describing their performance as solid support for the alkyne-functionalized enzymes cytochrome C (sp-CytC) and alkyne-functionalized trypsin (sp-trypsin).

**Synthesis of LP_MSNs with amino/phenyl-functionality**

T. Lebold showed in his doctoral thesis (LMU) that co-condensed SBA-15 type particles cannot be synthesized exclusively as amino-functionalized derivative, as 3-aminopropyl triethoxysilane (APTES) disrupts the mesostructure of the silica material.[30] However, a co-condensation approach can be successfully pursued for SBA-15 when APTES (5 mol% of the original TEOS amount employed for unfunctionalized SBA-15) is reacted together with phenyl triethoxysilane (PTES, 5 mol%) and TEOS (90 mol% of the original amount).[31] To generate amino/phenyl functionalized LP_MSNs, the silica source TEOS was mixed with 0.5 mol% APTES and 0.5 mol% PTES before the resulting precursor solution was introduced into an acidic solution consisting of the dual surfactant system Pluronic F127 and an increased amount of FC-4 (1.4 g), together with TMB. The as-synthesized LP_MSNs were hydrothermally treated according to the previously described procedure before the template was removed by solvent extraction in a mixture of ethanol, acetone and hydrochloric acid to retain

the colloidal behavior of the nanoparticles. The obtained, template-free LP_MSN-NH₂/Ph particles were investigated with nitrogen physisorption.
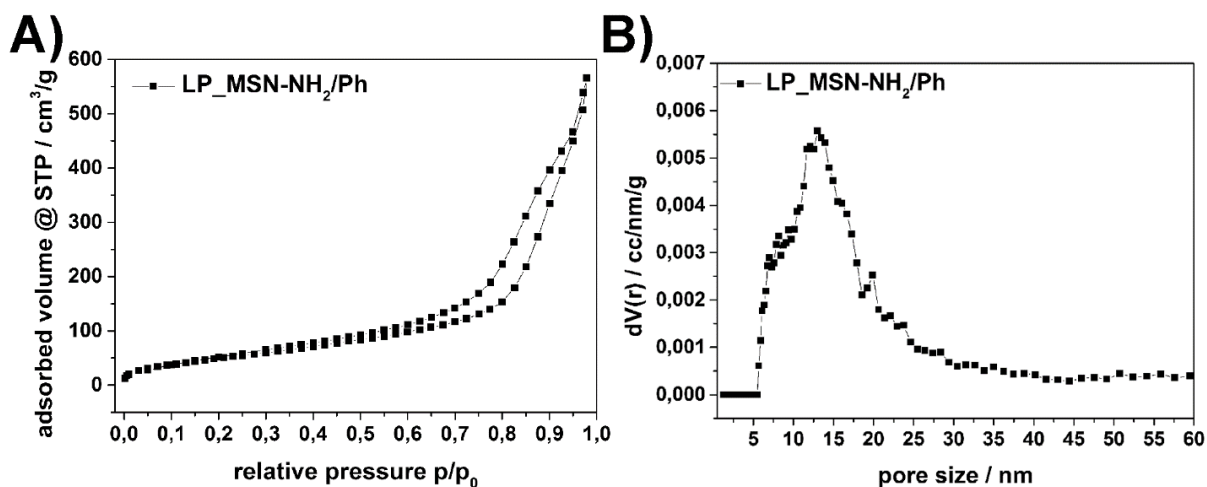


**Figure 6.11:** Nitrogen sorption data of LP_MSN-NH₂/Ph with 1 mol% functionality; **A)** nitrogen adsorption isotherm, and **B)** calculated NLDFT pore size distribution.

The isotherm of LP_MSN-NH₂/Ph can be interpreted as a hybrid form between a type II isotherm combined with a certain degree of type IV. The hysteresis can be characterized as an H3 hysteresis loop that results from aggregation and thus from a significant degree of textural porosity (Figure 6.11A). A monolayer formation of the adsorbate can be observed between $p/p_0 = 0$ and 0.02, followed by multilayer adsorption over a broad range. The lack of saturation at high $p/p_0$ values can be explained with the large structural pore diameter of our synthesized LP_MSN-NH₂/Ph, in combination with larger textural interparticle voids that are present between the dried LP_MSNs. The calculated pore size (Figure 6.11B), exhibiting a maximum at 13 nm, show the presence of a mesoporous MSN material, which was confirmed with transmission electron microscopy. The key features of the LP_MSN-NH₂/Ph derived from DLS measurements and $N_2$ physisorption are summarized in Table 6.5.

**Table 6.5:** Dynamic light scattering (DLS) after size separation centrifugation and nitrogen sorption data of LP_MSN-NH$_2$/Ph with 1 mol% functionality.

| Sample | Particle size[a] (nm) | BET surface area (m²/g) | Pore volume (cm³/g) | Pore size[b] (nm) |
|---|---|---|---|---|
| **LP_MSN-NH$_2$/Ph** | 90 | 176 | 0.8 | 13.0 |

[a]Average particle size after size separation centrifugation refers to the peak value of the particle size distribution derived from DLS measurements in ethanolic solution; [b]DFT pore size refers to the peak value of the pore size distribution.
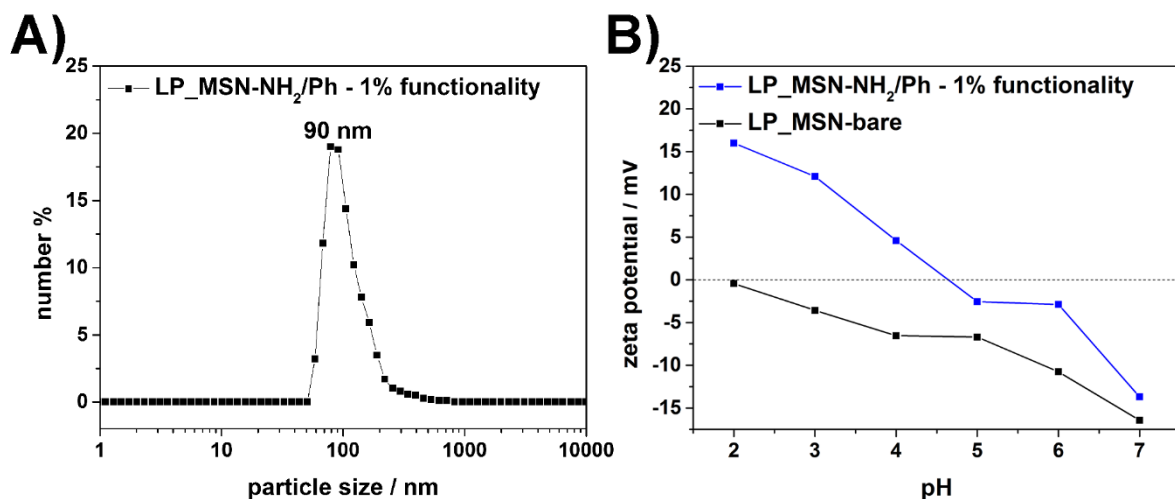


**Figure 6.12: A)** Dynamic light scattering data of LP_MSN-NH$_2$/Ph after size separation centrifugation and **B)** zeta potential measurements of LP_MSN-NH$_2$/Ph (blue) and unfunctionalized LP_MSN-bare (black).

Compared to unfunctionalized LP_MSNs (black curve), the sample LP_MSN-NH$_2$/Ph (blue curve) shows positive zeta potential values between pH 2 and pH 5, which is typical for materials with amino-functionality at the outer surface. With increasing pH, the degree of protonation declines, resulting in a decrease of the zeta potential values. At pH values between 5 and 7, the potential turns negative due to the deprotonation of the remaining silanol groups. The entire curve is typical for amino-functionalized nanoparticles and indicates the successful functionalization of LP_MSN by co-condensation. The isoelectric point (IEP) for the sample LP_MSN-NH$_2$/Ph is about 4.9, a value that is comparably high considering only 1 mol% overall functionalization within the nanoparticles. The IEP is about 1.9 for LP_MSN-bare, which results from the silanol groups of the silica framework leading to a more negative surface upon deprotonation. We note that an analysis of the LP_MSNs with spectroscopic methods did not

yield sufficient information about the successful incorporation of functional groups within the mesoporous framework, as only 1 mol% overall functionality is present in the nanoparticles.
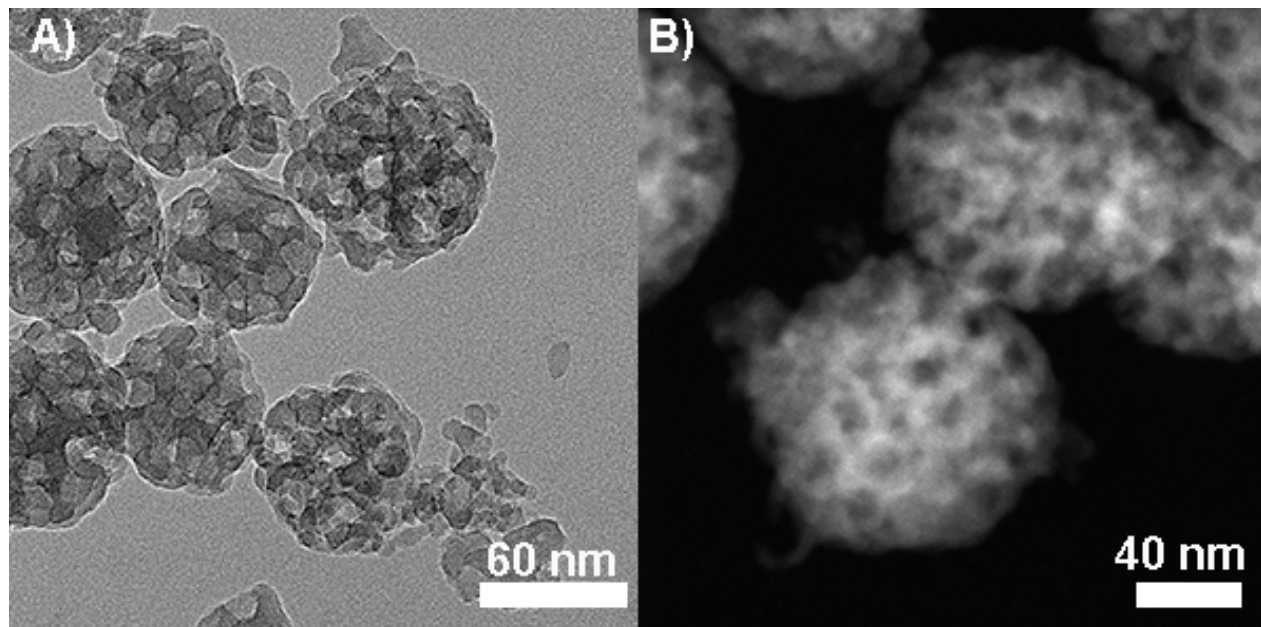


**Figure 6.13:** Transmission electron microscopy analysis of LP_MSN-NH$_2$/-Ph with 1 mol% amino/phenyl functionalization after size separation centrifugation. **A)** TEM micrograph and **B)** scanning TEM micrograph.

### 6.2.3 Hollow sphere mesoporous silica nanoparticles with amino/phenyl-functionalization

In this section we report about the unexpected formation of hollow sphere mesoporous nanoparticles by using a modified synthesis of the large-pore mesoporous nanoparticles. Here, the original synthesis of Gao *et al.* was modified with respect to the amount of applied silica precursor, as TEOS was partly substituted through organo-silanes (5 mol% phenyl triethoxysilane and 5 mol% 3-aminopropyl triethoxysilane)[7] to generate organo-functionalized LP_MSNs via a facile co-condensation approach. The respective organo-silanes were mixed with the 90 mol% of the original amount of TEOS at ambient temperature before the silica precursor solution was added drop-wise to the mildly acidic reaction mixture consisting of Pluronic F127, fluorocarbon surfactant FC-4 and TMB. Initially, the reaction mixture was stirred at 10 °C over night without the hydrothermal treatment steps as previously described,

but instead of the expected LP_MSNs with amino-functionality, hollow sphere nanoparticles (HS_MSNs) were obtained. Nitrogen adsorption revealed a hybrid-isotherm (type II with a certain amount of type IV) with a typical H3 hysteresis loop, indicating a certain degree of textural porosity, a low BET surface area of $A_s = 182$ m²/g, a low pore volume of 0.36 cm³/g and a rather broad NLDFT pore size distribution between 4.8 and 15 nm (Figure 6.14).
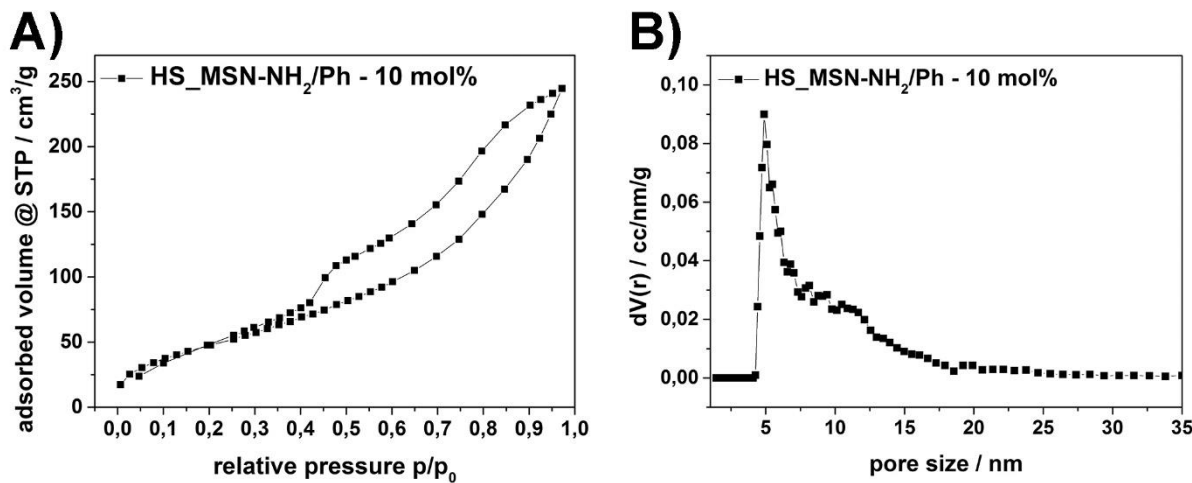


**Figure 6.14:** Nitrogen sorption data of hollow spheres HS_MSN-NH$_2$/Ph with 10 mol% functionality synthesized over night. **A)** Nitrogen sorption isotherm and **B)** DFT pore size distribution.

No saturation is reached at high relative pressures implying either high textural porosity or the presence of a large amount of unstructured material within the sample; the latter was confirmed by scanning electron microscopy (SEM, Figure 6.15).
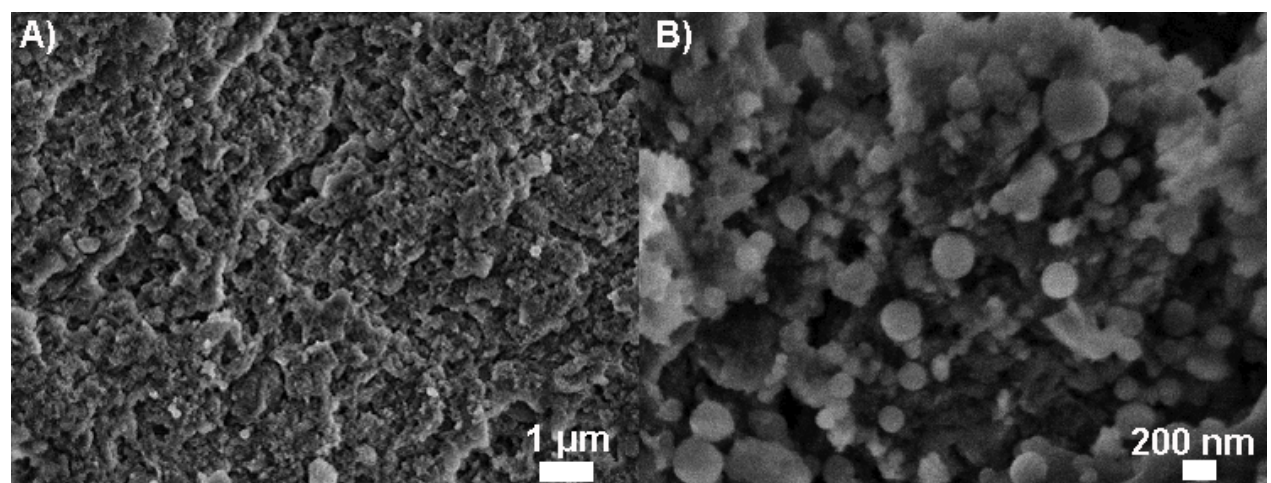


**Figure 6.15:** SEM micrographs of HS_MSN-NH$_2$/Ph (with 10 % organo-functionality consisting of 5 mol% PTES and 5 mol% APTES) synthesized with TMB at 10 °C overnight.

The micrographs show that only a small number of spherically shaped nanoparticles in a size range of 30 – 60 nm is present in the sample, whereas large parts of the sample consist of unstructured bulk material.

The same synthesis pathway was also examined with reduced stirring time in order to reduce silica precursor condensation and to limit the formation of the disordered structures present in the above-mentioned synthesis. Indeed, completely different hollow sphere morphologies were obtained following this synthetic pathway. The process of hollow sphere (HS) formation within the reaction time was followed by dynamic light scattering (Figure 6.16A) and was stopped 6 h after the initial TEOS addition. The synthesis was completed by a two-step hydrothermal treatment (1 d at 150 °C in the original synthesis solution, 2 d at 140 °C in 0.2 M hydrochloric acid) and the template was removed from the mesopores via solvent extraction. DLS measurements of the template-extracted nanoparticles in ethanol revealed a homogeneous sample without agglomeration (Figure 6.16B), with a maximum at 32 nm, which corresponds to the initial peak obtained for the as-synthesized LP_MSNs after 2 h.
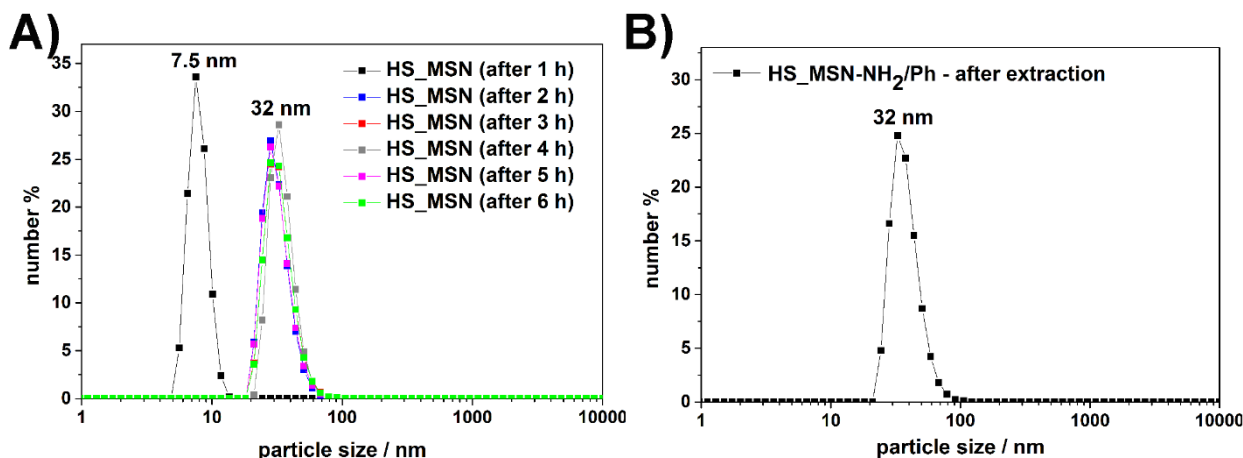


**Figure 6.16:** Dynamic light scattering (DLS) measurements of the sample HS_MSN-NH$_2$/Ph in ethanol. **A)** Time-dependent particle formation of HS_MSN-NH$_2$/Ph after initial TEOS addition to the dual surfactant solution and **B)** DLS of template-extracted HS_MSN-NH$_2$/Ph exhibiting a single peak with a maximum at 32 nm.

Nitrogen adsorption measurements yield a type IV isotherm typical for mesoporous materials (Figure 6.17A) showing a H1 hysteresis loop. The isotherm nearly reaches saturation at high p/p$_0$ values, indicating a homogeneous sample with barely any textural porosity. The isotherm

increases in the first part up to a relative pressure of 0.2, which can be attributed to the monolayer adsorption. Subsequently, multilayer adsorption takes place resulting in a linear slope of the isotherm at $p/p_0$ values between 0.2 and 0.45. At relative pressures of 0.45–0.95 capillary condensation occurs which results in a hysteresis loop between the adsorption and the desorption branch. Since the slope of the desorption branch at relative pressures $p/p_0$ between 0.5 and 0.8 is relatively constant, a broad NLDFT pore size distribution (Figure 6.17B) is obtained. The pore size distribution extracted from nitrogen sorption data indicates that a mesoporous system with bimodal pores (maxima at 6.6 nm and 19 nm) and very high pore volumes (Table 6.6) was synthesized. Transmission electron microscopy (TEM) shows hollow sphere silica particles (HS_MSNs) with an approximate diameter of 25–30 nm (Figure 6.17C and D). The sample is rather monodisperse and no impurities are detectable, which is also supported by the dynamic light scattering (DLS) results giving an average particle diameter of 32 nm after extraction. All particles possess only one large pore (light grey) which is surrounded by a thin silica layer (dark grey). The mean pore diameter visible in TEM is 12 – 15 nm whereas the width of the silica coating is between 5 – 9 nm. We note that these results seem to differ from the above-mentioned bimodal pore system; we attribute the peak at 6.6 nm to textural porosity between the dried particles (Figure 6.17C – red lines) and additionally to the windows into the hollow spheres, some of which can be seen in Figure 6.17D).
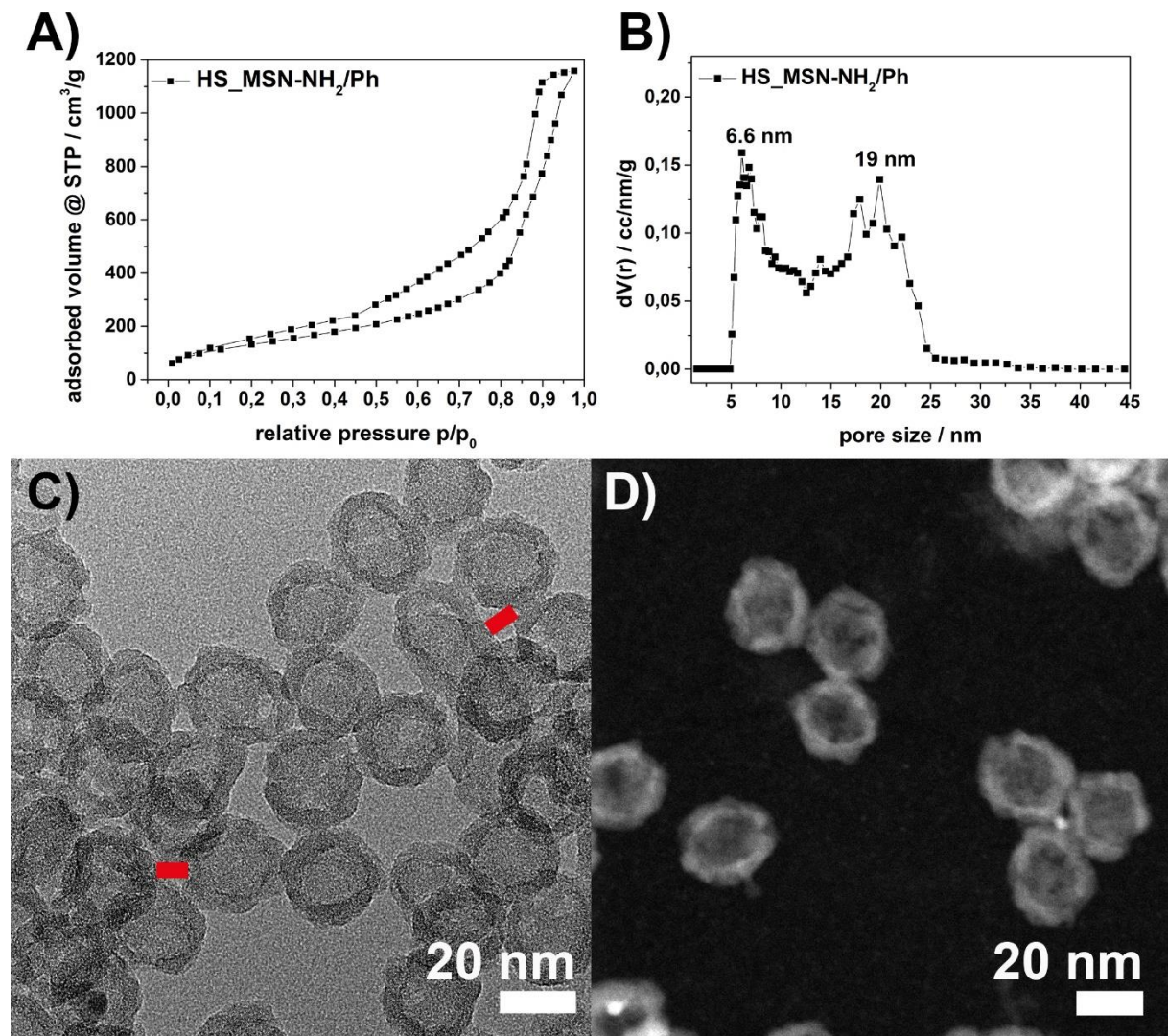
**Figure 6.17:** Characterization of silica hollow spheres HS_MSN-NH$_2$/Ph obtained after a reaction time of 6 h. **A)** Nitrogen sorption isotherm of HS_MSN-NH$_2$/Ph, **B)** calculated NLDFT pore size distribution showing a bimodal pore system, **C)** Transmission electron microscopy image of amino/phenyl-functionalized hollow sphere MSNs (red bars indicating interparticle porosity), and **D)** scanning transmission electron micrograph of the sample HS_MSN-NH$_2$/Ph.

**Table 6.6:** Dynamic light scattering (DLS) and nitrogen sorption data of HS_MSN-NH$_2$/Ph synthesized with TMB at 10 °C and a reaction time of 6 h.

| Sample | Particle size[a] (nm) | BET surface area (m$^2$/g) | Pore volume (cm$^3$/g) | Pore size[b] (nm) |
|---|---|---|---|---|
| **HS_MSN-NH$_2$/Ph – 6 h** | 32 | 486 | 1.13 | 6.6 & 19 |

[a]Average particle size refers to the peak value of the particle size distribution derived from DLS measurements in ethanolic solution; [b]DFT pore size refers to the two peak values of the pore size distribution.

To prove the functionality of the hollow sphere silica nanoparticles, zeta potential measurements of HS_MSN-NH$_2$/Ph and unfunctionalized LP_MSNs were recorded and additionally Raman spectroscopy was performed with the synthesized material. The zeta potential of the synthesized silica nanoparticles is highly dependent of the pH value of the aqueous solution (Figure 6.18A). A positive surface charge refers to protonable groups such as amino-moieties. The sample HS_MSN-NH$_2$/Ph (blue curve) shows, compared to LP_MSN-bare (LP_MSNs without organo-functionality, black curve), highly positive zeta potential values over the entire acidic pH range. The isoelectric point (IEP) for the sample HS_MSN-NH$_2$/Ph at a pH value of 5 is indicating amino-groups located at the outer surface of the hollow sphere silica nanoparticles, as the unfunctionalized LP_MSNs have an IEP = 2.0. As mentioned above, this is an effect of the silanol groups of the silica framework leading to a more negative surface upon deprotonation. The obtained zeta potential data for HS_MSN NH$_2$/Ph give a first indication of the successful incorporation of amino-moieties.
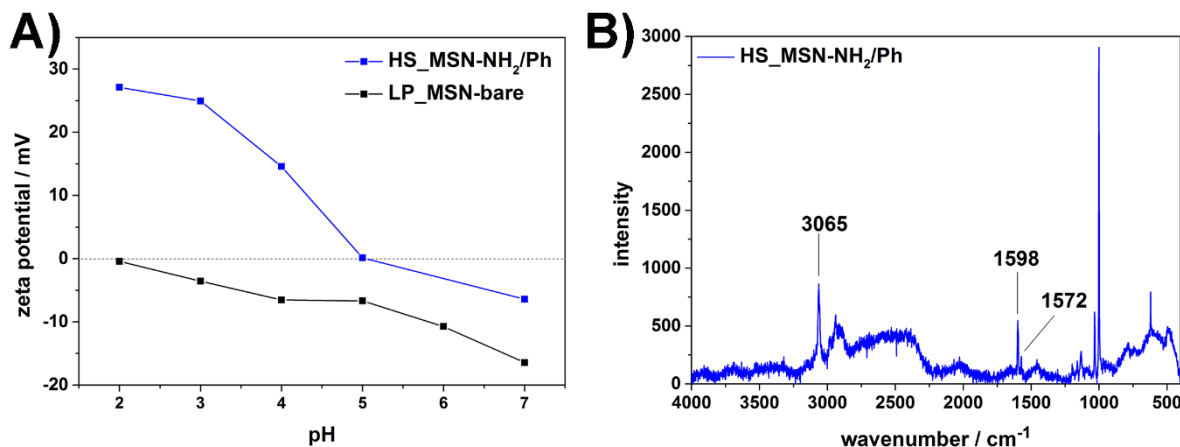
**Figure 6.18: A)** Zeta potential measurements of HS_MSN-NH$_2$/Ph (blue) and unfunctionalized LP_MSN-bare (black) **and B)** Raman spectrum of HS_MSN-NH$_2$/Ph.

The existence of functional groups in the sample HS_MSN-NH$_2$/Ph can be demonstrated with Raman spectroscopy (Figure 6.18B) since the phenyl-moieties in the sample exhibit strong bands. The HS_MSN-NH$_2$/Ph shows characteristic bands of the aromatic system at 3065 cm$^{-1}$ (C-H stretching vibration of aromatic rings), 1598 cm$^{-1}$ (-C=C- stretching vibration), 1572 cm$^{-1}$ (ring vibration) and a deformation vibration of the phenyl ring at 998 cm$^{-1}$. Additionally, the C-H stretching vibration modes of the alkyl chains (including ethoxy-groups on the silica framework) are present at 2983, 2939 and 2902 cm$^{-1}$. In addition to the above-mentioned analysis methods that already confirm the successful amino/phenyl-functionalization of the hollow spheres, the amino-moieties of the sample were reacted with carboxy-terminated gold nanoparticles (AuNPs, 3 nm diameter)[32] via an EDC amidation. The sample was subsequently washed thoroughly to remove the excess of unbound AuNPs and was investigated with scanning transmission electron microscopy (STEM, Figure 6.19). The staining can be imaged with STEM due to the z-contrast between gold and silica, giving a better contrast than TEM imaging.
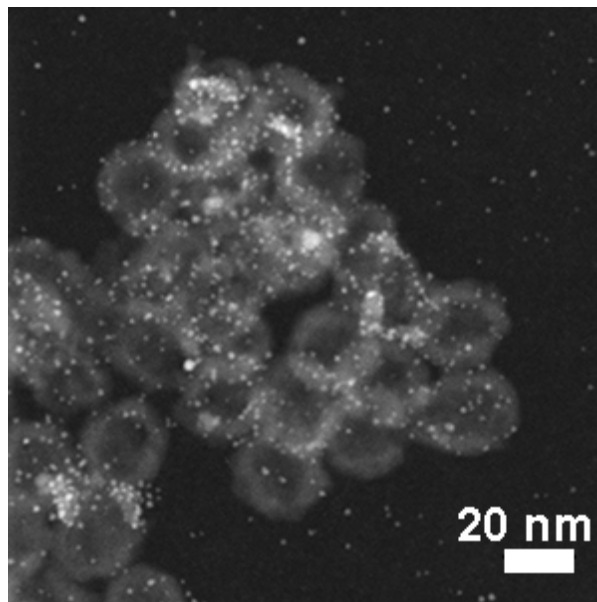
**Figure 6.19:** STEM micrograph of HS_MSN-NH$_2$/Ph (5 mol% PTES, 5 mol% APTES) stained with covalently attached AuNPs (3 nm).

The representative STEM image of HS_MSN-NH$_2$/Ph with covalently attached AuNPs shows an increased concentration of the gold nanoparticles (small white dots) on the silica material of the particles (grey circle), suggesting a successful amino-functionalization of the hollow spheres. We conclude from the obtained data for HS_MSN-NH$_2$/Ph the successful synthesis of organo-functionalized hollow sphere silica nanoparticles with a rather uniform particle size of around 32 nm and one single pore with an average diameter of 15 nm.

In addition to the newly developed synthesis pathway described above, the micellar expander TMB was substituted by an equal molar amount of TiPB. The influence of the different swelling agent on the synthesis of hollow sphere silica nanoparticles was studied in detail together with the influence of the reaction time (6 h and overnight). We followed the previously described fluorocarbon surfactant-assisted synthesis pathway with Pluronic F127 as structure directing agent under mildly acidic conditions, but changed the reaction temperature to 30 °C and substituted TMB against an equal molar amount of TiPB. TEOS (90 mol% of the original amount) was partly substituted through phenyl triethoxysilane (5 mol%) and APTES (5 mol%). The two-step hydrothermal treatment approach (1 d at 150 °C, 2 d at 140 °C in 0.2 M hydrochloric acid) and the template removal was identical for both samples. The obtained amino/phenyl functionalized silica nanoparticles were characterized with regard to their particle size, porosity and morphology with dynamic light scattering (DLS), nitrogen physisorption and transmission electron microscopy, respectively. Additionally, the organo-functionalization of

the synthesized HS_MSNs was investigated with zeta potential measurements. The obtained results are summarized in Figure 6.20 (DLS, nitrogen sorption and zeta potential measurements) and Figure 6.21 (TEM images).
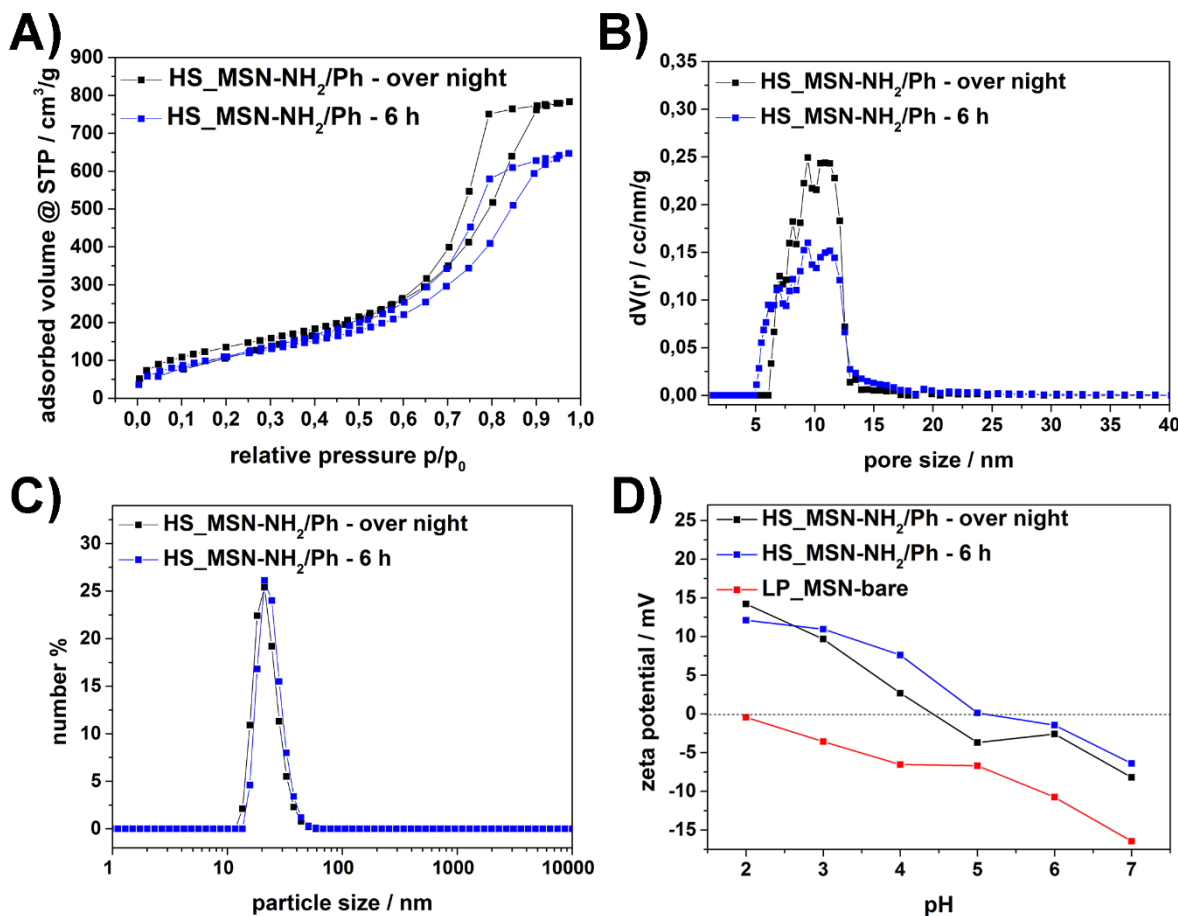


**Figure 6.20:** Analysis of amino/phenyl functionalized hollow sphere silica nanoparticles (HS_MSNs) synthesized with TiPB as micellar expander during different reaction times; HS_MSN-NH$_2$/Ph-overnight (black) and HS_MSN-NH$_2$/Ph-6 h (blue). **A)** Nitrogen sorption isotherms of template-free HS_MSNs, **B)** NLDFT pore size distributions, **C)** dynamic light scattering (DLS) data of the as-synthesized nanoparticles in ethanol, and **D)** zeta potential measurements of HS_MSN-NH$_2$/Ph-overnight (black), HS_MSN-NH$_2$/Ph-6h (blue) and LP_MSN-bare (LP_MSN without organo-functionality, red). The color coding (black, blue) is consistent in the different panels.

The nitrogen adsorption isotherms (Figure 6.20A) for both samples reveal a type IV isotherm which is typical for mesoporous materials. The first part of the isotherm at relative pressures between 0 and 0.2 p/p$_0$ can be assigned to monolayer adsorption of nitrogen. Both samples

show a multilayer adsorption at p/p$_0$ values between 0.2–0.6. The capillary condensation which follows after the multilayer adsorption ranges between p/p$_0$ = 0.6–0.9 for HS_MSN-NH$_2$/Ph-overnight and p/p$_0$ = 0.6–0.95 for HS_MSN-NH$_2$/Ph-6h. A slight shift to higher pressures for HS_MSN-NH$_2$/Ph-6h can be noted, whereas the absolute value of adsorbed nitrogen amount is increased for the sample HS_MSN-NH$_2$/Ph-overnight. At relative pressures higher than 0.92, both isotherms reach a plateau, indicating pore saturation followed by adsorption at the external surface of the nanoparticles. The particle size of the as-synthesized amino/phenyl functionalized nanoparticles was determined by dynamic light scattering in ethanol (Figure 6.20C); both samples show a nearly identical and very homogenous particle size distribution with a maximum at 24 nm for HS_MSN-NH$_2$/Ph-overnight and 22 nm for HS_MSN-NH$_2$/Ph-6h. The key features of the synthesized silica hollow spheres, obtained with dynamic light scattering and nitrogen adsorption, are summarized in Table 6.7.

**Table 6.7:** Dynamic light scattering (DLS) and nitrogen sorption data of HS_MSN-NH$_2$/Ph-overnight and HS_MSN-NH$_2$/Ph-6h synthesized with TiPB at 10 °C.

| Sample | Particle size[a] (nm) | BET surface area (m$^2$/g) | Pore volume (cm$^3$/g) | Pore size[b] (nm) |
|---|---|---|---|---|
| HS_MSN-NH$_2$/Ph - overnight | 22 | 503 | 1.18 | 6.5-12.5 |
| HS_MSN-NH$_2$/Ph – 6 h | 24 | 412 | 0.97 | 5.7-12.5 |

[a]Average particle size after size separation centrifugation refers to the peak value of the particle size distribution derived from DLS measurements in ethanolic solution; [b]DFT pore size refers to the peak value of the pore size distribution

The applied synthesis procedure leads to a lower BET surface area for the sample synthesized with a reaction time of 6 h (A$_s$ = 412 m$^2$/g compared to A$_s$ = 486 m$^2$/g for HS_MSNs synthesized at 10 °C), whereas the BET area for the sample HS_MSN-NH$_2$/Ph-overnight is slightly higher compared to the previously synthesized HS_MSN-NH$_2$/Ph, as is the pore volume (1.18 cm$^3$/g compared to 1.13 cm$^3$/g for HS_MSNs synthesized at 10 °C). In order to prove the successful incorporation of organo-functionality into the mesoporous framework of the HS_MSNs, zeta potential measurements with the template-free samples were carried out (Figure 6.20D). Both amino/phenyl functionalized HS_MSNs show the typical zeta potential values for silica nanoparticles with amino-moieties on the outer surface. It can be noted that the zeta potential values for the sample HS_MSN-NH$_2$/Ph-overnight are slightly higher than for

HS_MSN-NH$_2$/Ph - 6 h at pH 2, whereas the isoelectric point is higher for HS_MSN-NH$_2$/Ph-6h (IEP = 5.0 compared to 4.4 for HS_MSN-NH$_2$/Ph-overnight). The IEP = 5.0 is similar to that obtained for the sample synthesized at 10 °C and with TMB. From the results it can be concluded that extremely small hollow sphere silica nanoparticles with amino-moieties were synthesized with this novel synthesis procedure.

In order to investigate the homogeneity, the morphology and the shape of the synthesized nanoparticles, transmission electron microscopy analysis of both samples was performed (Figure 6.21).
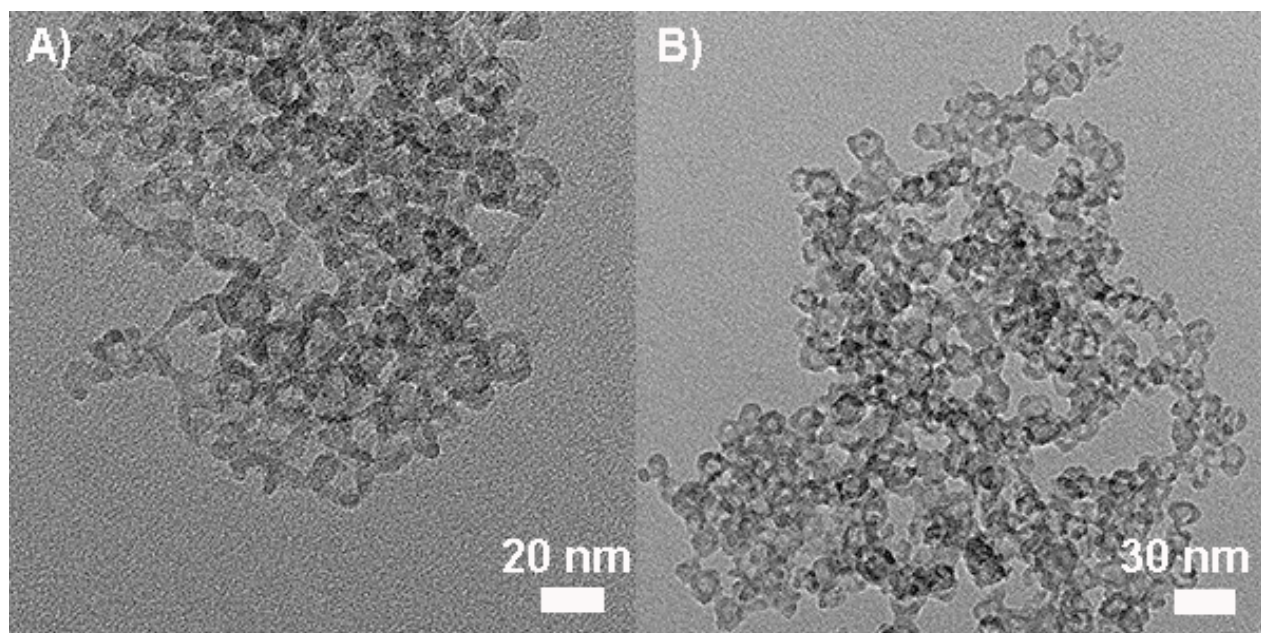


**Figure 6.21:** Transmission electron microscopy images of **A)** HS_MSN-NH$_2$/Ph stirred overnight at 30 °C and **B)** HS_MSN-NH$_2$/Ph stirred for 6 h.

Both samples, HS_MSN-NH$_2$/Ph-overnight and HS_MSN-NH$_2$/Ph-6 h, show small nanoparticles within a size range of $10 - 15$ nm and display no contamination with unstructured silica material. The particles are constituted of a silica shell (dark grey) that surrounds one single large pore (light grey) with pore diameters of $5 - 10$ nm, which is smaller than the value obtained for HS_MSNs synthesized with TMB at 10 °C. Additionally, the homogeneity is reduced compared to the previous sample and in both cases, the particles are partially fragmented. Additionally, it can be noted that a reduced reaction time leads to a strong decrease of particle numbers. It appears from the obtained TEM data that the employment of TiPB and

the higher synthesis temperature of 30 °C seem to disrupt the formation of hollow sphere silica nanoparticles, implying that his approach is unfavorable for the generation of amino-functionalized silica hollow spheres.

## 6.3  Conclusion

We report for the first time the FC-4 assisted synthesis of organo-functionalized large-pore MSNs *via* a co-condensation method. Different mesoporous silica nanoparticles with ultra-large pores (LP_MSNs) suitable for the adsorption of biomolecules were successfully synthesized using a dual-surfactant mediated synthesis pathway. A fluorocarbon surfactant-mediated synthesis at low temperatures and mildly acidic conditions with a dual surfactant system (FC-4 and Pluronic F127) and a micellar expander proved to be successful for the generation of LP_MSNs. The employment of fluorocarbon surfactant FC-4 was crucial for the synthesis procedure to yield nanoparticles of defined small sizes. Different silica nanoparticles with various pore sizes were generated throughout this work, ranging from LP_MSNs with a pore size of 8 nm to hollow spheres (HS_MSNs) offering a single pore of about 20 nm. Importantly, different functional groups (amino-, thiol- and azide-moieties) could be introduced into the silica framework via an one-pot co-condensation approach, which allows for the generation of a platform for post-synthesis modifications and immobilization of different cargo molecules, to be addressed in the following chapters. The impact of different molar ratios of 3-aminopropyl triethoxysilane (APTES) on the mesostructure formation was studied in detail together with the influence of temperature on the synthesis. Thus, in summary, we present the successful development of artificial hybrid nano-constructs based on structurally stable, mesoporous colloidal silica materials with defined morphologies and tuneable mesopores. These novel nanomaterials featuring large mesopores are suitable to act as solid support for biomolecules and for advanced host-guest chemistry and can be post-synthetically functionalized with stimuli-responsive trigger functions and cell-dependent recognition molecules. Both applications of these novel LP_MSNs will be discussed in the next chapter.

## 6.4  Experimental

**Chemicals:** Pluronic F127 (F127, Sigma), fluorocarbon surfactant 4 (FC-4, Yick-vik Chemicals), tetraethyl orthosilicate (TEOS, Fluka, >99%), 1,3,5-trimethylbenzene (TMB, Fluka, 96%), 1,3,5-triisopropylbenzene (TiPB, Fluka, >95%), ethanol absolute (EtOH, Aldrich, >99.5%), conc. hydrochloric acid (Aldrich, >95%, 37 wt%), 3-mercaptopropyl triethoxysilane (MPTES, ABCR, >92%), 3-aminopropyl triethoxysilane (APTES, Sigma, ≥ 98%), phenyl triethoxysilane (PTES, Sigma, 98%), acetone (reaction grade, Acros), N-(3-dimethylaminopropyl)-N′-ethylcarbodiimide (EDC, Sigma, 97%).

Unless otherwise noted, all reagents were used without further purification. Bi-distilled water from a Millipore system (Milli-Q Academic A10) was used for all syntheses and purification steps.

0.2 M HCl and 0.02 M HCl were prepared with bi-distilled water and conc. hydrochloric acid.

**Synthesis of unfunctionalized LP_MSNs with 1,3,5-triisopropylbenzene as micellar expander.** The synthesis of LP_MSNs at 30 °C followed a modified synthesis protocol published by Gao *et al.*.[7] Pluronic F127 (0.25 g) and fluorocarbon surfactant FC-4 (0.70 g) were dissolved in hydrochloric acid (HCl, 30 mL, 0.02 M). 1,3,5-Triisopropylbenzene (TiPB, 0.34 g, 1.66 mmol) was added and the solution stirred for 2 h at 30 °C. Tetraethyl orthosilicate (TEOS, 1.5 g, 7.2 mmol) was added drop-wise and the reaction mixture was stirred vigorously (1250 rpm) over night at 30 °C. The resulting particle suspension was hydrothermally treated under static conditions (150 °C, 1 d) before the mixture was centrifuged (15 min, 20500 rpm, 50228 rcf), re-suspended in hydrochloric acid (HCl, 30 mL, 0.2 M) and heated under static conditions (140 °C, 2 d). Parr autoclaves (100 mL) were used for post-synthetic hydrothermal treatment. After the addition of 50 mL bi-distilled H$_2$O, the LP_MSNs were collected by centrifugation (15 min, 20500 rpm, 50228 rcf), re-dispersed in 50 mL EtOH and extracted according to the procedure described below.

**Template removal from LP_MSNs.** The organic template was removed via extraction from LP_MSNs. For this purpose, 250 mg of the particles were refluxed for 2 h at 75 °C in a mixture of absolute EtOH (80 mL), acetone (40 mL) and conc. HCl (10 mL). This extraction step was

performed twice. The template-free LP_MSNs were separated by centrifugation (15 min, 20500 rpm, 50228 rcf) and washed with EtOH after each extraction step. LP_MSNs were obtained as colloidal suspension in EtOH. This extraction procedure was carried out for all samples unless otherwise noted.

**Size separation centrifugation of LP_MSNs.** In order to separate large agglomerates from the synthesized nanoparticles, a size separation centrifugation was performed (15 s, 3.000 rpm, 775 rcf) for selected samples. The resulting supernatant containing a nanoparticle yield of 50% (relative to the synthesis yield) was employed for all further applications. The obtained particles in ethanol were stored in tightly sealed glass vials.

**Synthesis of thiol functionalized large pore mesoporous silica nanoparticles (LP_MSN-SH).** Pluronic F127 (0.25 g) and fluorocarbon surfactant FC-4 (0.7 g) were dissolved in hydrochloric acid (HCl, 30 mL, 0.02 M), followed by the addition of TMB (0.20 g, 1.66 mmol), or 1,3,5-triisopropylbenzene (TiPB, 0.34 g, 1.66 mmol) respectively. The reaction mixture was stirred in a 100 mL polypropylene reactor for 2 h at 10 °C (for TMB) or 30 °C (for TiPB) before a mixture of tetraethyl orthosilicate (TEOS, 1.5 g, 7.2 mmol, 100 mol%) and 3-mercaptopropyl triethoxysilane (MPTES, 18.7 μL, 0.072 mmol, 1 mol%) was added drop-wise. The resulting suspension was stirred vigorously (1250 rpm) over night at 10 °C (or 30 °C for TiPB). The resulting particle suspension was hydrothermally treated in a 100 mL autoclave under static conditions (150 °C, 1 d). The mixture was centrifuged (15 min, 20500 rpm, 50228 rcf), re-suspended in hydrochloric acid (HCl, 30 mL, 0.2 M) and heated under static conditions (140 °C, 2 d). After the addition of 50 mL bi-distilled $H_2O$, the LP_MSNs were collected by centrifugation (15 min, 20500 rpm, 50228 rcf), re-dispersed in 50 mL EtOH and extracted according to the procedure described above.

**Synthesis of azide functionalized large pore mesoporous silica nanoparticles (LP_MSN-N$_3$).** A modified literature procedure was employed to synthesize LP_MSN-NH$_2$/Ph.[7, 27] Pluronic F127 (0.25 g) and an increased amount of fluorocarbon surfactant FC-4 (1.40 g) was dissolved in hydrochloric acid (HCl, 30 mL, 0.02 M), followed by the addition TMB (0.20 g, 1.66 mmol). The reaction mixture was stirred in a 100 mL polypropylene reactor for 2 h at 10 °C before a mixture of tetraethyl orthosilicate (TEOS, 1.5 g, 7.2 mmol) and (3-azidopropyl) triethoxysilane[29] (0.072 mmol) was added drop-wise. The resulting suspension was stirred vigorously (1250 rpm) over night at 10 °C. The resulting particle suspension was hydrothermally treated in a 100 mL autoclave under static conditions

(150 °C, 1 d). The mixture was centrifuged (15 min, 20500 rpm, 50228 rcf), re-suspended in hydrochloric acid (HCl, 30 mL, 0.2 M) and heated under static conditions (140 °C, 2 d). After the addition of 50 mL bi-distilled $H_2O$, the LP_MSNs were collected by centrifugation (15 min, 20500 rpm, 50228 rcf), re-dispersed in 50 mL EtOH and extracted according to the procedure described previously.

**Synthesis of amino/phenyl functionalized large pore silica nanoparticles (LP_MSN-NH$_2$/Ph) with 1 mol% functionality.** A modified literature procedure was employed to synthesize LP_MSN-NH$_2$/Ph.[7, 27] Pluronic F127 (0.25 g) and fluorocarbon surfactant FC-4 (1.4 g) were dissolved in hydrochloric acid (HCl, 30 mL, 0.02 M), followed by the addition of TMB (0.20 g, 1.66 mmol). The reaction mixture was stirred in a 100 mL polypropylene reactor for 2 h at 10 °C before a mixture of tetraethyl orthosilicate (TEOS, 1.5 g, 7.2 mmol, 100 mol%), phenyl triethoxysilane (PTES, 8.7 μL, 0.036 mmol, 0.5 mol%) and of 3-aminopropyl triethoxysilane (8.4 μL, 0.036 mmol, 0.5 mol%) was added drop-wise. The resulting suspension was stirred vigorously (1250 rpm) for 14 h at 10 °C. The resulting particle suspension was hydrothermally treated under static conditions (150 °C, 1 d). The mixture was centrifuged (15 min, 20500 rpm, 50228 rcf), re-suspended in hydrochloric acid (HCl, 30 mL, 0.2 M) and heated under static conditions (140 °C, 2 d). After the addition of 50 mL bi-distilled $H_2O$, the LP_MSN were collected by centrifugation (15 min, 20500 rpm, 50228 rcf), re-dispersed in 50 mL EtOH and extracted according to the procedure previously described.

**Synthesis of amino/phenyl functionalized large pore silica nanoparticles (LP_MSN-NH$_2$/Ph) with 10 mol% functionality.** Pluronic F127 (0.25 g) and fluorocarbon surfactant FC-4 (0.7 g) were dissolved in hydrochloric acid (HCl, 30 mL, 0.02 M), followed by the addition of TMB (0.20 g, 1.66 mmol). The reaction mixture was stirred in a 100 mL polypropylene reactor for 2 h at 10 °C before a mixture of TEOS (1.35 g, 6.43 mmol, 90 mol%), phenyl triethoxysilane (PTES, 87 μL, 0.36 mmol, 5 mol%) and of 3-aminopropyl triethoxysilane (84 μL, 0.36 mmol, 5 mol%) was added drop-wise. The resulting suspension was stirred vigorously (1250 rpm) at 10 °C overnight. The resulting particle suspension was hydrothermally treated under static conditions (150 °C, 1 d). The mixture was centrifuged (15 min, 20500 rpm, 50228 rcf), re-suspended in hydrochloric acid (HCl, 30 mL, 0.2 M) and heated under static conditions (140 °C, 2 d). After the addition of 50 mL bi-distilled $H_2O$, the

LP_MSNs were collected by centrifugation (15 min, 20500 rpm, 50228 rcf), re-dispersed in 50 mL EtOH and extracted according to the procedure described above.

**Synthesis of amino/phenyl functionalized hollow sphere silica nanoparticles (HS_MSN-NH₂/Ph).** A modified literature procedure was employed to synthesize HS_MSN-NH₂/Ph.[7, 27] Pluronic F127 (0.25 g) and fluorocarbon surfactant FC-4 (0.7 g) were dissolved in hydrochloric acid (HCl, 30 mL, 0.02 M), followed by the addition of TMB (0.20 g, 1.66 mmol). The reaction mixture was stirred in a 100 mL polypropylene reactor for 2 h at 10 °C before a mixture of TEOS (1.35 g, 6.43 mmol, 90 mol%), phenyl triethoxysilane (PTES, 87 µL, 0.36 mmol, 5 mol%) and of 3-aminopropyl triethoxysilane (84 µL, 0.36 mmol, 5 mol%) was added drop-wise. The resulting suspension was stirred vigorously (1250 rpm) for 6 h at 10 °C. The resulting particle suspension was hydrothermally treated under static conditions (150 °C, 1 d). The mixture was centrifuged (15 min, 20500 rpm, 50228 rcf), re-suspended in hydrochloric acid (HCl, 30 mL, 0.2 M) and heated under static conditions (140 °C, 2 d). After the addition of 50 mL bi-distilled H₂O, the LP_MSNs were collected by centrifugation (15 min, 20500 rpm, 50228 rcf), re-dispersed in 50 mL EtOH and extracted according to the procedure described above.

**Synthesis of amino/phenyl functionalized hollow sphere silica nanoparticles (HS_MSN-NH₂/Ph) with TiPB.** The hollow sphere silica nanoparticles were synthesized according to the above mentioned synthesis protocol. TMB (0.20 g, 1.66 mmol) was substituted by the same molar amount of TiPB (0.34 g, 1.66 mmol) and a synthesis temperature of 30 °C was employed.

**Covalent attachment of carboxy-terminated gold nanoparticles (3 nm) to HS_MSN-NH₂/Ph via an EDC-assisted amidation.** 1 mg of template-free HS_MSN-NH₂/Ph (111 µL of an ethanolic solution) was washed with absolute EtOH three times (1 mL for each washing step). Subsequently, 20 µL of a carboxy-terminated gold nanoparticle solution (AuNPs, 3 nm, 1 mg/mL in toluene) was added to the HS_MSN solution. EDC (1 µL, 5.7 µmol) was added and the reaction mixture was stirred overnight. The resulting AuNPs@HS_MSN-NH₂/Ph were extensively washed with 1 mL absolute EtOH (five times, 1 mL EtOH each) by centrifugation (5000 rpm, 1291 rcf, 1 min) in order to remove unbound AuNPs. The supernatant was discarded after each washing step and the purified AuNPs@HS_MSN-NH₂/Ph were investigated with scanning transmission electron microscopy (Figure 6.19).

**Characterization.** Centrifugation was performed using a Sorvall Evolution RC equipped with an SS-34 rotor or an Eppendorf centrifuge 5418 for small volumes. Nitrogen sorption measurements were performed with a Quantachrome NOVA 4000e or on a Quantachrome Autosorb iQ at -196 °C. Sample out-gassing was performed at 120 °C for 12 h at a pressure of 10 mTorr. Pore size and pore volume were calculated using a NLDFT equilibrium model for cylindrical pores of $N_2$ on silica, based on the desorption branch of the isotherm. The Brunauer-Emmett-Teller (BET) surface areas for all samples were calculated from the corresponding nitrogen sorption isotherms in the range of $p/p_0 = 0.05 - 0.2$. To calculate the total pore volume of the LP_MSNs, the amount of adsorbed nitrogen at the apparent plateau of the isotherm at high $p/p_0$ values was used. Dynamic light scattering (DLS) and zeta potential measurements were performed on a Malvern Zetasizer-Nano instrument equipped with a 4 mW He-Ne laser (633 nm) and an avalanche photodiode. DLS measurements were directly recorded on ethanolic colloidal suspensions at a concentration of 1 mg/mL. For the determination of the zeta potential profiles, three drops of the ethanolic particle suspension (ca. 3 wt%) were mixed with 1 mL of commercial Hydrion Buffer solution of the appropriate pH value prior to measurement. Hückel's approximation was used for interpretation. Raman spectra were recorded on a Jobin Yvon Horiba HR800 UV Raman microscope using a He-Ne laser emitting at $\lambda = 633$ nm. For scanning electron microscopy (SEM), a JEOL JSM-6500F scanning electron microscope was employed. Transmission electron microscopy (TEM) was performed on an FEI Titan 80-300 kV microscope operating at 300 kV or on a JEOL JEM-2011 at 200 kV. Scanning transmission electron microscopy (STEM) was performed on the above-mentioned Titan microscope. Samples were prepared by dispersing LP_MSNs (0.5 mg) in 2 mL absolute ethanol. A drop of the resulting diluted suspension was dried on a carbon-coated copper grid. Small angle X-ray scattering (SAXS) was performed on a Bruker D8 Discover diffractometer with Cu $K_\alpha$-radiation ($\lambda = 1.5406$ Å).

## 6.5   Appendix
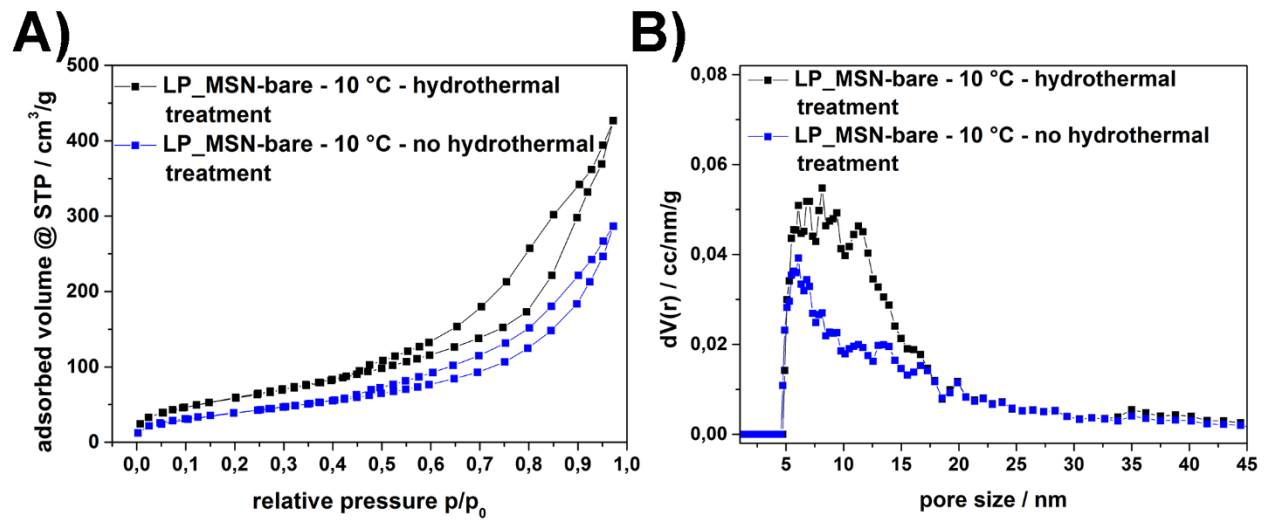


**Figure 6.22:** Nitrogen sorption analysis of template-free LP_MSN-bare synthesized with TMB at 10 °C with two-step hydrothermal treatment (black) and without (blue). **A)** Nitrogen sorption isotherms and **B)** calculated NLDFT pore size distribution.
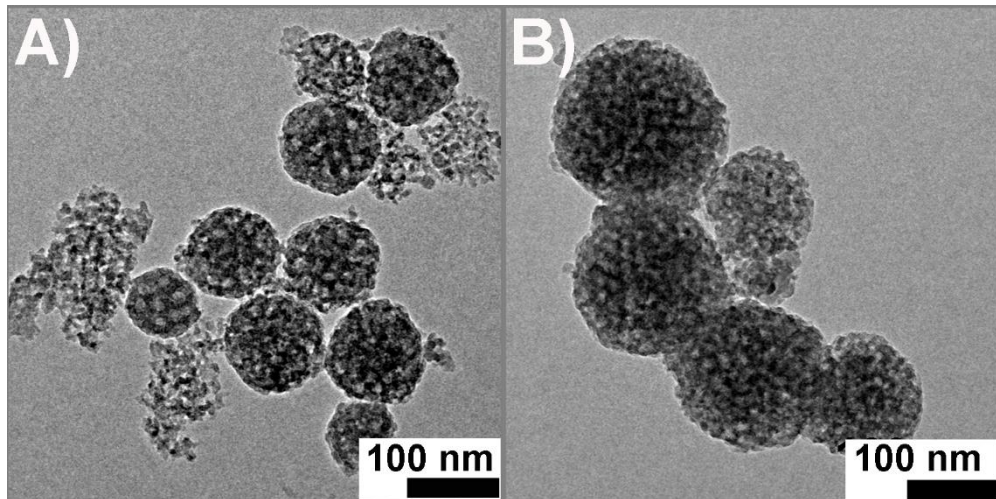


**Figure 6.23:** TEM micrographs of template-free LP_MSN-bare synthesized with TMB at 10 °C **A)** with two-step hydrothermal treatment of the as-synthesized LP_MSN-bare and **B)** without hydrothermal treatment.
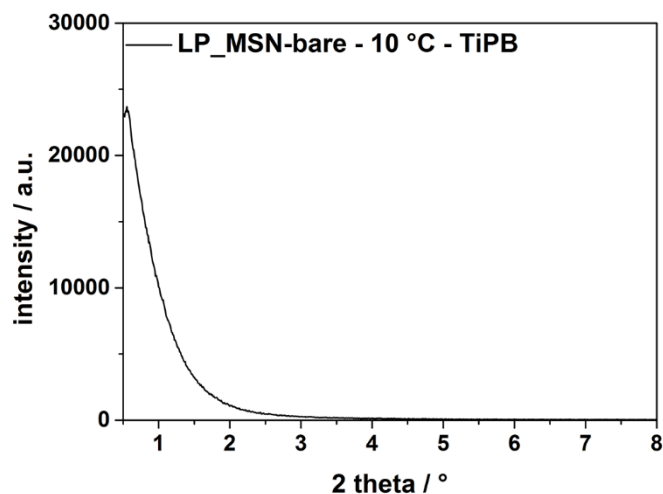
**Figure 6.24:** SAXS pattern of LP_MSN-bare synthesized with TiPB at 100 °C; (100) reflection at 0.55°.
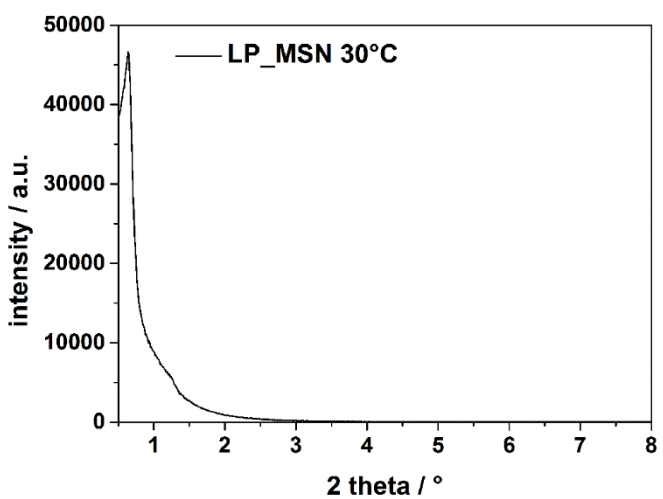


**Figure 6.25:** SAXS diffraction pattern of LP_MSN-bare synthesized with TiPB at 30 °C; (1 0 0) reflection at 0.63 °.
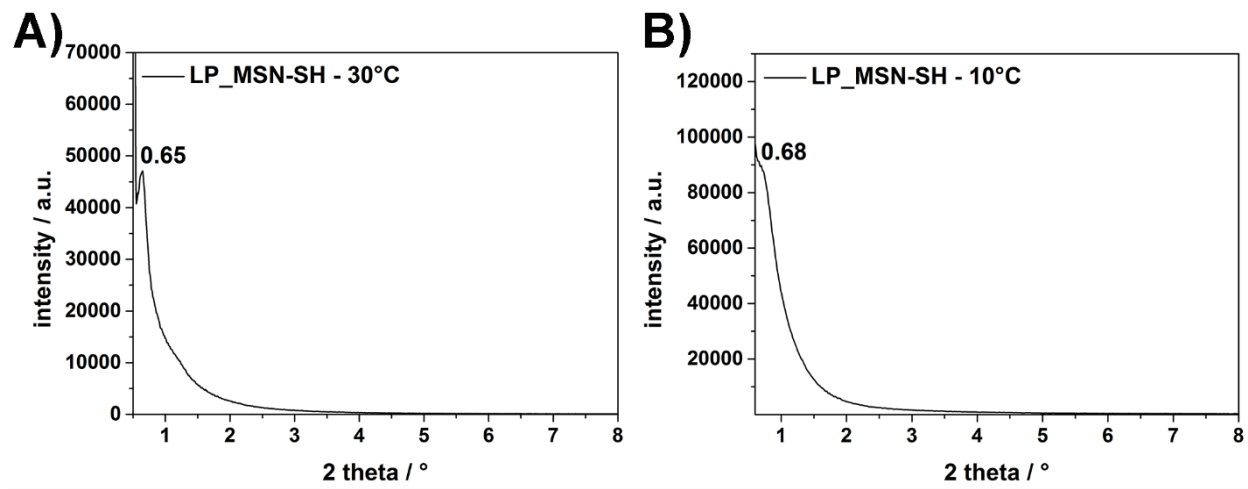
**Figure 6.26:** SAXS patterns of template-extracted LP_MSN-SH. A) synthesized at 30 °C with TMB and **B)** synthesized at 10 °C with TiPB.
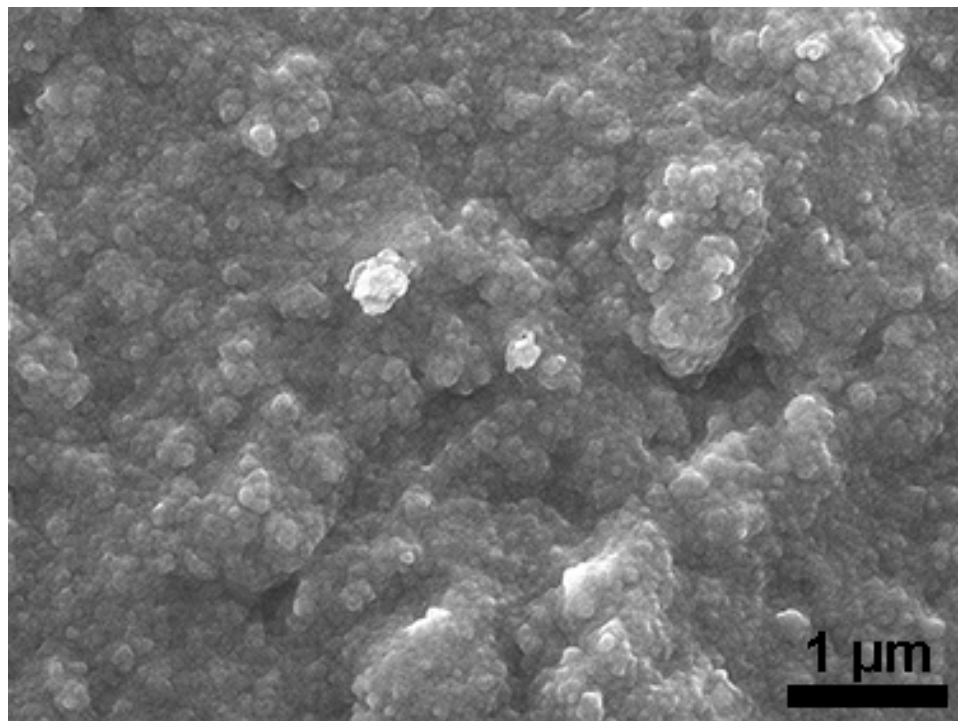


**Figure 6.27:** Scanning electron microscopy image of HS_MSN-NH$_2$/Ph-6h synthesized with TMB at 10 °C and a reaction time of 6 h.

## 6.6 References

1. Sauer, A. M.; Schlossbauer, A.; Ruthardt, N.; Cauda, V.; Bein, T.; Bräuchle, C. *Nano Lett.* **2010**, *10*, 3684-3691.

2. Schlossbauer, A.; Sauer, A. M.; Cauda, V.; Schmidt, A.; Engelke, H.; Rothbauer, U.; Zolghadr, K.; Leonhardt, H.; Bräuchle, C.; Bein, T. *Adv. Healthcare Mater.* **2012**, *1*, 316-320.

3. Mackowiak, S. A.; Schmidt, A.; Weiss, V.; Argyo, C.; von Schirnding, C.; Bein, T.; Bräuchle, C. *Nano Lett.* **2013**, *13*, 2576-2583.

4. Cauda, V.; Schlossbauer, A.; Kecht, J.; Zürner, A.; Bein, T. *J. Am. Chem. Soc.* **2009**, *131*, 11361-11370.

5. Möller, K.; Kobler, J.; Bein, T. *Adv. Funct. Mater.* **2007**, *17*, 605-612.

6. Han, Y.; Ying, J. Y. *Angew. Chem. Int. Ed.* **2005**, *44*, 288-292.

7. Gao, F.; Botella, P.; Corma, A.; Blesa, J.; Dong, L. *J. Phys. Chem. B.* **2009**, *113*, 1796-1804.

8. Na, H.-K.; Kim, M.-H.; Park, K.; Ryoo, S.-R.; Lee, K. E.; Jeon, H.; Ryoo, R.; Hyeon, C.; Min, D.-H. *Small* **2012**, *8*, 1752-1761.

9. Meng, H.; Xue, M.; Xia, T.; Zhao, Y.-L.; Tamanoi, F.; Stoddart, J. F.; Zink, J. I.; Nel, A. E. *J. Am. Chem. Soc.* **2010**, *132*, 12690-12697.

10. Thomas, C. R.; Ferris, D. P.; Lee, J. H.; Choi, E.; Cho, M. H.; Kim, E. S.; Stoddart, J. F.; Shin, J. S.; Cheon, J.; Zink, J. I. *J. Am. Chem. Soc.* **2010**, *132*, 10623-10625.

11. Lu, J.; Liong, M.; Sherman, S.; Xia, T.; Kovochich, M.; Nel, A. E.; Zink, J. I.; Tamanoi, F. *Nanobiotechnology* **2007**, *3*, 89-95.

12. Shen, J.; Kim, H. C.; Su, H.; Wang, F.; Wolfram, J.; Kirui, D.; Mai, J.; Mu, C.; Ji, L. N.; Mao, Z. W.; Shen, H. *Theranostics* **2014**, *4*, 487-97.

13. Wittig, R.; Rosenholm, J. M.; von Haartman, E.; Hemming, J.; Genze, F.; Bergman, L.; Simmet, T.; Linden, M.; Sahlgren, C. *Nanomedicine* **2013**.

14. Shim, M. S.; Kwon, Y. J. *Biomacromolecules* **2008**, *9*, 444-455.

15. Xia, T.; Kovochich, M.; Liong, M.; Meng, H.; Kabehie, S.; George, S.; Zink, J. I.; Nel, A. E. *ACS Nano* **2009**, *3*, 3273-3286.

16. Tietze, N.; Pelisek, J.; Philipp, A.; Roedl, W.; Merdan, T.; Tarcha, P.; Ogris, M.; Wagner, E. *Oligonucleotides* **2008**, *18*, 161-74.

17. Hom, C.; Lu, J.; Liong, M.; Luo, H.; Li, Z.; Zink, J. I.; Tamanoi, F. *Small* **2010**, *6*, 1185-1190.

18. Hartono, S. B.; Gu, W.; Kleitz, F.; Liu, J.; He, L.; Middelberg, A. P. J.; Yu, C.; Lu, G. Q.; Qiao, S. Z. *ACS Nano* **2012**, *6*, 2104-2117.

19. Stevenson, M.; Ramos-Perez, V.; Singh, S.; Soliman, M.; Preece, J. A.; Briggs, S. S.; Read, M. L.; Seymour, L. W. *J. Control. Release* **2008**, *130*, 46-56.

20. Schaffert, D.; Wagner, E. *Gene Ther.* **2008**, *15*, 1131-1138.

21. Ballarin-Gonzalez, B.; Howard, K. A. *Adv. Drug Deliv. Rev.* **2012**, *64*, 1717-29.

22. Zhao, D.; Feng, J.; Huo, Q.; Melosh, N.; Fredrickson, G. H.; Chmelka, B. F.; Stucky, G. D. *Science* **1998**, *279*, 548-552.

23. Zhao, D.; Huo, Q.; Feng, J.; Chmelka, B. F.; Stucky, G. D. *J. Am. Chem. Soc.* **1998**, *120*, 6024-6036.

24. Cao, L.; Man, T.; Kruk, M. *Chem. Mater.* **2009**, *21*, 1144-1153.

25. Cao, L.; Kruk, M. *Colloids Surf., A* **2010**, *357*, 91-96.

26. Tang, F.; Li, L.; Chen, D. *Adv. Mater.* **2012**, *24*, 1504-1534.

27. Zhou, X.; Qiao, S.; Hao, N.; Wang, X.; Yu, C.; Wang, L.; Zhao, D.; Lu, G. Q. *Chem. Mater.* **2007**, *19*, 1870-1876.

28. Kecht, J.; Schlossbauer, A.; Bein, T. *Chem. Mater.* **2008**, *20*, 7207-7214.

29. Gole, A.; Murphy, C. J. *Langmuir* **2007**, *24*, 266-272.

30. Lebold, T., *Doctoral Thesis, Mesoporous silica nanostructures: A versatile platform in Drug Delivery and Material Science*. Ludwig-Maximilians-University Munich: Munich, Germany, 2010.

31. Lebold, T.; Schlossbauer, A.; Schneider, K.; Schermelleh, L.; Leonhardt, H.; Bein, T.; Bräuchle, C. *Adv. Funct. Mater.* **2012**, *22*, 106-112.

32. Shimizu, T.; Teranishi, T.; Hasegawa, S.; Miyake, M. *J. Phys. Chem. B* **2003**, *107*, 2719-2724.

# 7 Click chemistry – a versatile method for enzyme immobilization onto large pore colloidal mesoporous silica nanoparticles

This chapter is based on the following publication:

Alexandra Schmidt, Martina Lichtnecker, Stefan Niedermayer, Kathrin Bader, and Thomas Bein, *to be submitted to ACS Nano 2014*
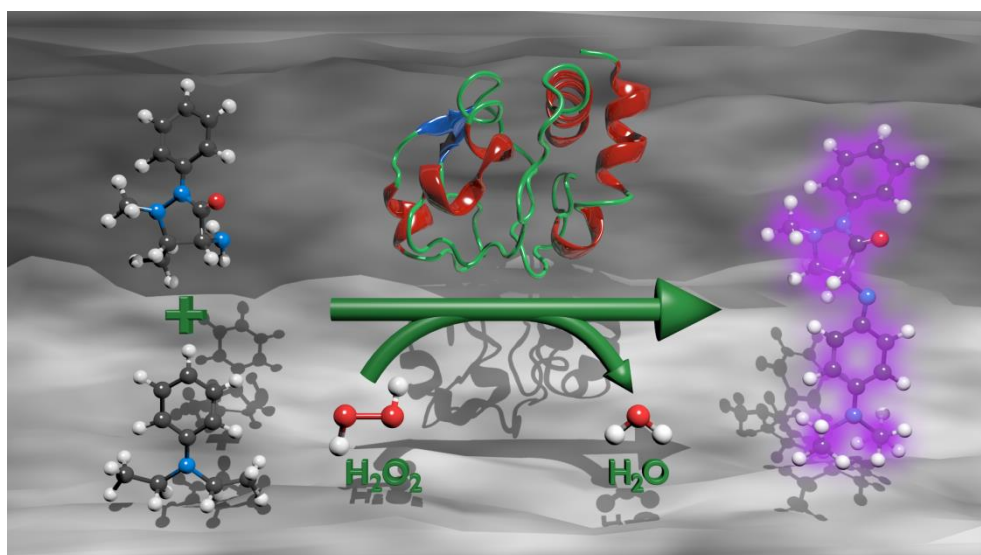


## Abstract

Various bio applications of mesoporous materials (e.g., the immobilization of enzymes or the delivery of biomolecules such as siRNA) require large pores for the successful adsorption of the rather large molecules of interest and protecting the fragile cargo from external forces such as degradation. We describe the facile synthesis of functionalized mesoporous silica nanoparticles with ultra-large pores (LP_MSNs) providing high loading capacity for the immobilization of two differently sized enzymes. The synthesis procedure yields homogeneous azide-functionalized LP_MSN-N$_3$ of about 120 nm in size with ultra-large pores of about 10 nm diameter. The azide-functionalized LP_MSN-N$_3$ were synthesized employing a fluorocarbon-mediated pathway with a dual surfactant system (F127 and FC-4) at 10 °C. Organo-moieties were incorporated into the mesoporous framework of LP_MSN via a co-condensation approach. Due to the azide-functionality these LP_MSNs are suitable for bio-orthogonal click chemistry reactions within the porous network. Two different acetylene-functionalized

enzymes (sp-cytochrome C and sp-trypsin) were immobilized in the pores of the obtained LP_MSNs by a copper-catalyzed 1,3-dipolar cycloaddition reaction. The covalent attachment of the enzymes within the mesopores allowed us to investigate the catalytic performance of the enzyme-silica systems. The enzymes are stable after bioconjugation with the silica support and show extremely high catalytic activity for the colorimetric reaction of 4-aminoantipyrine (4-AAP) and *N,N*-diethylaniline (DEA) in case of LP_MSN-CytC and the hydrolysis of p-toluene-sulfonyl-L-arginine methyl ester (TAME) by LP_MSN-Trypsin.

## 7.1  Introduction

Ordered mesoporous silica materials have attracted increasing attention due to the ability to tailor their structural and textural features including particle size, pore size, pore volume and surface area.[1-3] With the possibility to introduce various functionalities into the mesoporous framework, these materials have turned into interesting candidates for various biotechnological applications.[3-5] However, such applications often involve fairly large molecules of more than 5 nm in size that may not fit into the pores of established silica nanoparticles (ca. 4 nm). Additionally, the active molecules need to be immobilized while conserving their function. Considerable efforts have been made in the past years regarding the control of mesostructural diversity, compositional flexibility and morphology during the synthesis of mesoporous silica nanoparticles (MSNs).[2, 6-8] In recent years the synthesis of well-defined ultra-large pore mesoporous systems with small particle sizes (in the size-range of 100 – 200 nm) for the encapsulation of large biomolecules (i.e. enzymes or siRNA) has been addressed.[9-11] Synthesis strategies for the generation of MSNs with a diameter between 70 and 300 nm and very large pores (up to 17 nm) using a fluorocarbon surfactant and the triblock copolymer Pluronic® F127 have been published.[9, 12] To limit the growth of the nanoparticles, Han *et al*. additionally applied the cationic fluorocarbon surfactant FC-4 and obtained small particles in the range of 50-300 nm.[9] Gao *et al*. developed a new strategy to synthesize mesoporous silica nanoparticles with large pores (LP_MSN) at low temperatures (10 °C) by applying the triblock copolymer F127 as template and 1,3,5-trimethylbenzene (TMB) as swelling agent.[3] Based on a modified approach of the above-mentioned synthesis procedures, we were able to obtain LP_MSNs and directly functionalize them with organo-silanes during a co-condensation procedure. Due to

their large pores, our novel functionalized LP_MSNs can be loaded with large bioactive molecules and thus are promising candidates for numerous bio-applications, including biocatalysis. A promising way to introduce enzymes as biocatalysts in industrial applications is their immobilization onto inorganic mesoporous supports.[1, 13, 14] Organo-functionalized nanostructured mesoporous silica materials have attracted great attention among the available inorganic host systems as they offer outstanding properties for the immobilization and encapsulation of biomolecules.[1, 15, 16] As larger mesopores match the size of enzymes, mesoporous silica materials are also excellent candidates for enzyme immobilization,[17] yet the potential of LP_MSNs in this field still needs to be explored. Previous studies on established mesoporous silica materials (e.g. SBA-15) revealed that enzyme confinement within such hosts can increase the stability and reduce denaturation by protein unfolding, one major issue in industrial applications of biocatalysts.[18] However, as a consequence of immobilization onto the solid support, a decrease of the enzymatic activity relative to the free enzyme is often observed in such systems.[19, 20] Strong interactions between enzymes and the host materials can be obtained by complementary organo-functionalization within the porous network of the solid support, resulting in different catalytic activity and loading capacities.[21-23] As the functionalization of the mesoporous framework can be easily modified, the organo-moieties can be adjusted to the respective enzyme and the preferred attachment reaction. Furthermore, the application of mesoporous silica supports allows for the adjustment of pore- and particle size, structural arrangement and surface properties to optimize loading capacity and enzyme activity.[5, 24, 25] Recently, Lee *et al.* have reviewed different methods of covalent enzyme immobilization onto mesoporous silica supports.[26]

Here, we use the flexibility of silica functionalization for loading active enzymes and our newly developed MSNs with ultra-large pores to immobilize enzymes while retaining their activity. Kao *et al.* investigated the immobilization of the peroxidase cytochrome c in post-synthesis modified LP_MSN using glutaraldehyde, glutaric anhydride and succinimido-3-maleimidopropionate as covalent linkers.[27] They show that the orientation of the active site of cytochrome c is controlled by specific binding and that it correlates highly with the catalytic activity of the immobilized enzyme.

A modified azide-alkyne click chemistry approach established by Schlossbauer *et al.* was used to immobilize enzymes into the LP_MSNs, as this method is highly biocompatible and avoids unfavorable pore blocking.[28, 29] Two enzymes of different sizes, namely the peroxidase cytochrome C and the protease trypsin, were chosen for this study and were immobilized in an

efficient method in the newly developed MSNs. Low degrees of organo-functionalization were chosen for the LP_MSNs, as high degrees of modification can result in a reduction of the pore diameter, which hinders enzyme diffusion into the mesoporous channels and increases the probability of pore blocking. A novel co-condensation synthesis approach was developed to generate organo-functionalized MSNs with ultra-large pores suitable for highly biocompatible coupling methods. The catalytic activity of immobilized enzymes within the LP_MSNs was studied in detail and it was shown that the immobilized enzymes exhibit high stability and are highly active after covalent immobilization in the LP_MSNs.

## 7.2   Results and Discussion

### Synthesis of large pore MSNs

For the immobilization of alkyne-functionalized enzymes by a click chemistry approach, azide-functionalized mesoporous silica nanoparticles with ultra-large pores (LP_MSN-N$_3$) were synthesized using a modified sol-gel method at mildly acidic conditions and low temperatures (10 °C).[3] A co-condensation approach was chosen to introduce low amounts (1 mol% of the original TEOS amount) of azide-functionality into the mesoporous framework of the MSNs and to obtain a homogeneous distribution of organic-moieties within the silica material. Low degrees of organo-functionalization were chosen for the LP_MSNs, as high degrees of modification can result in a reduction of the pore diameter. This would impede the diffusion of enzyme molecules into the mesoporous channels and increase the likelihood of pore blocking.

The silica source tetraethyl orthosilicate (TEOS) was mixed with (3-azidopropyl) triethoxysilane before the resulting solution was introduced into an acidic solution consisting of the dual surfactant system Pluronic® F127 and FC-4, together with the micellar expander 1,3,5-trimethylbenzene (TMB). We modified a hydrothermal treatment process of the as-synthesized material in acidic media developed by Gao *et al.* in order to obtain LP_MSN-N$_3$ (cf. experimental section).[3] This hydrothermal treatment is required for the formation of ultra-large pores. Additionally, we found that the introduction of organo-moieties in the case of azide-silanes has no negative effect on the formation of the mesoporous structure, whereas amine-functionalities easily disrupt the nanoparticle formation. For all template-extracted

LP_MSN-N$_3$ samples, a size separation step (by centrifugation) with an overall yield of 50% was employed before the nanoparticles were used for further reactions.
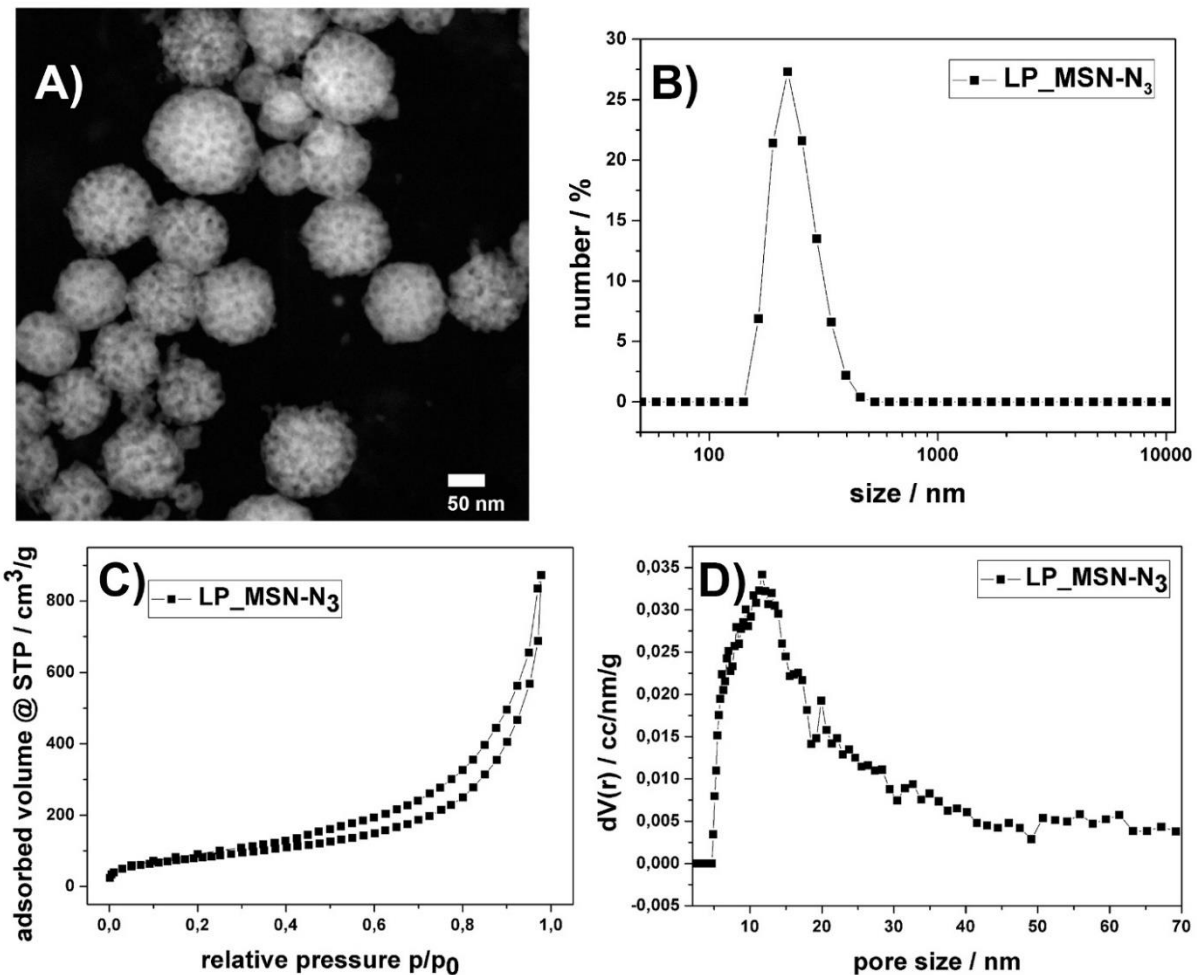


**Figure 7.1:** Characterization of LP_MSN-N$_3$. **A)** Scanning transmission electron microscopy (STEM) micrograph of template-extracted LP_MSN-N$_3$ after size separation centrifugation, **B)** dynamic light scattering (DLS) measurement showing a narrow size distribution (after size separation centrifugation), **C)** nitrogen sorption isotherms and **D)** pore size distribution obtained from nitrogen sorption measurement for LP_MSN-N$_3$.

Transmission electron microscopy images after size separation centrifugation (cf. experimental section) show spherically shaped nanoparticles with a fairly homogenous particle size distribution within a size range of 80 – 150 nm (Figure 7.1A). The large pores are present in each LP_MSN and evenly distributed over the entire nanoparticle. The size distribution data are in good accordance with the values obtained by dynamic light scattering, exhibiting a maximum at 220 nm (Figure 7.1B). We explain the moderately increased size obtained by DLS measurements compared to the TEM measurements with the larger hydrodynamic radius of the

LP_MSN-N$_3$ as compared to their real size - possibly weak agglomeration is also present. The mesoporous framework is highly regular, well-defined and clearly present in all particles (Figure 7.1A). The pore sizes are in a range of 9 – 13 nm (deduced from TEM measurements) and consistent with the maximum value of around 12 nm obtained from nitrogen sorption measurements (cf. 7.1D). The resulting isotherm shows a hybrid isotherm of a type II isotherm combined with a certain degree of type IV. The hysteresis can be characterized as an H3 hysteresis loop that results from aggregation and thus from a significant degree of textural porosity, indicated by the long tail in the pore size distribution (Figure 7.1C). Monolayer formation of the adsorbate can be observed between p/p$_0$ = 0 and 0.02, followed by multilayer adsorption over a broad range. The apparent lack of saturation (pore filling) at high p/p$_0$ could be due to a broad distribution of textural porosity between the particles in the dried LP_MSN. The interparticle voids, which are visible in the STEM micrograph (Figure 7.1A), are within a size-range of 15 – 30 nm. Summarizing, we obtained LP_MSNs exhibiting a pore size in the range of mesoporous materials (Figure 7.1D, maximum around 12 nm), with a pore volume of 0.8 cm$^3$/g and a BET surface area of A$_s$ = 246 m$^2$/g. In addition, infrared spectroscopy was carried out to verify the presence of azide-moieties within the framework of LP_MSN-N$_3$ (cf. appendix 7.6).

**Immobilization of alkyne-functionalized cytochrome C and trypsin onto LP_MSN-N$_3$ via a click chemistry approach**

Two enzymes of different dimensions, namely cytochrome C (CytC, 12 400 Da, 2.6 x 3.2 x 3.3 nm$^3$) and trypsin (23 400 Da, ca. 3.8 nm spherical)[17], were immobilized in the mesoporous nanoparticles. Specifically, a modified click chemistry approach was used to immobilize the enzymes within the mesoporous framework of our newly generated LP_MSNs, which required prior alkyne functionalization of the enzyme (cf. experimental section and Appendix 7.7).[28, 30] The latter was achieved by the EDC-activated attachment of 4-pentynoic acid to the amine moieties of CytC or trypsin, respectively (cf. appendix 7.7). In a second synthesis step, the LP_MSN-N$_3$ particles were incubated with the alkyne-functionalized enzymes for 1–2 h to ensure their diffusion into the large mesopores before the catalysts were added to the reaction mixture, in order to avoid pore blocking (cf. experimental section). Subsequently, a click reaction was performed according to a slightly modified procedure published by Maier *et al.*,

employing *N,N*-diisopropylethylamine as complexing agent to prevent the premature oxidation of Cu⁺ (Figure 7.2).[31] The nanoparticles were washed several times with buffer in order to remove excess and unbound enzyme molecules.
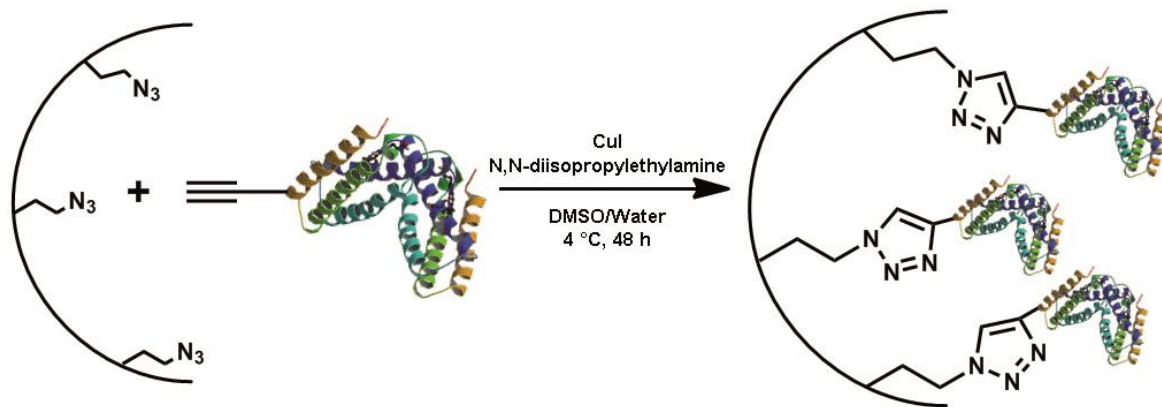


**Figure 7.2:** Scheme for enzyme immobilization in LP_MSNs using click chemistry. CuI was applied as catalyst and *N,N*-diisopropylethylamine as complexing agent.
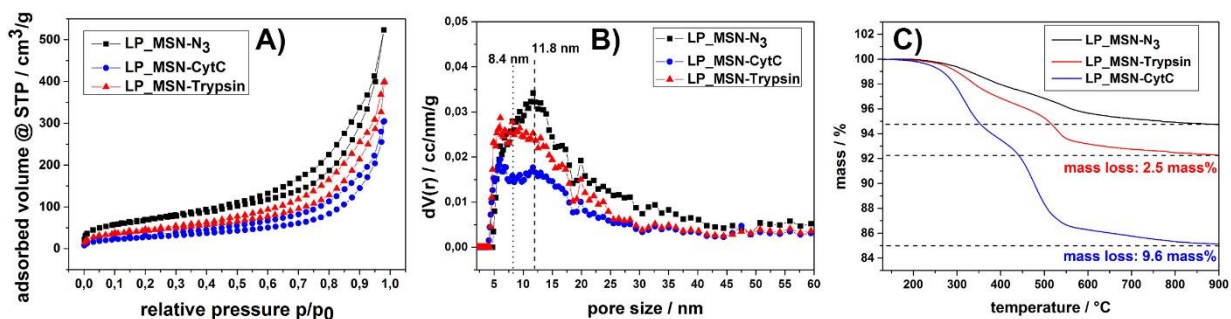


**Figure 7.3:** Nitrogen sorption data of LP_MSN-N$_3$ with immobilized enzymes. **A)** Isotherm of LP_MSN-N$_3$ (black), LP_MSN-CytC (blue) and LP_MSN-Trypsin (red). **B)** Pore size distribution for LP_MSN-N$_3$ (black), LP_MSN-CytC (blue) and LP_MSN-Trypsin (red). **C)** Thermogravimetric analysis data of LP_MSN-N$_3$ (black), LP_MSN-CytC (blue) and LP_MSN-Trypsin (red). All curves are normalized to 100% at 130 °C.

All obtained nitrogen sorption data show isotherms that appear as hybrids between type II and type IV isotherms, with a narrow H3-hysteresis loop. After the attachment of sp-enzymes the calculated BET-surface decreased significantly (Figure 7.3A and Table 7.1). This can be attributed to the uptake and covalent immobilization of the enzyme molecules within the large mesopores of the nanoparticles and the resulting pore filling. Accordingly, the pore volume and pore size decreased likewise (Figure 7.3B). The shrinkage of the pore size can also be attributed

to partial blocking of the pore openings by attached enzyme molecules. We assume that the decrease in pore volume in case of the sample LP_MSN-CytC is stronger than in LP_MSN-Trypsin, because a higher amount of sp-CytC could be incorporated into the mesoporous framework of our nanoparticles. These results are in good accordance with the obtained thermogravimetric analysis data (Figure 7.3C and Table 7.1 for relative mass loss), showing that more cytochrome C than trypsin was immobilized in the LP_MSNs. The higher functionalization degree of CytC as compared to trypsin is attributed to its relatively small dimension; the enzyme can easily diffuse into the mesopores without having much contact with the pore walls and the attached organic moieties, whereas the diffusion and subsequent attachment of trypsin might be sterically hindered due to repulsions with the pore walls.

**Table 7.1:** Nitrogen physisorption and thermogravimetric analysis data of LP_MSN-$N_3$ and LP_MSN-Enzyme.

| Sample | BET surface area [m²/g] | Pore size[a] [nm] | Relative mass loss[b] [%] |
|---|---|---|---|
| LP_MSN-$N_3$ | 155 | 11.8 | 5.2 |
| LP_MSN-CytC | 97 | 8.4 | 14.8 |
| LP_MSN-Trypsin | 153 | 8.4 | 7.7 |

[a]DFT pore size refers to the peak value of the pore size distribution. [b]Relative mass loss obtained by TGA; all curves are normalized to 130 °C

From the additional mass loss of 9.6% for the sample LP_MSN-CytC, the amount of attached enzyme can be estimated to 9.1 μmol per g silica (cf. appendix for calculation). This indicates that 13% of all azide-moieties have reacted with sp-CytC, as the amount of azide-moieties was estimated to 0.69 mmol per g silica. From the additional mass loss of 2.5%, the amount of immobilized trypsin can be estimated to 1.2 μmol per g silica (cf. appendix calculation 7.1) and the amount of azide-moieties can be estimated to 0.69 mmol per g silica. This indicates that only a small amount of sp-trypsin molecules were able to diffuse into the large mesopores and react with 1.7% of all azide-moieties of LP_MSN-$N_3$. A probable reason for this is the large molecular dimension of trypsin (ca. 3.8 nm spherical)[17], resulting in partial blocking of the pore openings by immobilized trypsin. All nitrogen sorption data are supported by the corresponding thermogravimetric analysis and the calculated relative mass losses that are summarized in

Table 7.1. In order to prove the successful attachment of sp-enzymes via click chemistry, vibrational spectroscopy was employed for the respective LP_MSN-enzyme samples (Figure 7.4 and cf. appendix 7.8 for LP_MSN-Trypsin). The symmetric and asymmetric $CH_2$ stretching vibrations of the enzyme appear in the range of 2960–2871 cm$^{-1}$ in the spectrum of LP_MSN-CytC and of free CytC. The peak at 2106 cm$^{-1}$ can be attributed to the asymmetric $N_3$ stretching vibration of LP_MSN-$N_3$ (asterisked peak) and decreases in intensity after linking of sp-CytC. At 1651 cm$^{-1}$ (dashed line) the C=O stretching vibration appears in the spectrum of LP_MSN-CytC, which is attributed to the amide bonds of the attached enzyme. The vibration at 1539 cm$^{-1}$ (second dashed line) is also only visible in the spectra of free CytC and LP_MSN-CytC and represents the N-H bending vibration of the peptide bonds of the enyzme. The peak at 1627 cm$^{-1}$ in the spectrum of LP_MSN-$N_3$ indicates the presence of traces of water within the sample. Below 1300 cm$^{-1}$, vibrations of the silica framework appear with strong intensity.
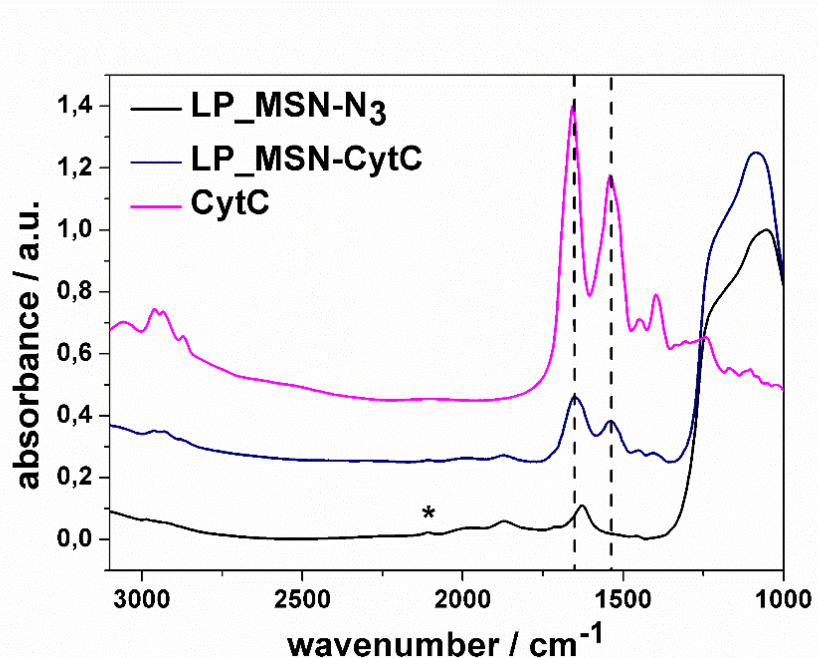


**Figure 7.4:** IR spectra of LP_MSN-$N_3$ (black), LP_MSN-CytC (blue) and free CytC (magenta). The spectra were normalized to the silica peak at about 1053 cm$^{-1}$ or divided by the maximum in case of CytC. The dashed lines at 1651 cm$^{-1}$ can be attributed to the C=O stretching vibration and at 1539 cm$^{-1}$ to the N-H bending vibration of the peptide bonds in sample LP_MSN-CytC. The spectra are offset on the y-axis by 0.25 units for clarity.

The results obtained by nitrogen sorption, thermogravimetric analysis and vibrational spectroscopy indicate the successful immobilization of CytC and trypsin within the porous

network of LP_MSN-N$_3$. In the following we address the catalytic properties of the immobilized enzymes.

**Catalytic activity determination of immobilized enzymes**

To characterize the properties of immobilized CytC, the catalysis of the colorimetric reaction of 4-aminoantipyrine (4-AAP) and *N,N*-diethylaniline (DEA) was studied by measuring the absorbance of the released quinoid dye at 550 nm (Figure 7.5A and cf. appendix 7.9). Different substrate concentrations were applied to improve the reaction conditions. The concentrations given in Table 7.3 (cf. experimental section) correspond to 4-AAP as the molar ratio of 4-AAP to DEA was kept constant (0.61). For determination of the reaction rate, the slopes in the linear region of the graphs (outlined square in Figure 7.5A) were applied as they represent the change of absorbance per time. The catalytic activity of the different samples was then determined by using Lambert-Beer's law (with $\varepsilon = 16500$ Lmol$^{-1}$cm$^{-1}$ from Lit.[32], Table 7.2).
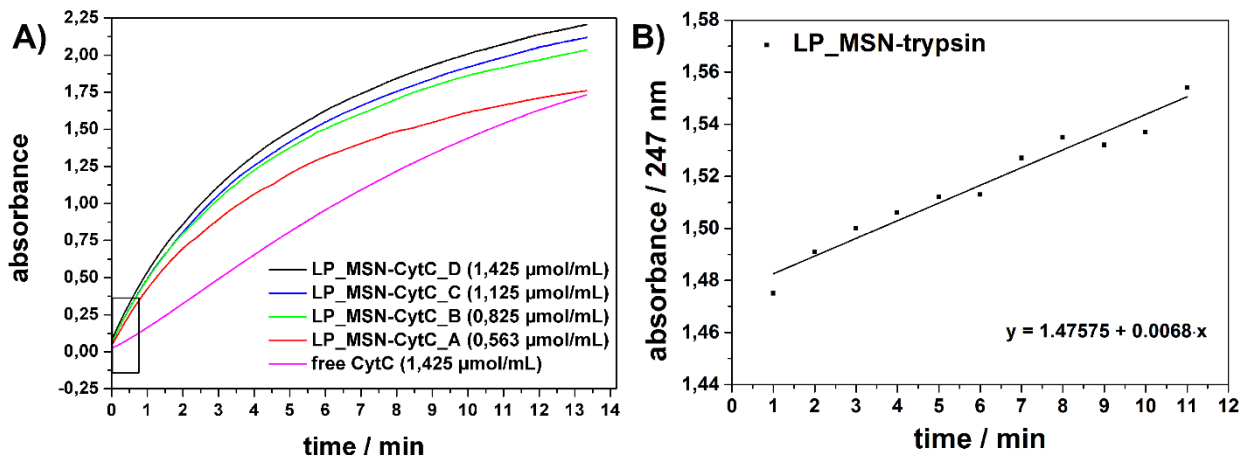


**Figure 7.5: A)** UV-Vis absorption measurement of LP_MSN-CytC_A–D and free CytC within a period of 800 s (13.3 min) at 550 nm, the slope in the linear region of the graphs (black box) was used to calculate the enzyme activities, the given concentrations correspond to 4-AAP. **B)** Activity determination of LP_MSN-trypsin by measuring the absorbance at 247 nm in a time range of 11 min and intervals of 1 min. The enzyme activity was determined from the slope of the obtained linear regression.

**Table 7.2:** Catalytic activity of LP_MSN-CytC and applied 4-AAP substrate concentration.

| Sample | BE4-AAP concentration [μmol*mL$^{-1}$] | Catalytic activity [10$^{-5}$ mol*L$^{-1}$ min$^{-1}$] |
|---|---|---|
| LP_MSN-CytC_A | 0.563 | 2.47 |
| LP_MSN-CytC_B | 0.825 | 2.57 |
| LP_MSN-CytC_C | 1.125 | 2.62 |
| LP_MSN-CytC_D | 1.425 | 2.80 |
| Free CytC | 1.425 | 0.96 |

With increasing substrate concentration, the catalytic activity of CytC increases likewise (cf. Table 7.2 ). This indicates that the substrate saturation of the enzyme was not reached in these experiments. Therefore, the highest applied amount of substrate was used to verify enzyme activity differences between immobilized and free CytC. The data revealed a 2.9 times higher activity of CytC immobilized in LP_MSNs (2.80 molL$^{-1}$min$^{-1}$) compared to an equal amount of free CytC (0.96 molL$^{-1}$min$^{-1}$). It can be assumed that the enzyme confinement within the large mesopores increases the stability of CytC, as shown in previous studies.[17, 33, 34] Aside from that, it further indicates a good pore size adjustment of the large pores of MSN to the molecular dimensions of CytC. The enzymatic activity in the MSN host is extremely high compared to values previously reported in the literature.

**Trypsin activity determination**

In order to determine the catalytic activity of the attached trypsin molecules, an N$_\alpha$-$p$-tosyl-L-arginine methyl ester hydrochloride (TAME) assay was performed.[28] Thereby, the catalyzed hydrolysis of (TAME) was measured by recording the absorption of the produced N$_\alpha$-$p$-tosyl-L-arginine at 247 nm with UV-Vis spectroscopy (Figure 7.5B, cf. experimental section). The enzyme activity was determined from the slope of the obtained linear regression after the parameters were adjusted in several experiments. As the slope of the linear regression is 0.0068 min$^{-1}$ and E$_w$ is 1.847·10$^{-4}$ mg trypsin / 0.1 mL solution (calculated from TGA data, cf. Figure 7.3C), the activity can be calculated to 102 units/mg (enzyme). Here, one unit is defined as the amount of enzyme releasing 1 μmol N$_\alpha$-$p$-tosyl-L-arginine per minute under denoted conditions. For comparison, previous studies of Schlossbauer *et al.* obtained an activity of 346.3 units/mg for native trypsin and an activity of 65.6 units/mg for trypsin immobilized in

SBA-15 with a pore size of 8 nm.[28] This indicates that immobilized trypsin suffers from a certain loss of activity. The higher catalytic activity within LP_MSNs compared to SBA-15 with smaller pores might be associated (i) with the nanoscale size of the host and (ii) with the larger pore diameter involved in our present study. The catalytic activity within the pores might even be further improved by additional functionalization of LP_MSN-N$_3$ with amine moieties, since trypsin has an optimal operating pH of about 8.[35] These effects will have to be investigated in future studies.

## 7.3 Conclusion

We report for the first time the FC-4 assisted synthesis of organo-functionalized LP_MSNs via a co-condensation method. This direct approach to introduce organo-moieties into the mesoporous network is highly beneficial since different functionalities can be efficiently introduced at controlled concentrations. This method further avoids additional grafting steps that may be difficult with colloidal systems. Our low temperature synthesis yields mesoporous silica nanoparticles within a size range of about 100 nm that exhibit ultra-large pore sizes of 11 nm and bear an azide-functionality. This organo-functionalization makes the LP_MSNs suitable for a biocompatible click chemistry approach. We chose to immobilize two enzymes of different molecular dimensions, namely cytochrome C and trypsin, covalently to the LP_MSN-N$_3$ host. The peroxidase cytochrome C (2.6 x 3.2 x 3.3 nm$^3$) and the protease trypsin (3.8 nm spherical)[17] were successfully modified with an alkyne-linker to allow for a Cu(I)-catalyzed click reaction. The enzymes were allowed to diffuse into the mesopores before the catalysts were added to the reaction mixture, thus avoiding unfavorable pore blocking and low catalytic activity. Compared to the small amount of azide-functionalization in the LP_MSNs, a high-density enzyme immobilization in the LP_MSN-N$_3$ host could be achieved. We could demonstrate in this study that both enzymes are still highly active in their immobilized state. Strikingly, for the case of LP_MSN-CytC we observed a 2.9 times higher activity of the immobilized enzyme compared to free cytochrome C. Thus, we conclude that the confined attachment of sp-CytC within the framework leads to a favorable confined state of the enzyme, resulting in high activity. In the case of trypsin we could also prove a high and persisting activity after attachment to the solid support. We propose that the high activity of the enzymes

immobilized in large-pore MSNs is at least partially caused by the extremely short diffusion distances in the nanoscale host systems. Overall, we present a highly promising colloidal MSN-system with ultra-large pores for the immobilization of biomolecules that can be further exploited in numerous ways.

## 7.4   Experimental

**Materials.** Pluronic F127 (F127, Sigma), fluorocarbon surfactant 4 (FC-4, Yick-vik Chemicals), tetraethylorthosilicate (TEOS, Fluka, >99%), 1,3,5-trimethylbenzene (TMB, Fluka, 96%), N-ethylcarbodiimide hydrochloride  (EDC, Fluka, 97%), trypsin from bovine pancreas (Sigma, lyophilized, essentially salt-free, TPCK treated), ethanol (EtOH, Aldrich, >99.5%), conc. hydrochloric acid (Aldrich, >95%, 37 wt%), 4-pentynoic acid (Fluka, 97%,) Nα-p-tosyl-L-arginine methyl ester hydrochloride (TAME, Sigma)**,** phosphate buffer solution (Sigma), tris(hydroxymethyl) aminomethane (TRIS, Sigma, 99.8 %), 2-(N-morpholino)ethanesulfonic acid (MES, Sigma, 99.5 %), disodium hydrogen phosphate ($Na_2HPO_4$, Sigma, >99%), monosodium hydrogen phosphate ($NaH_2PO_4$, Sigma, >99%), sodium hydroxide (1 M, Sigma), cytochrome C from bovine heart (Fluka, >95%), (3-chloropropyl) triethoxysilane (CPTES, Fluka, 95%), diethyl ether ($Et_2O$, Sigma, >98%), sodium azide (Fluka, 99%), *N,N*-diisopropylethylamine (Sigma, 99%), Cu(I)I (Sigma, 98%), 4-aminoantipyrine (4-AAP, Sigma, >98%), *N,N*-diethylaniline (DEA, Sigma, >99%) hydrogen peroxide (Sigma, 30 wt%).

Unless otherwise noted, all reagents were used without further purification.  Bi-distilled water from a Millipore system (Milli-Q Academic A10) was used for all syntheses and purification steps.

**Preparation of Buffer Solutions**

**MES buffer.** 2-(N-morpholino)ethanesulfonic acid (MES, 1.95 g) was dissolved in water (500 mL). The pH was adjusted to 5.5 using sodium hydroxide (1 M). The volume was adjusted to 1 L by addition of bidistilled water.

**Citric acid phosphate buffer (McIlvaine buffer).** An aqueous solution (250 mL) of citric acid (9.61 g, 0.05 mol) and an aqueous solution (250 mL) of disodium hydrogen phosphate ($Na_2HPO_4$, 7.10 g, 0.05 mol) were prepared. The two solutions were mixed under pH-control with a pH meter to obtain a pH value of 5.5.

**Sodium phosphate buffer (10 mM, pH 7.2).** Monosodium hydrogen phosphate (5.84 g, 48.7 mmol) and disodium hydrogen phosphate (15.47 g, 109.0 mmol) were dissolved in 10 L of water (10 mM). The pH was adjusted to 7.2 using a pH-meter.

**TRIS buffer (pH 8.1).** Tris(hydroxymethyl)aminomethane (TRIS, 5.57 g) and calcium chloride dihydrate (CaCl2 · 2 $H_2O$, 169 mg) were dissolved in water (60 mL). The pH was adjusted to 8.1 using HCl (1 M). The volume was adjusted to 100 mL by addition of distilled water.

**Synthesis of alkyne-modified enzymes (sp-enzymes)**

Cytochrome C (sp-CytC). To a freshly prepared, cooled solution (4 °C) of cytochrome c (15 mg, 1.21 µmol) in MES buffer (pH 5.5, 15 mL, 10 mM), an aqueous solution (750 µL) of 4-pentynoic acid (0.1 M, 7.36 mg, 0.08 mmol) was added. The resulting mixture was vortexed for 2 min and then stored at 4 °C for 15 min. Subsequently, EDC (14.9 mg, 0.08 mmol) was added to the solution. The reaction was vortexed again for 2 min and then kept at 4 °C for 4 h without stirring. Afterwards, the obtained solution was dialyzed in a cold room at 4 °C against sodium phosphate buffer (10 mM, pH 7.2, 10 L) for a period of 24 h. The concentration of sp-CytC (0.48 mg/mL) was determined with UV-Vis spectroscopy (proteinA280). The alkyne-functionalized CytC was used for click reactions without further purification.

<u>Trypsin (sp-Tryp).</u> Alkyne-functionalized trypsin was synthesized according to Gole *et al.* as described above.[3] The concentration of sp-Trypsin (1.03 mg/mL) was determined with UV-Vis spectroscopy (proteinA280).

**Synthesis of (3-azidopropyl) triethoxysilane**

(3-azidopropyl)triethoxysilane was synthesized according to a procedure published by Nazakawa *et al.*.[4] (3-chloropropyl) triethoxysilane (10 g, 41.7 mmol) and sodium azide (10 g, 154 mmol) were heated in anhydrous DMF (100 mL) under inert gas conditions to 90 °C for 4 h. Low boiling materials were removed from the mixture under reduced pressure. The crude oily product was dissolved in diethyl ether, resulting in precipitation of salts, which were removed by filtration. Et$_2$O was removed *in vacuo* and the residual oil was distilled (95 °C). (3-azidopropyl)triethoxysilane was obtained as colorless liquid and used without further purification.

**Synthesis of azide functionalized large pore mesoporous silica nanoparticles (LP_MSN-N$_3$).** A modified literature procedure was employed to synthesize LP_MSN-N$_3$.[5, 6] Pluronic F127 (0.25 g) and fluorocarbon surfactant FC-4 (1.40 g) was dissolved in hydrochloric acid (HCl, 30 mL, 0.02 M), followed by the addition of TMB (0.20 g, 1.66 mmol). The reaction mixture was stirred in a 100 mL polypropylene reactor for 2 h at 10 °C before a mixture of tetraethyl orthosilicate (TEOS, 1.5 g, 7.2 mmol) and (3-azidopropyl) triethoxysilane was added drop-wise. The resulting suspension was stirred vigorously (1250 rpm) over night at 10 °C. The resulting particle suspension was hydrothermally treated under static conditions (150 °C, 1d). The mixture was centrifuged (15 min, 20500 rpm, 50228 rcf), re-suspended in hydrochloric acid (HCl, 30 mL, 0.2 M) and heated under static conditions (140 °C, 2d). Parr autoclaves (100 mL) were used for post-synthetic hydrothermal treatment.

After the addition of 50 mL bi-distilled H$_2$O, the LP_MSN were collected by centrifugation (15 min, 20500 rpm, 50228 rcf), re-dispersed in 50 mL EtOH and extracted according to the procedure described below.

**Template removal from LP_MSN-N$_3$.** The organic template was removed via extraction from LP_MSN-N$_3$. Thus, 250 mg of the particles were refluxed for 2 h at 75 °C in a mixture of absolute EtOH (120 mL), acetone (80 mL) and conc. HCl (10 mL). This extraction step was performed twice. The template-free LP_MSNs were separated by centrifugation (15 min, 20500 rpm, 50228 rcf) and washed with EtOH after each extraction step. LP_MSN-N$_3$ were obtained as colloidal suspension in EtOH.

**Size separation centrifugation of LP_MSN-N₃**. In order to separate large agglomerates from the synthesized nanoparticles, a size separation centrifugation was performed (15 sec, 3.000 rpm, 775 rcf). The resulting supernatant comprising a nanoparticle yield of 50% (relative to the synthesis yield) was employed for all further applications. The obtained particles in ethanol were stored in tightly sealed glass vials.

**Immobilization of sp-enzymes in large pore mesoporous silica nanoparticles (LP_MSN-Enzyme)**

Immobilization of alkyne-functionalized cytochrome C (LP_MSN-CytC)

An ethanolic suspension containing 50 mg LP_MSN-N₃ was centrifuged (15 min, 20500 rpm, 50228 rcf) and re-dispersed in 10 mL of water. This washing step was repeated twice. Subsequently, the LP_MSN-N₃ was re-dispersed in 3.5 mL of water and 3.5 mL of the buffered sp-CytC solution (containing 1.67 mg, 0.14 µmol sp-CytC). The resulting mixture was stirred at 4 °C for 2 h. In the meantime, *N,N'*-diisopropylethylamine (1.33 µL, 7.63 µmol) was added to a solution of Cu(I)I (1 mg, 5.25 µmol) dissolved in 5 mL DMSO and stirred for 30 min at ambient temperature. 50 µL of this freshly prepared solution was added to the reaction mixture containing LP_MSN-N₃ and sp-CytC to catalyze the covalent attachment of the enzyme via click chemistry. The resulting suspension was stirred for 48 h at 4 °C. Subsequently, the particles were collected by centrifugation (15 min, 20500 rpm, 50228 rcf) and re-dispersed in 30 mL of water. This washing procedure was repeated three times. LP_MSN-CytC were obtained as colloidal solution in water and were stored at -20 °C until further use.

Trypsin (LP_MSN-Tryp). sp-Trypsin was immobilized onto LP_MSN-N₃ via a click chemistry approach accordingly the synthesis procedure described above for sp-CytC. An ethanolic suspension containing 50 mg LP_MSN-N₃ was centrifuged (15 min, 20500 rpm, 50228 rcf) and re-dispersed in 10 mL water. This washing step was repeated twice. The obtained pellet of LP_MSN-N₃ was re-dispersed in a mixture of sp-trypsin (3.50 mL, 3.6 mg, 0.15 µmol, 1 eq) and water (3.50 mL) for one hour before the freshly prepared ligand solution was added. LP_MSN-Trypsin was obtained as colloidal solution in water after several washing steps.

**Catalytic activity determination of LP_MSN-CytC.** The catalytic activity of LP_MSN-CytC was determined by a method published by Saito *et al.* [7] Fresh solutions of 4-aminoantipyrine (4-AAP, 7.5 mM 15.2 mg, 75 µmol in 10 mL water) and *N,N*-diethylaniline (DEA, 7.5 mM 12 µL, 75 µmol in 10 mL of a 1:1 wt% mixture of water and ethanol) were prepared shortly before the experiment. 100 µl of an aqueous suspension of LP_MSN-CytC (containing 15.6 µg (1.26 nmol) cytochrome c, calculated from TGA-data) were mixed in Hellma Suprasil precision cells with different volumes of the prepared DEA- and 4-AAP-solution and with distinct amounts of McIlvaine buffer (pH 5.5). Detailed information on the volumes is given in Table T1. Subsequently, 50 µl $H_2O_2$ were added to the solution and a total volume of 1 mL was obtained (see Table 7.3). The time-dependent formation of the dye was determined by measuring the absorbance (550 nm, 800 s and intervals of 1 s). All spectra were background corrected.

**Table 7.3:** Applied volumes of enzyme solution, DEA, 4-AAP, McIlvaine buffer and $H_2O_2$.

| Experiment name | Volume of enzyme solution | Volume of DEA solution[µL] | Volume of 4-AAP solution [µL] | Volume of McIlvaine-buffer (pH 5.5) [µL] | Volume of $H_2O_2$ (1 wt%) | Total volume [µL] |
|---|---|---|---|---|---|---|
| **LP_MSN-CytC_A** | 100 µL LP_MSN-CytC | 125 | 75 | 650 | 50 | 1000 |
| **LP_MSN-CytC_B** | 100 µL LP_MSN- CytC | 190 | 110 | 550 | 50 | 1000 |
| **LP_MSN-CytC_C** | 100 µL LP_MSN- CytC | 250 | 150 | 450 | 50 | 1000 |
| **LP_MSN-CytC_D** | 100 µL LP_MSN- CytC | 310 | 190 | 350 | 50 | 1000 |
| **free CytC** | 100 µL CytC -solution | 310 | 190 | 350 | 50 | 1000 |

**Catalytic activity determination of LP_MSN-Tryp via TAME assay.** Schwert and Takenaka have developed a sensitive spectrophotometric assay for trypsin and chymotrypsin using synthetic substrates,[8] which was modified by Hummel *et al.* utilizing N-*p*-tosyl-L-arginine methyl ester hydrochloride as substrate.[9] Based on the procedure published by Schlossbauer *et al.*[28] the TAME assay was carried out employing a 0.01 M TAME stock solution (7.56 mg TAME dissolved in 2 mL $H_2O$) and an aqueous suspension of LP_MSN-Tryp particles (containing 37.0 µg trypsin/mL - calculated from TGA-data). 200 µL TAME stock solution

(2 µmol TAME) and 1.23 µL TRIS buffer (pH 8.1) were mixed in a precision cell shortly before LP_MSN-Trypsin (75 µL - containing 2.77 µg, 0.12 nmol trypsin) was added. Subsequently, the time-dependent formation of the colored product was determined by UV-VIS spectroscopy (247 nm, 660 s, intervals of 1 min) under continuous stirring of the mixture. All spectra were background corrected.

**Characterization.** Centrifugation was performed using a Sorvall Evolution RC equipped with an SS-34 rotor or an Eppendorf centrifuge 5418 for small volumes. Nitrogen sorption measurements were performed with a Quantachrome NOVA 4000e or on a Quantachrome Autosorb iQ at -196 °C. Sample out-gassing was performed at 22 °C for 12 h at a pressure of 10 mTorr. Pore size and pore volume were calculated using a NLDFT equilibrium model for cylindrical pores of $N_2$ on silica, based on the desorption branch of the isotherm. The Brunauer-Emmett-Teller (BET) surface areas for all samples were calculated from the corresponding nitrogen sorption isotherms in the range of $p/p_0 = 0.05 - 0.2$. To calculate the total pore volume of the LP_MSNs, the amount of adsorbed nitrogen at the apparent plateau of the isotherm at high $p/p_0$ values is used. Dynamic light scattering (DLS) and zeta potential measurements were performed on a Malvern Zetasizer-Nano instrument equipped with a 4 mW He-Ne laser (633 nm) and an avalanche photodiode. DLS measurements were directly recorded with ethanolic colloidal suspensions at a concentration of 1 mg/mL. Transmission electron microscopy (TEM) was performed on a FEI Titan 80-300 kV microscope operating at 300 kV. Scanning transmission electron microscopy (STEM) was also performed on the Titan microscope. Samples were prepared by dispersing LP_MSNs (0.5 mg) in 2 mL absolute ethanol. A drop of the resulting diluted suspension was dried on a carbon-coated copper grid. Thermogravimetric analysis was performed on a Netzsch STA 440 C TG/DSC with a heating rate of 10 K/min in a stream of synthetic air of about 25 mL/min. All IR measurements were performed on a Thermo Scientific Nicolet iN10 IR Microscope in reflexion-absorption mode with a liquid nitrogen-cooled MCT-A detector. All spectra are background corrected. The signals were normalized to the most intensive silica band. UV-VIS measurements were performed on a Perkin Elmer Lambda 1050 spectrophotometer with a deuterium arc lamp (UV region) and a tungsten filament (visible region). The detector was an InGaAs integrating sphere detector. Time-based enzyme activity assays were performed in Hellma Suprasil precision cells (path length 10 mm). For small sample amounts (2 µL of the sample) a NanoDrop 2000c

spectrometer from Thermo Scientific Fisher was employed for UV-Vis measurements. The absorbance at 280 nm (mode A280) was used to determine enzyme concentrations. For enzymatic color reactions with the NanoDrop 2000c spectrometer, the samples were measured in a Brand UV- micro cuvette (light path 10 mm).

## 7.5 Appendix
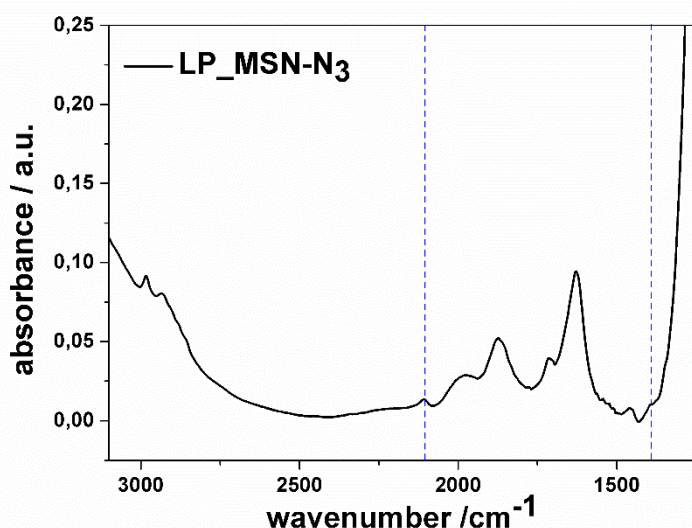


**Figure 7.6:** IR spectra of LP_MSN-N$_3$. The dashed lines indicate the typical vibrations arising from the azide-functionality.

IR spectroscopy was carried out to verify the presence of azide moieties in LP_MSN-N$_3$ (Figure 7.6). The asymmetric CH$_2$ stretching vibrations of the azidopropyl-moieties are visible between 2985 cm$^{-1}$ and 2935 cm$^{-1}$. Furthermore, the CH$_2$ bending vibration appears at 1461 cm$^{-1}$. The vibrations at 2105 cm$^{-1}$ and 1376 cm$^{-1}$ exhibit very small intensities and can be attributed to the symmetric and asymmetric stretching vibration of the N$_3$-groups (outlined by dashed lines). The vibration at 1678 cm$^{-1}$ appears with medium intensity and can be attributed to the vibrations of residual amounts of water in the sample. Vibrations of the silica framework are visible below 1300 cm$^{-1}$ with strong intensities.

**Alkyne-functionalization of enzymes**
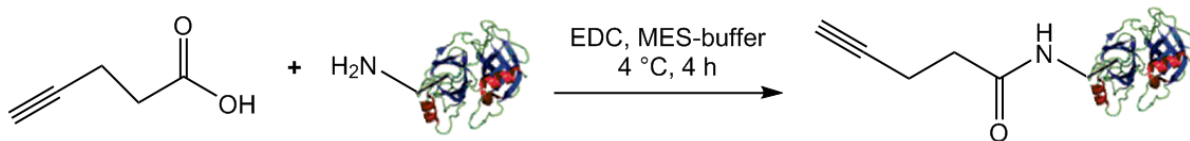


**Figure 7.7:** EDC activated attachment of 4-pentynoic acid to the respective enzyme (CytC or trypsin). The reaction was carried out in MES buffer (pH 5.5) at 4 °C.
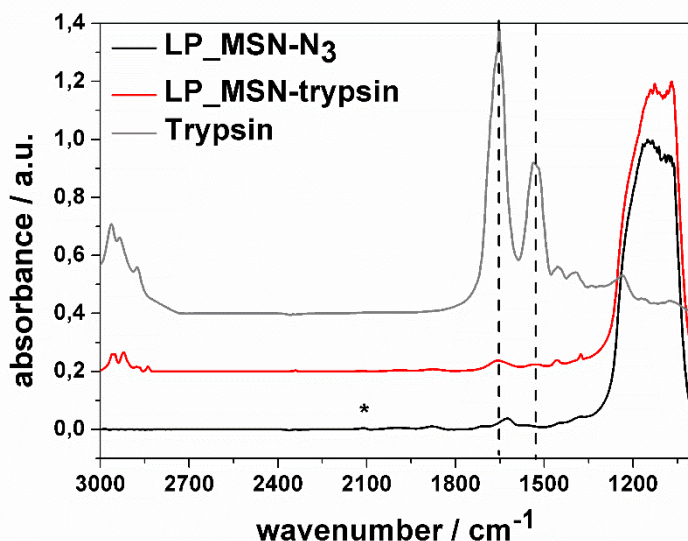


**Figure 7.8:** IR spectra of LP_MSN-N$_3$ (black), LP_MSN-trypsin (red) and free trypsin (grey). The spectra were normalized to the silica peak or divided by the maximum in case of trypsin. The spectra are offset by a value of 0.2 for clarity reasons. The modes at 1656 cm$^{-1}$ (dashed lines) can be attributed to the C=O stretching vibration and those at 1531 cm$^{-1}$ to the N-H bending vibration of the peptide bonds in sample LP_MSN-Trypsin.
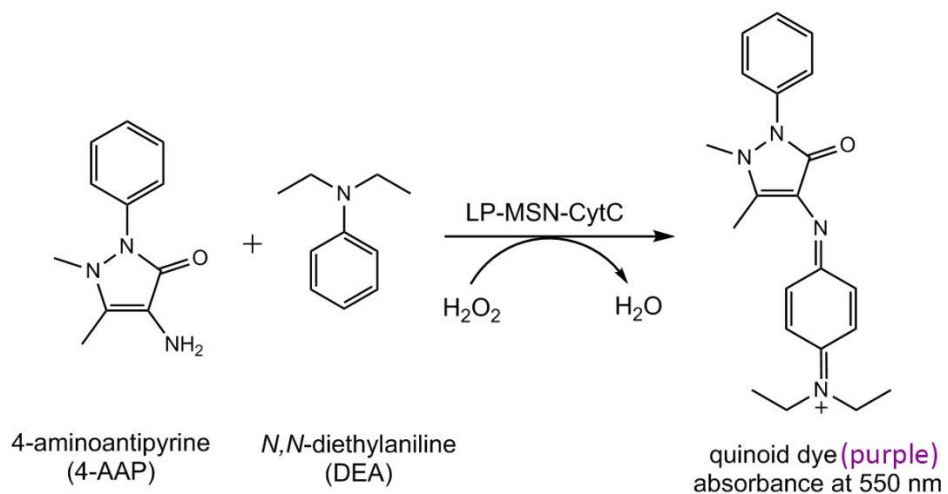
**Figure 7.9:** Color reaction of 4-aminoantipyrine (4-AAP) and *N,N*-diethylaniline (DEA) with $H_2O_2$, catalyzed by LP_MSN-CytC particles.



**Figure 7.10:** Image of the sample LP_MSN-CytC at the time points t = 0 sec and t = 800 sec after the start of the reaction of 4-aminoantipyrine (4-AAP) and *N,N*-diethylaniline (DEA) with $H_2O_2$.

**Calculation 7.1:** Example for the calculation for thermogravimetric analysis (TGA) of sample LP_MSN-N$_3$ and LP_MSN-CytC.

1 g sample LP_MSN-N$_3$ contains 53 mg azide-residues (mass loss 5.3%, $M_w(C_3H_6N_3)$=81.05 g*mol$^{-1}$)

$$\frac{53\ mg}{(100\% - 5.3\%)\ g} = 56\ mg\ azide - residues\ /\ g\ silica$$

$$\frac{0.056\ g}{81.05\ \frac{g}{mol}} = 0.69\ mmol\ azide - residues\ /\ g\ silica$$

1 g sample LP_MSN-CytC contains 96 mg CytC (additional mass loss 9.6%, $M_w(CytC)$ = 12400 gmol$^{-1}$)

$$\frac{96\ mg}{(100\% - 5.3\% - 9.6\%)\ g} = 113\ mg\ CytC\ /\ g\ silica$$

$$\frac{0.113\ g}{12400\ \frac{g}{mol}} = 9.1\ \mu mol\ CytC\ /\ g\ silica$$

## 7.6   References

1.    Hartmann, M. *Chem. Mater.* **2005**, *17*, 4577-4593.

2.    Cauda, V.; Schlossbauer, A.; Kecht, J.; Zürner, A.; Bein, T. *J. Am. Chem. Soc.* **2009**, *131*, 11361-11370.

3.    Gao, F.; Botella, P.; Corma, A.; Blesa, J.; Dong, L. *J. Phys. Chem. B.* **2009**, *113*, 1796-1804.

4.    Rosenholm, J. M.; Meinander, A.; Peuhu, E.; Niemi, R.; Eriksson, J. E.; Sahlgren, C.; Linden, M. *ACS Nano* **2009**, *3*, 197-206.

5.    Zhou, Z.; Taylor, R. N. K.; Kullmann, S.; Bao, H.; Hartmann, M. *Adv. Mater.* **2011**, *23*, 2627-2632.

6.    Jin, H.; Qiu, H.; Sakamoto, Y.; Shu, P.; Terasaki, O.; Che, S. *Chem. Eur. J.* **2008**, *14*, 6413-6420.

7. Lin, Y. S.; Haynes, C. L. *J. Am. Chem. Soc.* **2010**, *132*, 4834-4842.

8. Wu, S. H.; Mou, C. Y.; Lin, H. P. *Chem. Soc. Rev.* **2013**, *42*, 3862-3875.

9. Han, Y.; Ying, J. Y. *Angew. Chem. Int. Ed.* **2005**, *44*, 288-292.

10. Hartono, S. B.; Gu, W.; Kleitz, F.; Liu, J.; He, L.; Middelberg, A. P. J.; Yu, C.; Lu, G. Q.; Qiao, S. Z. *ACS Nano* **2012**, *6*, 2104-2117.

11. Na, H.-K.; Kim, M.-H.; Park, K.; Ryoo, S.-R.; Lee, K. E.; Jeon, H.; Ryoo, R.; Hyeon, C.; Min, D.-H. *Small* **2012**, *8*, 1752-1761.

12. Zhou, X.; Qiao, S.; Hao, N.; Wang, X.; Yu, C.; Wang, L.; Zhao, D.; Lu, G. Q. *Chem. Mater.* **2007**, *19*, 1870-1876.

13. Kim, J.; Grate, J. W.; Wang, P. *Chem. Eng. Sci.* **2006**, *61*, 1017-1026.

14. Zhao, X. S.; Bao, X. Y.; Guo, W.; Lee, F. Y. *Mater. Today* **2006**, *9*, 32-39.

15. Ispas, C.; Sokolov, I.; Andreescu, S. *Anal. Bioanal. Chem.* **2009**, *393*, 543-554.

16. Li, Z.; Barnes, J. C.; Bosoy, A.; Stoddart, J. F.; Zink, J. I. *Chem. Soc. Rev.* **2012**, *41*, 2590-2605.

17. Zhou, Z.; Hartmann, M. *Chem. Soc. Rev.* **2013**, *42*, 3894-3912.

18. Yiu, H. H. P.; Wright, P. A. *J. Mater. Chem.* **2005**, *15*, 3690-3700.

19. Yang, X. Y.; Li, Z. Q.; Liu, B.; Klein-Hofmann, A.; Tian, G.; Feng, Y. F.; Ding, Y.; Su, D. S.; Xiao, F. S. *Adv. Mater.* **2006**, *18*, 410-414.

20. Rosales-Hernández, M. C.; Mendieta-Wejebe, J. E.; Correa-Basurto, J.; Vázquez-Alcántara, J. I.; Terres-Rojas, E.; Trujillo-Ferrara, J. *Int. J. Biol. Macromol.* **2007**, *40*, 444-448.

21. Hudson, S.; Cooney, J.; Hodnett, B. K.; Magner, E. *Chem. Mater.* **2007**, *19*, 2049-2055.

22. Lei, C.; Shin, Y.; Liu, J.; Ackerman, E. J. *J. Am. Chem. Soc.* **2002**, *124*, 11242-11243.

23. Hoffmann, F.; Cornelius, M.; Morell, J.; Fröba, M. *Angew. Chem. Int. Ed.* **2006**, *45*, 3216-3251.

24. Zhou, Z.; Inayat, A.; Schwieger, W.; Hartmann, M. *Microporous Mesoporous Mater.* **2012**, *154*, 133-141.

25. Fried, D. I.; Brieler, F. J.; Fröba, M. *ChemCatChem* **2013**, *5*, 862-884.

26. Lee, C.-H.; Lin, T.-S.; Mou, C.-Y. *Nano Today* **2009**, *4*, 165-179.

27. K. C. Kao; C. H. Lee; T. S. Lin; Mou, C. Y. *J. Mater. Chem.* **2010**, *20*, 4653-4662.

28. Schlossbauer, A.; Schaffert, D.; Kecht, J.; Wagner, E.; Bein, T. *J. Am. Chem. Soc.* **2008**, *130*, 12558-12559.

29. Fried, D. I.; Schlossbauer, A.; Bein, T. *Microporous Mesoporous Mater.* **2011**, *147*, 5-9.

30. Gole, A.; Murphy, C. J. *Langmuir* **2007**, *24*, 266-272.

31.     Maier, K.; Wagner, E. *J. Am. Chem. Soc.* **2012**, *134*, 10169-10173.

32.     Huang, I. P.; Cai, R.; Mao, L.; Liu, Z.; Huang, H. *Anal. Sci.* **1999**, 889-894.

33.     Lee, C. H.; Lang, J.; Yen, C. W.; Shih, P. C.; Lin, T. S.; Mou, C. Y. *J. Phys. Chem. B.* **2005**, *109*, 12277-12786.

34.     Cheng, Y.-Y.; Chang, H.-C.; Hoops, G.; Su, M.-C. *J. Am. Chem. Soc.* **2004**, *126*, 10828-10829.

35.     Sipos, T.; Merkel, J. R. *Biochemistry* **1970**, *9*, 2766-2775.

# 8   Post-synthesis modification of mesoporous silica nanoparticle with large pores and their investigation on a cellular level

This chapter is based on a collaboration with:

Veronika Weiss, Martina Lichtnecker, Katharina Braunger and Christoph Bräuchle
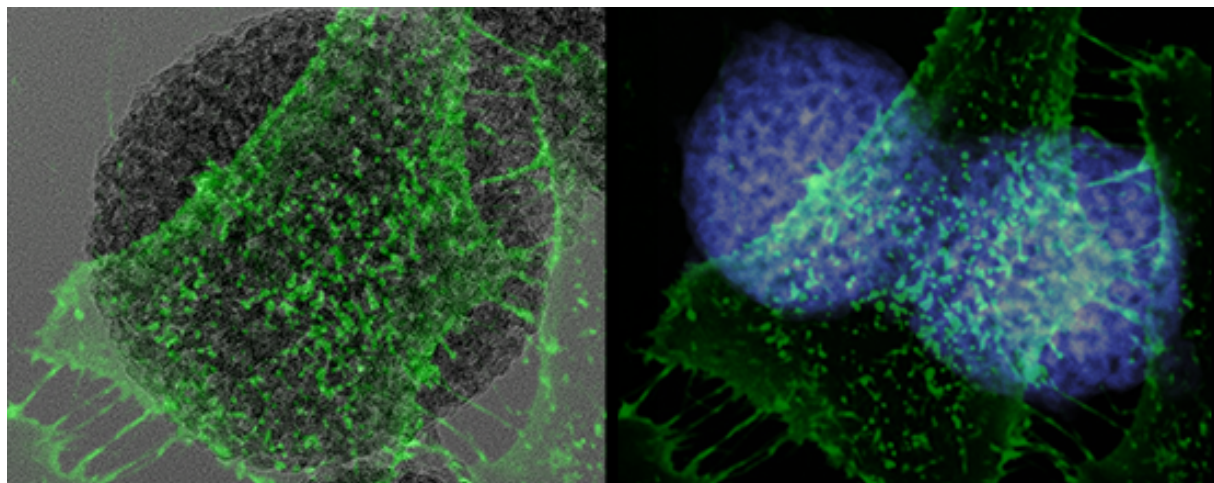
## Abstract

The successful synthesis of mesoporous silica nanoparticles with ultra-large pores (LP_MSNs) bearing different organo-functionalities and their application as solid support for enzymes has been discussed in previous chapters of this work. In brief, a fluorocarbon-mediated synthesis pathway at low temperatures (10 °C) was employed to generate LP_MSNs with pore sizes up to 15 nm, which are necessary for the delivery of large biomolecules (e.g. siRNA). The organo-functionalities were introduced via a co-condensation approach to obtain a homogeneous distribution of amino/phenyl-moieties within the nanoparticle. This chapter focuses on the post-synthesis modification of the novel LP_MSNs with amino/phenyl-moieties to design a multi-functional carrier-system with high loading capacities and stimuli-responsive release mechanisms. Specifically, we present a system based on colloidal large pore mesoporous silica nanoparticles equipped with an on-board red-light photosensitizer and capped by a supported lipid bilayer (SLB) to prevent premature release from the mesopores. The functionality of the organo-modified drug delivery vehicles was studied in detail on a cellular level with fluorescence imaging in close collaboration with the group of Prof. C. Bräuchle.

## 8.1 Introduction

Mesoporous silica nanoparticles (MSNs) with pore sizes of around 4 nm have been widely studied in the past years as promising drug delivery vehicles based on the possibility to fine-tune their functional properties for biocompatibility and the specific functionalization of the nano-carrier (e.g., attachment of targeting ligands).[1-5] Release on-demand drug delivery systems with stimuli-responsive capping and endosomal escape systems have recently attracted high interest as they allow for precise control over the endosomal escape of nano-vehicles.[2, 6] Spatial and temporal control over cargo release was achieved with intracellular triggers such as change in pH[7, 8], redox reactions[6, 9, 10] or the presence of certain enzymes within the cell compartments.[11] Additionally, external triggers including light[2, 3] or heat[12-14] can stimulate the controlled release of the adsorbed cargo. However, most of the above-mentioned stimuli-responsive nano-carrier systems are based on standard MSNs (pore sizes of 2 − 4 nm), which limits their applications as host-system to relatively small molecules (e.g. chemotherapeutics like doxorubicin and paclitaxel).[4, 15, 16] A few studies have reported the successful delivery of larger molecules such as nucleic acids with conventional MSNs.[1, 17] Li *et al*. demonstrated the packing of siRNA into the mesopores of magnetic MSNs containing a $Fe_3O_4$-core by using a chaotropic salt solution during the adsorption process.[17] However, the generation of silica nanoparticles with ultra-large pores and well-defined small particle sizes (LP_MSNs) is highly desirable for the intracellular delivery of large biomolecules. Therefore the synthesis of mesoporous silica nanoparticles with ultra-large pores (7 - 20 nm) has recently attracted much attention and several different synthesis approaches are known today.[18-20] Gao *et al.* reported the successful modification of LP_MSNs, generated by employing a fluorocarbon-surfactant mediated synthesis pathway, with aminopropyl-moieties to enable sufficient uptake of plasmid DNA.[19] Hartono *et al.* also used a fluorocarbon-mediated synthesis pathway and functionalized the obtained LP_MSNs with poly-L-lysine for efficient gene delivery with siRNA.[21] Although the alternative synthesis pathway of Ryoo and co-workers is not based on a fluorocarbon-mediated synthesis approach, LP_MSNs with pore sizes of up to 23 nm were obtained employing a distinct hydrothermal treatment; the resulting system with siRNA cargo molecules was studied *in vitro* and *in vivo* without observing a notable cytotoxicity.[20] All above-mentioned systems have in common that the respective organo-functionality was introduced via a post-synthesis grafting approach. We have already reported the successful synthesis of organo-modified LP_MSNs based on a fluorocarbon surfactant mediated synthesis approach using

co-condensation (cf. chapter 6), and first applications as host-system for two different enzymes (cf. chapter 7). Here we will focus on the successful modification of LP_MSNs with stimuli-responsive triggers, the adsorption of differently sized cargo molecules and the sealing of the mesopores with a biocompatible supported lipid bilayer (SLB), which can be opened through red-light activation of an attached photosensitizer. Moreover, the interactions of these newly generated LP_MSNs with live cells were studied in close collaboration with the group of Prof. C. Bräuchle.

## 8.2   Results and Discussion

We have successfully synthesized amino/phenyl-functionalized mesoporous silica nanoparticles with ultra-large pores (LP_MSN-NH$_2$/Ph) employing a modified sol-gel method at mildly acidic conditions and low temperatures (10 °C).[19] For this purpose, the silica source tetraethyl orthosilicate (TEOS) was mixed with 3-aminopropyl triethoxysilane (APTES, 0.5 mol% of the original TEOS amount) and phenyl triethoxysilane (PTES, 0.5 mol%) before the silica precursor mixture was introduced into an acidic solution consisting of the dual surfactant system Pluronic F127 and FC-4, together with the micellar expander 1,3,5-trimethylbenzene (TMB). We applied a hydrothermal treatment of the as-synthesized material in acidic media developed by Gao *et al.* in order to obtain LP_MSN-NH$_2$/Ph (cf. experimental section).[19] The template-extracted LP_MSNs were thoroughly characterized with regard to their size and functionality by nitrogen sorption, dynamic light scattering, transmission electron microscopy and IR-spectroscopy (cf. chapter 6).
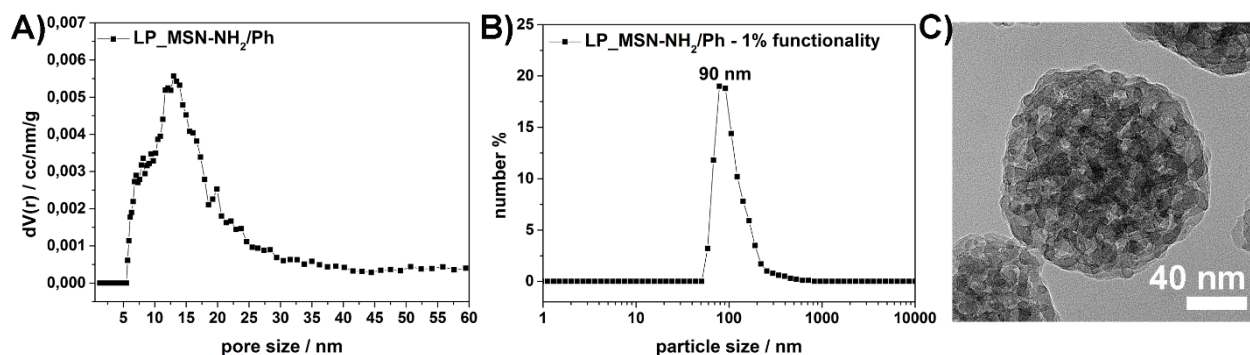


**Figure 8.1:** Characteristic data of the template-free LP_MSN-NH$_2$/Ph **A)** Calculated NLDFT pore size distribution, **B)** dynamic light scattering measurement in ethanolic solution and **C)** transmission electron micrograph after size separation centrifugation.

In brief, the isotherm of LP_MSN-NH$_2$/Ph can be interpreted as a hybrid form between a type II isotherm combined with a certain degree of type IV behavior, exhibiting an H3 hysteresis. An average pore size of 13 nm was calculated from nitrogen physisorption data (Figure 8.1A). The size separated LP_MSNs show a narrow size distribution with a maximum at 90 nm in dynamic light scattering measurements, which was confirmed by transmission electron microscopy. A detailed characterization of the sample LP_MSN-NH$_2$/Ph is given in Chapter 6.

As the generated LP_MSN-NH$_2$/Ph particles are of a similar size and exhibit similar surface properties as standard MSNs, it was investigated whether a supported lipid bilayer (SLB) is suitable to cap the mesopores of the LP_MSNs. We have previously reported that SLB-capped MSNs are highly promising candidates for drug delivery applications (cf. chapter 4) due to their excellent biocompatibility[2, 22] and prospects for post-synthesis modification including functionalities such as targeting ligands.[3] In brief, a fluorescent cargo (calcein and FITC-dextrans of different sizes) was adsorbed into the MSN pores in an overnight reaction under continuous stirring (Figure 8.2–1) before the LP_MSNs were enclosed by a supported lipid bilayer (SLB) to prevent premature release of the cargo from the MSN core (Figure 8.2–2). The SLB was generated around the nanoparticle via a solvent exchange method published by Cauda *et al.*[22] consisting of a lipid mixture of 70 v% of 1,2-dioleoyl-sn-glycero-3-phosphocholine (DOPC) and 30 v% of 1,2-dioleoyl-3-trimethylammonium-propane (DOTAP).
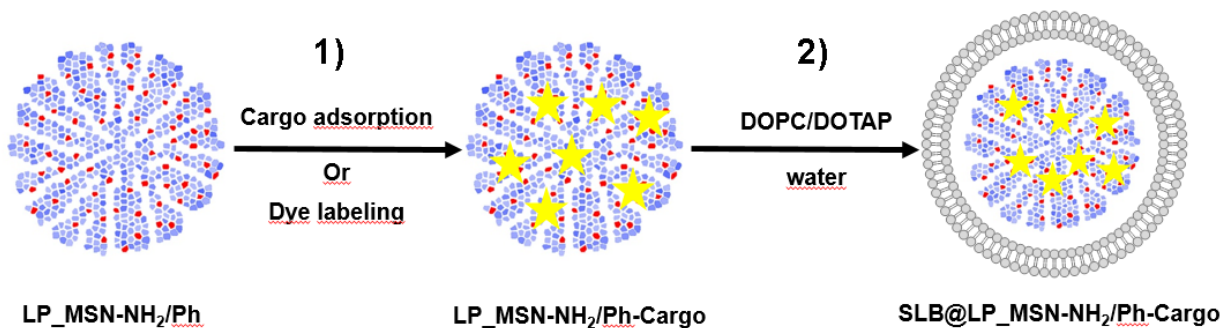


**Figure 8.2:** Schematic synthesis pathway of **1)** cargo adsorption (e.g. calcein) or covalent labeling with fluorescent dyes, and **2)** generation of a Supported DOPC-DOTAP Lipid Bilayer (SLB) around the LP_MSNs.

To prove the integrity of the enclosure mechanism, time-dependent fluorescence release experiments were carried out with the obtained SLB@LP_MSN-NH$_2$/Ph-Cargo samples. As

the LP_MSNs offer larger pores than conventional MSNs, FITC-dextrans of different sizes (3 – 5 kDa and 10 kDa) were employed as non-membrane permeable model drugs in addition to the standard dye calcein (cf. appendix 8.15). All time-based fluorescence release experiments were measured with our custom-made release setup consisting of a reservoir cap which is sealed by a dialysis membrane (MWCO = 14000 g/mol), allowing only the smaller dye molecules to diffuse into the water-filled cuvette.[11] All three samples were measured in the closed state applying the respective excitation/emission wavelengths of the cargo molecules at 37 °C, mimicking physiological temperatures. In comparison to the time-based release experiment with calcein, a slight premature release of dye molecules was observed (for both FITC-dextran sizes; Figure 8.3A for 5 kDa FITC-Dextran, Figure 8.3B for FITC-Dextran (10 kDa)). We assume that small amounts of the large sugar molecules are interacting with the lipids at the outer surface of the SLB around the LP_MSNs and therefore are able to diffuse into the cuvette. A leaky SLB can be excluded as both samples reach a saturation plateau after 2.5 h at a fluorescence intensity of an order of magnitude lower than the intensity of the cargo that can ultimately be released. After a defined elapsed time (3 h for each sample) the membrane was disrupted by the addition of a detergent (Triton-X); a strong increase of released FITC-dextran (5 kDa and 10 kDa, respectively) could be observed and a second saturation plateau was reached after an additional 9 h (Figure 8.3B). These results indicate that the larger FITC-dextran molecules were successfully encapsulated in the pores of LP_MSNs and released after disintegration of the SLB-membrane. The later drop in fluorescence intensity could be explained by bleaching of the dye.
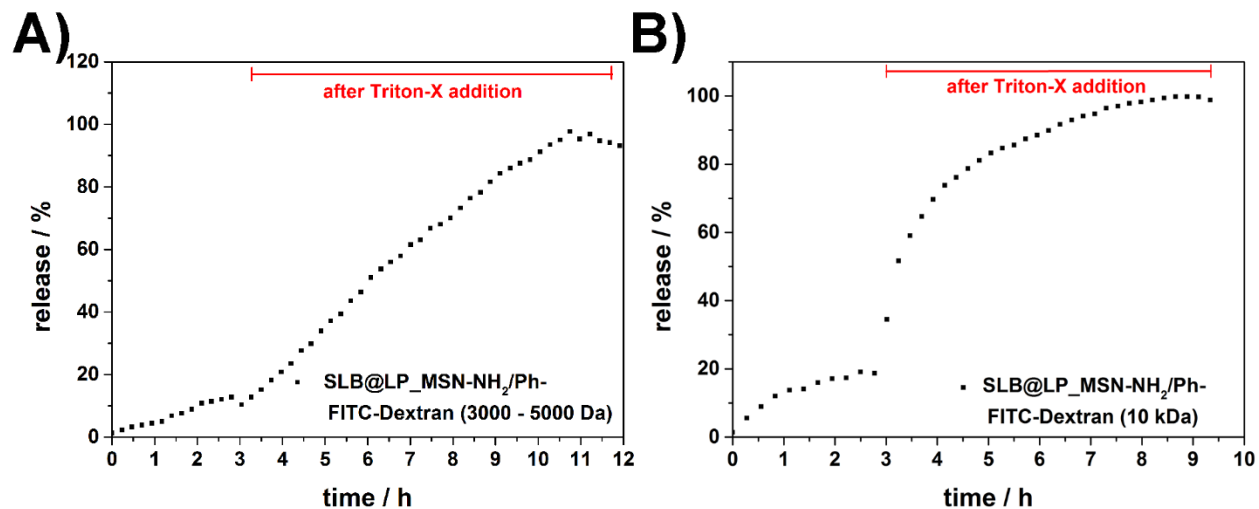
**Figure 8.3:** Dye release kinetics of SLB@LP_MSN-NH$_2$/Ph-Cargo as a function of time. After a three-hour incubation experiment (37 °C) with SLB-sealed LP_MSNs, Triton-X was added. **A)** FITC-Dextran (3 − 5 kDa). The inflection of the curve after 11 h presumably is a result of photobleaching of FITC. The curve was normalized to 100% for the amount released after 11 h. **B)** FITC-Dextran (10 kDa). Saturation of released FITC-dextran was reached after about 9 h. The curve was normalized to 100% for the amount released after about 9 h.

The above results show a successful enclosure of our LP_MSNs with a supported lipid bilayer, which demonstrates that the system is suitable for the adsorption of differently-sized cargo molecules. As additional proof for the integrity of the SLB@LP_MSNs, fluorescence microscopy was employed. For this purpose, the fluorescent dye Atto633 was covalently attached to the LP_MSN-NH$_2$/Ph through maleimide coupling (after size separation centrifugation) in an overnight reaction followed by subsequent washing steps to ensure that no free dye remains in the mesopores of the nanoparticles. This is also an additional proof for the successful functionalization of the LP_MSNs with organo-moieties. Note that additionally a defined amount of DOPC was substituted by the fluorescent lipid DOPC-Bodipy (DOPC : DOTAP : DOPC-Bodipy 65 : 30 : 5 v%) to enable fluorescence co-localization experiments (cf. experimental section). LP_MSN-NH$_2$/Ph-Atto633 were surrounded by the above-mentioned labeled SLB and investigated thoroughly with fluorescence imaging on a coverslip. For this purpose, a defined amount of nanoparticle solution in water was placed on a coverslip and subsequently imaged (Figure 8.4). The LP_MSNs are evenly distributed throughout the sample and show a perfect co-localization of the fluorescently labeled compounds (yellow;

merged image of green (DOPC-Bodipy) and red (Atto633)) indicating a successful generation of the SLB around the LP_MSNs. Additionally it can be noted that almost no large aggregates of nanoparticles are present within the sample, which is important for further applications.
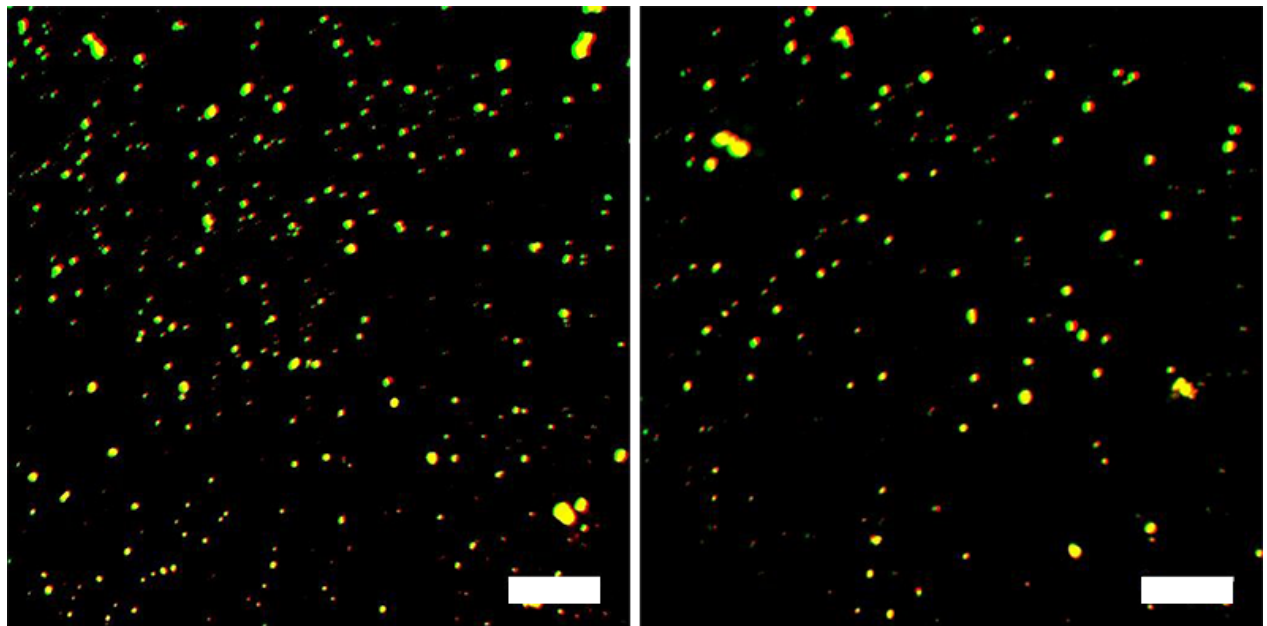


**Figure 8.4:** Co-localization experiments of SLB@LP_MSN-NH$_2$/Ph at different concentrations. The LP_MSNs are labeled with Atto633-maleimide (red), the SLB contains a certain amount of DOPC-Bodipy (green), merged image of both channels (yellow). Scalebar: 10 µm.

The above experiments demonstrate the successful generation of a biocompatible supported lipid bilayer around the LP_MSN-NH$_2$/Ph particles, and effective uptake of large cargo molecules. These results served as starting point for the development of a stimuli-responsive nano-carrier system based on LP_MSNs.

As already mentioned above, it is important to gain control over the nano-carriers via external triggers in order to enable a release on-demand of the incorporated cargo molecules from the mesopores of the silica nanoparticles. For this purpose, a red-light sensitive photosensitizer, Al(III) phthalocyanine chloride disulfonic acid (AlPcS$_{2a}$), was covalently attached to the outer surface of the LP_MSN-NH$_2$/Ph via a sulfonamide bond (Figure 8.5); an excess of AlPcS$_{2a}$ was employed for the reaction in order to avoid cross-linking of the nanoparticles as the photosensitizer bears two sulfonic acid groups that are available for the reaction. We note that no additional PEG-spacer was needed for this system in comparison to the previously described MSNs, as the pores of the LP_MSN-NH$_2$/Ph are larger than AlPcS$_{2a}$ and thus cannot be blocked.

The sample was thoroughly washed after the reaction by subsequent centrifugation until the supernatants were free of $AlPcS_{2a}$ (cf. appendix 8.16)
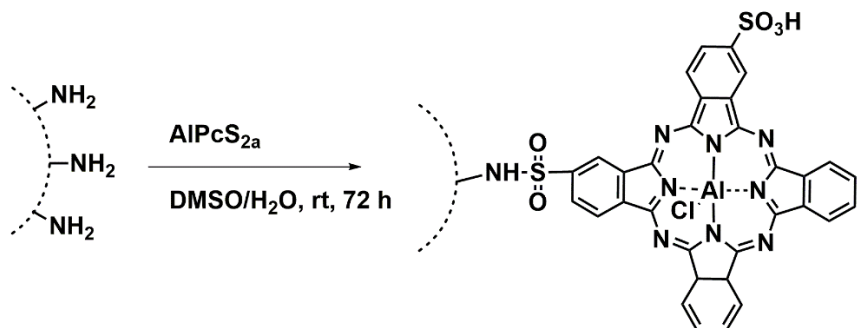


**Figure 8.5:** Covalent attachment of the red-light sensitive photosensitizer $AlPcS_{2a}$ to the amino-modified silica surface.

The functionalized inorganic-organic hybrid nanoparticles were characterized regarding porosity and successful post-synthesis modification by nitrogen physisorption, thermogravimetric analysis and IR spectroscopy. Figure 8.6A compares the nitrogen sorption isotherms obtained before and after organo-functionalization with the photosensitizer. Both isotherms can be interpreted as hybrid forms between a type II isotherm combined with a certain fraction of type IV isotherm. The hysteresis can be characterized as an H3 hysteresis loop that results from aggregation and thus from a significant degree of textural porosity in the dried powder sample (Figure 8.6A). The monolayer formation of the adsorbate can be observed between $p/p_0 = 0$ and 0.02, followed by multilayer adsorption over a broad range. The lack of saturation at high $p/p_0$ values can be explained with the large pore diameter of the LP_MSN-NH$_2$/Ph sample combined with a broad distribution of textural porosity between the dried LP_MSNs. The isotherm of LP_MSN-NH$_2$/Ph-AlPcS$_{2a}$ is slightly shifted to a higher adsorbed volume and thus results in a higher BET surface area ($A_s$ = 176 m$^2$/g for LP_MSN-NH$_2$/Ph and $A_s$ = 246 m$^2$/g for LP_MSN-NH$_2$/Ph-AlPcS$_{2a}$), the origin of which is not clear. The calculated pore size maximum remains the same after the reaction (13 nm, Figure 8.6B), indicating that $AlPcS_{2a}$ was predominantly attached on the outer surface of the LP_MSNs, which is supported by the calculated values (cf. appendix calculation 8.1).
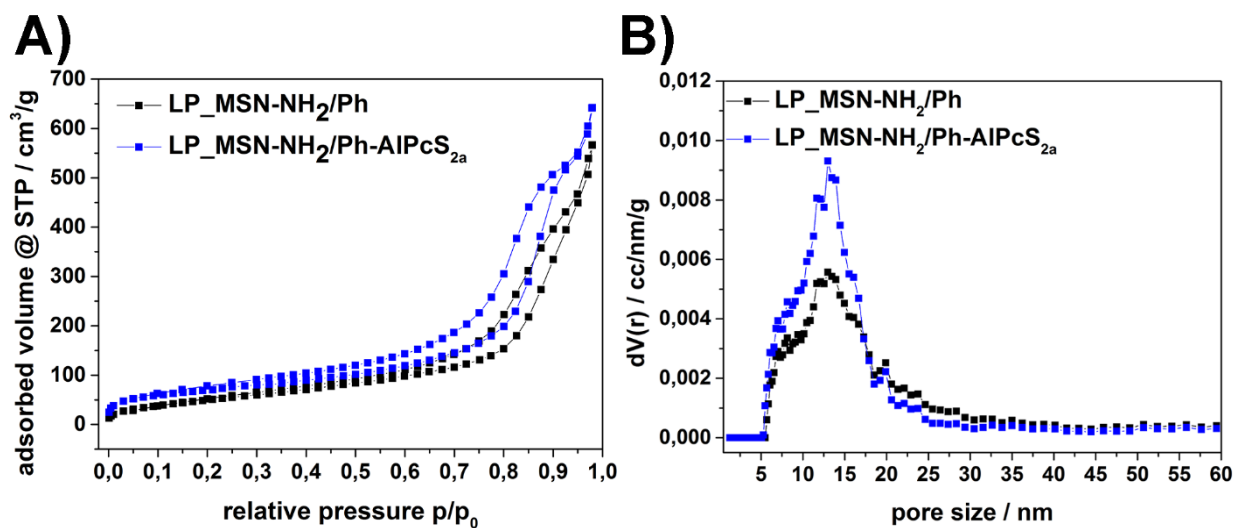
**Figure 8.6** Nitrogen physisorption data of LP_MSN-NH$_2$/Ph (black) and LP_MSN-NH$_2$/Ph-AlPcS$_{2a}$ (blue) **A)** Sorption isotherms, **B)** calculated NLDFT pore size distributions.

The successful attachment of AlPcS$_{2a}$ was demonstrated with thermogravimetric analysis (TGA, Figure 8.7A) and a detailed comparison of the IR spectra of LP_MSN-NH2/Ph and LP_MSN-NH$_2$/Ph-AlPcS$_{2a}$ (8.7B). The additional mass loss of 4.5% for LP_MSN- NH$_2$/Ph-AlPcS$_{2a}$ is quite high considering the low level of organo-functionality present within the sample and available for post-synthesis modification (only 0.5 mol% of the silica precursor consists of 3-aminopropyl triethoxysilane). This can be explained by the relatively large mass of the attached PS. The amount of attached AlPcS$_{2a}$ was calculated to be 67 µmol per gram LP_MSN-NH$_2$/Ph (cf. appendix calculation 8.1), which implies that 25% of the amino-groups have reacted with AlPcS$_{2a}$.
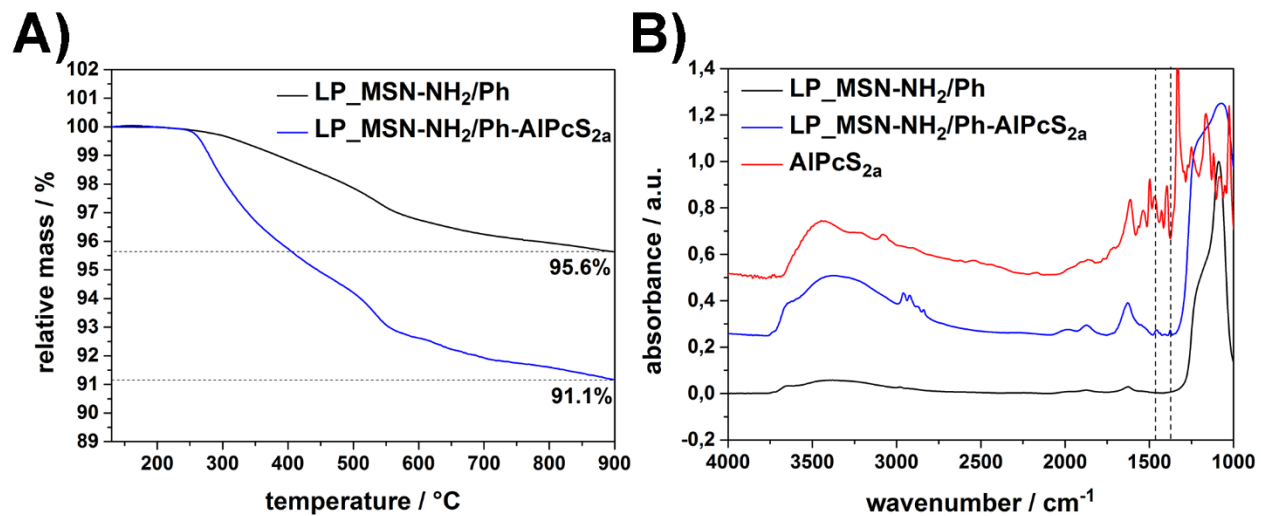
**Figure 8.7: A)** Thermogravimetric analysis of the samples LP_MSN-NH$_2$/Ph (black) and LP_MSN-NH$_2$/Ph-AlPcS$_{2a}$ (blue). The curves are normalized at 130 °C. B) Infrared spectra of LP_MSN-NH$_2$/Ph (black) and LP- MSN-NH$_2$/Ph-AlPcS$_{2a}$ (blue), normalized to the silica peak at 1087 cm$^{-1}$ and AlPcS$_{2a}$ (red, normalized to the strongest peak). The spectra of LP- MSN-NH$_2$/Ph-AlPcS$_{2a}$ and AlPcS$_{2a}$ are shifted along the y-axis by a value of 0.25 for clarity.

Data derived from IR spectroscopy yield information about the organo-functionality of the LP_MSN samples. Both spectra show typical bands of the silica framework appearing below 1300 cm$^{-1}$ with strong intensities. Additionally, the C-H stretching vibration modes of the alkyl chains (including ethoxy-groups on the silica framework) are present between 2940 and 2840 cm$^{-1}$. The marked peak at 1456 cm$^{-1}$ (dashed line) represents aromatic stretching vibrations of AlPcS$_{2a}$ and can be found in the spectra of LP_MSN-AlPcS$_{2a}$ and AlPcS$_{2a}$. The asymmetric SO$_2$ stretching vibration of the newly formed sulfonamide bond arises at 1377 cm$^{-1}$ (second dashed line) and is only visible in the spectrum of LP_MSN-NH$_2$/Ph-AlPcS$_{2a}$. The key features of the post-synthesis modified materials are summarized in table 8.1.

**Table 8.1:** Nitrogen physisorption and thermogravimetric analysis (TGA) data of LP_MSN-NH$_2$/Ph and LP- MSN-NH$_2$/Ph-AlPcS$_{2a}$.

| Sample | BET surface area (m²/g) | Pore volume (cm³/g) | Pore size[a] (nm) | Relative mass[b] loss (%) |
|---|---|---|---|---|
| **LP_MSN-NH$_2$/Ph** | 176 | 0.8 | 13 | 4.4 |
| **LP_MSN-NH$_2$/Ph-AlPcS$_{2a}$** | 246 | 0.9 | 13 | 8.9 |

[a] DFT pore size refers to the peak value of the pore size distribution; [b]Taken from the values at 900 °C; the curves are normalized to 130 °C

Since the results shown above suggest a successful post-synthesis functionalization of the LP_MSNs with the red-light sensitive photosensitizer, the next aim was to generate a biocompatible supported lipid bilayer as capping system for non-membrane permeable cargos around the LP_MSN-NH$_2$/Ph-AlPcS$_{2a}$. A size separation centrifugation step was employed to remove larger aggregates from the particle suspension before the PS was attached to the outer surface of the nanoparticles. Figure 8.8 depicts the synthesis approach: In a first step, cargo molecules of different sizes (calcein, propidium iodide and Alexa-Fluor-Dextran 10 kDa) were adsorbed into the mesopores of the LP_MSNs. After adsorption of the model drugs into LP_MSN-NH$_2$/Ph-AlPcS$_{2a}$, the outer surface was sealed by a supported lipid bilayer consisting of DOPC and DOTAP (70 : 30 v%) by a solvent induced self-assembly (Figure 8.8).
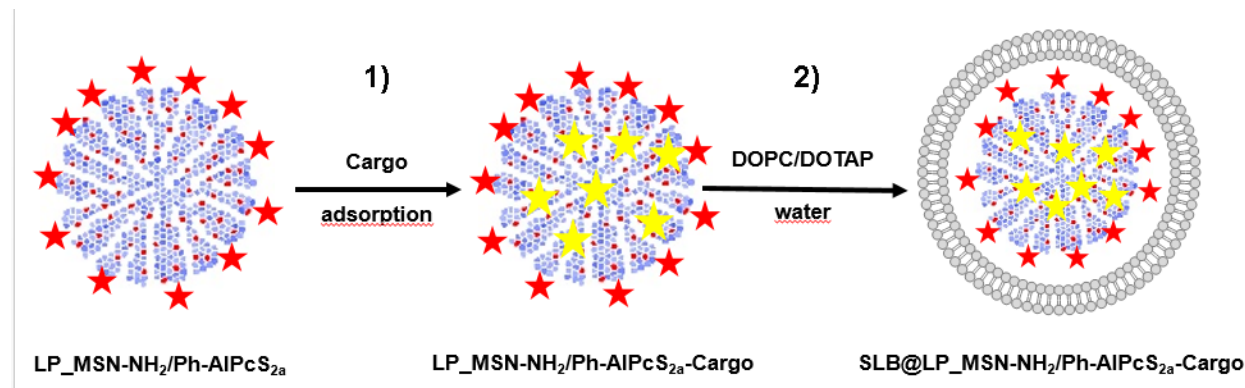


**Figure 8.8: 1)** Cargo adsorption into the mesopores of photosensitizer-modified sample LP_MSN-NH$_2$/Ph-AlPcS$_{2a}$. **2)** Generation of a supported lipid bilayer (SLB) consisting of DOPC and DOTAP around the LP_MSN-NH$_2$/Ph-AlPcS$_{2a}$.

The permeability of the SLB and the stimuli-responsive opening of the SLB by photoactivation with red light were examined in a cuvette release experiment (cf. experimental section) with calcein as fluorescent cargo. We note that only after photoactivation with red light (639 nm, 1 min, 5.4 W/cm$^2$) a significant amount of cargo is released, demonstrating the impermeability of the SLB for calcein before photoactivation. The amount of released cargo over a 3 h time period before opening the SLB is minimal; we assume that a small amount of calcein is trapped in the lipid bilayer and is therefore able to diffuse out of the reservoir. A saturation plateau was reached 9 hours after the SLB was disrupted by singlet oxygen.
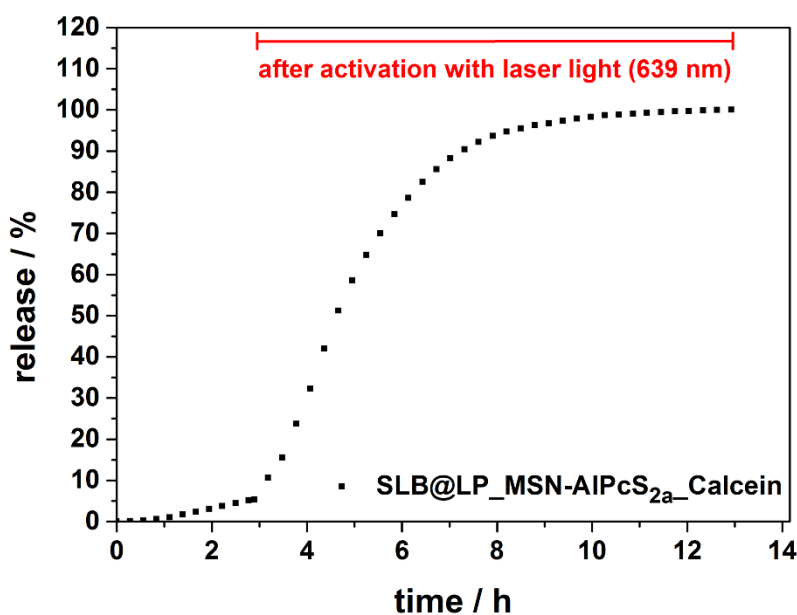


**Figure 8.9:** Dye release kinetics from SLB@LP_MSN-NH$_2$/Ph-AlPcS$_{2a}$-Calcein as a function of time at 37 °C. **1)** SLB capped LP_MSN-NH$_2$/Ph-AlPcS$_{2a}$-Calcein before photoactivation (0-3 h) and **2)** time-based release of calcein after activation of the photosensitizer (639 nm, 1 min, 5.4 W/cm$^2$) at 37 °C. The release curve was normalized to the value obtained after 12 h.

The *in vial* release experiment with LP_MSNs modified with an on-board photosensitizer showed successful cargo release upon activation with red light at moderate intensities and the resulting membrane rupture by singlet oxygen. As these results imply the successful generation of a nano-carrier based on LP_MSNs, the modified particles were investigated on a cellular level. HeLa cells were incubated for a total time period of 21 h with the dye-loaded LP_MSN-system to enable a significant uptake of the SLB-capped LP_MSNs via endocytosis. After this period, substantial co-localization exhibiting a dot-like pattern of the particles was

observed for AlPcS$_{2a}$ (red) and calcein (green) in optical microscopy, indicating that no premature release of calcein had occurred upon endosomal uptake of the nanoparticles. A small amount of spread photosensitizer appears to be visible in the cytosol; out-of-focus fluorescence could be a possible explanation for this. The activation of the photosensitizer (639 nm, 0.6 W/mm$^2$) leads to a cascaded membrane rupture induced by singlet oxygen. In a first step the integrity of the SLB on the SLB@LP_MSNs is destroyed, resulting in pore opening and thus cargo release from the mesopores. This step is followed by the rupture of the endosomal membrane thus allowing the fluorescent dye to be released into the cytoplasm of the cell. These events were monitored with fluorescence imaging at defined time points after photosensitizer activation (t = -1 ; t = 1 and t = 6 min).
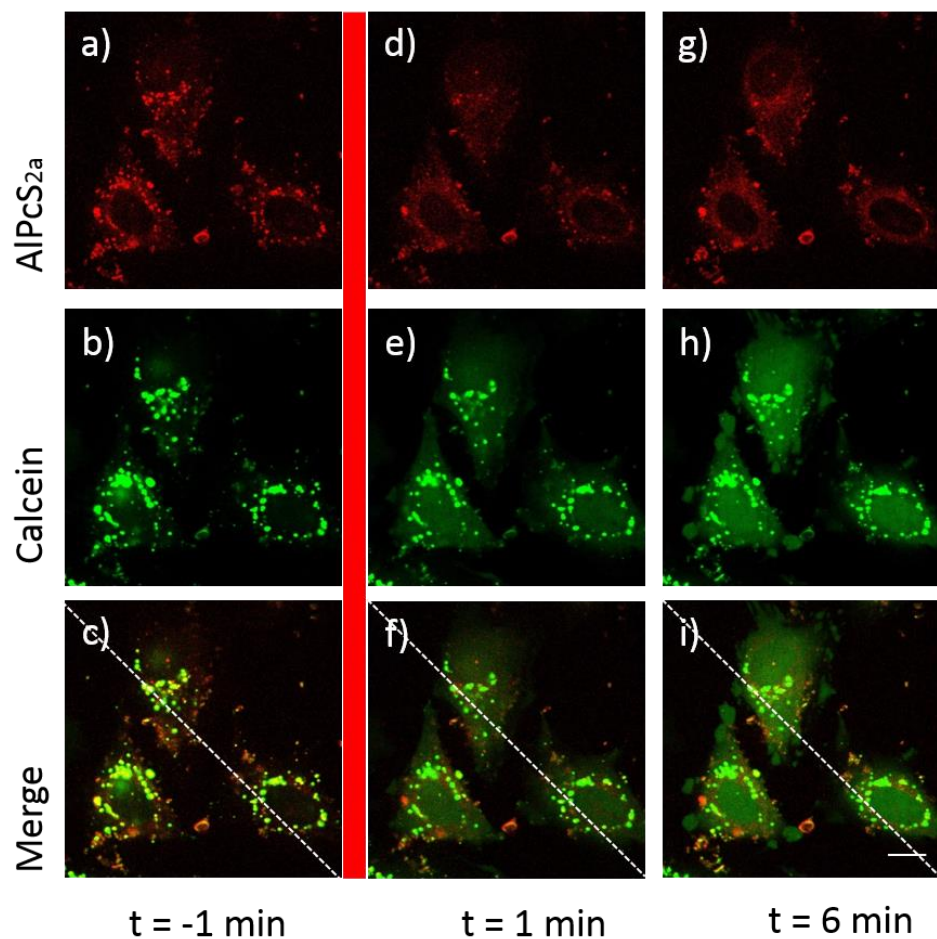


**Figure 8.10:** Fluorescence microscopy of SLB@LP_MSN-NH$_2$/Ph-AlPcS$_{2a}$-Calcein inside HeLa cells after an incubation time of 21 h. **(a-c)** AlPcS$_{2a}$ (red) and calcein (green) are mainly co-localized (yellow) prior to photoactivation. The red line indicates photoactivation with 0.6 W/mm$^2$ of red light (639 nm). **(d-f)** 1 min after photoactivation, **(g-i)** 6 min after photoactivation. Scalebar: 10 μm.

Intensity profiles for AlPcS$_{2a}$ (red curve) and calcein (green curve) were determined along the dashed white lines (Figure 8.10c-i) and are summarized in Figure 8.11. These profiles indicate an increased calcein release over a distinct time-frame as calcein de-quenches by dilution within the cell compartments. Additionally, we also note that a comparably weak increase in the intensity of the photosensitizer was observed. As the particles where washed thoroughly until no free photosensitizer could be observed by UV-VIS spectroscopy (cf. appendix 8.16) before cargo adsorption and subsequent cell experiments, it is highly unlikely that free PS was present in the sample. It could be possible that the sulfonamide bond is cleaved upon laser activation enabling some of the PS to diffuse into the cytoplasm and leading to the observed signal. However, this effect did not occur with AlPcS$_{2a}$-modified standard MSNs.[3] Another possible explanation could be the existence of a small amount of LP_MSNs in lysosomes due to the prolonged uptake time of the non-targeted LP_MSNs. The more acidic environment within lysosomes (pH = 4) might cause a hydrolysis of the sulfonamide.
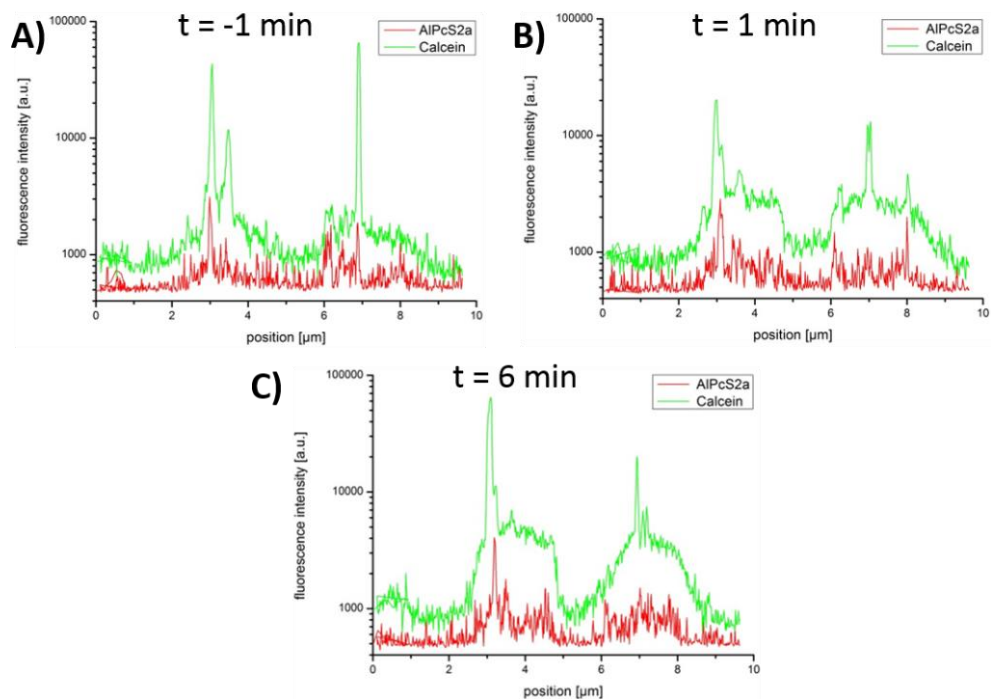


**Figure 8.11:** Intensity profiles of calcein (green) and red-light photosensitizer AlPcS$_{2a}$ (red) fluorescence along the white dashed lines (Figure 8.10) in the activation series of SLB@LP_MSN-NH$_2$/Ph-AlPcS$_{2a}$-Calcein for **A)** t = -1 min **B)** t = 1 min and **C)** t = 6 min with t = 0 min denoting the point of photosensitizer activation.

In a second study, the membrane-impermeable cargo propidium iodide (PI, 668 g/mol) was delivered to HeLa cells with SLB@LP_MSN-NH$_2$/Ph-AlPcS$_{2a}$. PI interacts with the nucleic acids of ribosomal RNA, thus an accumulation in the nucleoli of the cells can be observed upon successful release from the mesopores. In brief, PI was adsorbed into the mesopores of LP_MSN-NH$_2$/Ph-AlPcS$_{2a}$ and a DOPC/DOTAP-SLB was subsequently generated to cap the mesopores and to prevent premature cargo release. The HeLa cells were incubated for 21 h with SLB@LP_MSN-NH$_2$/Ph-AlPcS$_{2a}$-PI to allow for a sufficient uptake by the cells before the samples were imaged by fluorescence microscopy. We note that the images do not show single confocal planes but an average of the intensity over multiple slices to improve the signal-to-noise ratio. Significant co-localization between propidium iodide (green channel) and AlPcS$_{2a}$ (red channel) can be seen in the merged signal (yellow), however, different slices were recorded and an evaluation of the data is complicated by the abundance of nanoparticles. Importantly, no staining of the nucleoli can be observed before photoactivation (Figure 8.12 a/c) implying a successful capping of the LP_MSNs. After activation with red light (639 nm, 1.2 W/mm$^2$, 1 min) and subsequent rupture of the membranes, PI is able to diffuse out of the mesopores. Due to photobleaching events upon photoactivation, a strong decrease in fluorescence was observed (Figure 8.12 d/f), but after 10 min an accumulation of PI in the nucleoli of the cells is visible (Figure 8.12 j/l) indicating a successful membrane rupture and subsequent delivery of PI to the cytosol. Reference experiments with the sample supernatant after particle separation (subsequent centrifugation) showed no significant nucleoli staining. Again, a slight spreading of free photosensitizer did occur in this experiment.
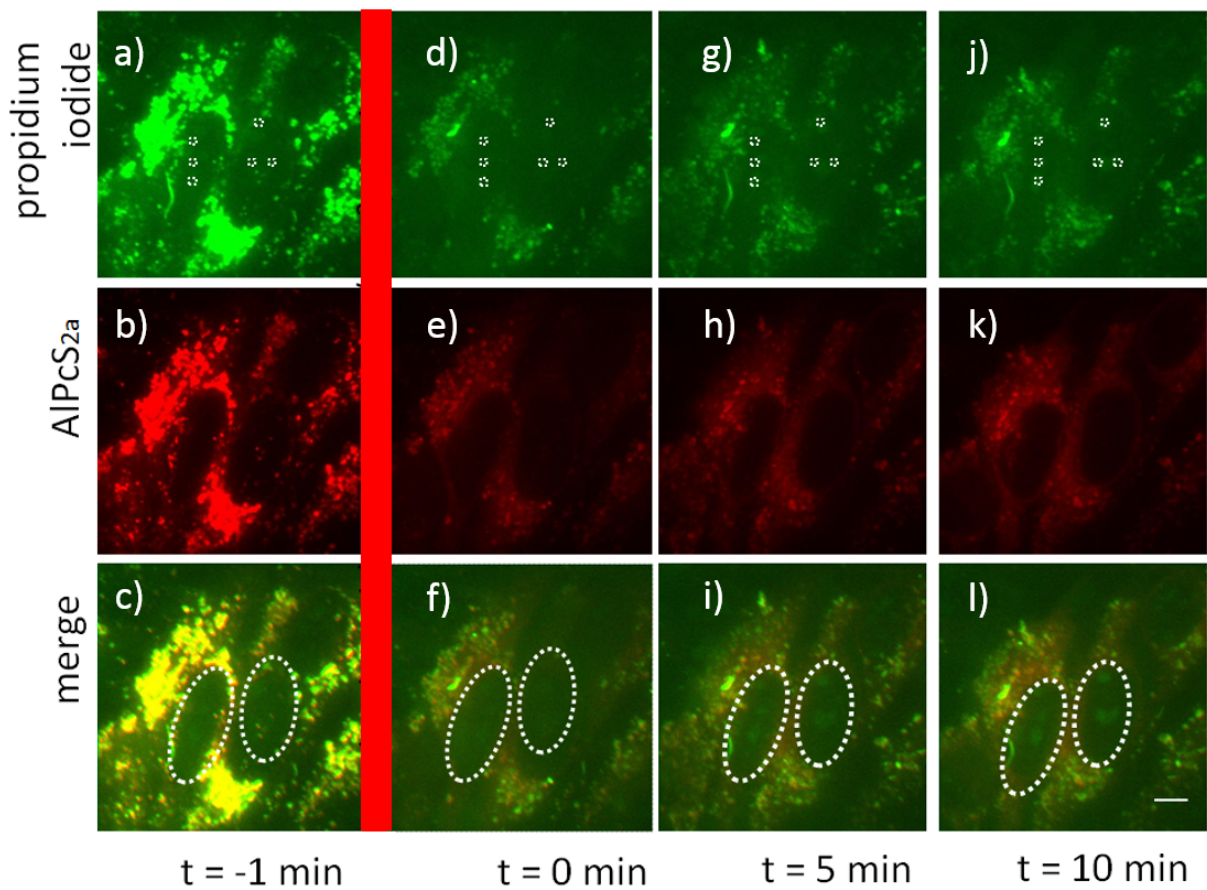
**Figure 8.12:** Fluorescence microscopy of propidium iodide-loaded SLB@LP_MSN-NH$_2$/Ph-AlPcS$_{2a}$ particles inside HeLa cells after an incubation time of 21 h. Several z-planes (34) were averaged in order to improve the signal-to-noise ratio **(a-c)** Propidium iodide (green) and AlPcS$_{2a}$ (red) before photoactivation. The red line indicates photoactivation with 1.2 W/mm$^2$ of red light (639 nm). **(d-f)** after photoactivation, **(g-i)** 5 min and **(j-k)** 10 min after photoactivation. Fluorescence intensity for the nucleoli indicated with white squares was measured; after photoactivation strong photobleaching effects were observed. Scale bar: 10 μm.

The fluorescence intensity was measured in the region of six clearly visible nucleoli (white squares in Figure 8.12 a/d/g/j) and plotted, setting the intensity at t = -1 to 100% (Figure 8.13). The intensities in the region of interest (ROI) are increasing as a function of time, after strong photobleaching first led to fluorescence decrease directly after activation.
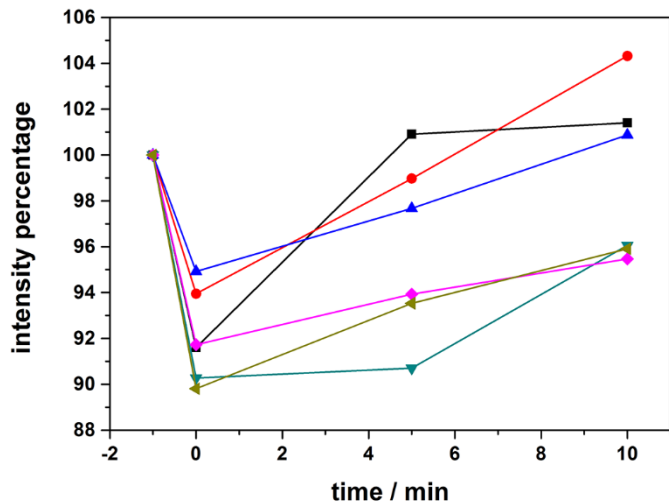
**Figure 8.13**: Propidium iodide intensities for the time points t = -1 min, t = 0 min, t = 5 min and t = 10 min after photoactivation for the six different nucleoli. The data are derived from the region of the nucleoli (within the outlined squares in Figure 8.12). The intensity at time point t = -1 min was normalized to 100%. The decrease in intensity at 0 min is caused by photobleaching due to photoactivation with 639 nm.

To conclude, we successfully synthesized a release on-demand system based on LP_MSN-NH$_2$/Ph with an on-board red light sensitive photosensitizer and were able to incorporate small fluorescent cargo molecules into the mesopores. Additionally, tight capping by a supported lipid bilayer around the nanoparticles was proven by cuvette and cell experiments.

As LP_MSNs also offer the possibility to adsorb larger cargo molecules in their mesopores, Alexa-Fluor-Dextran (AFD488, 10 kDa, radius ~2.3 nm) was chosen as fluorescent model drug for larger molecules. Previously described cuvette release experiments already suggested a successful adsorption into LP_MSN-NH$_2$/Ph without an external trigger attached. In order to investigate the stimuli-responsive nano-carrier system with AFD488, a defined amount of the dye-labeled sugar molecules was adsorbed into the mesopores (cf. experimental section) of the LP_MSN-NH$_2$/Ph-AlPcS$_{2a}$ particles, which were subsequently sealed by a singlet oxygen-responsive DOPC/DOTAP-SLB. To prove the functionality of the newly developed system, HeLa cells were incubated with the sample SLB@LP_MSN-NH$_2$/Ph-AlPcS$_{2a}$-AFD488 for 23 h prior to the measurement. As mentioned above for the measurement of PI-loaded LP_MSNs, z-projections from confocal cuts covering the entire height of the cells were analyzed instead of confocal cuts. The co-localization study shows that the tightly capped LP_MSNs contain AFD-488 (green) as cargo molecule and AlPcS$_{2a}$ (red); no premature release into the cytosol

was observed before PS activation (639 nm, 1.2 W/mm$^2$, 1 min), whereas typical release kinetics were visible after photoactivation, similar to the results obtained for calcein and propidium iodide. The given scaling was chosen to visualize the spreading of AFD-488 in the cytoplasm region without particles and therefore the particle fluorescence appears to be overexposed.

Only a slight increase of AFD-488 fluorescence could be detected in the cells (illustrated by the intensity profiles plotted along the dashed white lines), whereas most of the dye remains inside the nanoparticles. We assume that the diffusion of the large dextran cargo was hindered due to steric or charge effects and might need a longer time frame to diffuse out. Additionally, it has to be mentioned that fluorescence labeled dextrans, in comparison with other dyes used in this thesis (calcein and PI) are more difficult to visualize as they lack self-quenching or other fluorescence enhancing effects. Successful *in vial* (for LP_MSN-NH$_2$/Ph loaded with FITC-Dextran 10 kDa) and *in vitro* cargo release experiments (for different cargoes, including Alexa-Fluor-Dextran 10 kDa) showed successful adsorption and subsequent release of the large molecular weight cargo molecules serving as model drugs for siRNA. Additionally, the LP_MSNs were successfully modified with the red-light sensitive photosensitizer AlPcS$_{2a}$, which allows for on-demand endosomal escape upon light activation and thus cargo release from the mesopores into the cytosol.
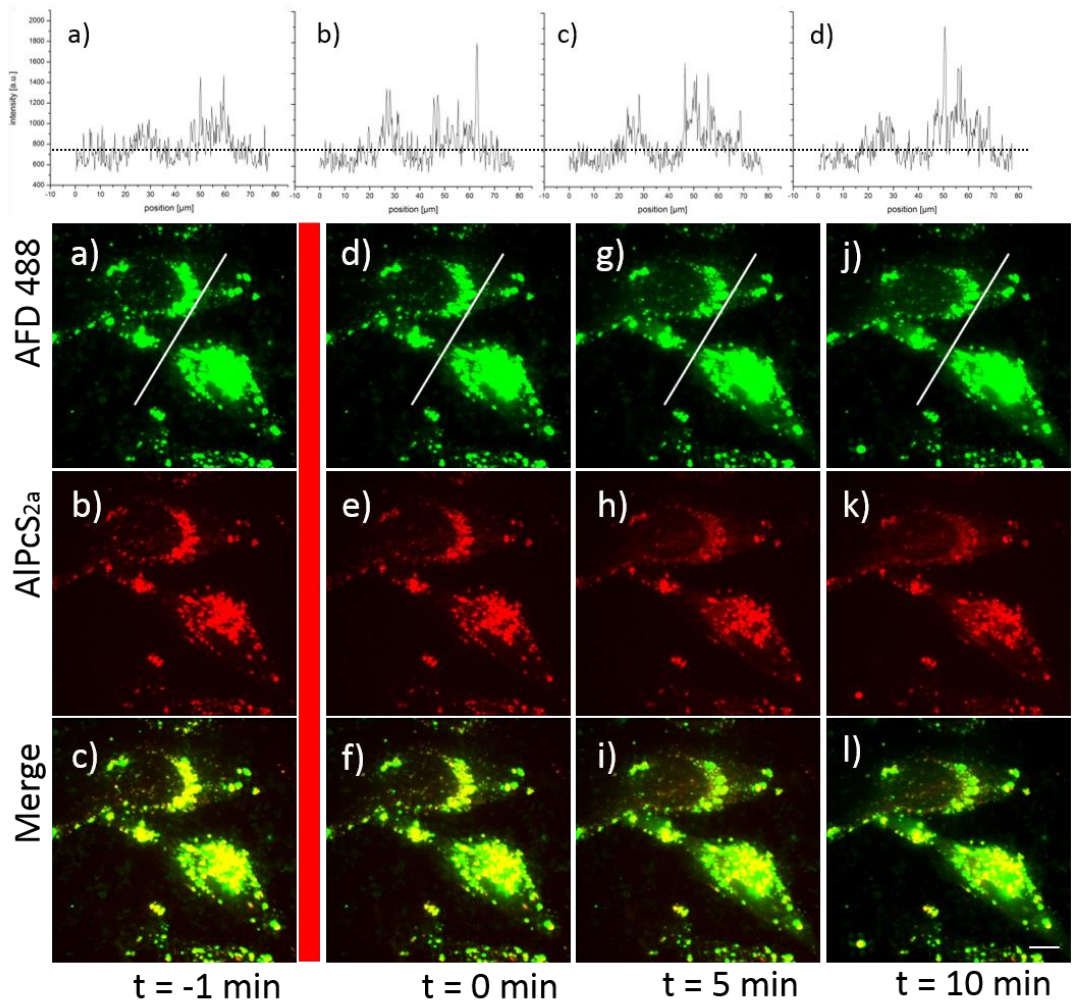
**Figure 8.14: Bottom**: Fluorescence microscopy of Alexa-Fluor-dextran-488 (AFD) loaded SLB@LP_MSN-NH$_2$/Ph-AlPcS$_{2a}$ after 23 h incubation of HeLa cells. The channels represent z-projections of the entire height of the cells from the confocal cuts. The signals of AF488-dextran (green), AlPcS$_{2a}$ (red) and the merged signal are displayed, respectively. **(a-c)** AFD488 (green) and AlPcS$_{2a}$ (red) are in the same regions (yellow) prior to photoactivation. The red line indicates the photoactivation with 1.2 W/mm$^2$ of red light (639 nm) leading to a rupture of the SLB. **(d-f)** after photoactivation, **(g-i)** 5 min and **(j-l)** 10 min after photoactivation. Intensity profiles were measured along the white lines. The scale bar represents 10 μm. **Top:** fluorescence intensity of AFD along the white line at the time points t = -1, 0, 5, and 10 min with t = 0 min denoting the point of photosensitizer activation (639 nm, 1.2 W/mm$^2$, 1 min).

## 8.3 Conclusions

In this work, amino/phenyl-functionalized mesoporous silica nanoparticles with ultra-large pores (LP_MSNs) generated by a co-condensation approach were successfully modified with an on-board photosensitizer and a biocompatible supported lipid bilayer (SLB) for pore capping. This system provides an on-demand release mechanism proven by *in vial* and *in vitro* cargo release experiments with model drugs of different sizes (calcein, propidium iodide, and fluorescently-labeled dextran 10 kDa). Significant uptake into HeLa cells was achieved throughout this study and endosomal entrapment, a major bottle-neck in drug delivery, was overcome by photoactivation. Upon activation with red light the photosensitizer generates singlet oxygen, resulting in a cascaded membrane rupture and thus, cargo release into the cytosol of living cells. We were able to demonstrate the efficient delivery and release of small and large molecular weight cargo such as fluorescently-labeled dextrans (up to 10 kDa), making the new system a promising candidate for the delivery of bioactive peptides or nucleic acids (siRNA) for advanced drug delivery applications.

## 8.4 Experimental

**Chemicals.** Pluronic F127 (F127, Sigma), fluorocarbon surfactant 4 (FC-4, Yick-vik Chemicals), tetraethyl orthosilicate (TEOS, Fluka, >99%), 1,3,5-trimethylbenzene (TMB, Fluka, 96%), 3-aminopropyl triethoxysilane (APTES, Sigma, $\geq$ 98%), phenyl triethoxysilane (PTES, Sigma, 98%), ethanol absolute (EtOH, Aldrich, >99.5%), conc. hydrochloric acid (Aldrich, >95%, 37 wt%), acetone (reaction grade, Acros), Atto633-maleimide (Atto633-Mal, Atto-Tec), *N,N*-dimethylformamide (DMF, anhydrous, Aldrich), Al(III) phthalocyanine chloride disulfonic acid (AlPcS$_{2a}$, Frontier Scientific), dimethyl sulfoxide (DMSO, Sigma, >99.5%), calcein (Sigma), propidium iodide (PI, Sigma, $\geq$ 98%), FITC-dextran (3000–5000 Da, Sigma), FITC-dextran (10 kDa, Sigma), Alexa-Fluor-488-dextran (AFD488, Invitrogen) 1,2-dioleoyl-sn-glycero-3-phosphocholine (DOPC, Avanti Polar Lipids), 1,2-dioleoyl-3-trimethylammonium-propane (chloride salt) (DOTAP, Avanti Polar Lipids), Bodipy-labeled 1,2-dioleoyl-sn-glycero-3-phosphocholine (DOPC-Bodipy, Invitrogen).

All chemicals were used as received without further purification. Doubly distilled water from a Millipore system (Milli-Q Academic A10) was used for all synthesis and purification steps.

**Synthesis of amino/phenyl functionalized large pore silica nanoparticles (LP_MSN-NH2/Ph) with 1 mol% functionality.** A modified literature procedure was employed to synthesize LP_MSN-NH2/Ph.[18, 19] Pluronic F127 (0.25 g) and fluorocarbon surfactant FC-4 (1.4 g) were dissolved in hydrochloric acid (HCl, 30 mL, 0.02 M), followed by the addition of TMB (0.20 g, 1.66 mmol). The reaction mixture was stirred in a 100 mL polypropylene reactor for 2 h at 10 °C before a mixture of tetraethyl orthosilicate (TEOS, 1.5 g, 7.2 mmol, 100 mol%), phenyl triethoxysilane (PTES, 8.7 μL, 0.036 mmol, 0.5 mol%) and of 3-aminopropyl triethoxysilane (8.4 μL, 0.036 mmol, 0.5 mol%) was added drop-wise. The resulting suspension was stirred vigorously (1250 rpm) for 14 h at 10 °C. The resulting particle suspension was hydrothermally treated in a 100 mL Parr reactor under static conditions (150 °C, 1d). The mixture was centrifuged (15 min, 20500 rpm, 50228 rcf), re-suspended in hydrochloric acid (HCl, 30 mL, 0.2 M) and heated under static conditions (140 °C, 2d). After the addition of 50 mL bi-distilled $H_2O$, the LP_MSNs were collected by centrifugation (15 min, 20500 rpm, 50228 rcf), re-dispersed in 50 mL EtOH and extracted according to the procedure described below.

**Template removal from LP_MSN.** The organic template was removed via extraction from LP_MSNs. For this purpose, 250 mg of the particles were refluxed for 2 h at 75 °C in a mixture of absolute EtOH (80 mL), acetone (40 mL) and conc. HCl (10 mL). This extraction step was performed twice. The template-free LP_MSNs were separated by centrifugation (15 min, 20500 rpm, 50228 rcf) and washed with EtOH after each extraction step. LP_MSNs were obtained as colloidal suspension in EtOH. This extraction procedure was carried out for all samples unless otherwise noted.

**Size separation centrifugation of LP_MSNs.** In order to separate larger agglomerates and impurities from the synthesized nanoparticles, a size separation centrifugation was performed (15 sec, 3.000 rpm, 775 rcf). The resulting supernatant comprising a nanoparticle yield of 50% (relative to the synthesis yield) was employed for all further applications. The obtained particles in ethanol were stored in tightly sealed glass vials.

**Adsorption of fluorescent cargos into the mesopores of LP_MSN-NH₂/Ph.** 0.5 mg of the sample LP_MSN-NH$_2$/Ph in ethanol were centrifuged and re-dispersed in 1 mL water. This washing step was repeated twice with 1 mL water each. Then, the suspension was centrifuged again and re-dispersed in:

- 500 µL calcein (1 mM stock solution in water),
- 375 µL water and 125 µl FITC-Dextran (3 – 5 kD, 1 mg/mL stock solution in water),
- 250 µL water and 250 µL FITC-Dextran (10 kD; 5 mg/mL stock solution in water)

The respective reaction mixtures were stirred overnight in the dark yielding the sample LP_MSN-NH$_2$/Ph-Cargo.

**Supported DOPC/DOTAP lipid bilayer (SLB) around LP_MSN-NH₂/Ph-Cargo**

The amount of 0.5 mg of LP_MSN-NH$_2$/Ph-Cargo was separated by centrifugation (4 min, 14000 rpm, 16873 rcf). A mixture of 70 µL DOPC and 30 µL DOTAP (each 2.5 mg/mL in 60 : 40 H$_2$O : EtOH) were added to the resulting pellet, mixed extensively, and sonicated for 10 s. To form the supported lipid bilayer around the MSN via the solvent exchange method, 700 µL of water were added. The resulting suspension was mixed and sonicated for 10 s, yielding DOPC/DOTAP-SLB@LP_MSN-NH$_2$/Ph-Cargo.

**Time-based fluorescence release experiments of the sample DOPC/DOTAP@ LP_MSN-NH₂/Ph-Cargo.** Time-based fluorescence release experiments were recorded on a PTI fluorescence system equipped with a PTI 814 photomultiplier detector and a PTI A1010B Xenon arclamp driven by a PTI LPS-220B lamp power supply. For temperature settings, a Quantum Northwest TC 125 sample holder was used. Our previously described custom-made release cuvette system was employed for all experiments. All samples were measured at a temperature of 37 °C with slits of 1-1.2-1-1-1 (2-2.2-2-2-2 for FITC-Dextran 10 kDa). For calcein an excitation wavelength of 495 nm was used (emission maximum at 516 nm), whereas FITC-dextran with an emission maximum at 520 nm was excited with 490 nm.

0.5 mg of the respective DOPC/DOTAP@ LP_MSN-NH$_2$/Ph-Cargo (Cargo = Calcein, FITC-Dextran 5 kDa or FITC-Dextran 10 kDa) sample was used for the experiment. 200 µL of

the particle suspension was filled into the reservoir cap sealed with a dialysis membrane (Molecular weight cut-off 14000 g/mol) allowing released dye molecules to pass into the fluorescence cuvette. Each sample was measured for 3 h in the closed state before the SLB was disrupted by added detergent. For this purpose, the LP_MSNs were transferred to an Eppendorf cup and mixed with 5 µL of a 1 mM stock solution of TritonX100 to disrupt the membrane. Afterwards, the sample was measured again for defined time periods.

**Dye-labeling of LP_MSN-NH$_2$/Ph with Atto633-maleimide.** The amount of 1 mg of LP_MSN-NH$_2$/Ph was washed three times with absolute ethanol (1 mL each) by repeated centrifugation (4 min, 14000 rpm, 16873 rcf) and re-dispersion, before 5 µL Atto633-maleimide (13.4 nmol, 1 mg Atto633-Mal dissolved in 500 µL anhydrous DMF) was added to the LP_MSN solution. The reaction mixture was allowed to stir at ambient temperature for 14 hours in the dark. The sample was washed four times with 1 mL absolute ethanol by successive centrifugation (4 min, 14000 rpm, 16873 rcf) and re-dispersion to remove unbound dye.

**Generation of supported dye-labeled DOPC/DOTAP lipid bilayer (SLB) around LP_MSN-NH$_2$/Ph-Atto633.** The amount of 0.5 mg of LP_MSN-NH$_2$/Ph-Atto633 was washed thoroughly with water (five times, 1 mL each) by successive centrifugation (4 min, 14000 rpm, 16873 rcf). Afterwards, a mixture of 65 µL DOPC, 5 µl DOPC-Bodipy and 30 µL DOTAP (each 2.5 mg/mL in 60:40 H$_2$O : EtOH) were added to the resulting pellet, mixed extensively, and sonicated for 10 s. To form the supported lipid bilayer around the MSN via the solvent exchange method, 700 µL of water were added. The resulting suspension was mixed and sonicated for 10 s, yielding SLB_bodipy@LP_MSN-NH$_2$/Ph-Atto633.

**Attachment of the photosensitizer AlPcS$_{2a}$ to LP_MSN-NH$_2$/Ph.** 1 mg of LP_MSN-NH$_2$/Ph in ethanolic solution was centrifuged (4 min, 14000 rpm, 16873 rcf) and re-suspended in a 500 µL water/DMSO mixture (2:1). Subsequently, 20 µL of an AlPCS$_{2a}$ stock solution (2 mg in 1 mL DMSO) were added to the MSNs. The reaction mixture was stirred in the dark at room temperature for 72 h. The resulting LP_MSN-NH$_2$/Ph-AlPcS$_{2a}$ was extensively washed by centrifugation (4 min, 14000 rpm, 16873 rcf) with a water/DMSO mixture (1:1) in order to remove excess photosensitizer. All supernatants were investigated with a Nanodrop UV-VIS in order to monitor the content of free photosensitizer. Results of these measurements are given in the Appendix. In order to remove DMSO from the mesopores, the sample was washed three times with bi-destilled water after no free PS could be detected. The colloidal solution of sample LP_MSN-NH$_2$/Ph-AlPcS$_{2a}$ was immediately used for further experiments.

**Adsorption of fluorescent cargo molecules into the mesopores of LP_MSN-NH2/Ph-AlPcS2a**

The amount of 0.5 mg of the sample LP_MSN-NH$_2$/Ph-AlPcS$_{2a}$ in ethanol was centrifuged and re-dispersed in 1 mL water. This washing step was repeated twice with 1 mL water each. Then, the suspension was centrifuged again and re-dispersed in:

- 500 µL calcein (1 mM stock solution in water),
- 250 µL water and 250 µl propidium iodide (1 mM stock solution in water),
- 100 µL water and 10 µL Alexa-Fluor-488-Dextran (10 kD; 2 mg/mL in PBS)

The respective reaction mixtures were stirred overnight in the dark yielding the sample LP_MSN-NH$_2$/Ph-AlPcS$_{2a}$-Cargo. A supported lipid bilayer consisting of DOPC and DOTAP was built around the LP_MSNs prior to measurements (see detailed synthesis procedure above).

**Time-based fluorescence release experiments of the sample DOPC/DOTAP@LP_MSN-NH2/Ph-AlPcS2a-Calcein.** Fluorescence time-based release experiments were recorded on a PTI fluorescence system equipped with a PTI 814 photomultiplier detector and a PTI A1010B Xenon arclamp driven by a PTI LPS-220B lamp power supply. For temperature settings, a Quantum Northwest TC 125 sample holder was used. Our previously described custom-made release cuvette system was employed for all experiments. All samples were measured at a temperature of 37 °C with slit positions 1-1.2-1-1-1. An excitation wavelength of 495 nm was employed (emission maximum at 516 nm).

The amount of 0.5 mg of DOPC/DOTAP@ LP_MSN-NH$_2$/Ph-AlPcS$_{2a}$-Calcein was used for the experiment. 200 µL of the particle suspension was filled into the reservoir cap sealed with a dialysis membrane (molecular weight cut-off 14000 g/mol) allowing released dye molecules to pass into the fluorescence cuvette. In order to monitor the release of adsorbed dyes upon membrane rupture with singlet oxygen, the sample was excited with 0.56 W / mm$^2$ of 633 nm light for 1 minute prior the measurement.

**Cell culture.** HeLa cells were cultivated in Dulbecco's modified Eagle's medium (DMEM):F12 (1:1) (Invitrogen) with Glutamax I medium supplemented with 10 % fetal bovine serum (FBS) at 37 °C in a 5% CO$_2$ humidified atmosphere. The cells were seeded on collagen

A-coated LabTek chambered cover glass (Nunc). For live cell imaging the cells were seeded 24 or 48 h before measuring, at a cell density of $2x10^4$ or $1x10^4$ cells/cm$^2$.

**Spinning disc confocal microscopy.** Confocal microscopy for live-cell imaging was performed on a setup based on the Zeiss Cell Observer SD utilizing a Yokogawa spinning disk unit CSU-X1. The system was equipped with a 1.40 NA 100x Plan apochromat oil immersion objective from Zeiss. For all experiments the exposure time was 0.1 s and the frame rate varied between 3 frames/s and 1 frame/30s, depending on the specific requirements of the experiment. Cells were incubated with the corresponding particles 21 - 23 h prior to the measurements at 37 °C under a 5% $CO_2$ humidified atmosphere. Shortly before imaging, the medium was replaced by $CO_2$-independent medium (Invitrogen). During the measurements all cells were kept on a heated microscope stage at 37 °C.

Calcein and Alexa-Fluor derivatives were imaged with approximately 0.4 W/mm$^2$ of 488 nm excitation light. PI was excited with 0.39 W/mm$^2$ and Bodipy with 0,72 W/mm$^2$ of 561 nm; AlPcS$_{2a}$ was excited with 0.12 W/mm$^2$ of 639 nm for imaging and for photoactivation with 0.6 or 1.2 W/mm$^2$. In the excitation path a quad-edge dichroic beamsplitter (FF410/504/582/669-Di01-25x36, Semrock) was used. For two color detection of calcein, Alexa-Fluor derivatives and AlPcS$_{2a}$ a dichroic mirror (560 nm, Semrock) and band-pass filters 525/50 and 690/60 (both Semrock) were used in the detection path. For detection of PI or Bodipy and AlPcS2a a dichroic mirror with 660 nm (Semrock) and band-pass filters 629/60 (both Semrock) were used. Separate images for each fluorescence channel were acquired using two separate electron multiplier charge coupled devices (EMCCD) cameras (Photometrics Evolve$^{TM}$).

**Characterization.** Centrifugation was performed using a Sorvall Evolution RC equipped with a SS-34 rotor or an Eppendorf centrifuge 5418 for small volumes (1.5 mL maximum). Dynamic light scattering (DLS) and zeta potential measurements were performed on a Malvern Zetasizer-Nano instrument equipped with a 4 mW He-Ne laser (633 nm) and an avalanche photodiode. DLS measurements were directly recorded on ethanolic colloidal suspension at a constant concentration of 1 mg/mL. Transmission electron microscopy (TEM) and Scanning TEM were performed on a FEI Titan 80-300 kV microscope operating at 300 kV. UV-VIS spectra were recorded with a NanoDrop ND 1000 spectrometer. Amounts of 2 μL of sample were used and all presented spectra are background corrected for the respective solvent.

## 8.5   Appendix
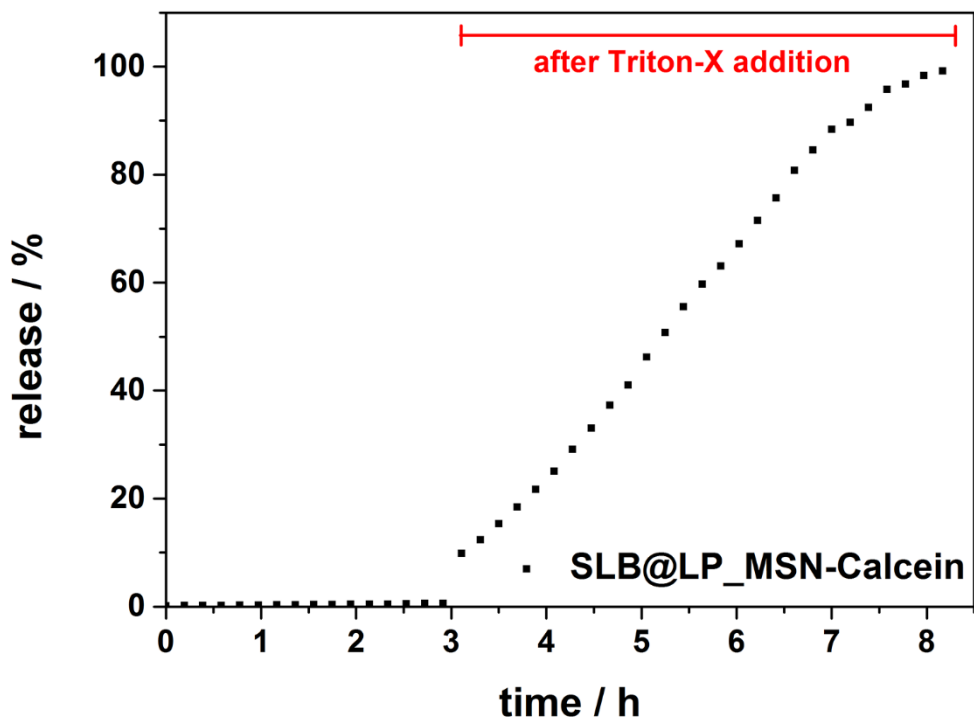


**Figure 8.15:** Dye release kinetics from SLB@LP_MSN-NH$_2$/Ph-Calcein as a function of time. After a 3 h release experiment at 37 °C with supported lipid bilayer capped LP_MSN-NH$_2$/Ph-Calcein, Triton-X was added to disrupt the SLB, resulting in a burst of dye release. 100% was set for the amount released after 8 h.
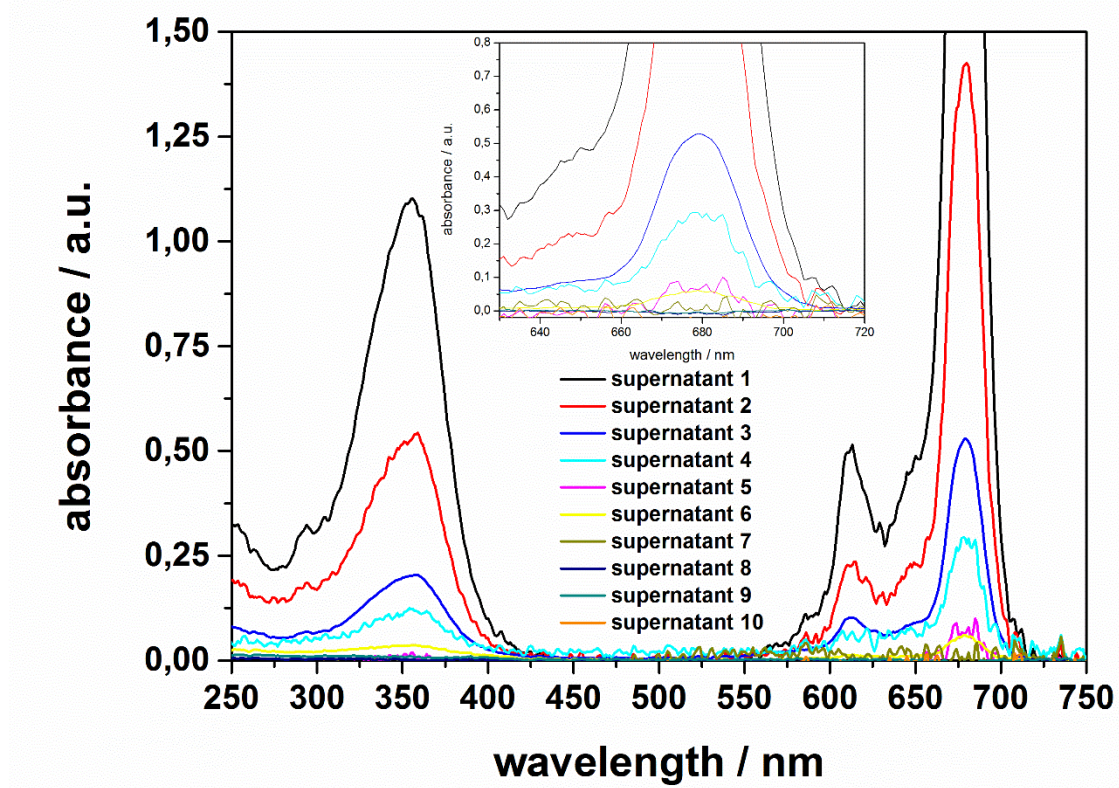
**Figure 8.16:** UV-Vis spectra of the supernatants resulting from the washing procedure of LP_MSN-NH$_2$/Ph-AlPcS$_{2a}$. No free photosensitizer could be detected in supernatants 8, 9 and 10.

**Calculation 8.1**: Calculation of the surface functionalization based on thermogravimetric analysis (TGA) of sample LP_MSN-NH$_2$/Ph

1 g sample LP_MSN-NH$_2$/Ph contains 44 mg NH$_2$/Ph-residues (mass loss 4.4%, M$_w$(C$_3$H$_6$Ph/C$_3$H$_6$NH$_2$ 50:50)=88.5 g*mol$^{-1}$)

$$\frac{44\ mg}{(100\% - 4.4\%)\ g} = 46\ mg\ NH2/Ph - residues\ /\ g\ silica$$

$$\frac{0.046\ g}{88.5\ \frac{g}{mol}} = 0.52\ mmol\ NH2/Ph - residues/g\ silica => 0{,}26\ mmol\ NH2/g\ silia$$

1 g sample LP_MSN-AlPcS$_{2a}$ contains 45 mg AlPcS$_{2a}$ (additional mass loss 4.5%, M$_w$(AlPcS$_{2a}$) = 735,1 gmol$^{-1}$)

$$\frac{45\ mg}{(100\% - 4.4\% - 4.5\%)\ g} = 49\ mg\ AlPcS_{2a}\ /\ g\ silica$$

$$\frac{0.049\ g}{735{,}1\ \frac{g}{mol}} = 0{,}067\ mmol\ AlPcS_{2a} - residues\ /\ g\ silica$$

Amount of NH$_2$ moieties that have reacted with AlPcS$_{2a}$:

$\frac{0{,}067\ mmol}{0{,}26\ mmol} = 25{,}8\%$ of NH$_2$ moieties

BET surface of LP_MSN-NH$_2$/Ph = 176 m$^2$/g

BET surface of non-porous silica spheres of the same size = 45 m$^2$/g

$\frac{45\ m^2/g}{176\ m^2/g} = 25{,}6\%$ of NH$_2$ moieties on the particle surface LP_MSN-NH$_2$/Ph.

## 8.6  References

1. Ashley, C. E.; Carnes, E. C.; Phillips, G. K.; Padilla, D.; Durfee, P. N.; Brown, P. A.; Hanna, T. N.; Liu, J.; Phillips, B.; Carter, M. B.; Carroll, N. J.; Jiang, X.; Dunphy, D. R.; Willman, C. L.; Petsev, D. N.; Evans, D. G.; Parikh, A. N.; Chackerian, B.; Wharton, W.; Peabody, D. S.; Brinker, C. J. *Nat. Mater.* **2011**, *10*, 389-397.

2. Schlossbauer, A.; Sauer, A. M.; Cauda, V.; Schmidt, A.; Engelke, H.; Rothbauer, U.; Zolghadr, K.; Leonhardt, H.; Bräuchle, C.; Bein, T. *Adv. Healthcare Mater.* **2012**, *1*, 316-320.

3. Mackowiak, S. A.; Schmidt, A.; Weiss, V.; Argyo, C.; von Schirnding, C.; Bein, T.; Bräuchle, C. *Nano Lett.* **2013**, *13*, 2576-2583.

4. Meng, H.; Xue, M.; Xia, T.; Zhao, Y.-L.; Tamanoi, F.; Stoddart, J. F.; Zink, J. I.; Nel, A. E. *J. Am. Chem. Soc.* **2010**, *132*, 12690-12697.

5. Li, Z.; Barnes, J. C.; Bosoy, A.; Stoddart, J. F.; Zink, J. I. *Chem. Soc. Rev.* **2012**, *41*, 2590-2605.

6. Liu, R.; Zhao, X.; Wu, T.; Feng, P. *J. Am. Chem. Soc.* **2008**, *130*, 14418-14419.

7. Schlossbauer, A.; Dohmen, C.; Schaffert, D.; Wagner, E.; Bein, T. *Angew. Chem. Int. Ed.* **2011**, *50*, 6828-6830.

8. Tarn, D.; Xue, M.; Zink, J. I. *Inorg. Chem.* **2013**, *52*, 2044-2049.

9.  Sauer, A. M.; Schlossbauer, A.; Ruthardt, N.; Cauda, V.; Bein, T.; Bräuchle, C. *Nano Lett.* **2010**, *10*, 3684-3691.

10. Luo, Z.; Cai, K.; Hu, Y.; Zhao, L.; Liu, P.; Duan, L.; Yang, W. *Angew. Chem. Int. Ed.* **2011**, *50*, 640-643.

11. Schlossbauer, A.; Kecht, J.; Bein, T. *Angew. Chem. Int. Ed.* **2009**, *48*, 3092-3095.

12. Schlossbauer, A.; Warncke, S.; Gramlich, P. M.; Kecht, J.; Manetto, A.; Carell, T.; Bein, T. *Angew. Chem. Int. Ed.* **2010**, *49*, 4734-4737.

13. Martelli, G.; Zope, H. R.; Capell, M. B.; Kros, A. *Chem Commun (Camb)* **2013**, *49*, 9932-9934.

14. Barhoumi, A.; Wang, W.; Zurakowski, D.; Langer, R. S.; Kohane, D. S. *Nano Lett.* **2014**.

15. Muhammad, F.; Guo, M.; Qi, W.; Sun, F.; Wang, A.; Guo, Y.; Zhu, G. *J. Am. Chem. Soc.* **2011**, *133*, 8778-8781.

16. Lu, J.; Liong, M.; Sherman, S.; Xia, T.; Kovochich, M.; Nel, A. E.; Zink, J. I.; Tamanoi, F. *Nanobiotechnology* **2007**, *3*, 89-95.

17. Gan, Q.; Lu, X.; Yuan, Y.; Qian, J.; Zhou, H.; Lu, X.; Shi, J.; Liu, C. *Biomaterials* **2011**, *32*, 1932-1942.

18. Han, Y.; Ying, J. Y. *Angew. Chem. Int. Ed.* **2005**, *44*, 288-292.

19. Gao, F.; Botella, P.; Corma, A.; Blesa, J.; Dong, L. *J. Phys. Chem. B.* **2009**, *113*, 1796-1804.

20. Na, H.-K.; Kim, M.-H.; Park, K.; Ryoo, S.-R.; Lee, K. E.; Jeon, H.; Ryoo, R.; Hyeon, C.; Min, D.-H. *Small* **2012**, *8*, 1752-1761.

21. Hartono, S. B.; Gu, W.; Kleitz, F.; Liu, J.; He, L.; Middelberg, A. P. J.; Yu, C.; Lu, G. Q.; Qiao, S. Z. *ACS Nano* **2012**, *6*, 2104-2117.

22. Cauda, V.; Engelke, H.; Sauer, A.; Arcizet, D.; Bräuchle, C.; Rädler, J.; Bein, T. *Nano Lett.* **2010**, *10*, 2484-2492.

# 9    Functionalization with organo-lithium reagents and post-synthesis modification of mesoporous MCM-41

This chapter is based on the following publication:

## Abstract

The mesoporous framework of MCM-41 can be modified with numerous metal-organic reagents, enabling the introduction of functional groups to the surface of the silica material. We demonstrate the direct organic functionalization of mesoporous silica with easily accessible lithiated aromatic compounds. For this purpose, several bromine-containing aromatic compounds were lithiated and the products were used for the *in situ* functionalization of MCM-41. In combination with the remarkably reduced cost for the synthesis and the unique features of these novel functionalized inorganic-organic hybrid materials, lithiated aromatic compounds are promising candidates for the post-synthesis modification of mesoporous silica materials. Here we focus on heteroatom-bearing compounds such as esters, ethers and other heteroaromatics (e.g., 4-bromoanisole, 4-bromobenzaldehyde dimethylacetal and 2-bromothiophene). The resulting inorganic-organic hybrid materials offer the possibility for further functionalization, depending on the application of the respective material. The high specific surface areas, the well-defined pore size distribution and the typical 2D hexagonal array of the porous channels were retained during the synthesis of the inorganic-organic hybrid materials. Additionally, we achieved high loading capacities for our novel organic-inorganic hybrid materials.

## 9.1  Introduction

Ever since the development of MCM-41 by Beck *et al.*[1, 2] in 1992 there has been an increasing interest in the field of mesoporous silica materials. Their scope of applications has grown in the last two decades, ranging from solid supports for catalysts[3, 4] and gas sensors[5] to nano-carriers for advanced drug delivery applications.[6-8] Mesoporous materials offer the possibility to tune particle morphology, pore size and pore topology according to the needs of the application, and it is possible to modify their internal and external surface via molecular functionalization. Among the numerous mesoporous silica materials that are known today, MCM-41 has been widely used as a promising solid support for organic catalysts: For example, Das *et al.*[9] attached a Jacobsen catalyst onto MCM-41 and Yang *et al.* immobilized dicyano functionalized arenes together with palladium(0) for Heck-Reactions in the mesoporous network.[10] Various pathways enabling the introduction of molecular functionalities into mesoporous frameworks are known.[11] Specifically, post-synthesis grafting and co-condensation represent two important approaches for introducing molecular functionality. Both of these methods rely on the use of organo-silanes such as 3-aminopropyl triethoxysilane (APTES), but only a limited number of such silanes is commercially available. However, it is of interest to incorporate complex structures and a broad variety of functionalities into the mesoporous framework of silica materials at affordable costs. Whereas the availability of appropriate organo-silane reagents is limited, numerous bromo-functionalized aliphatic and aromatic compounds are readily available or can be easily synthesized with standard organic methods.

If a pathway could be opened that would ultimately replace the bromine atom in brominated organic molecules with a surface silicon atom in mesoporous silica, a wealth of organic moieties could be immobilized in these hosts. This would offer the unique possibility to design promising catalysts directly and to incorporate them into the mesoporous framework of the solid support. The approach of employing metal-organic compounds for the direct organic modification of mesoporous silica materials was developed independently by Lim *et al.* and by some of us.[12, 13] We found a synthetic method that offers a broad spectrum of functionalities for the modification of the solid support.[13] Initially the synthesis was based on Grignard reactants, followed by the reaction of lithiated arene compounds with the silica framework.[14] Very low temperatures are employed during the synthesis, which can be an advantage when grafting sensitive organic moieties. The functionalization with metal-organic reagents offers the possibility to introduce

multiple functionalities into the mesoporous framework of silica materials. The procedure developed by Angloher *et al.* has already been employed to generate promising catalysts for Michael-additions.[15, 16] In the above publication, nitrogen-containing arene compounds were immobilized on the solid support. Here we focus on the immobilization of oxygen- and sulfur-containing molecules that offer interesting possibilities for further functionalization. Moreover, we further improved the synthesis procedure by using *tert*-butyllithium (tBuLi) as lithiating agent instead of n-butyllithium (nBuLi) to prevent unwanted by-products.

## 9.2   Results and Discussion

MCM-41 was synthesized according to a procedure published by Kumar *et al.*.[17] The organic template was removed by calcination in air, yielding template-free mesoporous MCM-41 as white powder, which was characterized before further reactions were conducted (resulting data are shown together with those of modified materials). Since reactions with metal-organic reagents require a moisture- and oxygen free environment, template-free MCM-41 was outgassed *in vacuo* at 150 °C for 6 h und kept under nitrogen atmosphere before the actual synthesis of the inorganic-organic hybrid materials was started.

We followed different protocols in order to synthesize organo-functionalized MCM-41 (details see experimental section). In a first approach, several 4-bromo-arenes were lithiated with 0.8 equivalents of n-butyllithium (nBuLi) in anhydrous hexane. The molar ratio of 0.8 equivalents nBuLi and 1 equivalent aromatic compound was employed to avoid the coupling of unreacted nBuLi with the surface of the mesoporous material. The resulting 4-lithioarenes were subsequently reacted with MCM-41. This post-synthesis functionalization of MCM-41 was carried out for 4 h at a specified temperature and was quenched with water afterwards. All samples were purified via soxhlet extraction in dichloromethane to remove unreacted reagents from the mesopores. The incorporation of the lithiated arenes (Ar-Li) proved to be successful and was verified with ^{13}C and [29]Si magic angle spinning (MAS) solid state NMR (ssNMR) (Figure 9.3B for ^{13}C ssNMR of the reaction of 4-lithiobenzaldehyde dimethylacetal with MCM-41 and Figure 9.11 (cf. appendix) for ^{13}C ssNMR of the reaction of 4-lithioanisole with MCM-41). However, the ^{13}C ssNMR spectrum of MCM-41_ArOMe (reaction with 4-lithioanisole) and MCM-41_BDMA (reaction with 4-lithiobenzaldehyde dimethylacetal) showed that in addition to the aromatic peaks, butyl-moieties are present in the synthesized materials as well. We found these butyl-residues attached to the mesoporous framework in each spectrum. As it is possible that nBuLi itself reacts with the silicon atoms of MCM-41 forming

a Si-butyl bond, this reation was studied in more detail. For this purpose, template-free MCM-41 was reacted with the same molar amount of nBuLi (2.5 mmol) that had been used for the conversion of 4-bromoanisole to 4-lithioanisole at different temperatures (-78 °C, -20 °C and ambient temperature). The obtained materials were characterized with $^{13}$C and $^{29}$Si ssNMR, and additionally thermogravimetric analysis was performed (cf. appendix 9.9). The synthesis temperature strongly affects the degree of functionalization of the silica atoms, as demonstrated in the $^{29}$Si ssNMR spectrum (cf. appendix 9.8). When MCM-41 is reacted with nBuLi at -78 °C, only mono-functionalization of the silica framework occurs, indicated by the appearance of $T_2/T_3$ peaks in Figure 9.8 (black curve, cf. appendix). Higher temperatures (-20 °C and ambient temperature) lead to additional bi-functionalization of the silica atoms as indicated by the newly appearing $D_2$ peak (green and red curve in Figure 9.8, appendix). However, a detailed analysis of the obtained $^{13}$C ssNMR spectra of MCM-41_nBuLi (Figure 9.1A) revealed that the peaks do not match the pattern resulting from MCM-41_ArOMe (Figure 9.1B). One peak is shifted to higher magnetic fields ($\delta$ = 48 ppm) in the case of MCM-41_ArOMe, which does not correspond to an n-butyl-chain linked directly to the silica framework.
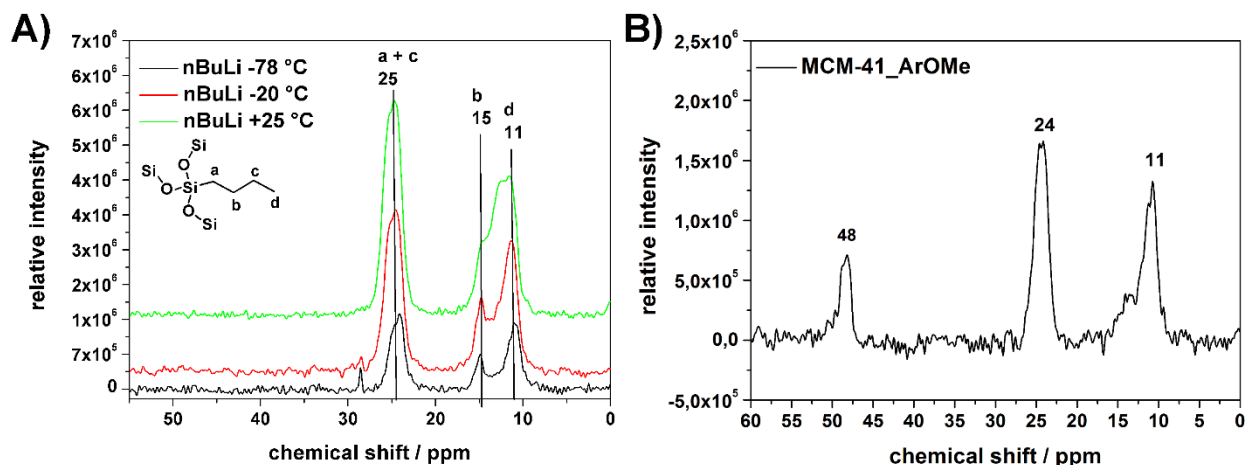


**Figure 9.1:** $^{13}$C magic angle spinning solid state NMR (MAS ssNMR) spectra **A)** of the reaction of n-butyllithium with MCM-41 at different temperatures, and **B)** reaction of MCM-41 with 4-lithioanisole at -78 °C.

Given the above insights, we ask about the nature and origin of the butyl groups in the pores. Butylbromide is a by-product of the bromine-lithium-exchange reaction with 4-bromoanisole (or 4-bromobenzaldehyde dimethylacetal (BDMA)), which is able to react with the siloxane

groups of the silica framework (cf. appendix Figure 9.7). The change of the chemical shift to higher magnetic fields ($\delta = 48$ ppm instead of 25 ppm) indicates that the butyl-chain is bound to an electron-withdrawing heteroatom, which is oxygen in this case. A variation of the reaction temperature for the reaction of 4-lithioanisole with MCM-41 did not result in an elimination of the peak at $\delta = 48$ ppm.

Since the butoxy signal together with the distinct aromatic peaks was present in all obtained ^{13}C ssNMR spectra of MCM-41_Arene (MCM-41_ArOMe, MCM41_BDMA, MCM-41_Thiophene and MCM-41_ArNMe2) the synthesis protocol was modified. Instead of 0.8 equivalents (2.5 mmol) nBuLi, 2 equivalents *tert*-butyllithium (tBuLi, 5 mmol) and anhydrous diethyl ether were employed for the lithiation of the bromo-containing aromatic compounds. The synthesis pathway is given in appendix Figure 9.7 (cf. experimental section). In a first reaction, 4-Br-BDMA was lithiated with tBuLi in anhydrous Et2O, yielding 4-Li-BDMA as reactive intermediate that was subsequently reacted with template-free MCM-41 at low temperatures.
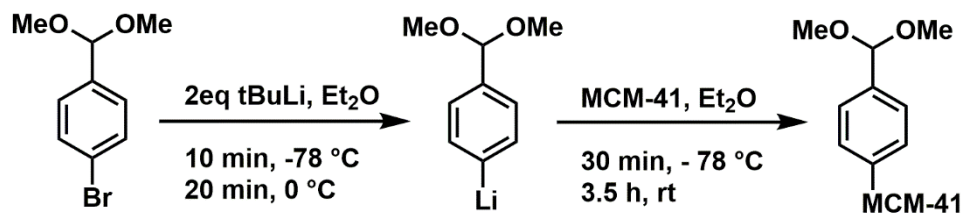


**Figure 9.2:** Reaction of 4-bromobenzaldehyde dimethylacetal (Br-BDMA) with 2 eq tBuLi at low temperatures and subsequent reaction with MCM-41.

It is known that the use of 2 equivalents of tBuLi eliminates butylbromide from the reaction itself;[18] one equivalent tBuLi lithiates the arene whereas the second equivalent reacts with the *in situ* generated *tert*-butylbromide, yielding only gaseous by-products (isobutene and isobutane) and LiBr.

This novel synthesis approach was studied with 4-bromoanisole and 4-bromobenzaldehyde dimethylacetal as model systems with the reaction parameters given in Figure 9.2. The resulting inorganic-organic hybrid materials were purified via soxhlet extraction for 3 h in dichloromethane to ensure that no unreacted precursor is present in the mesopores

(cf. experimental section). The materials were analyzed with ssNMR and the results were compared with the data for the reaction with 0.8 eq nBuLi. The data are summarized in Figure 9.3A, B and D (for MCM-41_BDMA) and Figure 9.11 and 9.12 (for MCM-41_ArOMe, cf. appendix).
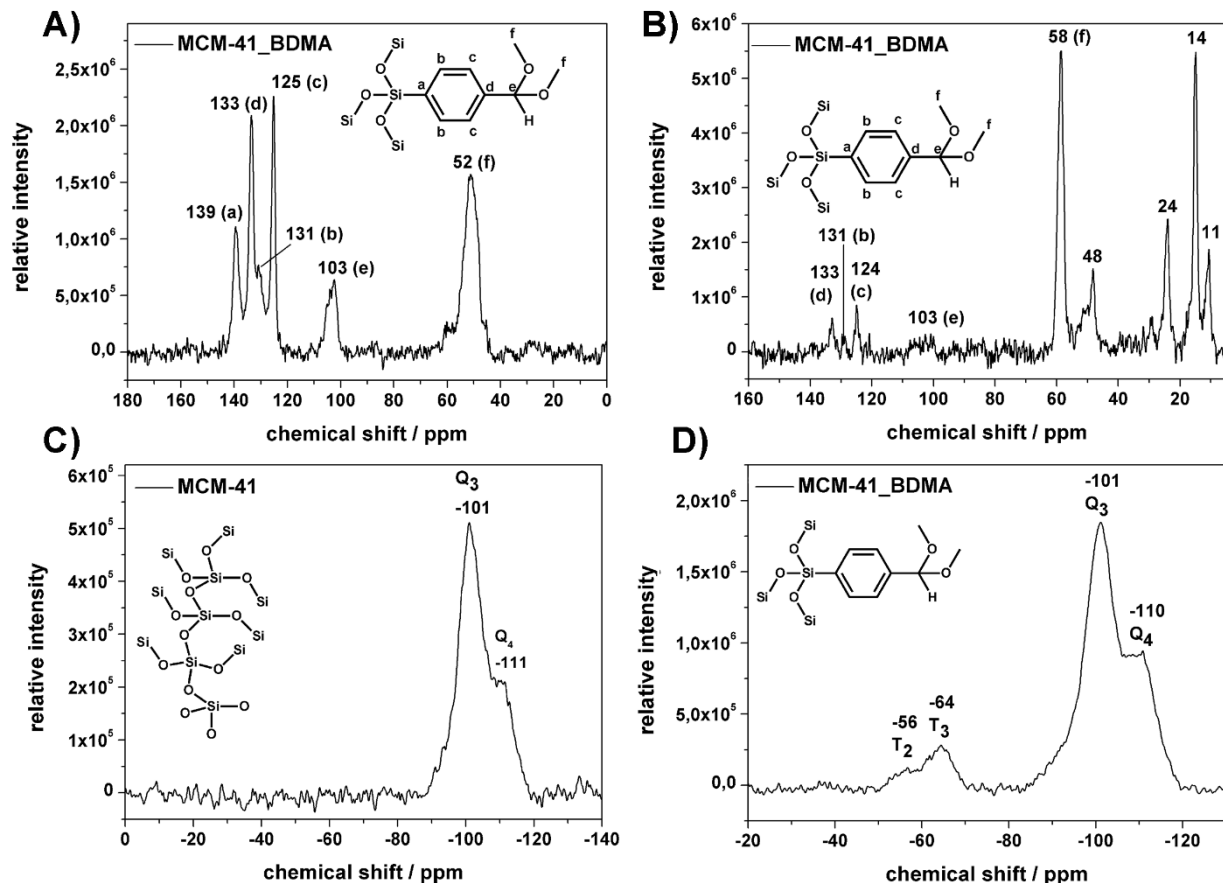


**Figure 9.3:** Organo-functionalization of MCM-41 with 4-bromobenzaldehyde dimethylacetal. **A)** ^{13}C ssNMR of MCM-41_BDMA – halogen-lithium-exchange carried out with 2 eq tBuLi, **B)** ^{13}C ssNMR of MCM-41_BDMA, lithiation with n-BuLi, **C)** ^{29}Si ssNMR of template-free, unfunctionalized MCM-41, **D)** ^{29}Si ssNMR of MCM-41_BDMA with tBuLi.

As discussed previously for MCM-41_ArOMe, the lithiation of the bromo-containing compound with nBuLi and subsequent reaction of the Ar-Li species with MCM-41 results in the attachment of butyl-fragments to the mesoporous framework, which is also the case for MCM-41_BDMA. The ^{13}C ssNMR of these reactions (Figure 9.3B) shows the distinct peaks at $\delta = 11, 14, 25$ and 48 ppm whereas no alkyl peaks are visible in the spectrum when 4-Li-BDMA

was generated with tBuLi. Despite the different reactivity of 4-bromoanisole, the same result was obtained for MCM-41_ArOMe (cf. appendix 9.11). Figure 3D shows the $^{29}$Si ssNMR spectrum of MCM-41_BDMA, indicating the successful attachment of 4-Li-BDMA to the mesoporous framework of MCM-41. Both species, $Q_3/Q_4$ ($\delta$ = -101 and -110 ppm – corresponding to the silica species A in Figure 9.7) and $T_2/T_3$ ($\delta$ = -55 and -65 ppm - corresponding to silica species B in Figure 9.7) were observed in the $^{29}$Si ssNMR spectra of MCM-41_BDMA, indicating mono-functionalization of the silica atoms in MCM-41. Bi-functionalized silica species that are indicated by the $D_2$ peak (species C in Figure 9.7, cf. appendix) are not present.

In order to analyze the mesostructure of the inorganic-organic hybrid material, nitrogen sorption measurements were carried out for template-free MCM-41 and MCM-41_BDMA. The organo-functionalized sample exhibits a type IV isotherm (Figure 9.4A, empty squares) typical for a mesoporous material with a high surface area of 763 $m^2g^{-1}$ and a pore size of 2.9 nm (Figure 9.4B). Compared to MCM-41 (filled squares) the BET area is reduced by a value of 250 $m^2g^{-1}$ and the pore size is smaller, which confirms the successful incorporation of the aromatic system into the mesoporous framework.
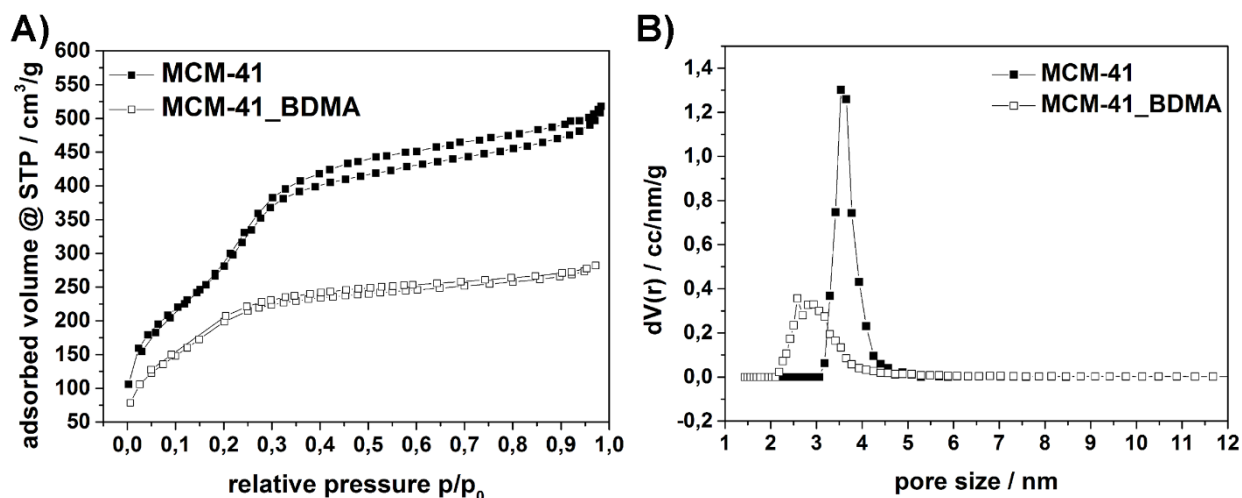


**Figure 9.4:** Nitrogen sorption data of MCM-41 and MCM-41_BDMA. **A)** Nitrogen sorption isotherms of calcined MCM-41 (filled squares) and MCM-41_BDMA (empty squares), and **B)** pore size distribution of calcined MCM-41 (filled squares) and MCM-41_BDMA (empty squares).

Additional analysis of MCM-41_BDMA and MCM-41_ArOMe (Ar-Li generated with tBuLi) with transmission electron microscopy (TEM) shows that the typical hexagonal 2D

mesostructure of MCM-41 was retained under the given reaction conditions (cf. appendix Figures 9.19 for MCM-41, 9.20 for MCM-41_BDMA and 9.21 for MCM-41_ArOMe).

As the lithiation with tBuLi proved to be successful for 4-bromoanisole and 4-benzaldehyde dimethylacetal, the novel synthesis procedure was extended to several additional aromatic compounds, shown as precursor 4-bromo arenes in Figure 5.
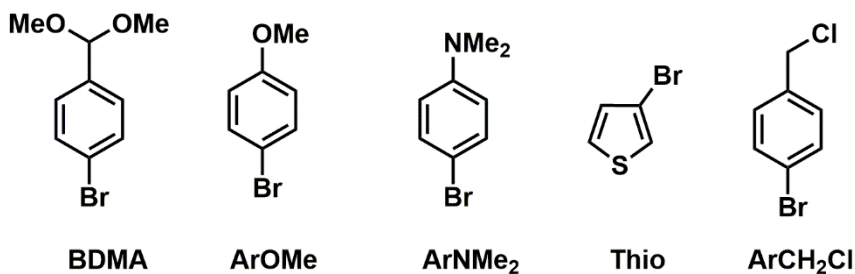


**Figure 9.5:** Overview of the aromatic compounds that were successfully bound to MCM-41 in this work.

All chosen aromatic compounds feature the possibility to be modified in a second post-synthesis reaction via various reaction pathways. MCM-41_BDMA, for example, can be converted to the corresponding aldehyde, which offers numerous options for further modifications.

For all synthesized inorganic-organic hybrid materials (MCM-41_Arene), $^{13}$C and $^{29}$Si ssNMR studies were performed to confirm the covalent attachment of the respective aromatic compounds. All modified materials show $T_2/T_3$ species in the $^{29}$Si ssNMR spectra corresponding to mono-functionalized silica atoms within the framework. The attachment of *tert*-butyl fragments to the mesoporous material can be excluded for all compounds, as none of the $^{13}$C ssNMR spectra (cf. appendix, Figure 9.13 for MCM-41_ArNMe₂, Figure 9.14 for MCM-41_Thiophene and Figure 9.15 for MCM-41_ArCH₂Cl) show the typical signals of the *tert*-butyl group. This is a significant improvement compared to the previously described method, as solely the aromatic system reacts with the framework. All materials were characterized with nitrogen sorption and thermogravimetric analysis. The key features of the resulting inorganic-organic hybrid materials obtained with these methods are summarized in Table 9.1. All functionalized materials exhibit a type IV isotherm typical for mesoporous materials (cf. appendix 9.16) and possess high specific surface areas and a well-defined pore size distribution (cf. appendix 9.17).

**Table 9.1:** Key features of organically functionalized mesoporous MCM-41 obtained by nitrogen adsorption measurements and thermogravimetric analysis.

| Sample | BET surface area [m²/g] | Pore size[a] [nm] | Relative mass loss[b] [%] |
|---|---|---|---|
| MCM-41 | 962 | 3.4 | 3 |
| MCM-41_ArOMe | 670 | 2.8 | 20 |
| MCM-41_BDMA | 763 | 2.9 | 21 |
| MCM-41_Thiophene | 730 | 3.0 | 14 |
| MCM-41_ArNMe$_2$ | 565 | 2.9 | 12 |
| MCM-41_ArCH$_2$Cl | 724 | 3.0 | 18 |

[a]DFT pore size refers to the peak value of the pore size distribution. [b]Relative mass loss obtained from TGA analysis. All samples were normalized to 100% at 75 °C (cf. appendix 9.18).

The expected decrease of the specific surface area and the pore size after the post-synthesis modification can be explained with the steric requirements of the organic moieties attached within the mesopores. We note that the decrease of the BET area is more prominent for MCM-41_ArNMe$_2$.

The typical 2D hexagonal array of the pore channels of the MCM-41 material was retained under the applied synthesis conditions. This was demonstrated by TEM measurements (cf. appendix 9.19 for template-free MCM-41, 9.20 for MCM-41_ArOMe and 9.21 for MCM-41_BDMA). Moreover, all small angle diffractograms of the organo-functionalized MCM-41 compounds show the typical 100 reflection at 2.3° 2θ (cf. appendix 9.22), suggesting that the mesostructure is preserved.

## 9.3 Conclusion

In this study, the nature of the lithiating agent used for the generation of reactive arene intermediates for the functionalization of mesoporous silica was optimized in order to eliminate undesired alkylation of the pore surface. We show that the lithiation of para-bromo arenes with tert-butyllithium is highly favorable compared to the lithiation with n-butyllithium. As a result, alkyl signals resulting from attached n-butyl groups disappear entirely from the corresponding $^{13}$C MAS ssNMR spectra in all reactions, and only the characteristic peaks of the employed aromatic moieties are visible. Following this route, we were able to introduce several different

functionalities into the mesoporous framework of MCM-41, showing the generality of the approach. All functionalities are directly attached to the surface silicon atoms through an aromatic ring system (in contrast to classical organo-silane grafting reagents bearing the functional groups). All the aromatic systems presented here offer the possibility for further chemical modifications, thus opening up numerous possibilities for chemical functionalization. In addition, the mild reaction conditions at low temperatures and the short reaction times of the organo-functionalizations are of great advantage as they prevent degradation of most organic compounds. Moreover, this functionalization strategy can be generalized to other mesoporous host systems such as SBA-15 or even colloidal mesoporous silica nanoparticles with different pore sizes. In conclusion, the direct modification of mesoporous hosts with various aromatic molecules was demonstrated to be fast and highly efficient, offering an attractive variety of post-synthesis modifications for mesoporous materials for future applications.

## 9.4   Experimental

**Materials.** Tetraethyl orthosilicate (TEOS, Fluka, >98%), cetyltrimethylammonium bromide (CTAB, Aldrich, 95%), aqueous ammonia (25 w%, Fluka), n-butyllithium (nBuLi, Aldrich, obtained as 1.7 M solution in pentane), *tert*-butyllithium (tBuLi, Aldrich, obtained as 1.7 M solution in pentane), 1-bromo-4-(chloromethyl)benzene (Br-ArCH$_2$Cl, Aldrich, >97%), 4-bromobenzaldehyde dimethylacetal (Br-BDMA, Aldrich, 98%), 2-bromothiophene (Aldrich, 98%), 4-bromoanisole (Br-ArOMe, Aldrich, >99%), 4-bromo-N,N-dimethylaniline (Br-ArNMe$_2$, Aldrich, 97%), sodium azide (Aldrich, 99%), methanol (MeOH, Fluka, >99%), diethyl ether (Et$_2$O, ), dichloromethane (Acros, >99%), absolute ethanol (EtOH, Aldrich, >99.5%), n-hexane (anhydrous, Sigma, >95% ).

Unless otherwise noted, all reagents were used without further purification. Bi-distilled water from a Millipore system (Milli-Q Academic A10) was used for syntheses and purification steps.

**Experimental procedures**

**Synthesis of mesoporous MCM-41.** MCM-41 was synthesized according to a procedure published by Kumar *et al.*[1] We employed the four-fold reaction scale of the original recipe, which is easily scalable. Absolute EtOH (50 g), aqueous ammonia (25 w%, 40 mL) and CTAB

(9.56 g, 26.3 mmol) were dissolved in water (450 mL) in a 500 mL polypropylene reactor under continuous stirring. Subsequently, tetraethyl orthosilicate (40 g, 192 mmol) was added drop-wise to the stirred template solution. Afterwards, the reaction mixture was stirred at room temperature for 2 h at 500 rpm. The white precipitate was filtered off, washed with EtOH until the filtrate was ammonia free (neutral pH-value). The obtained colorless powder was dried at 60 °C in air for 16 h. The template was removed via calcination in air, using a ramping profile with a heating rate of 1 °C min$^{-1}$ up to a temperature of 550 °C. The temperature was kept for 5 h.

**Preparation of MCM-41 for post-synthesis functionalization with lithiated organo compounds.** For each reaction, 500 mg template-free MCM-41 in a 50 mL Schlenk-flask was dried at 150 °C *in vacuo* for 6 h. Afterwards, the mesoporous material was allowed to cool to ambient temperature before Et$_2$O (anhydrous, 20 mL) was added. The suspension was cooled to -78 °C under continuous stirring.

**Temperature dependent reaction of nBuLi with MCM-41.** Three batches of 500 mg dried MCM-41 each were suspended in anhydrous n-hexane (20 mL) cooled to the desired temperature under continuous stirring (-78 °C, -20 °C and ambient temperature). nBuLi (1.6 mL, 2.5 mmol) was added drop-wise to the suspension and the reaction mixture was stirred for 4 h at the given temperature in a 50 mL Schlenk-flask. Afterwards, the reaction mixture was quenched with EtOH and water (10 mL each) and filtered off. The obtained white powders were subsequently washed with methanol (30 mL), water (50 mL) and methanol (30 mL) and dried at 60 °C in air.

**Lithiation of 4-bromoanisole (or 4-bromobenzaldehyde dimethylacetal, respectively) with nBuLi and subsequent reaction with MCM-41 (yielding sample MCM-41_ArOMe or MCM-41_BDMA respectively)**

The respective 4-bromoarene (4-bromoanisole or 4-bromobenzaldehyde dimethylacetal, respectively) was dissolved in anhydrous Et$_2$O (10 mL) and cooled to -78 °C under continuous stirring. nBuLi (2.5 mmol, 0.8 eq) was added drop-wise and the reaction mixture was stirred for 30 min at -78 °C, before it was transferred to the Schlenk-flask (50 mL) containing MCM-41. The *in situ* generated Ar-Li compound was added drop-wise to the stirred suspension of MCM-41 at -78 °C. The resulting reaction mixture was stirred at -78 °C for 10 minutes and was then allowed to warm to ambient temperature and was stirred for another 4 h. Afterwards

the reaction mixture was quenched with water (10 mL) and filtered off. The obtained yellowish powder was subsequently washed with methanol (30 mL), water (50 mL) and methanol (30 mL) and dried at 60 °C in air.

**Lithiation of different 4-bromoarenes with tBuLi (yielding samples MCM-41_Arene)**

All reactions were performed according to this synthesis protocol unless otherwise noted.

The respective 4-bromo compound (2.5 mmol, 1 eq) was dissolved in anhydrous $Et_2O$ (10 mL) and cooled to -78 °C under continuous stirring. tBuLi (5 mmol, 2 eq) was added drop-wise and the reaction mixture was stirred for 10 min at -78 °C before the cryo-bath was removed. The reaction mixture was allowed to warm up for a period of 20 min before it was transferred to the flask containing MCM-41.

**Reaction of lithiated arenes (Ar-Li) with MCM-41.** The *in situ* generated Ar-Li compound was added drop-wise to the stirred suspension of MCM-41 at -78 °C. The resulting reaction mixture was stirred at -78 °C for 10 minutes and was then allowed to warm to ambient temperature and was stirred for another 4 h. Afterwards the reaction mixture was quenched with water (10 mL) and filtered off. The obtained yellowish powder was subsequently washed with methanol (30 mL), water (50 mL) and methanol (30 mL) and dried at 60 °C in air.

**Purification of the MCM-41_Arene compounds.** The obtained MCM-41_Arene samples were extracted with dichloromethane (70 mL) employing a soxhlet apparatus (50 °C, 3 h), under reflux conditions. After purification, the powder was dried at 60 °C over night and was used for subsequent characterization.

**Characterization.** Nitrogen sorption measurements were performed with a Quantachrome NOVA 4000e. Sample out-gassing was performed at 120 °C for 12 h at a pressure of 10 mTorr. Pore size and pore volume were calculated using a NLDFT equilibrium model for cylindrical pores of $N_2$ on silica, based on the desorption branch of the isotherm. The Brunauer-Emmett-Teller (BET) surface areas for all samples were calculated from the corresponding nitrogen sorption isotherms in the range of $p/p_0 = 0.05 - 0.2$. To calculate the total pore volume, the amount of adsorbed nitrogen at the apparent plateau of the isotherm at high $p/p_0$ values was used. Transmission electron microscopy (TEM) was performed on a FEI Titan 80-300 kV

microscope operating at 300 kV. Samples were prepared by dispersing 0.5 mg sample in 2 mL absolute ethanol. A drop of the resulting diluted suspension was dried on a carbon-coated copper grid. Thermogravimetric analysis was performed on a Netzsch STA 440 C TG/DSC instrument with a heating rate of 10 K/min in a stream of synthetic air of about 25 mL/min.

## 9.5 Appendix
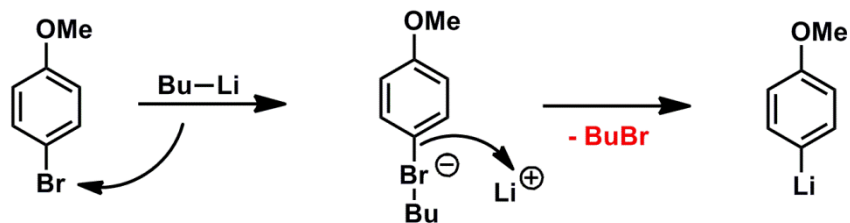


**Figure 9.6:** Possible generation of butylbromide (BuBr) from 4-bromoanisole upon lithiation. This reaction is possible for all arenes employed in this work.
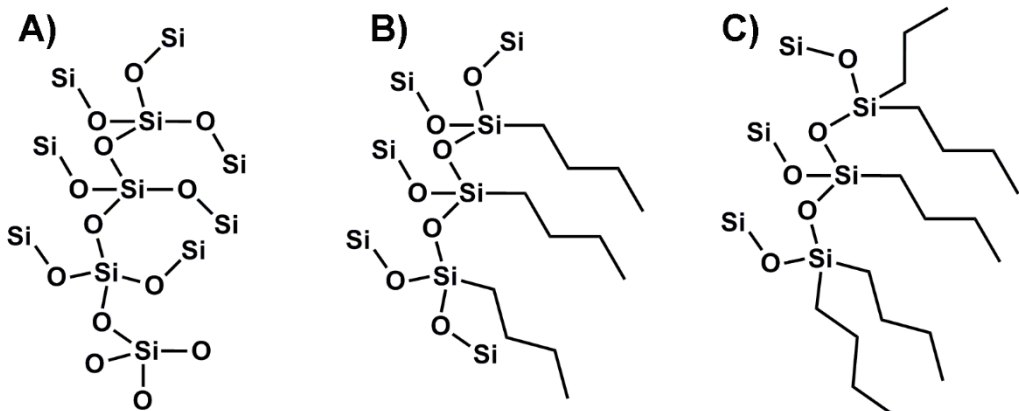


**Figure 9.7:** Possible degrees of organo-functionalization of the silica framework (fragment, schematic). A) Mesoporous silica framework without functionalization, B) monofunctionalized silica species, and C) mono and bi-functionalized silica framework.
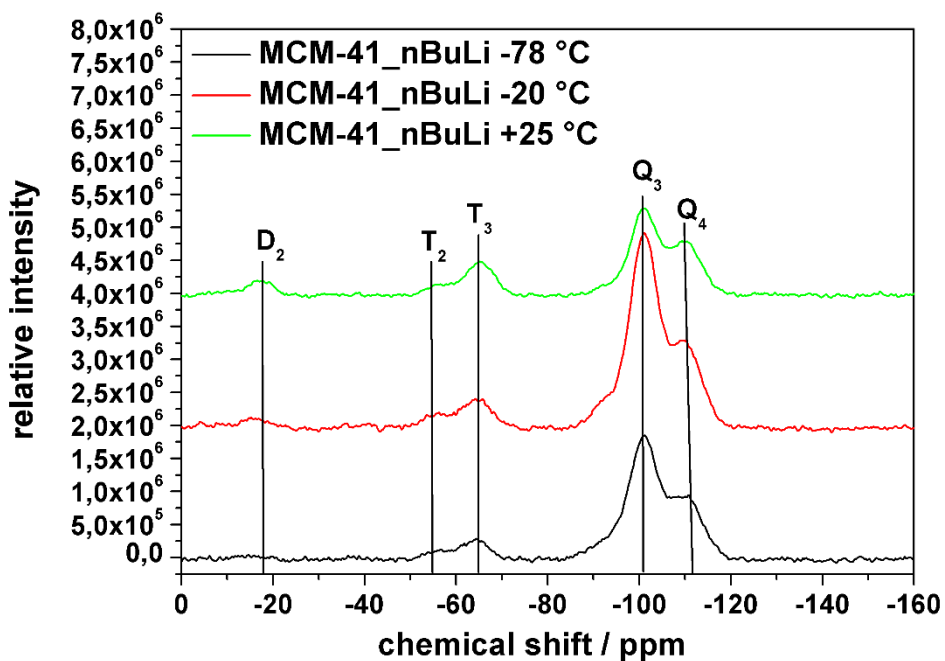
**Figure 9.8:** $^{29}$Si ssNMR of the temperature dependent reaction of MCM-41 with nBuLi at -78 °C (black), -20 °C (red) and at ambient temperature (green).

Figure 9.8 shows the effect of different synthesis temperatures on the reaction of MCM-41 with n-butyllithium (nBuLi). When MCM-41 is reacted with nBuLi at -78 °C, only mono-functionalization of the silica framework is observed ($T_2/T_3$ peaks in Figure 9.8). Higher temperatures (-20 °C and ambient temperature) lead to additional bi-functionalization of the silicon atoms, which is indicated by the increasing $D_2$ peak. The patterns visible in Figure 9.8 correspond to the above-mentioned silica species A, B, C shown in Figure 9.7. The $Q_3/Q_4$ ($\delta$ = -101 and -110 ppm) peaks are typical for non-functionalized, highly condensed silica material, whereas $T_2/T_3$ ($\delta$ = - 5 and -65 ppm) correspond to silica species B, and the $D_2$ peak ($\delta$ = -18 ppm) to species C. The $^{29}$Si ssNMR spectra demonstrate the importance of the reaction temperature for the synthesis of the inorganic-organic hybrid materials.
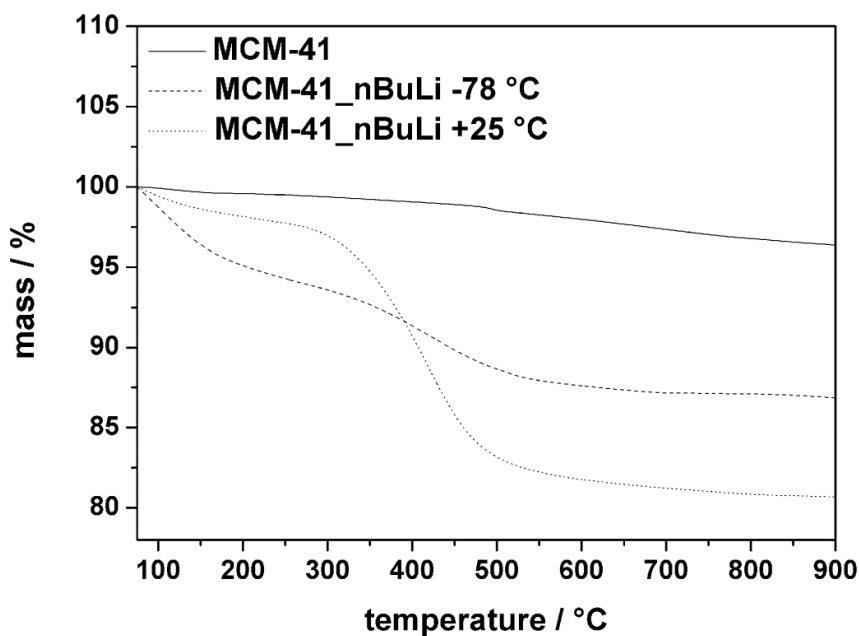
**Figure 9.9:** Thermogravimetric analysis data of MCM-41 (black line), MCM-41_nBuLi synthesized at -78 °C (dashed line) and MCM-41_nBuLi synthesized at 25 °C (dotted line). The mass was normalized to 100% at 75 °C for all three samples.

The above $^{29}$Si ssNMR results are in agreement the thermogravimetric analysis data (Figure 9.9), showing a distinctly higher mass loss for the sample reacted at ambient temperature (dotted curve, mass loss 19%), indicating a much higher degree of organic functionalization. The reaction at -78 °C (solid black curve, mass loss 4%) shows no $D_2$ peak in the NMR spectrum.

**Reaction of lithiated 4-bromoarenes (Ar-Li species generated with tBuLi) with MCM-41**
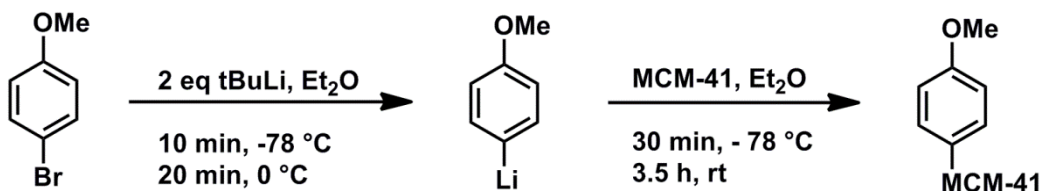


**Figure 9.10:** Reaction of 4-bromoanisole with 2 eq tBuLi and subsequent reaction of the lithiated compound with MCM-41.

The above reaction parameters were employed for all 4-bromo arenes investigated in this work. The detailed synthesis procedure for the reactions is given in the experimental section.

**$^{13}$C and $^{29}$Si solid state NMR (ssNMR) data of organo-functionalized MCM-41 materials**
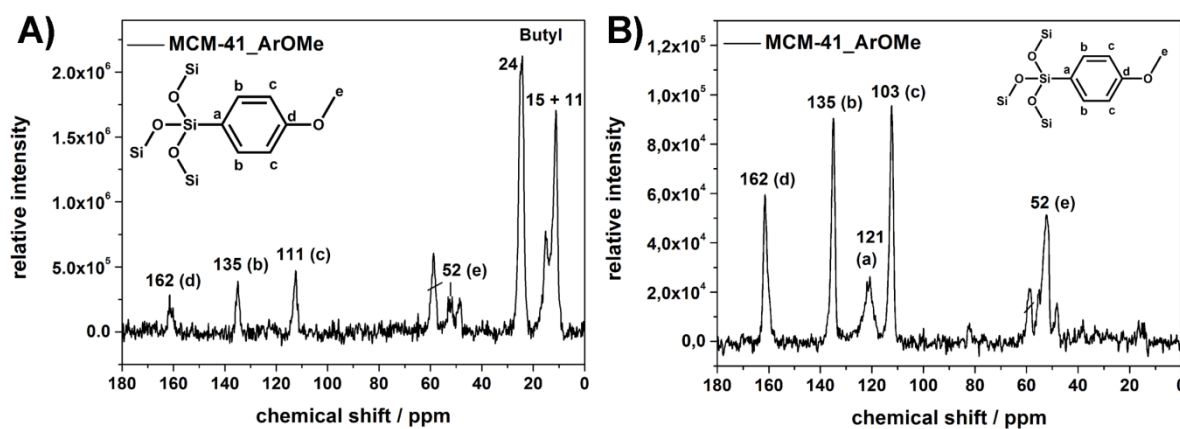


**Figure 9.11:** Comparison of $^{13}$C ssNMR data of MCM-41_ArOMe generated by different lithiation approaches for 4-bromoanisole. **A)** Reaction of MCM-41 with 4-lithioanisole, (Ar-Li generated by nBuLi), and **B)** reaction of MCM-41 with 4-lithioanisole, generated with 2 eq tBuLi according to Figure 9.10. The peak at $\delta = 60$ ppm can be attributed to dichloromethane from Soxhlet extraction.

When 4-bromoansiole is lithiated with nBuLi and subsequently reacted with template-free MCM-41, the surface-bound butyl-fragments are clearly visible with high intensity in the obtained $^{13}$C ssNMR (Figure 9.11A, $\delta = 11, 15, 25$ ppm). Additionally, we note that the intensity at $\delta = 48$ ppm (derived from the reaction of butylbromide with the silanol oxygen of MCM-41 in a nucleophilic substitution, $S_N2$) is significantly lower than in the case of MCM-41_BDMA (Figure 9.3B) suggesting that less butylbromide was generated during the reaction.

Nonetheless, surface-bound butyl-moieties were present in all synthesized samples when the arene was lithiated with nBuLi. In comparison, the reaction of 4-bromoanisole with 2 eq tBuLi does not show the above-mentioned butyl-based peaks. Only the signals of the aromatic compounds are visible in the spectrum (Figure 9.11B), confirming that only the arene was successfully attached to MCM-41.
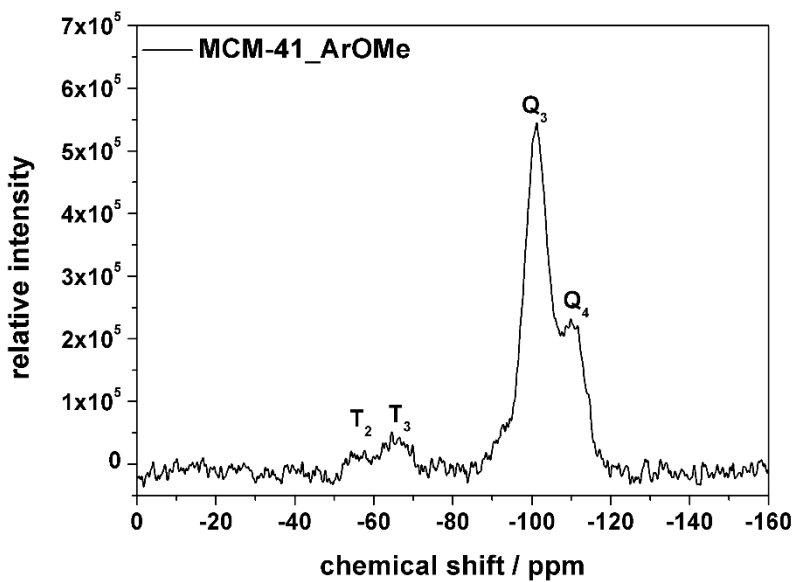
**Figure 9.12:** $^{29}$Si ssNMR of MCM-41_ArOMe, Ar-Li generated by lithiation of 4-bromoanisole with tBuLi.

Both silica-based species – $Q_3/Q_4$ ($\delta$ = -101 and -110 ppm – corresponding to the silica species A in Figure 9.7) and $T_2/T_3$ ($\delta$ = -55 and -65 ppm - corresponding to silica species B in Figure 9.7) were observed in the $^{29}$Si ssNMR spectra of the inorganic-organic hybrid materials (Figure 9.3D for MCM-41_BDMA and Figure 9.12 for MCM-41_ArOMe). Bi-functional silica species indicated by $D_2$ (species C in Figure 9.7) are not present in any of the synthesized MCM-41_Aryl samples.
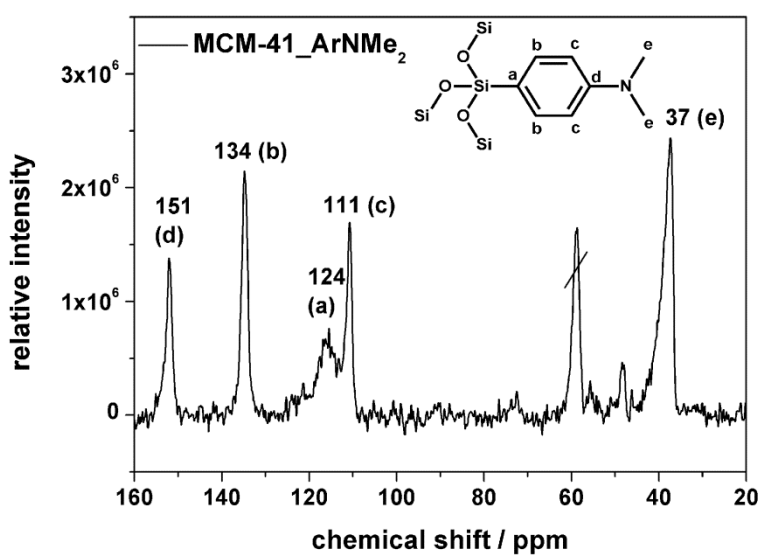
**Figure 9.13:** $^{13}C$ ssNMR of MCM-41_ArNMe₂, Ar-Li species generated with tBuLi.
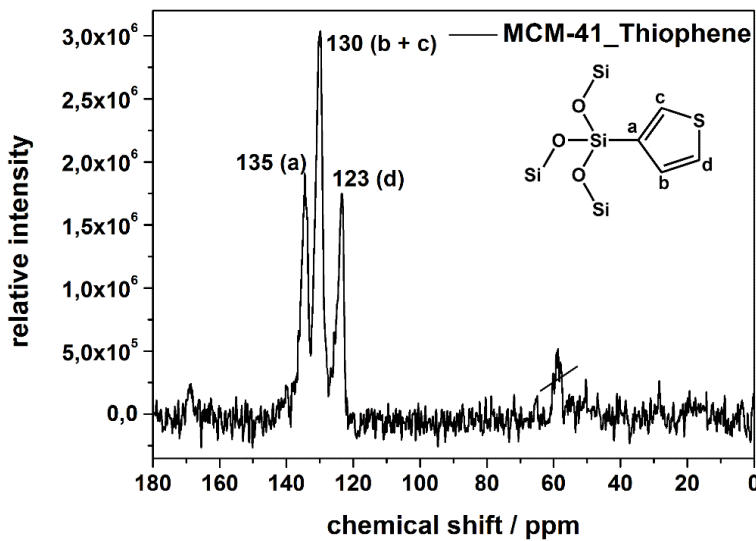


**Figure 9.14:** $^{13}C$ ssNMR of MCM-41_Thiophene, Ar-Li species generated with tBuLi.
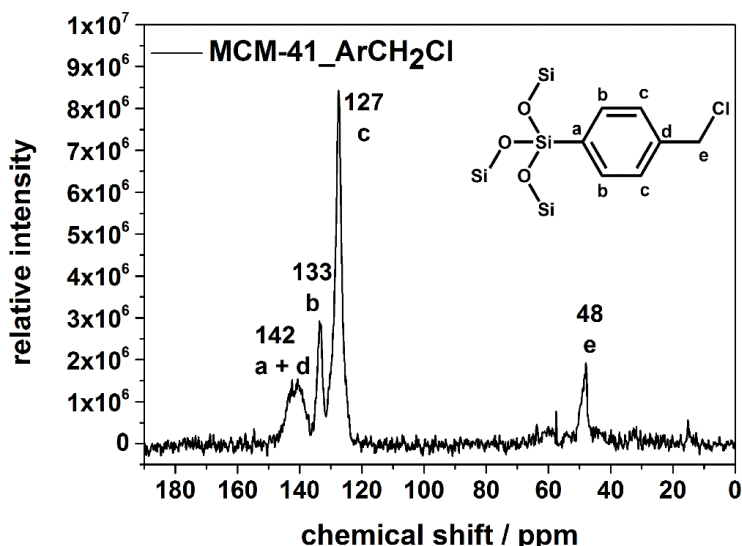
**Figure 9.15:** $^{13}C$ ssNMR of MCM-41_ArCH$_2$Cl generated with tBuLi.

## Nitrogen sorption measurements

Nitrogen sorption measurements were performed on a Quantachrome Instruments NOVA 4000e. All six samples (15 mg each) were heated to 120 °C for 12 h *in vacuo* (10 mTorr) to outgas the samples before nitrogen sorption was measured at liquid nitrogen temperature. For the calculation of pore sizes and pore volumes, a non-local density functional theory (NLDFT) equilibrium model of nitrogen on silica was used. A summary of the obtained values for BET area and pore size distribution of the synthesized materials is given in Table 9.1. All organo-functionalized MCM-41 samples exhibit a type IV isotherm typical for mesoporous materials with high surface areas, which are summarized in Table 9.1 of the main text.
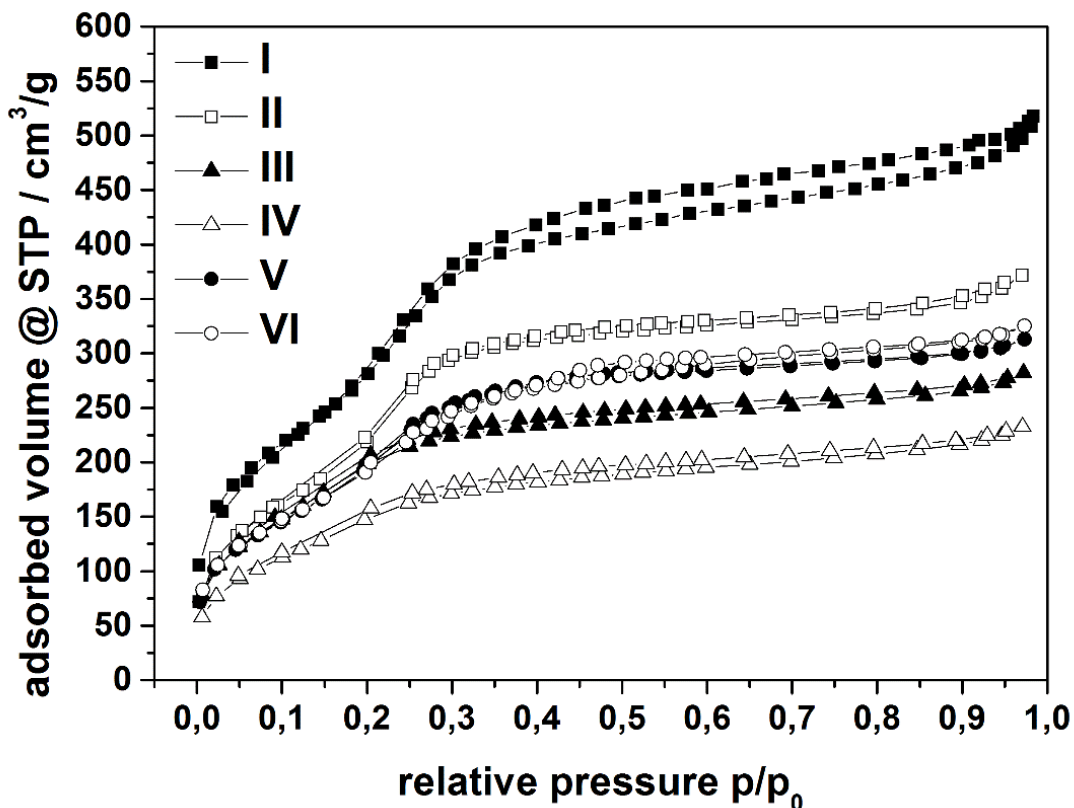
**Figure 9.16:** Nitrogen sorption isotherms of the samples MCM-41 (**I**, filled squares), MCM-41_ArOMe (**II**, empty squares), MCM-41_BDMA (**III**, filled triangles), MCM-41_ArNMe$_2$ (**IV**, empty triangles), MCM-41_Thiophene (**V**, filled circles) and MCM-41_ArCH$_2$Cl (**VI**, empty circles).

Pore size distributions calculated from the nitrogen sorption data of the organic-inorganic hybrid materials (Figure 9.17). All MCM-41_Arene samples exhibit a narrow pore size distribution with an average pore size of around 2.9 nm depending on the immobilized aromatic system. The exact values are given in Table 9.1 of the main text.
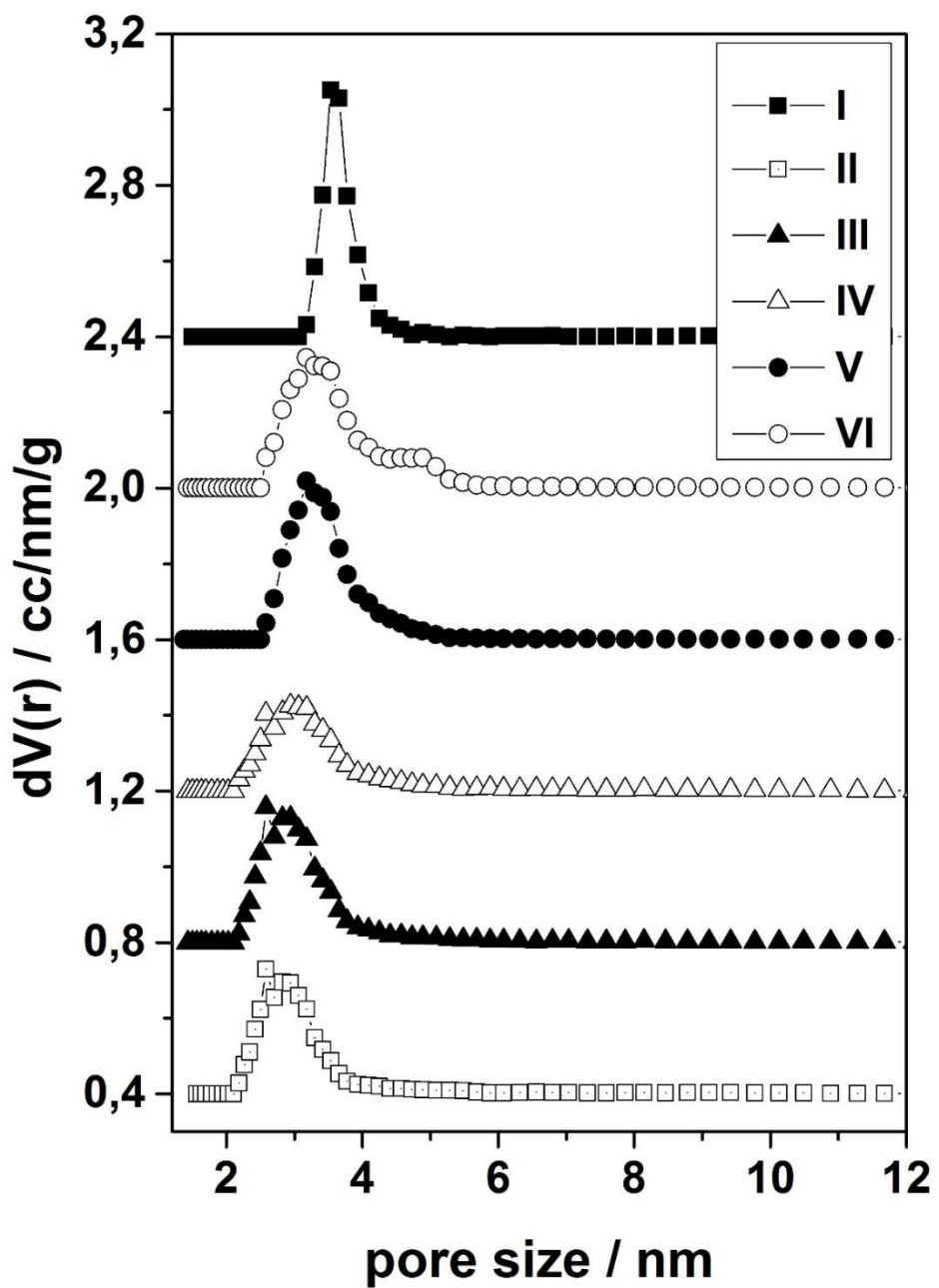
**Figure 9.17:** Pore size distributions of the samples MCM-41 (**I**, filled squares), MCM-41_ArOMe (**II**, empty squares), MCM-41_BDMA (**III**, filled up triangles), MCM-41_ArNMe$_2$ (**IV**, empty up triangles), MCM-41_Thiophene (**V**, filled circles) and MCM-41_ArCH$_2$Cl (**VI**, empty circles). For clarity reasons, all curves are shifted along the y-axis by a value of 0.4 each. MCM-41 was scaled by multiplying the data with a value of 0.5.
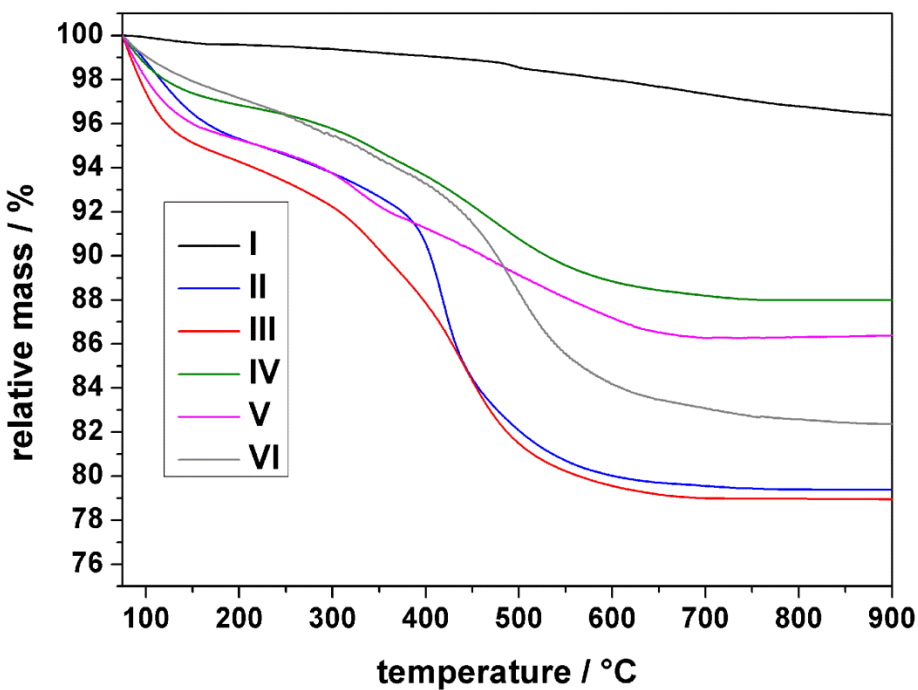
**Figure 9.18:** Thermogravimetric analysis data of the samples MCM-41 (**I**, black curve) MCM-41_ArOMe (**II**, blue curve), MCM-41_BDMA (**III**, red curve), MCM-41_ArNMe$_2$ (**IV**, green curve), MCM-41_Thiophene (**V**, pink curve) and MCM-41_ArCH$_2$Cl (**VI**, grey curve). The mass was normalized to 100% at 75 °C for all six samples.

**Transmission electron microscopy of the synthesized materials**

All samples were investigated with an FEI Titan 80-300 transmission electron microscope operating at 300 kV with a high-angle annular dark field detector. A droplet of the diluted MCM-41 suspension in absolute ethanol was dried on a carbon-coated copper grid.

The TEM micrograph in Figure 9.19 shows template-extracted mesporous MCM-41, whereas the images in Figure 9.20 and 9.21 show examples of organo-functionalized MCM-41 synthesized with 2 eq tBuLi (MCM-41_BDMA and MCM-41_ArOMe, respectively). The images indicate that the mesostructure was not significantly affected by the post-synthesis modification.
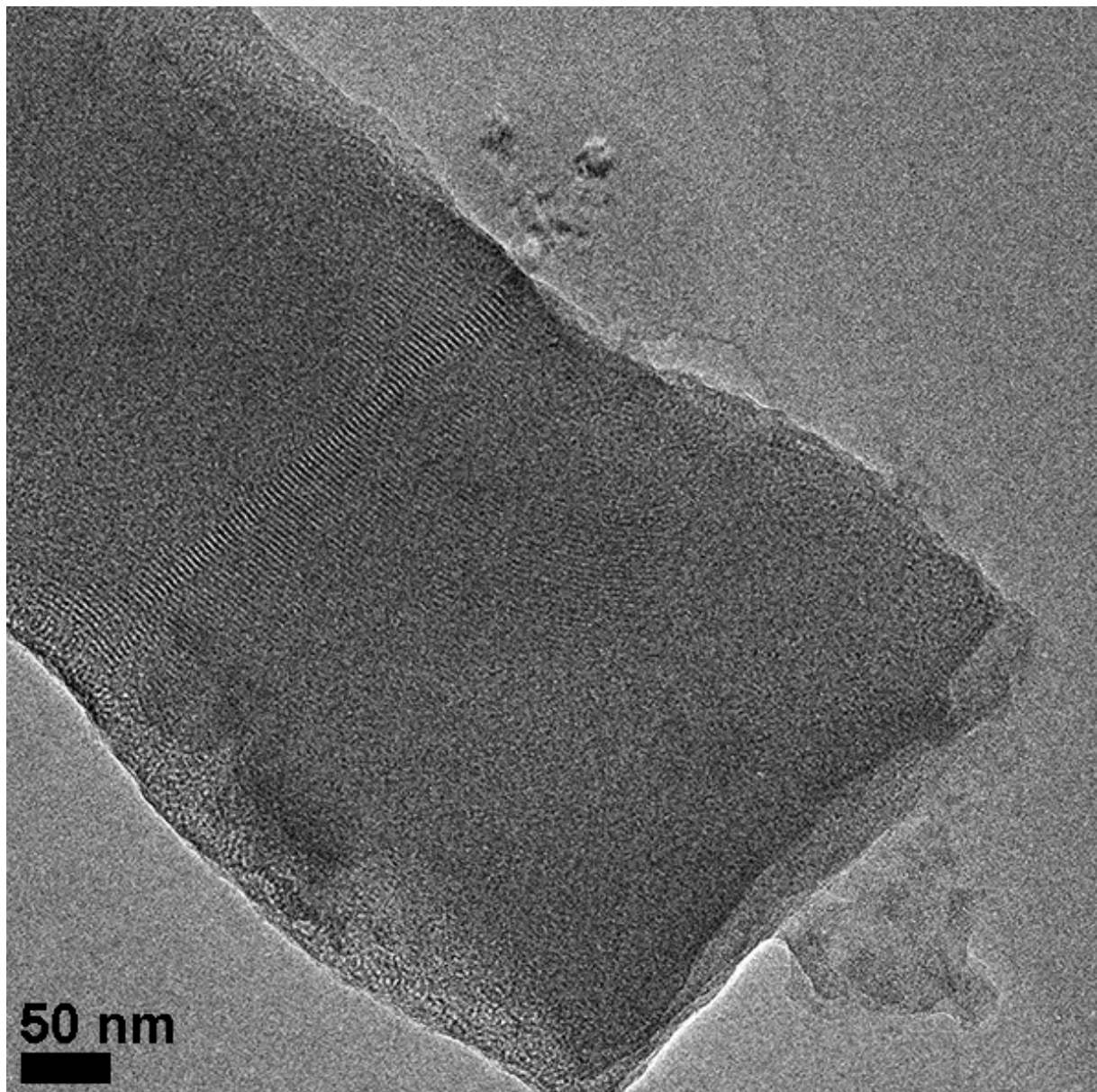
**Figure 9.19:** TEM micrograph of template-free MCM-41.
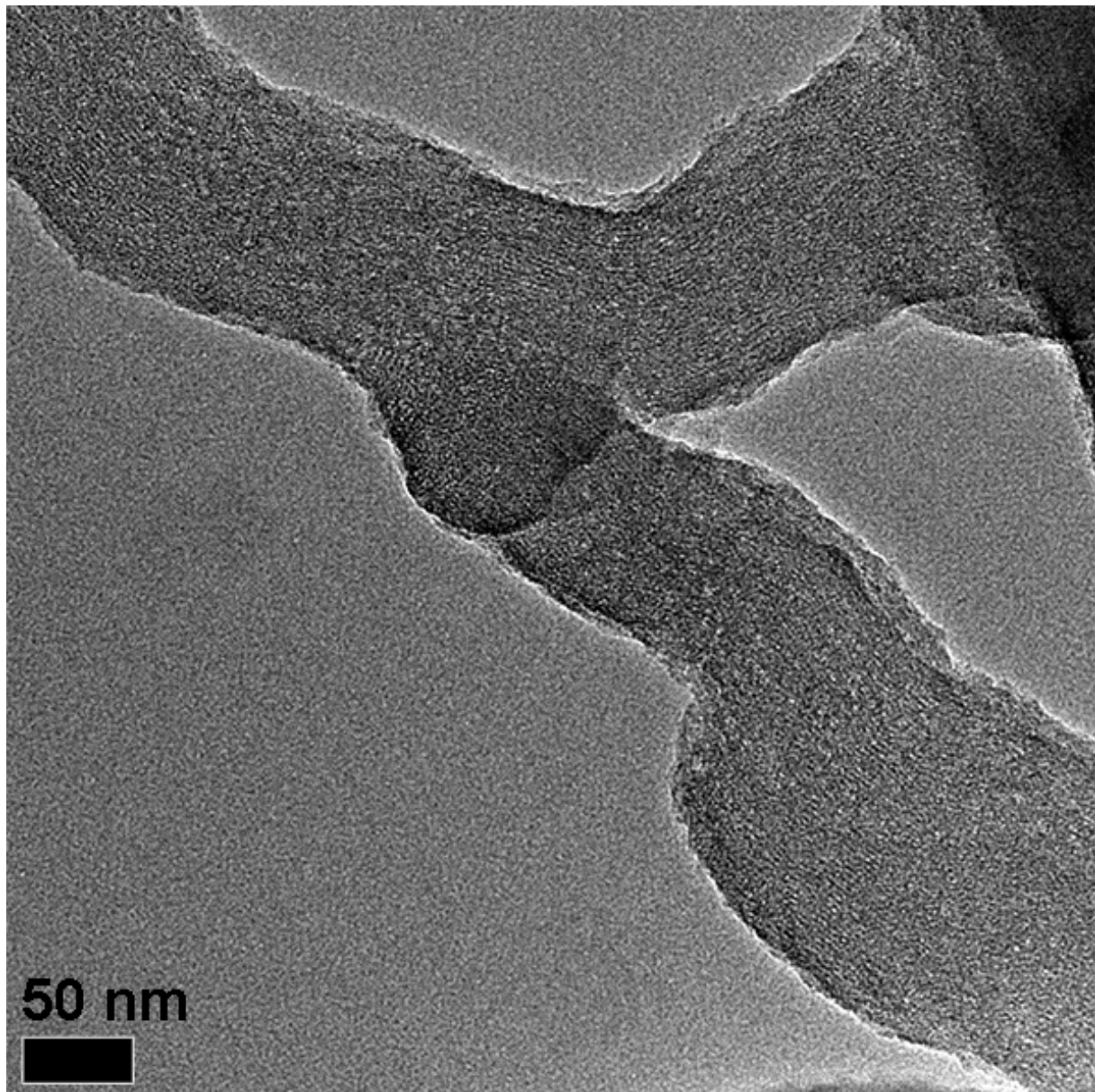
**Figure 9.20:** TEM micrograph of MCM-41_BDMA synthesized with 2 eq tBuLi.
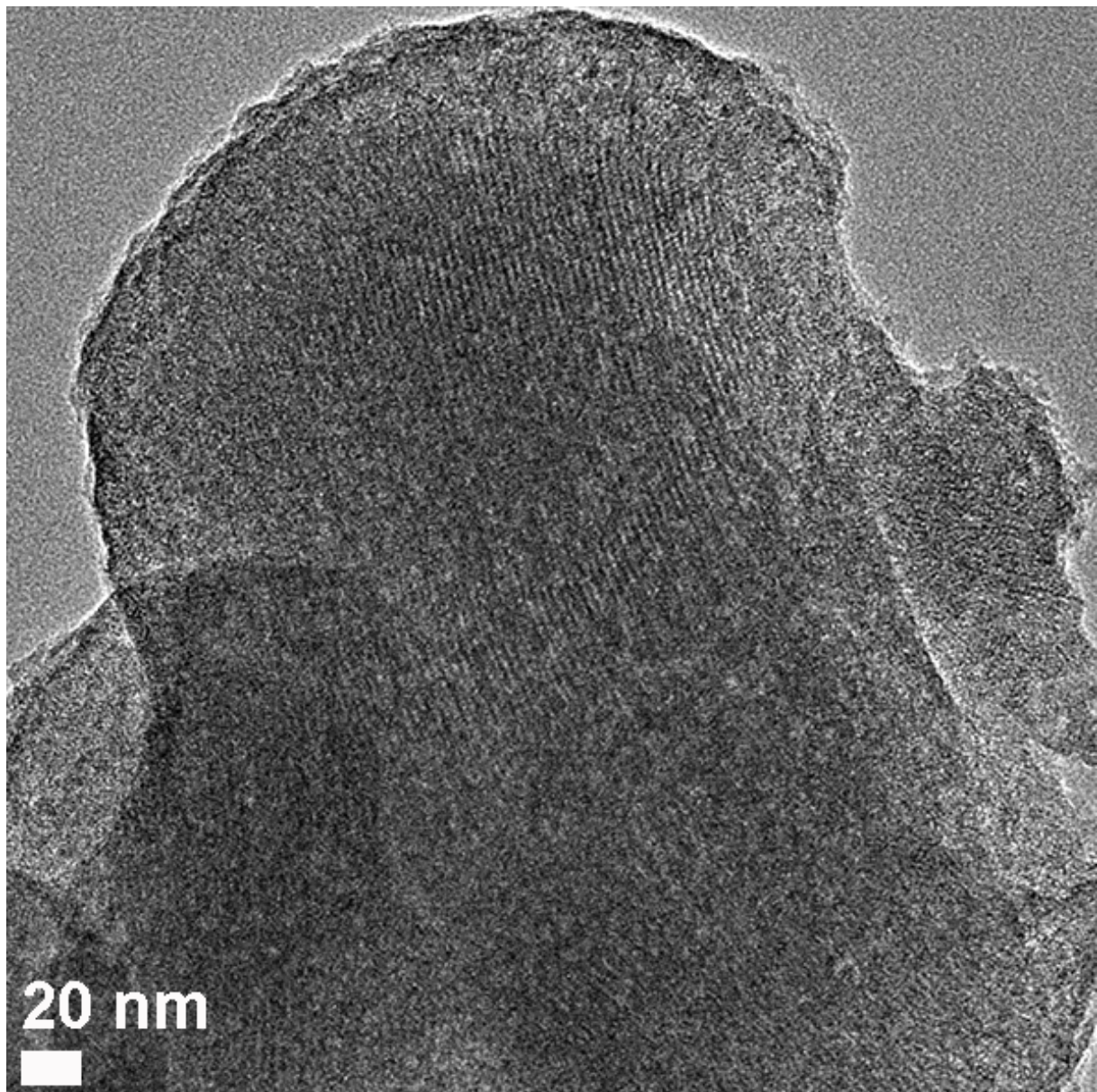
**Figure 9.21:** TEM micrograph of MCM-41_ArOMe synthesized with 2 eq tBuLi.
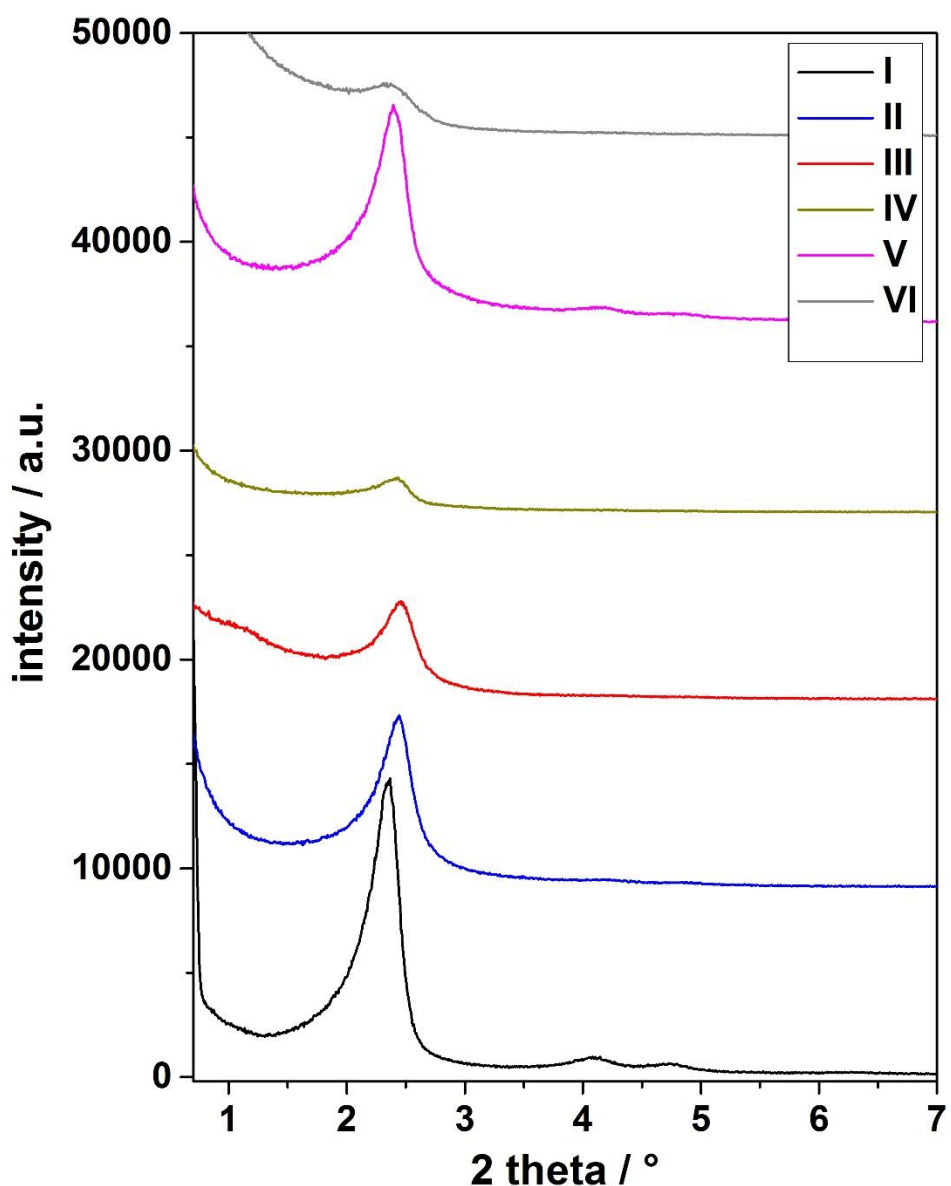
**Figure 9.22:** SAXS data of the samples MCM-41 (**I**, black curve) MCM-41_ArOMe (**II**, blue curve), MCM-41_BDMA (**III**, red curve), MCM-41_ArNMe$_2$ (**IV**, green curve), MCM-41_Thiophene (**V**, pink curve) and MCM-41_ArCH$_2$Cl (**VI**, grey curve). The curves are shifted by a value of 9.000 along the y-axis..

## 9.6   References

1.  Beck, J. S.; Vartuli, J. C.; Roth, W. J.; Leonowicz, M. E.; Kresge, C. T.; Schmitt, K. D.; Chu, C. T. W.; Olson, D. H.; Sheppard, E. W. *J. Am. Chem. Soc.* **1992,** *114*, 10834-10843.

2.  Kresge, C. T.; Leonowicz, M. E.; Roth, W. J.; Vartuli, J. C.; Beck, J. S. *Nature* **1992,** *359*, 710-712.

3.  Hudson, S.; Cooney, J.; Hodnett, B. K.; Magner, E. *Chem. Mater.* **2007,** *19*, 2049-2055.

4.  Engström, K.; Johnston, E. V.; Verho, O.; Gustafson, K. P. J.; Shakeri, M.; Tai, C.-W.; Bäckvall, J.-E. *Angew. Chem. Int. Ed.* **2013,** *52*, 14006-14010.

5.  Wagner, T.; Haffer, S.; Weinberger, C.; Klaus, D.; Tiemann, M. *Chem. Soc. Rev.* **2013,** *42*, 4036-4053.

6.  Ashley, C. E.; Carnes, E. C.; Phillips, G. K.; Padilla, D.; Durfee, P. N.; Brown, P. A.; Hanna, T. N.; Liu, J.; Phillips, B.; Carter, M. B.; Carroll, N. J.; Jiang, X.; Dunphy, D. R.; Willman, C. L.; Petsev, D. N.; Evans, D. G.; Parikh, A. N.; Chackerian, B.; Wharton, W.; Peabody, D. S.; Brinker, C. J. *Nat. Mater.* **2011,** *10*, 389-97.

7.  Li, Z.; Barnes, J. C.; Bosoy, A.; Stoddart, J. F.; Zink, J. I. *Chem. Soc. Rev.* **2012,** *41*, 2590-2605.

8.  Mackowiak, S. A.; Schmidt, A.; Weiss, V.; Argyo, C.; von Schirnding, C.; Bein, T.; Bräuchle, C. *Nano Lett.* **2013,** *13*, 2576-83.

9.  Das, P.; Silva, A.; Carvalho, A.; Pires, J.; Freire, C. *J. Mater. Sci.* **2009,** *44*, 2865-2875.

10. Yang, H.; Zhang, G.; Hong, X.; Zhu, Y. *J. Mol. Catal. A: Chem.* **2004,** *210*, 143-148.

11. Bruhwiler, D. *Nanoscale* **2010,** *2*, 887-892.

12. Lim, J. E.; Shim, C. B.; Kim, J. M.; Lee, B. Y.; Yie, J. E. *Angew. Chem. Int. Ed.* **2004,** *43*, 3839-3842.

13. Angloher, S.; Bein, T. *J. Mater. Chem.* **2006,** *16*, 3629-3634.

14. Angloher, S.; Kecht, J.; Bein, T. *J. Mater. Chem.* **2008,** *18*, 3103-3108.

15. Angloher, S.; Kecht, J.; Bein, T. *Microporous Mesoporous Mater.* **2008,** *115*, 629-633.

16. Liang, Y.; Erichsen, E. S.; Anwander, R. *Microporous Mesoporous Mater.* **2014,** *190*, 316-323.

17. Kumar, D.; Schumacher, K.; du Fresne von Hohenesche, C.; Grün, M.; Unger, K. K. *Colloids Surf., A* **2001,** *187–188*, 109-116.

18. Pampillón, C.; Mendoza, O.; Sweeney, N. J.; Strohfeldt, K.; Tacke, M. *Polyhedron* **2006,** *25*, 2101-2108.

# 10 Conclusion and Outlook

The focus of the present work was the synthesis and characterization of custom-made colloidal multifunctional mesoporous silica nanoparticles (MSNs) for advanced drug delivery applications and the generation of novel silica materials. The functionalized, stimuli-responsive nano-carriers developed in this work meet various requirements for controlled cargo delivery in targeted cancer diagnosis and therapy.

In a first project (chapter 3), a fluorimetric reporter system based on colloidal mesoporous silica nanoparticles (MSNs) was developed. The MSNs were modified with a blue-light sensitive photosensitizer, protoporphyrin IX (PpIX) and capped with a DOPC-based supported lipid bilayer (SLB). In this study, photochemical internalization (PCI) with an on-board photosensitizer and the redox-labile disulfide-bridge approach (of a corresponding dye-quencher system) was combined to create highly potent multifunctional MSNs acting as fluorimetric reporters. The photosensitizer allows escaping the endosomal entrapment through the formation of highly reactive singlet oxygen, which is followed by the subsequent disintegration of both membranes in a cascaded manner. Endosomal uptake of the SLB-capped MSNs and individual endosome lysis events were studied in three different cell lines (fibroblast, normal and carcinoma cell lines). The release-on-demand system resulted in more broadly distributed lysis times than expected, particularly for Renca, a renal carcinoma cell line. An analysis of the nanoparticle load per endosome, endosome size and uptake characteristics indicated that Renca cells not only take up a lower amount of MSNs in comparison with the fibroblast cells, but also have larger endosomes, and a lower nanoparticle load per endosome. An existing stochastic pi calculus model for intracellular gold nanoparticle distribution was extended to our reporter-system, enabling one to understand how different factors (e.g., PpIX load per NP) affect the distributions. Model results indicated that the lysis time distribution is primarily determined by the minimum net PpIX required to burst an endosome, a factor influenced by the NP load per endosome, as well as the endosome size. Future work could involve the subsequent modification of the SLB@MSN system with different lipid compositions or the insertion of pH-sensitive membrane destabilization proteins.

In chapter 4, the synthesis of uniform spherical multifunctional core-shell MSNs with sizes of 70 nm and pores of 5 nm (25% higher value compared to more standard MSNs) is described. In order to further improve the drug delivery system based on mesoporous silica nanoparticles, PEGylated MSNs with an on-board phthalocyanine-based photosensitizer (AlPcS$_{2a}$) were synthesized, the latter being excitable with red light near the therapeutic window. The

photosensitizer triggers endosomal release and enables efficient intracellular drug delivery. The use of red light provides good biocompatibility and allows for a deeper penetration into tissues, which is highly favorable in comparison to other approaches. Supported lipid bilayers (consisting of DOPC and DOTAP) coating the MSNs (SLB@MSNs) were obtained by solvent-induced self-assembly. Additionally, two different targeting ligands, folic acid (FA) and epidermal growth factor (EGF), were inserted via diffusion into the SLB@MSNs. These targeting ligands were chosen because their receptors are commonly overexpressed throughout a wide range of cancer cells. Cellular uptake of targeted MSNs into KB and HeLa cells and endosomal escape events were monitored with fluorescence live-cell-imaging. We aim to further develop the light-responsive opening mechanism by employing newly designed photo-switchable supported lipid membranes as capping systems around MSNs, thus avoiding the generation of singlet oxygen with this approach.

In chapter 5 the synthesis of a novel pH-responsive multifunctional drug delivery vehicle based on polymer-functionalized colloidal mesoporous silica nanoparticles (MSNs) is presented. The outer surface of core-shell MSNs is covalently modified with the bi-functional pH-responsive polymer poly(2-vinylpyridine) (PVP), which permits subsequent attachment of polyethylene glycol (PEG), targeting ligands (folate) and external triggers (red-light sensitive photosensitizer). The integrity of the polymer shell at different pH-values was investigated in detail with *in vial* and *in vitro* techniques. Additionally, stability tests in cell medium revealed an extraordinary shielding behavior towards inorganic components, implying a tight capping of the polymer shell and thus a long-term stability of the nano-vehicles, which is highly favorable for drug delivery applications. The system was successfully employed for the delivery of membrane-permeable and membrane-impermeable cargo molecules (DAPI and calcein, respectively) to different cell lines, and investigated with fluorescence live-cell imaging. First *in vivo* experiments in mouse models (not discussed in this thesis) were successfully carried out and yielded promising results. Therefore, future work with the newly developed pH-responsive nano-carriers will focus on the successful, targeted delivery of chemotherapeutics (e.g. doxorubicin) *in vivo*.

A major interest of this work was the development of organo-modified mesoporous silica nanoparticles with ultra-large pores ($7 - 15$ nm) and defined small sizes ($\leq 200$ nm, LP_MSNs), allowing multiple molecular functionalization (chapter 6). Both the successful optimization of

the pore diameter and the molecular functionalization of the mesopores in order to allow the facile control of diffusion and attachment of larger guest molecules into the host were demonstrated. An increase in pore diameter to values between 7 and 13 nm was achieved with different micellar expanders (TMB and TiPB) that partition into the surfactant aggregates. Moreover, high molecular weight surfactants (Pluronic F127) and a novel fluorinated co-surfactant (fluorocarbon surfactant FC-4) were employed at low synthesis temperatures (10 °C and 30 °C). The impact of specific hydrothermal treatment steps on the pore diameter was investigated in detail. Importantly, we reported for the first time the successful synthesis of organo-functionalized LP_MSNs (LP_MSN-SH, LP_MSN-NH$_2$/Ph and LP_MSN-N$_3$) via a co-condensation approach, allowing multiple prospective applications of the newly synthesized nanoparticles. Future work could address the fine-tuning of the developed hybrid nano-vehicles with ultra-large pores modified with recognition and trigger functions, ultimately allowing the control of various cell functions (e.g., endosomal escape events or the disruption of the cytoskeleton by cell-active cargo molecules).

Based on the newly generated LP_MSNs bearing azide-moieties (LP_ MSN-N$_3$), we also developed a colloidal nano-carrier system suitable for bioorthogonal click chemistry reactions (chapter 7). Enabling the immobilization/adsorption of larger biomolecules a basis for the great interest in LP_MSNs. We chose to immobilize two enzymes of different molecular dimensions, namely cytochrome C (CytC) and trypsin, in our LP_MSN-N$_3$. The peroxidase CytC (2.6 x 3.2 x 3.3 nm$^3$) and the protease trypsin (3.8 nm, spherical) were successfully modified with an alkyne-linker to allow for a click reaction under mild reaction conditions. Compared to the small amount of azide-functionalization present in the LP_MSNs, a high-density cargo immobilization was achieved in the LP_MSN-N$_3$. The activity of CytC immobilized within the large mesopores shows extraordinary high values, 2.9 times higher than the native enzyme in solution. We assume that the wall functionalities stabilize the conformational state of the enzyme. For immobilized trypsin, we also observed higher activity than reported in the literature. A promising future application of the successfully synthesized LP_MSN-CytC particles could be their use in antigen-detection tests in co-operation with Dr. S. Thalhammer from the Helmholtz Zentrum München.

In chapter 8, the successful synthesis of colloidal amino/phenyl-functionalized mesoporous silica nanoparticles with ultra-large pores (LP_MSNs), suitable for the post-synthesis modification with a red-light sensitive on-board photosensitizer and a DOPC-DOTAP supported lipid bilayer (SLB) for efficient pore capping was reported. This system provides an

on-demand release mechanism proven by *in vial* and *in vitro* cargo release experiments with model drugs of different sizes (calcein, propidium iodide, fluorescently-labeled dextran 10 kDa). Endosomal entrapment, a major bottle-neck in drug delivery applications, was successfully overcome upon activation of the photosensitizer with red-light after significant uptake into HeLa cells. We were able to successfully demonstrate the efficient delivery and release of small to large molecular weight cargos (up to 10 kD) from our SLB@LP_MSN-NH$_2$/Ph-AlPcS$_{2a}$. Future work based on this system could aim at the use of near-infrared or two-photon excitation for externally triggered cargo release, and the adsorption and intracellular release of oligonucleotides (e.g., siRNA). Additionally, other release mechanisms such as pH- or redox-triggered opening of gates together with the attachment of different targeting ligands (e.g. aptamers, antibodies) onto the outer surface of the nano-carriers for enhanced cell uptake should be addressed in future work.

Another project of this work was the organo-functionalization of MCM-41 with lithiated aromatic compounds, which was discussed in detail in chapter 9. Different 4-bromo arenes were reacted with *tert*-butyllithium (*t*BuLi) and subsequently with MCM-41 under mild reaction conditions. In detailed $^{13}$C MAS ssNMR studies it was shown that this approach (halogen-lithium exchange with 2 equivalents of *t*BuLi instead of lithiation with nBuLi) is highly favorable compared to previously described procedures, since only gaseous by-products are generated showing no side-reactions with the silica framework. Different functionalities were introduced into the mesoporous framework of MCM-41. The immobilized aromatic systems offer the possibility for further post-synthesis modification, yielding a flexible platform for custom-made modifications (e.g., for the synthesis of heterogeneous catalysts). We emphasize that the above procedure is not limited to MCM-41 but can also be employed with other mesoporous silica host systems such as SBA-15 or mesoporous silica nanoparticles. Summarizing, the direct modification of mesoporous hosts with aromatic molecules through silicon-carbon bonds was demonstrated to be a fast and highly efficient method offering a variety of possible post-synthesis modifications for mesoporous materials with potential for future applications.

In conclusion, the successful synthesis and characterization of tailor-made multifunctional mesoporous silica nanoparticles (MSNs) for advanced drug delivery applications was demonstrated in this work. MSNs with different pore sizes, particle morphologies and post-

synthesis functionalization were created, enabling the generation of stimuli-responsive release on-demand nano-carriers for controlled cargo delivery to meet the demands of targeted cancer therapy and diagnosis.